

Fall 12-18-2016

NOVEL CONCEPTS IN SEMICONDUCTOR DISK LASERS

Zhou Yang
University of New Mexico

Follow this and additional works at: https://digitalrepository.unm.edu/ose_etds



Part of the [Optics Commons](#)

Recommended Citation

Yang, Zhou. "NOVEL CONCEPTS IN SEMICONDUCTOR DISK LASERS." (2016). https://digitalrepository.unm.edu/ose_etds/
56

This Dissertation is brought to you for free and open access by the Engineering ETDs at UNM Digital Repository. It has been accepted for inclusion in Optical Science and Engineering ETDs by an authorized administrator of UNM Digital Repository. For more information, please contact disc@unm.edu.

Zhou Yang

Candidate

Physics and Astronomy

Department

This dissertation is approved, and it is acceptable in quality and form for publication:

Approved by the Dissertation Committee:

Mansoor Sheik-Bahae, Chairperson

Jeffrey G. Cederberg

Daniel Feezell

Arash Mafi

NOVEL CONCEPTS IN SEMICONDUCTOR DISK LASERS

BY

ZHOU YANG

B.S., Applied Physics, University of Science and Technology of China, 2008
M.S., Optical Science and Engineering, The University of New Mexico, 2010

DISSERTATION

Submitted in Partial Fulfillment of the
Requirements for the Degree of

**Doctor of Philosophy
Optical Science and Engineering**

The University of New Mexico
Albuquerque, New Mexico

Dec, 2016

© Zhou Yang, 2016

DEDICATION

To my family.

ACKNOWLEDGMENTS

First and foremost, I would like to thank my advisor Prof. Mansoor Sheik-Bahae for granting me the opportunity to work with him. He is always supportive of my ventures into various topics and discussions with him are always insightful. His advice has proved invaluable time and again when I've encountered difficulties in my research. His guidance continues to inspire and encourage me.

I owe Dr. Jeffrey Cederberg a great debt of gratitude for his help and encouragement throughout our collaboration. His state-of-the-art material growth technique allowed me to make much greater progress than would have otherwise been possible. I am also very grateful to Prof. Daniel Feezell for providing us with samples and for his insightful comments. I thank Prof. Arash Mafi along with all of my committee members for their time and constructive criticism. I particularly appreciate the astute observations of Prof. Kevin Malloy, and the thought-provoking discussions we engaged in.

I am also very grateful to my good friend and mentor, Dr. Alexander Albrecht, who first introduced me to the field of semiconductor disk lasers and who has so generously shared his expertise. His knowledge and superb instincts have helped me avoid many detours in my research. I also want to thank Klarissa Petti for proofreading this manuscript.

Working with this group has been a wonderful experience and I am honored to call its members my colleagues. A special thanks to Dr. Chengao Wang, for his instruction in the use of liftoff and bonding technology, which has made the research in this dissertation possible. Thank you to my "ultrafast" friends Dr. Chia-Yeh Li and Aram Gragossian for their multifaceted help and support. For loaning us great equipment, I would like to acknowledge Shawn Hackett. I am also very appreciative of other current and former group members, including Dr. Mike Hasselbeck, Dr. Wendy Patterson, Dr. Daniel Bender, Dr. Denis Seletskiy, Dr. Seth Melgaard, Mohammad Ghasemkhani, Nathan Giannini, Saeid Rostami, and Junwei Meng; I learned a great deal from each of them.

I am grateful to Behsan Behzadi, Ruslan Hummatov, and Dr. Stephen Boyd for their help with the COMSOL simulation, and to Noel Dawson and Douglas Wozniak for the AFM measurements. I am also thankful to Anthony Gravagne and other staff members in the mechanical shop for machining a great many high-quality and custom parts for me in a timely manner. Thanks also to all current and former front office staff for their assistance in placing orders.

Finally, I would like to thank my family. I am deeply indebted to them for their unwavering love and support during the past eight years. A special thank you to my parents, who have always encouraged me to pursue my dream and provided me with the environment necessary for doing so. Without their endless love, I could not have focused on my work. I want to thank my wife and parents-in law for their support and understanding.

NOVEL CONCEPTS IN SEMICONDUCTOR DISK LASERS

By

Zhou Yang

B.S., Applied Physics, University of Science and Technology of China, 2008
M.S., Optical Science and Engineering, The University of New Mexico, 2010
Ph.D., Optical Science and Engineering, The University of New Mexico, 2016

ABSTRACT

Optically-pumped semiconductor disk lasers (SDLs) have received much attention in recent years for a myriad of applications requiring intracavity access, good beam quality, wavelength versatility, and high output powers. The traditional scheme of these lasers feature a semiconductor distributed Bragg reflector (DBR) integrated with the active region, together forming an active mirror in an external free-space cavity. The active mirror component is fabricated by either epitaxial growth or post-growth processing. This places certain restrictions on SDL design, as material system choices become limited. It further

hinders laser performance with regard to its thermal management and laser bandwidth (tuning range).

This dissertation is concerned with developing SDL's without the integrated semiconductor DBR in order to mitigate the aforementioned restrictions. We exploit epitaxial lift-off and van der Waals bonding technique to investigate novel DBR-free SDL geometries. Active regions are directly bonded onto various destination substrates, such as right angle prisms forming a total internal reflection (TIR) geometry, or onto optical windows in a transmission arrangement. A quasi-continuous operation is demonstrated using TIR geometry while schemes for continuous-wave operation are proposed in standing wave as well as various monolithic ring cavities. We demonstrate a standing wave monolithic SDL cavity, and analyze its performance.

With the transmission geometry, multi-watt continuous-wave (CW) operation is achieved by employing single-crystal chemical vapor deposition (CVD) diamond windows as heatspreaders: 2 W output power is obtained at 1.15 μm , and more than 6 W is collected at 1 μm . Numerical thermal analysis suggests that DBR-free SDLs outperform traditional SDLs in thermal management when employing two diamond heatspreaders sandwiching the active region. Additionally, significantly broader wavelength tuning range (80 nm) is demonstrated compared with typical SDLs, in good agreement with our extended integrated modal-gain model. Implications of such bandwidth enhancement for mode-locking operation and ultrashort pulse generation is presented.

Finally, we propose a novel gain-embedded meta-mirror (GEMM) concept based on subwavelength grating structures. Our theoretical analysis show that an SDL constructed based on this concept could offer superior thermal management capability with promising potentials for high-power scaling.

Table of Contents

Chapter 1 Introduction

1.1	Outline.....	1
1.2	Semiconductor lasers	3
1.2.1	Semiconductor disk laser history.....	6
1.2.2	VECSELs: state-of-the-art.....	13
1.3	References.....	22

Chapter 2 DBR-free Semiconductor Disk Lasers: Analysis

2.1	DBR-free geometries: Advantages and opportunities.....	28
2.2	Thermal analysis.....	30
2.3	Integrated gain analysis.....	36
2.3.1	Integrated gain factor.....	38
2.3.2	Mode structure.....	43
2.4	Reflectance analysis: transfer matrix method.....	48
2.5	Summary.....	50
2.6	References.....	51

Chapter 3 DBR-free Semiconductor Disk Lasers: Device Fabrication

3.1	Introduction.....	53
3.2	Substrate surface cleaning and preparation.....	56
3.3	Lift-off and bonding.....	58
3.3.1	Lift-off	59

3.3.2 Bonding.....	65
3.3.3 Cleaning.....	66
3.4 Post-processing: thermal treatment.....	66
3.5 Surface quality study.....	69
3.5.1 Surface morphology study with optical microscope.....	70
3.5.2 Surface topography study with AFM.....	71
3.6 Photoluminescence and carrier lifetime characterization.....	73
3.7 Summary.....	74
3.8 References.....	75

Chapter 4 Total Internal Reflection Based DBR-free Semiconductor Disk Lasers

4.1 TIR DBR-free SDLs.....	79
4.1.1 Proof-of-concept: lasers near 1 μm	79
4.1.2 Laser designs for longer wavelength.....	85
4.2 Monolithic geometries.....	87
4.2.1 Monolithic standing-wave cavity geometry.....	88
4.2.2 Monolithic ring cavity designs.....	98
4.3 Summary.....	101
4.4 References.....	102

Chapter 5 Transmission Geometry DBR-free Semiconductor Disk Lasers

5.1 DHS based transmission geometry DBR-free SDL.....	104
5.2 QW based transmission geometry DBR-free SDLs at 1 μm	110
5.3 QW based transmission geometry DBR-free SDLs at 1.16 μm	124
5.4 Brewster's angle geometry DBR-free SDLs.....	129

5.5	Ring cavity geometry.....	131
5.6	Integrated gain model revisit: longitudinal mode spacing.....	135
5.7	PL peak blueshift analysis.....	138
5.8	Summary.....	142
5.9	References.....	144

Chapter 6 Summary and Outlook

6.1	Summary.....	149
6.2	Other approaches for power scaling.....	150
6.3	Mode-locking.....	152
6.4	High reflectivity subwavelength grating.....	155
6.4.1	Introduction to subwavelength grating.....	155
6.4.2	Guided mode resonance.....	157
6.5	References.....	162

Chapter 1

Introduction

1.1 Outline

Optically pumped semiconductor disk lasers (SDLs), also known as vertical external-cavity surface-emitting lasers (VECSELs) or optically pumped semiconductor lasers (OPSLs), are essentially regarded as versatile and efficient brightness converters when pumped by high-power diode lasers. These lasers, in general, offer the merits of high output power, good beam quality, wavelength flexibility, and intracavity access [1]. In the typical SDL design, semiconductor distributed Bragg reflectors (DBRs) are integrated behind the active region, as shown in Fig. 1.1, which poses certain restrictions for SDL design and performance. In this dissertation, we present novel SDL schemes, analysis, and implementation without using any semiconductor DBRs. To avoid confusion, we will henceforth refer to these lasers as DBR-free SDLs, and to the traditional SDLs with integrated semiconductor DBRs as VECSELs.

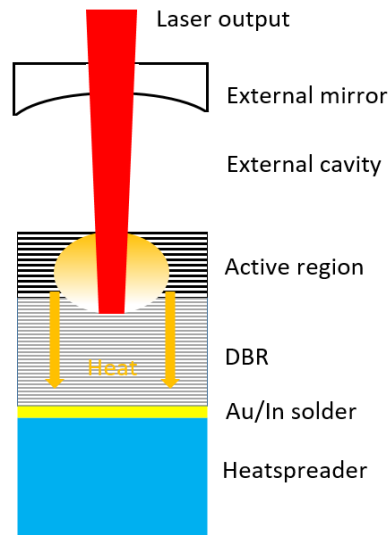


Figure 1.1 Schematic diagram of typical VECSEL with an extracavity heatspreader. The orange ellipse and arrows represent generated heat in the chip and heat diffusion process.

This dissertation is organized as follows:

Chapter 1 will briefly review semiconductor lasers, including edge-emitting lasers, surface-emitting semiconductor lasers, and state-of-the-art VECSELS.

Chapter 2 will elaborate on the motivation to discard the active mirror configuration, including the advantages of DBR-free geometries and the opportunities inherent therein, particularly from the perspectives of thermal management and integrated gain. With numerical thermal analysis, a comparison is made of the temperature increase in active regions among typical VECSEL and DBR-free SDL geometries. The integrated gain is analyzed with an extended integrated gain model, which shows distinct features on gain spectra for a DBR-free geometry. The results are compared with the full reflectance analysis based on the transfer matrix method.

Chapter 3 will describe the device fabrication process in detail, including substrate surface preparation, growth substrate lift-off, and device bonding. Results of post-bonding thermal treatments as they relate to improvement of bonding strength will also be discussed. In addition, surface morphology and topography of the bonding results using optical and atomic force microscopes will be studied. Finally, a comparison of photoluminescence spectra and carrier lifetime both before and after fabrication will be examined.

Chapter 4 will discuss total internal reflection (TIR) based DBR-free SDL designs, including a TIR based V-shaped cavity and a monolithic cavity, along with their laser performance characterizations.

Chapter 5 will focus on transmission based geometries. We will pay special attention to the high power continuous wave (CW) operation and broad laser tuning range, which have been achieved with the transmission geometry utilizing two distinct quantum well (QW) configurations. Then we will revisit the integrated gain model to compare its predictions with experimental results. For the bonded samples, the abnormal phenomena of photoluminescence peak blueshift with pump power will also be analyzed.

Chapter 6 will summarize the work and discuss the ongoing and future work on DBR-free SDLs. One of the directions is investigating other potential power scaling approaches, including the multichip and slab laser geometries. We also discuss the potential advantages

of DBR-free SDLs for mode-locking operation and ultrashort pulse generation. In that regard, we will present a few preliminary results with VECSELs, including the use of two-dimensional materials (TDMs), such as WS₂, as saturable absorbers. Finally, we introduce a novel active mirror concept, based on high reflectivity subwavelength gratings (SWG) bonded onto diamond heatspreaders, which we call gain-embedded meta-mirror (GEMM). We present preliminary analysis of such a structure with two quantum wells, and show the feasibility of laser operation, power scaling and its outstanding thermal management.

1.2 Semiconductor lasers

Shortly after the demonstration of laser in ruby in 1960 [2], the first semiconductor injection laser was reported in 1962 in GaAs p-n junction via electrical pumping [3]. With various material system choices and the bandgap engineering technique, as shown in Fig. 1.2, semiconductor lasers cover a significant portion of the spectrum from ultraviolet (UV) to mid-infrared (MIR). Most importantly, in contrast to gas or other solid state gain media, the active atomic species in semiconductors are closely packed and their wave functions interfere, forming broad band structures—conduction and valence bands—rather than discrete energy levels. For example, the energy level diagram of Nd³⁺ in Nd:YAG is shown in Fig. 1.3 (a). Rather than a few discrete states, semiconductors have continuum states, as shown in Fig. 1.3 (b), which provide a broad pump and laser wavelength choice. Furthermore, semiconductor active regions can be fabricated down to single atomic layer precision by epitaxial growth. With a double heterostructure—a narrow bandgap semiconductor layer sandwiched between two wide bandgap barrier layers—it forms a potential well for carriers. When the center layer thickness is comparable to the carriers' thermal de Broglie wavelength $\lambda_{\text{th}} = \frac{h}{p} = \frac{h}{\sqrt{2mkT}}$ (h is the Planck constant, m is the carrier effective mass, k is Boltzmann constant, and T is the temperature), the quantum confinement effect takes place and only discrete states are available. This can be utilized to tailor the density of states and the emission wavelength by tuning the layer thickness, providing QW-based semiconductor lasers with wavelength flexibility and low threshold. Additionally, semiconductor lasers are compact, reliable, and boast a long operational

lifetime. Semiconductor lasers have been integrated into test instrumentation, consumer electronics, such as cell phones (VCSEL based Time-of-Flight sensor), computer mice, and optical storage devices, and, most importantly, short, intermediate, and long distance telecommunication systems. With low cost and high power, semiconductor lasers are also widely used as optical pump sources for solid state and fiber lasers.

Based on cavity configurations, semiconductor lasers can be categorized as edge-emitting or in-plane lasers, and surface-emitting lasers. For an edge-emitting laser, the laser cavity is formed in the semiconductor layer plane and the laser is typically coupled out

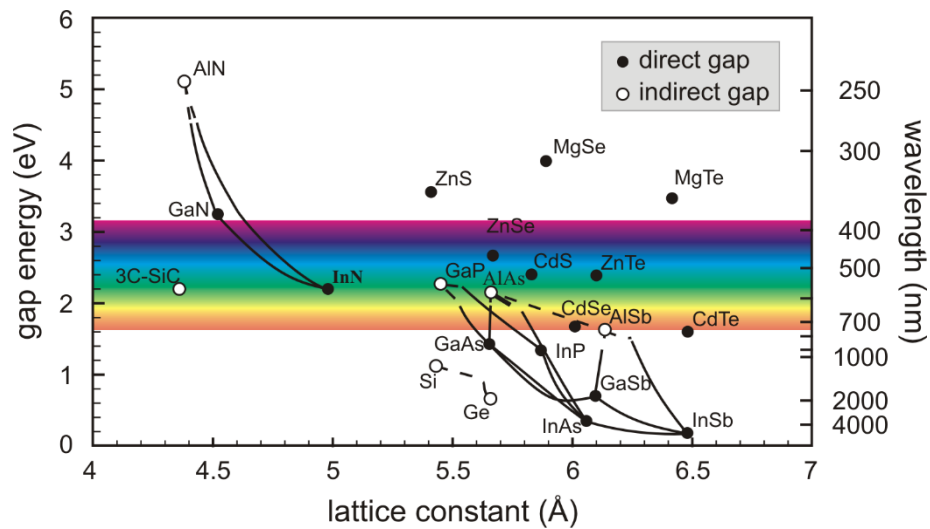


Figure 1.2 Common semiconductor material systems. All the bandgap values and lattice constants are for 300 K [4].

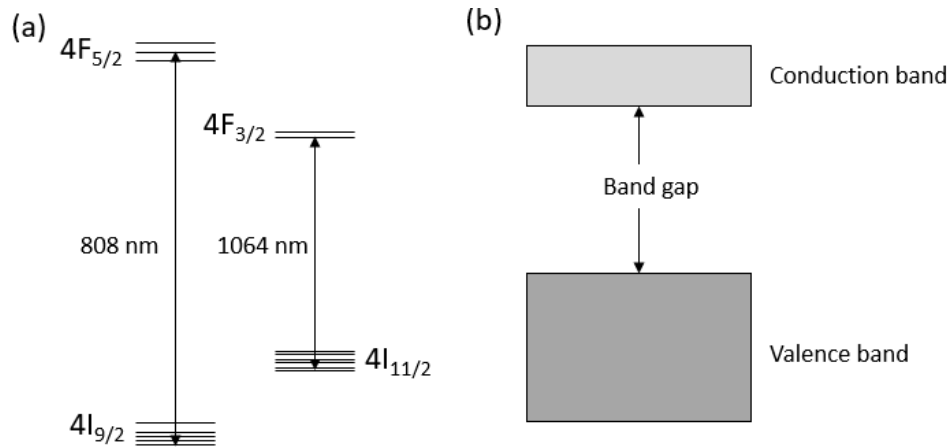


Figure 1.3 (a) The energy level structure and certain transitions of Nd^{3+} in Nd:YAG; (b) Semiconductor band structure.

from a cleaved facet mirror, as shown in Fig. 1.4 (a). Owing to their engineered density of states and the reduced threshold resulting therefrom, QWs are preferred as active regions. In edge-emitting lasers, carriers are usually generated through electrical injection. The excited carriers can recombine radiatively via stimulated emission, coupling into the laser mode. The spontaneous and nonradiative recombination pathways, such as defect and impurity recombination, or Auger recombination (collision with other carriers and deposition of extra energy in the semiconductor lattice), can reduce device efficiency and may increase the thermal load. Therefore, the confinement of current, carriers, and photons is crucial to device performance.

For carrier and optical mode confinement, a waveguide structure is usually introduced via lateral patterning and current confinement is realized with narrow strip electrodes. To scale up the power, a broader waveguide is needed, which results in multimode output. Due to internal heating and high laser intensity, the output power is limited by heat dissipation or optical damage. Multiple laser bars are routinely assembled into one-dimensional or two-dimensional arrays, forming high power modules with high efficiency but poor beam quality [5], which is suitable for many industrial and medical applications.

The first surface-emitting laser was demonstrated in 1966 [7], but became viable only after 1990 with the introduction of integrated semiconductor DBRs, wherein the laser cavity is formed perpendicular to the semiconductor layer plane with either two integrated semiconductor DBRs, such as vertical cavity surface-emitting lasers (VCSELs), as shown in Figs. 1.4 (b) and 1.5, or with one integrated DBR and at least one external mirror, such

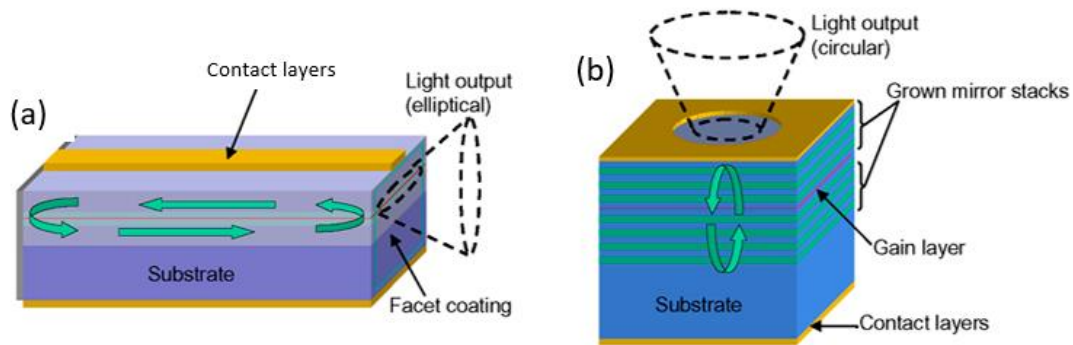


Figure 1.4 Semiconductor lasers schematics [6]: (a) Edge-emitting laser structure; (b) surface-emitting laser structure.

as a VECSEL. Typical VCSELs are electrically pumped, but optical pumping is also feasible. With an electrical pumping scheme, the active region is kept thin, less than one micrometer, due to the concern of electrical resistance and associated heating. In high power operation, higher order transverse modes are favored, due to internal heating or spatial-hole burning, and the beam quality degrades. VCSEL geometry allows for two-dimensional array arrangement [8], which provides output power up to tens of kilowatts with beam profile control. A detailed discussion of VECSEL development, design, and current progress will be presented in section 1.2.2.

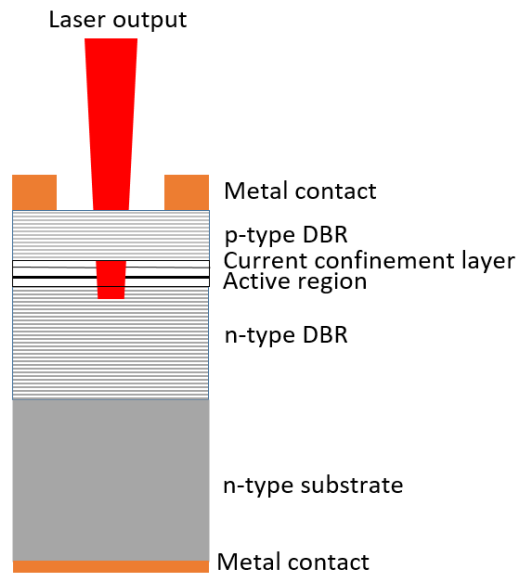


Figure 1.5 Schematic of an electrical-pumped VCSEL.

1.2.1 Semiconductor disk laser history

Even though the first high power VECSELs were not reported until 1997 [9], SDLs can be dated back to 1966 [7]. The first surface-emitting semiconductor laser [7] was optically pumped with a pulsed laser diode. The gain medium was a 2 μm thick, single-crystalline CdSe platelet, which was attached to the front surface of the pump laser diode via vacuum grease. The setup is shown in Fig 1.6. At 77 K, pulsed lasing was achieved. After analyzing the longitudinal mode spacing, it was found that the laser cavity actually consisted of the CdSe platelet and the air gap. The same group sandwiched a CdSe platelet between two sapphire heatspreaders, one of which was coated on one side with aluminum of 90%

reflectivity. With a He-Ne laser as pump source, CW operation was realized [10]. This was the first CW semiconductor laser at a visible wavelength. Unfortunately, this device worked at cryogenic temperatures and had fairly low power.

At almost the same time, a so called “radiating mirror”—essentially the active mirror of today—was proposed and demonstrated [11], as shown in Fig.1.7 (a). It included all the features of the current VECSEL design, except the resonant periodic gain structure (PGS): external cavity, active mirror geometry, and back side cooling. The heat extraction effectiveness was also emphasized. In experiments, GaAs, GaSe wafers, and CdSe plates were employed as gain media. The laser diagram for the latter is shown in Fig. 1.7 (b). By

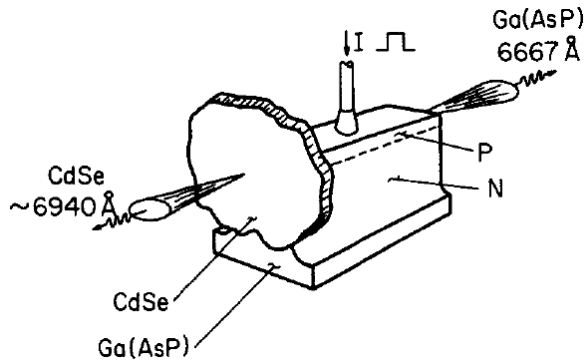


Figure 1.6 Laser setup for an ultrathin CdSe platelet laser [7]. The 2 μm thick single-crystalline CdSe platelet is mounted onto the front surface of a GaAsP diode laser with vacuum grease at 77 K. The diode operates quasi-continuously emitting at 666.7 nm.

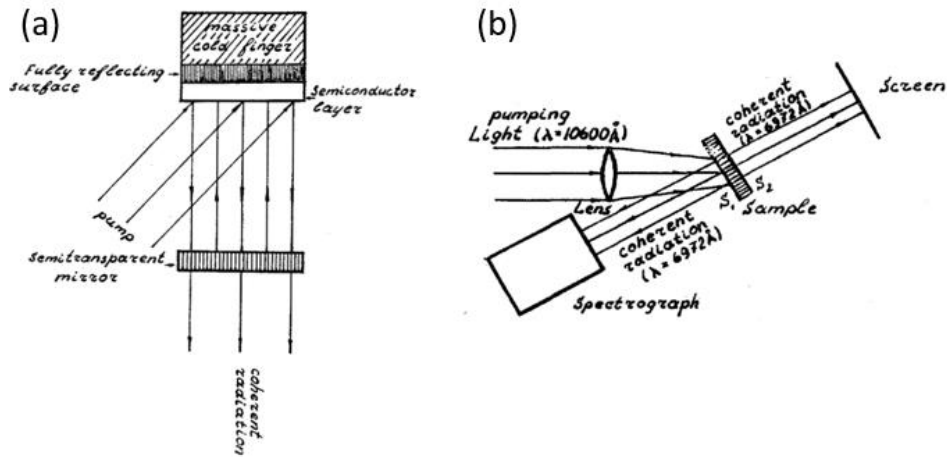


Figure 1.7 [11] (a) Schematic for a semiconductor laser design with an active mirror. The semiconductor active region layer is integrated with a fully reflecting surface, which is conveniently heat-sunk. Laser emission is perpendicular to the semiconductor’s multi-layer structure. (b) Block diagram of a two-photon pumped CdSe laser. The screen represents the spectrometer detection plane.

utilizing the uncoated semiconductor-air interfaces as mirrors, however, there were no external cavities and the active regions were heat-sunk from the areas surrounding the pump spots. All experiments were carried out under pulsed pumping conditions, by either an electron beam source or a Q-switched laser with two-photon pumping. Both the GaAs and CdSe lasers operated at 77 K, and only the GaSe laser at room temperature.

Another CdSe platelet laser with multilayer dielectric high reflective (HR) coatings on both surfaces was reported [12] and this is essentially a VCSEL geometry. Similar platelet gain media, including CdS, CdSSe, and InGaAsP, were further pursued with external cavity laser geometries [13] in the 1980s, some even achieving mode locking [14, 15]. In these laser setups, the platelet active regions were mounted with silicone oil onto sapphire mirrors, one side of which was HR coated, at cryogenic temperatures in a dewar, as shown in Fig. 1.8. The laser cavity was formed with an output coupler and a sapphire mirror. Shared between the pump and laser beams inside the cavity were a microscope objective and a polarizing beamsplitter. The pump spot was kept small, about 5 μm in diameter, so as to lower the thermal load and avoid lateral lasing. With a thin CdS platelet, CW operation was achieved with 9 mW pump power [13]. A dispersive element, either a prism [13] or birefringent filter [15], was inserted into the cavity for wavelength tuning and a tuning range of over 6 nm was observed [13]. The optical-to-optical efficiency was about 10% in CW operation, limited by the Fresnel reflection losses of the microscope objective. Similar lasers were further mode-locked using synchronous pumping [14] with a mode-locked argon laser. With 100 ps long pump pulses, output pulses as short as 4 ps were achieved with an optical-to-optical efficiency of up to 20% [15].

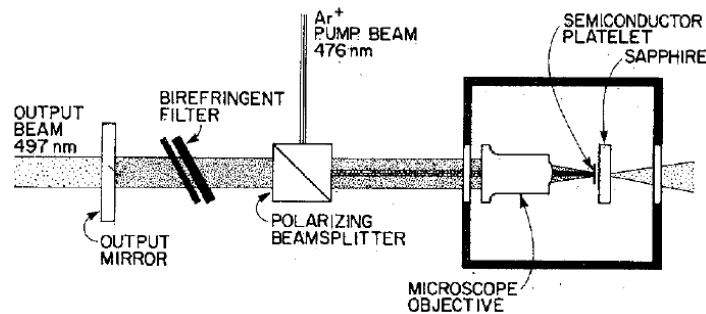


Figure 1.8 Schematic for optically pumped semiconductor platelet laser [15]. The semiconductor platelet is attached to a sapphire window in a dewar at cryogenic temperatures. The sapphire window is HR coated on the side opposite the sample.

There were also efforts to build an ultrashort external cavity semiconductor laser with dielectric mirrors [16]. Rather than being directly coated [12], mirrors were glued onto the active region, forming an ultrathin wedged cavity with 40-50 fs long cavity roundtrip time, as shown in Fig. 1.9. The active region was a double heterostructure sample with 0.6 μm thick GaAs surrounded by AlGaAs barrier layers. A mode-locked dye laser (0.9 ps pulses) was employed to pump the active region. Varying the pump position changed the cavity length and laser wavelength, and laser operation from 770 nm to 890 nm was observed. Such broad wavelength range was attributed to the high carrier density, approximately $2 \times 10^{20} \text{ cm}^{-3}$, which brought a significant amount of carriers into the L and X valleys. The output pulse width varied from 3 ps at 790 nm to 8 ps at 890 nm. With a similar geometry, about 1 ps pulses were observed [17]. It is also worth noting that the thin film was removed from the substrate by selective etching, or lift-off technology.

Using the lift-off technique and the ultrashort cavity geometry, thin film lasers with InGaAsP of various compositions [18] were reported lasing from 830 nm to 1590 nm. An image of a epoxied film-mirror assembly is shown in Fig. 1.10. Interference fringes were observed between the top mirror and the thin film.

After being ignored for a long time thereafter, the idea of optically pumped surface-emitting lasers was revived in 1991 [19]. The laser geometry is shown in Fig. 1.11. A mechanically thinned, broadband anti-reflection (AR) coated GaAs wafer was mounted onto an air-cooled copper heat sink. The pump laser was a gain switched Ti:sapphire laser near the GaAs bandgap with 38 ns, 2.5 kW peak power pulses at a 4 kHz repetition rate.

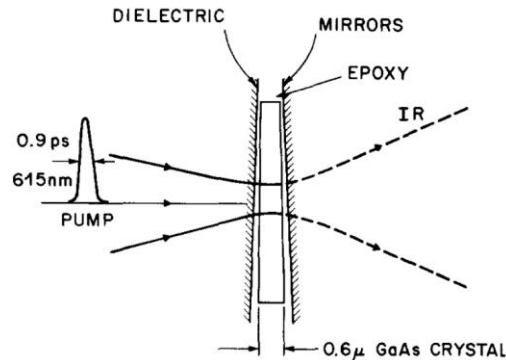


Figure 1.9 Schematic for an optically pumped semiconductor laser in an ultrashort wedged cavity [16]. The GaAs double heterostructure sample is epoxied between two HR mirrors.

Because of the high pump peak power, it was possible to use a 135 μm thick wafer as the gain medium. The output pulses were about 20 ns, which meant the laser operated quasi continuously. Up to 40% peak power slope efficiency was obtained, corresponding to 28% overall efficiency. Peak output power up to 500 W was collected and the peak intracavity intensity was about 50% of the pump damage threshold. Further power scaling by increasing gain volume was also discussed.

In 1997 the first optically pumped high power VECSEL was demonstrated [9]. Since then, VECSELs have experienced rapid development, with significantly improved critical parameters (including power, wavelength coverage, and linewidth), enabling their function in a wide variety of applications. To date, the endeavors were almost exclusively focused on the successful active mirror geometry, in spite of some intrinsic limitations, which will be mentioned in section 2.1.

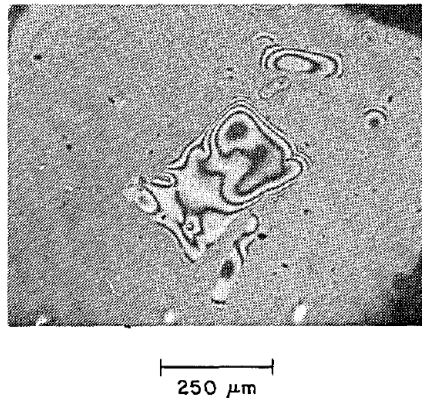


Figure 1.10 Thin film laser (InGaAsP film epoxied between two dielectric mirrors) imaged with monochromatic light [18]. The glue was measured to be about 0.1 μm thick with an electron microscope and the film was about 1 μm thick, 220 μm by 330 μm in area. Fringes are due to interference between the upper mirror and the top surface of the film.

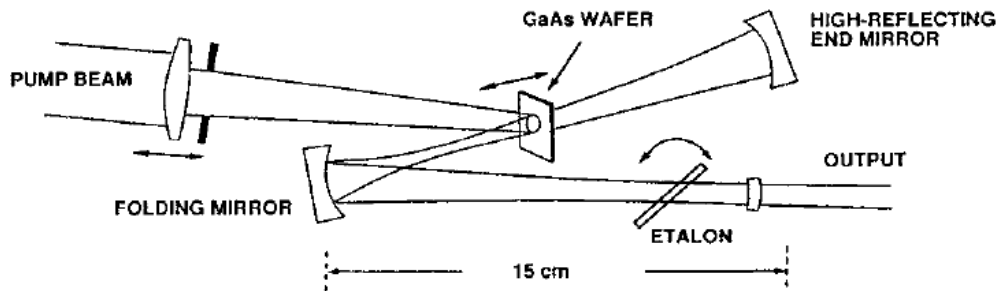


Figure 1.11 Schematic for optically pumped GaAs disk laser [19]. The GaAs wafer is 135 μm thick and is pumped with a gain switched T:sapphire laser at 2.5 kW peak pump power.

The InP-based material system, where no good semiconductor DBR exists, hindered the development of longer-wavelength (between 1.3 μm and 1.6 μm) VECSELs for a long time. In [20], the solution was to replace the integrated semiconductor DBR with an external mirror, like the later mentioned DBR-free geometry, but without lift-off and bonding processes. The gain structure consisted of an InP window layer to restrain surface combination and oxidation, 30 groups of dual AlGaInAs QWs in a PGS, and a laser transparent Fe-doped InP substrate as the mechanical support.

This experimental configuration is shown in Fig. 1.12. A diode pumped Q-switched Nd:YAG laser at 1064 nm was utilized to pump the active region in the barrier pumping scheme. With a pump transparent mirror, the geometry enabled direct end-pumping, leading to better pump and laser mode overlap. At 5 kHz pump pulse repetition rate, up to 1.5 kW peak output power was collected with 8.3 kW peak pump power and about 18% slope efficiency. This was the first room temperature high-peak-power nanosecond semiconductor QW laser at 1360 nm.

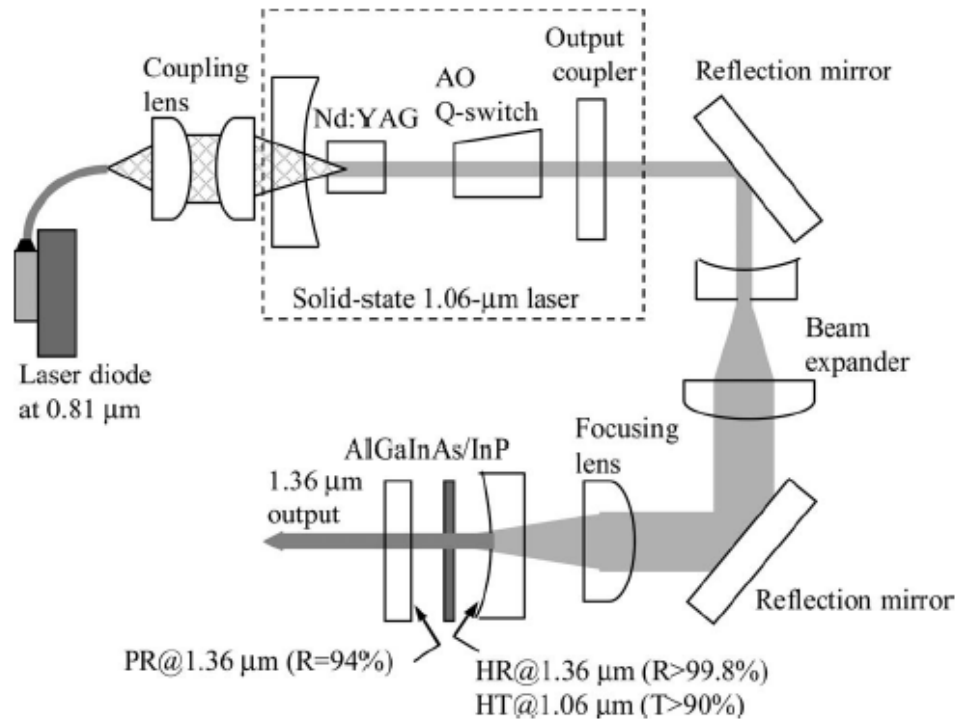


Figure 1.12 Schematic for room temperature optically pumped AlGaInAs laser at 1360 nm [20]. The pump source is a Q-switched Nd:YAG laser at 1064 nm. Both wafer surfaces are AR coated. The active region is mounted on a copper heat sink without active cooling.

The same group reported a similar wafer design, consisting of an eye-safe 1570 nm laser with 290 W peak output power [21]. In the plano-plano cavity, the thermal lens effect helped to stabilize the cavity. No active cooling was applied to the active region.

In reference [22], the substrate was capillary bonded onto a diamond, which was both high transmission (HT) coated at the pump wavelength and HR coated at the laser wavelength, and acting as both a mirror and heatspreader. The laser schematic is shown in Fig. 1.13 (a). This idea was extended with two diamond heatspreaders (one diamond was HT coated for the pump laser and HR coated for the laser, while the other was HR coated for the pump laser and HT for the laser). Two configurations—a stack cavity and separate cavity configurations [23]—are shown in Figs. 1.13 (b) and (c), respectively. Silicon wafers were employed as output couplers (OCs) and both copper mounts were cooled with

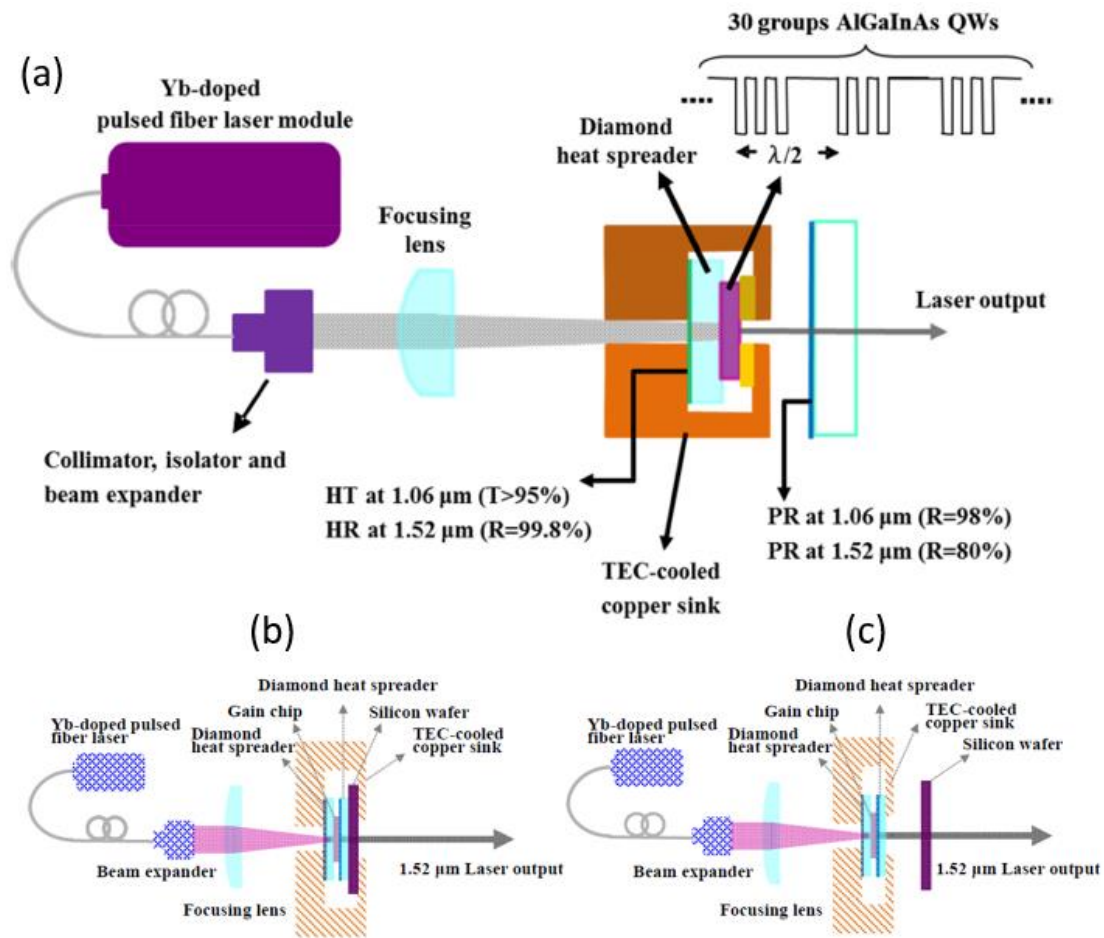


Figure 1.13 Different heat extraction schemes: (a) with single diamond heatspreader [22], (b) and (c) with double diamond heatspreaders [23] eye-safe laser geometries. (b) and (c) are the silicon output coupler stack cavity and separate cavity configurations.

thermoelectric coolers (TECs).

Under pulsed pumping condition, such laser geometry works well for an InP material system. This approach, however, is not widespread, since laser transparent growth substrates are not available for most material systems. In contrast, with the lift-off and van der Waal bonding technique, which will be discussed in chapter 3, there is no laser transparency requirement on growth substrates. In addition, thermal conductive heatspreaders can be bonded directly onto active regions, and thereby have much lower thermal resistance.

1.2.2 VECSELS: state-of-the-art

One way to scale up VCSEL output power without sacrificing beam quality is to expand the fundamental mode size, which requires good thermal management and uniform pumping schemes. These are difficult to achieve for the monolithic VCSEL geometry. A half-VCSEL configuration, typically called a VECSEL, achieved by replacing one of the integrated semiconductor DBRs with an external mirror, was demonstrated by Kuznetsov et al. [9] in 1997 with more than 500 mW output power in TEM₀₀ mode.

With larger size cavity modes, it is challenging to electrically pump the active region efficiently and uniformly, due to Joule heating and Coulomb interaction. Therefore, the optical pumping scheme is adopted. Either the barrier layers or QWs (or quantum dots, QDs) (in-well pumping) [24] can be optically pumped, leading to different quantum defects, which is the energy difference between pump photon and emission photon. To make good use of the pump power, optically pumped VECSELS' active regions are much thicker than VCSEL's.

For higher modal gain, the discrete gain layers (QW or QD) are positioned at the antinodes of the standing wave and the window layer thickness is carefully designed to align the semiconductor subcavity resonance with the design wavelength at the lasing condition, forming a resonant periodic gain (RPG) structure [25]. Compared to bulk gain medium, the RPG doubles the modal gain [25]. A wide-gap window layer is grown on top of the active region, to confine the generated carriers and reduce surface recombination

losses. A VECSEL chip structure is shown in Fig. 1.14. In the material growth process, this structure can be grown in two configurations, either the bottom emitter or the top emitter, depending on whether the active region or the DBR is grown first. Top emitters are convenient for growth diagnosis, while bottom emitters can be easily heat-sunk from the back of the DBR via soldering to an extracavity heatspreader, such as diamond.

A typical VECSEL chip forms a subcavity, with approximately 100% reflectivity from the semiconductor DBR and 30% reflectivity from the air-semiconductor interface. The subcavity effect strongly modulates the effective gain. By adjusting the window layer thickness, it can transit from a resonant to antiresonant cavity, which may affect the laser bandwidth. Due to the thermo-optic effect, the subcavity effect is temperature dependent, which has been used to check subcavity structure. With an optimum wafer design, the QW gain peak overlaps with the subcavity resonance under the lasing condition at an elevated temperature, which can be confirmed with the temperature dependent reflectivity [26] of a top emitter chip. When the active region is overheating, both the material and modal gain could decrease, which leads to the drop in slope efficiency and even output power.

When pumping, the quantum defect and energy lost in nonradiative recombination are deposited in the active region as heat. In addition, semiconductor DBRs often absorb the pump leakage and generate heat. Without an efficient heat extraction scheme, increasing pump power raises the active region temperature. Further increasing pump power leads to

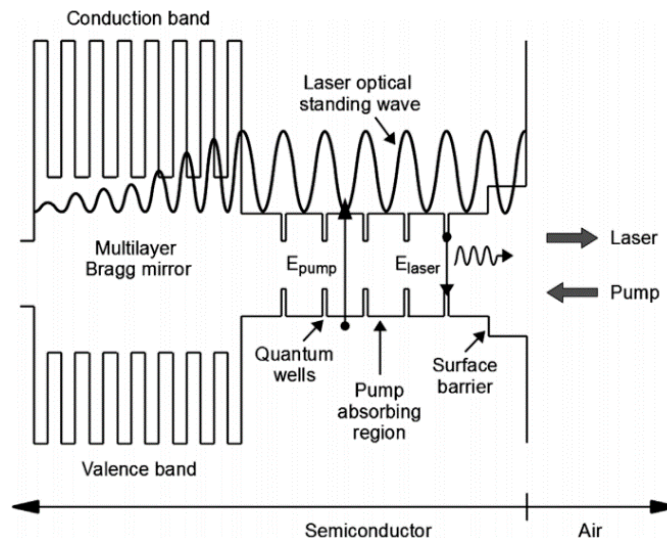


Figure 1.14 Optically pumped SDL chip structure and operating principles [1].

a drop of the material gain and at a certain degree, output power roll-over, as shown in Fig. 1.15 when pump power is higher than $P_{\text{roll-over}}$, and possibly even optical damage. Also, the effective gain, which is the overlap between the VECSEL subcavity resonance and the QW gain peak, is temperature dependent. The InGaAs QW gain peak usually redshifts at a rate of 0.3 nm/K and the subcavity resonance at 0.1 nm/K [27]. Therefore, thermal management is the key to VECSEL power scaling.

For a typical VECSEL geometry as shown in Fig. 1.1, the laser threshold condition [28] can be written as

$$R_{\text{DBR}} R e^{-\alpha} e^{2\Gamma g_{\text{th}} N_w d_w} = 1 \quad (1.1)$$

where R_{DBR} and R are the reflectivity of the integrated DBR and external mirror, α is total roundtrip loss coefficient, excluding the transmission from the mirror and DBR, Γ is the longitudinal mode confinement factor of the RPG structure [29], g_{th} is the threshold gain, N_w and d_w are the number and thickness of QWs. Therefore, the threshold gain is

$$g_{\text{th}} = \frac{\alpha - \ln(RR_{\text{DBR}})}{2\Gamma N_w d_w} \quad (1.2)$$

Right below threshold, there is no stimulated emission and the carrier rate equation is

$$\frac{dn}{dt} = \frac{\alpha_e P}{h\nu_p (\pi r_0^2)} - \frac{n}{\tau} \quad (1.3)$$

where n is the carrier density, P is the incident pump power, α_0 is the average pump

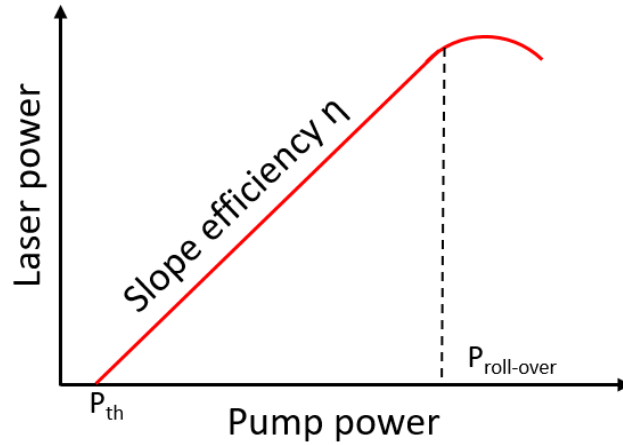


Figure 1.15 Laser output power as a function of pump power. P_{th} is the threshold pump power, η is the laser slope efficiency with respect to the incident pump power, $P_{\text{roll-over}}$ is the thermal rollover pump power.

absorption coefficient, ν_p is the pump frequency, h is Planck constant, r_0 is the pump spot radius (since the pump laser usually exhibits a flat-top intensity profile, there is no factor of $\frac{1}{2}$ like for a Gaussian beam), and τ is the carrier lifetime. With in-well pumping scheme, α_e is equal to α_w , which is the pump absorption coefficient in the QW; in contrast, with the barrier pumping scheme, $\alpha_e = \frac{2\alpha_b d_b + \alpha_w d_w}{d_w}$, where d_b and α_b are the barrier layer thickness and pump absorption coefficient. The pump is absorbed in both the thick barrier and thin QW layers. But since the carrier lifetime in QWs is much shorter than in the barriers, most generated carriers fall into the QWs and recombine there. At steady state, $dn/dt=0$ and the carrier density is

$$n_0 = \frac{\alpha_e P \tau}{h \nu_p (\pi r_0^2)} \quad (1.4)$$

With the three pathways previously mentioned, the carrier lifetime is

$$\frac{1}{\tau} = A + Bn + Cn^2 \quad (1.5)$$

where A , B , and C are the coefficients of nonradiative, radiative, and Auger recombination. A phenomenological expression of QW gain is

$$g = g_0 \ln\left(\frac{n}{n_{tr}}\right) \quad (1.6)$$

where g_0 is a fitting parameter and n_{tr} is the transparency carrier density. For high-Q cavities used in typical VECSELs, this is a good approximation. The threshold carrier density n_{th} is

$$n_{th} = n_{tr} e^{\frac{\alpha - \ln(RR_{DBR})}{2\Gamma N_w d_w g_0}} \quad (1.7)$$

By bringing the threshold carrier density back to Eq. 1.4, the threshold pump power is

$$P_{th} = \frac{h \nu_p (\pi r_0^2)}{\alpha_e \tau} n_{tr} e^{\frac{\alpha - \ln(RR_{DBR})}{2\Gamma N_w d_w g_0}} \quad (1.8)$$

As shown in Fig. 1.15, when the pump power is between P_{th} and $P_{roll-over}$, the output power scales linearly with the pump power $P_{output} = \eta(P - P_{th})$, where η is the laser slope efficiency. The efficiency η depends on multiple factors: pump absorption efficiency η_{abs} ,

quantum defect η_q , internal quantum efficiency η_{int} , and output coupling efficiency η_{oc} . Assuming barrier pumping, the pump absorption efficiency is

$$\eta_{abs} = e^{-N_w(\alpha_w d_w + 2\alpha_b d_b)} \quad (1.9)$$

and the quantum defect is the photon energy ratio between laser and pump photon,

$$\eta_q = \frac{h\nu_l}{h\nu_p} = \frac{\lambda_p}{\lambda_l} \quad (1.10)$$

The internal quantum efficiency η_{int} is the portion of carriers resulting in stimulated emission and its analytical expression can be solved with rate equations. It depends on the intracavity power, carrier density (pump power), and material parameters. The output coupling efficiency is

$$\eta_{oc} \approx \frac{(1 - R)}{2 - R - e^{-2\alpha}} \quad (1.11)$$

The laser slope efficiency can be written as

$$\eta = \eta_{abs}\eta_q\eta_{int}\eta_{oc} \quad (1.12)$$

Another important parameter for a VECSEL is the roll-over pump power $P_{roll-over}$. The detailed thermal roll-over mechanism was described previously and it is complicated to derive analytically for multiple reasons: First, the temperature raise in the active region strongly depends on the wafer design and thermal management scheme. Second, the prediction of temperature dependent material gain involves detailed microscopic modeling [30]. For high power operation, high roll-over pump power is needed. One way to increase the value, is to decrease heat generation, by improving the material quality (higher η_{int}) and reducing the quantum defect (higher η_q); the other way is to facilitate heat extraction from the active region.

For VECSELs, one common thermal management approach is to apply cooling power behind the DBR, resulting in the heat flow from VECSEL chip to heatsink being approximately one-dimensional. To facilitate heat conduction, the high thermal resistance growth substrate is usually either thinned or fully removed. For the latter, the bottom emitter chip is usually flip-chip soldered onto a high thermal conductivity extracavity heatspreader, like diamond, and the substrate is subsequently removed by wet etching. For

top emitters, heat can be removed from the active region with a capillary bonded intracavity heatspreader, with low thermal resistance and optical losses. Extracavity heatspreaders can be either directly cooled with water jet impingement [31] or TECs, or indirectly cooled by attaching them to a liquid-cooled mount. Intracavity heatspreaders are usually cooled indirectly, although recently a front liquid cooling scheme [32] has also been proposed.

For a VECSEL chip, a simple straight cavity can be formed with a concave external mirror. A V-shaped cavity, as shown in Fig. 1.16 (a) is also common. More complicated cavity configurations, like Z-shaped cavities and even double V ring cavities [33], have been reported.

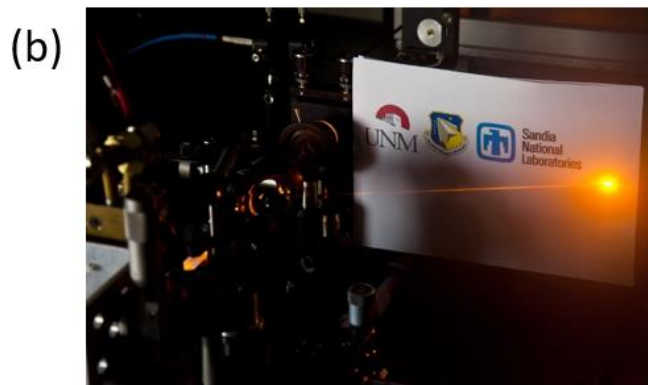
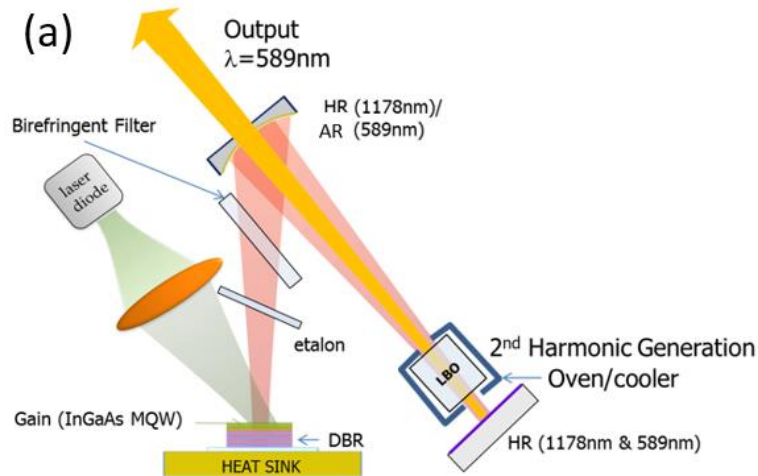


Figure 1.16 (a) Schematic for intracavity frequency doubled VECSEL at 1178 nm. Birefringent filter plate and etalon are inserted for wavelength tuning. LBO is a nonlinear optic crystal for second harmonic generation. The turning curved mirror is HR coated at 1178 nm and AR coated at 589 nm, and the end mirror after the oven is HR coated at both 1178 nm and 589 nm. (b) Second harmonic output at 589 nm [34].

Due to extra thermal resistance, perfect power scaling is still out of reach. To date, VECSELs have been demonstrated with more than 100 W output power near 1 μm [35], and more than 50 W at 1.178 μm [36]. Under optimum output coupling condition, near 1 μm , typical diode pumped InGaAs QW-based VECSELs achieve about 40% slope efficiency with respect to incident pump power.

Semiconductor lasers are known for broad gain bandwidth. By inserting a birefringent filter (BRF) into the cavity at Brewster's angle, the lasing wavelength can be tuned. Compared to edge-emitting lasers [37] with similar QW composition, however, SDLs have shown much narrower tuning range. Many efforts were devoted to broadening the gain spectrum, including improving the material gain bandwidth with QDs or QWs of various compositions, and modifying the PGS design. To date, a specially designed InGaAs QW based VECSEL with 43 nm [38] and a QD based VECSEL with 60 nm tuning range [39] have been reported, both near 1 μm . In comparison, an InGaAs QW-based external cavity edge-emitting laser has demonstrated a tuning range of up to 170 nm [37]. The reasons for this will be discussed in further detail in section 4.3. High power single-frequency operation has also been achieved with BRF and/or etalon [40].

Due to easy access to the high intracavity power, VECSELs have been used for cavity enhanced absorption measurements and nonlinear conversion processes, such as laser spectroscopy [41] and intracavity laser cooling of rare-earth doped solids [42]. Significant expansion of VECSELs' wavelength coverage is possible through nonlinear processes such as second harmonic generation, sum [43] and difference [44] frequency generation, and optical parametric oscillation [45], thus enabling various applications [46, 47]. As shown in Fig. 1.16 (b), an LBO crystal is employed for intracavity second harmonic generation in a VECSEL lasing at 1178 nm. Currently, commercial optically pumped frequency doubled VECSELs at 532 nm (Sapphire series and Verdi G, from Coherent Inc. [48]) can provide up to 20 W power and frequency tripled VECSELs are also available [49].

Mode-locked VECSELs have also experienced rapid progress. Due to their relatively broad gain bandwidth, VECSELs are good for ultrashort pulse generation. For a long time, VECSELs were passively mode locked with semiconductor saturable absorber mirrors (SESAMs) [50], which usually consists of a semiconductor DBR with low-temperature

grown QW or QD layers [51] to achieve short recovery time. A typical SESAM mode-locked VECSEL setup is shown in Fig. 1.17. Compared to other mode-locked solid state lasers, VECSELs have much higher repetition rates, usually in the GHz range, good for optical frequency comb applications. With short carrier lifetime, mode-locked VECSELs are free from Q-switching instability. SESAMs have also been monolithically integrated into the VECSEL chips, forming the MIXSEL (mode-locked integrated external-cavity surface-emitting laser) [52], which allows short cavity geometries with a repetition rate of up to 100 GHz. To date, using SESAMs, optical peak powers levels up to a few kilowatts and pulse durations on the order of 100 fs [51] have been reported. Other saturable absorbers and mode-locking mechanisms are pursued for applications which require higher peak power, such as micromachining.

Of particular interest are single-layer graphene films. With its unique band structure, graphene has a constant absorption of 2.3% over a broad band ranging from visible to near infrared (NIR) [53]. With such large absorbance and limited states, the intraband transition can be saturated under high excitation due to Pauli blocking [54] and this saturation process is broadband with fast recovery time. The parameters, including unsaturated loss, modulation depth, and saturation fluence, when integrated onto a mirror, can be engineered by varying the position relative to the end mirror [55, 56]. With this approach, an average output power of up to 10 W and about 350 fs pulses have been reported [56]. In addition to graphene, many other graphene analogues—TDMs—have been studied extensively as

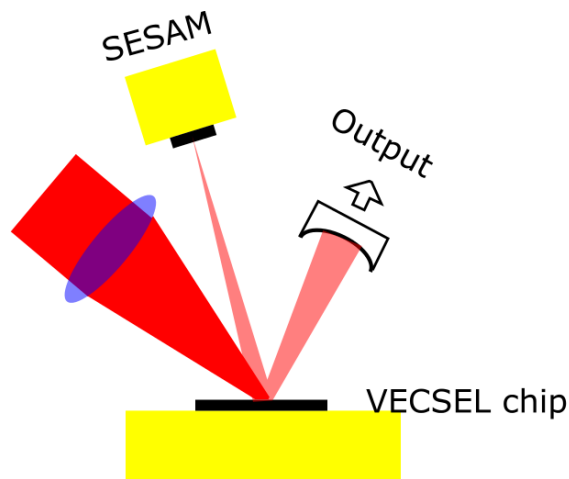


Figure 1.17 Schematic of typical SESAM mode-locked VECSEL.

saturable absorbers. Black phosphorus, for example, has demonstrated even better characteristics [57] than graphene. However, to the best of our knowledge, there has been no report on VECSELs mode-locked with a TDM other than graphene.

Recently, reports of SESAM-free or self-mode-locked VECSELs [58, 59, 60] have attracted considerable attention. Even though pulsing behavior was instable (long-term instability and CW background) during first observations, stable mode-locking operation was later demonstrated [61] with sub-picosecond pulses. Our group first proposed negative Kerr-lensing in the active region as the mode-locking mechanism [62] and, based on the estimated n_2 coefficient for the active region, a hard aperture was inserted into the cavity, as shown in Fig. 1.18 (a). Mode-locking operation can be initiated by adjusting either the aperture opening (hard aperture) or pump focus (soft aperture), as shown in Fig. 1.18 (b). With the z-scan technique, the measured nonlinear coefficient of the gain structure under pumping [63] is close to the estimation in [62]. The Kerr-lens mode-locking mechanism allows simple and cost-effective ultrafast SDL designs, and potentially higher peak powers.

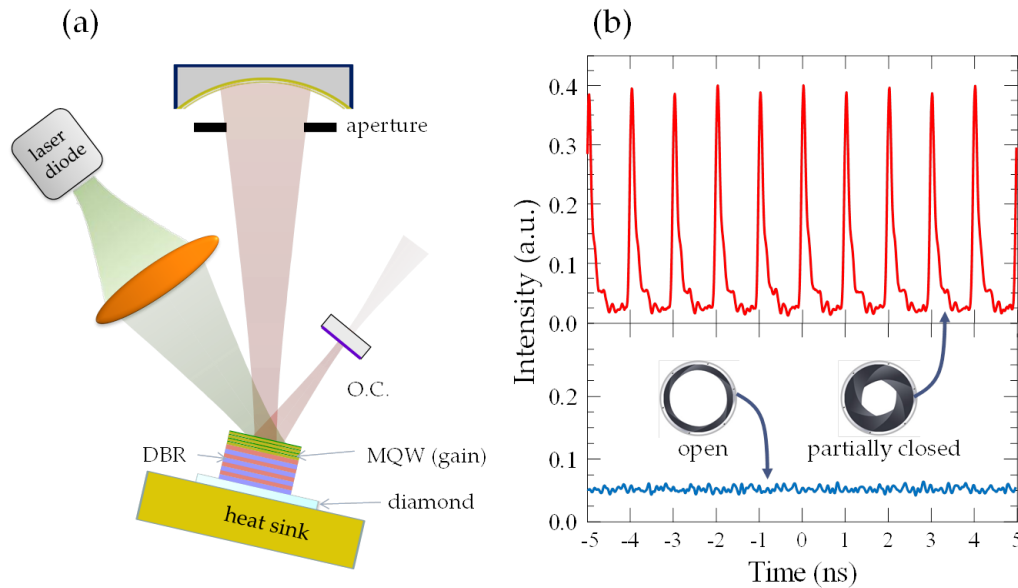


Figure 1.18 (a) V-shaped VECSEL cavity schematic. A hard aperture is inserted near the curved mirror for mode control. (b) Laser time-traces for fully open (blue trace, CW) and partially-closed (red trace, pulse train) aperture [62].

1.3 References

- [1] O. G. Okhotnikov, *Semiconductor Disk Lasers*, Wiley-VCH, 2010.
- [2] T. H. Maiman, "Stimulated optical radiation in ruby," *Nature*, vol. 187, pp. 493-494, 1960.
- [3] R. N. Hall, G. E. Fenner, J. D. Kingsley, T. J. Soltys, and R. O. Carlson, "Coherent light emission from GaAs junctions," *Phys. Rev. Lett.*, vol. 9, no. 9, pp. 366-368, 1962.
- [4] S. Montanari, "Fabrication and characterization of planar Gunn diodes for monolithic microwave integrated circuits," Ph. D dissertation, University of Aachen, RWTH, Germany, 2005.
- [5] F. Bachmann, P. Loosen, and R. Poprawe, *High Power Diode Lasers: Technology and Applications*, New York: Springer-Verlag, 2007.
- [6] J.-F. Seurin, "Harnessing light for high-power applications," SPIE Newsroom, 2009.
- [7] G. E. Stillman, M. D. Sirkis, J. A. Rossi, M. R. Johnson, and N. Holonyak Jr., "Volume excitation of an ultrathin single-mode CdSe laser," *Appl. Phys. Lett.*, vol. 9, no. 7, pp. 268-269, 1966.
- [8] H. Moench, R. Conrads, C. Deppe, G. Derra, S. Cronenborn, X. Gu, G. Heusler, J. Kolb, M. Miller, P. Pekarski, J. Pollman-Retsch, A. Pruijmboom, and U. Weichmann, "High power VCSEL systems and applications," *Proc. SPIE*, 9348, 93480W, San Francisco, CA, USA, 2015.
- [9] M. Kuznetsov, F. Hakimi, R. Sprague, and A. Mooradian, "High-power (>0.5 W CW) diode-pumped vertical-external-cavity surface-emitting semiconductor lasers with circular TEM₀₀ beams," *IEEE Photon. Technol. Lett.*, vol. 9, no. 8, pp. 1063-1065, 1997.
- [10] M. R. Johnson, N. Holonyak Jr., M. D. Sirkis, and E. D. Boose, "Volume excitation of an ultrathin continuous-wave CdSe laser at 6900 Å output," *Appl. Phys. Lett.*, vol. 10, no. 10, pp. 281-282, 1967.
- [11] N. G. Basov, O. V. Bogdankevich, and A. Z. Grasyuk, "Semiconductor lasers with radiating mirrors," *IEEE J. Quantum Electron.*, vol. QE-2, no. 9, pp. 594-597, 1966.
- [12] V. N. Smiley, A. L. Lewis, and H. F. Taylor, "Mode hopping and tuning of thin CdSe platelet lasers," *J. Opt. Soc. Am.*, vol. 60, no. 10, pp. 1321-1324, 1970.
- [13] C. B. Roxlo, D. Bebelaar, and M. M. Salour, "Tunable CW bulk semiconductor platelet laser," *Appl. Phys. Lett.*, vol. 38, no. 7, pp. 507-509, 1981.

- [14] C. B. Roxlo and M. M. Salour, "Synchronously pumped mode-locked CdS platelet laser," *Appl. Phys. Lett.*, vol. 38, no. 10, pp. 738-740, 1981.
- [15] C. B. Roxlo, R. S. Putnam, and M. M. Salour, "Optically pumped semiconductor platelet lasers," *IEEE J. Quantum Electron.*, vol. QE-18, no. 3, pp. 338-342, 1982.
- [16] T. C. Damen, M. A. Duguay, J. Shah, J. Stone, J. M. Wiesenfeld, and R. A. Logan, "Broadband tunable picosecond semiconductor lasers," *Appl. Phys. Lett.*, vol. 39, no. 2, pp. 142-145, 1981.
- [17] M. A. Duguay, T. C. Damen, J. Stone, J. M. Wiesenfeld, and C. A. Burrus, "Picosecond pulses from an optically pumped ribbon-whisker laser," *Appl. Phys. Lett.*, vol. 37, no. 4, pp. 369-370, 1980.
- [18] J. Stone, J. M. Wiesenfeld, A. G. Dentai, T. C. Damen, M. A. Duguay, T. Y. Chang, and E. A. Caridi, "Optically pumped ultrashort cavity $\text{In}_{1-x}\text{Ga}_x\text{As}_y\text{P}_{1-y}$ lasers: picosecond operation between 0.83 and 1.59 μm ," *Opt. Lett.*, vol. 6, no. 11, pp. 534-536, 1981.
- [19] H. Q. Le, S. Di Cecca, and A. Mooradian, "Scalable high-power optically pumped GaAs laser," *Appl. Phys. Rev.*, vol. 58, no. 18, pp. 1967-1969, 1991.
- [20] K. W. Su, S. C. Huang, A. Li, S. C. Liu, Y. F. Chen, and K. F. Huang, "High-peak-power AlGaInAs quantum-well 1.3 μm laser pumped by a diode-pumped actively Q-switched solid-state laser," *Opt. Lett.*, vol. 31, no. 13, pp. 2009-2011, 2006.
- [21] S. C. Huang, H. L. Chang, K. W. Su, A. Li, S. C. Liu, Y. F. Chen, and K. F. Huang, "AlGaInAs/InP eye-safe laser pumped by a Q-switched Nd:GdVO₄ laser," *Appl. Phys. B*, vol. 94, pp. 483-487, 2009.
- [22] C.-P. Wen, P.-H. Tuan, H.-C. Liang, K.-F. Huang, and Y.-F. Chen, "Compact high-peak-power end-pumped AlGaInAs eye-safe laser with a heat-spreader diamond coated as a cavity mirror," *IEEE J. Sel. Top. Quantum Electron.*, vol. 21, no. 1, pp. 1500105, 2015.
- [23] C. P. Wen, P. H. Tuan, H. C. Liang, C. H. Tsou, K. W. Su, K. F. Huang, and Y. F. Chen, "High-peak-power optically-pumped AlGaInAs eye-safe laser with a silicon wafer as an output coupler: comparison between the stack cavity and the separate cavity," *Opt. Express*, vol. 23, no. 24, pp. 30749-30754, 2015.
- [24] S. S. Bayertt, M. Zorn, T. Kubler, H. Wenzel, M. Weyers, A. Giesen, G. Trankle, and U. Brauch, "Optical in-well pumping of semiconductor disk lasers with high optical efficiency," *IEEE J. Quantum Electron.*, vol. 41, no. 12, pp. 1439-1449, 2005.
- [25] M. Y. A. Raja, S. R. J. Brueck, M. Osinski, C. F. Schaus, J. G. McInerney, T. M. Brennan, and B. E. Hammons, "Resonant periodic gain surface-emitting semiconductor lasers," *IEEE J. Quantum Electron.*, vol. 25, no. 6, pp. 1500-1512, 1989.

- [26] J. L. Shen, C. Y. Chang, W. C. Chou, M. C. Wu, and Y. F. Chen, "Temperature dependence of the reflectivity in absorbing Bragg reflectors," *Opt. Express*, vol. 9, no. 6, pp. 287-293, 2001.
- [27] R. G. Bedford, M. Kolesik, J. L. A. Chilla, M. K. Reed, T. R. Nelson, and J. V. Moloney, "Power-limiting mechanism in VECSELs," *Proc. SPIE*, 5814, pp. 199-208, Bellingham, WA, USA, 2005.
- [28] M. Kuznetsov, F. Hakimi, R. Sprague, and A. Mooradian, "Design and characteristic of high-power (>0.5 W CW) diode-pumped vertical-external-cavity surface-emitting semiconductor lasers with circular TEM₀₀ beams," *IEEE J. Sel. Top. Quantum Electron.*, vol. 5, no. 3, pp. 561-573, 1999.
- [29] S. W. Corzine, R. S. Geels, J. W. Scott, R.-H. Yan, and L. A. Coldren, "Design of Fabry-Perot surface-emitting lasers with a periodic gain structure," *IEEE J. Quantum Electron.*, vol. 25, no. 6, pp. 1513-1524, 1989.
- [30] J. Hader, G. Hardesty, T.-L. Wang, M. J. Yarborough, Y. Kaneda, J. V. Moloney, B. Kunert, W. Stolz, and S. W. Koch, "Predictive microscopic modeling of VECSELs," *IEEE J. Quantum Electron.*, vol. 46, no. 5, pp. 810-817, 2010.
- [31] A. R. Albrecht, T. J. Rotter, C. P. Hains, A. Stintz, G. Xin, T.-L. Wang, Y. Kaneda, J. V. Moloney, K. J. Malloy, and G. Balakrishnan, "High-power 1.25 μm InAs QD VECSEL based on resonant periodic gain structure," *Proc. SPIE*, 7919, 791904, San Francisco, CA, USA, 2011.
- [32] C. J. C. Smyth, S. Mirkhanov, A. H. Quarterman, and K. G. Wilcox, "Thermal management of VECSELs by front surface direct liquid cooling," *Proc. SPIE*, 9734, 973413, San Francisco, CA, USA, 2016.
- [33] T. J. Ochalski, A. de. Burca, G. Huyet, J. Lyytikäinen, M. Guina, M. Pessa, A. Jasik, J. Muszalski, and M. Bugajski, "Passively modelocked bi-directional vertical external ring cavity surface emitting laser," in *CLEO*, San Jose, CA, USA, 2008.
- [34] A. R. Albrecht, "Private communication," 2015.
- [35] B. Heinen, T.-L. Wang, M. Sparenberg, A. Weber, B. Kunert, J. Hader, S. W. Koch, J. V. Moloney, M. Koch, and W. Stolz, "106 W continuous-wave output power from vertical-external-cavity surface-emitting lasers," *Electron. Lett.*, vol. 48, no. 9, pp. 516-517, 2012.
- [36] E. Kantola, T. Leinonen, S. Ranta, M. Tavast, J.-P. Penttinen, and M. Guina, "1180 nm VECSEL with 50 W output power," *Proc. SPIE*, 9349, 93490U, San Francisco, CA, USA, 2015.
- [37] L. E. Eng, D. G. Mehuys, M. Mittelstein, and A. Yariv, "Broadband tuning (170 nm) of InGaAs quantum well lasers," *Electron. Lett.*, vol. 26, no. 20, pp. 1675-1677, 1990.

- [38] C. Borgentun, J. Bengtsson, A. Larsson, F. Demaria, A. Hein, and P. Unger, "Optimization of a broadband gain element for a widely tunable high-power semiconductor disk laser," *IEEE Photon. Technol. Lett.*, vol. 22, no. 13, pp. 978-980, 2010.
- [39] M. Butkus, J. Rautiainen, O. G. Okhotnikov, C. J. Hamilton, G. P. A. Malcolm, S. S. Mikhlin, I. L. Krestnikov, D. A. Livshits, and E. U. Rafailov, "Quantum dot based semiconductor disk lasers for 1–1.3 μm ," *IEEE J. Sel. Top. Quantum Electron.*, vol. 17, no. 6, pp. 1763-1771, 2011.
- [40] F. Zhang, B. Heinen, M. Wichmann, C. Möller, B. Kunert, A. Rahimi-Iman, W. Stolz, and M. Koch, "A 23-watt single-frequency vertical-external-cavity surface-emitting laser," *Opt. Express*, vol. 22, no. 11, pp. 12817-12822, 2014.
- [41] A. Garnache, A. A. Kachanov, F. Stoeckel, and R. Planel, "High-sensitivity intracavity laser absorption spectroscopy with vertical-external-cavity surface-emitting semiconductor lasers," *Opt. Lett.*, vol. 24, no. 12, pp. 826-828, 1999.
- [42] A. R. Albrecht, D. V. Seletskiy, J. G. Cederberg, A. Di Lieto, M. Tonelli, J. V. Moloney, G. Balakrishnan, and M. Sheik-Bahae, "Intracavity laser cooling using a VECSEL," *Proc. SPIE*, 8275, 827505, San Francisco, CA, USA, 2012.
- [43] A. Harkonen, J. Rautiainen, T. Leinonen, Y. A. Morozov, L. Orsila, M. Guina, M. Pessa, and O. G. Okhotnikov, "Intracavity sum-frequency generation in dual-wavelength semiconductor disk laser," *IEEE Photon. Technol. Lett.*, vol. 19, no. 19, pp. 1550-1552, 2007.
- [44] M. Scheller, J. M. Yarborough, J. V. Moloney, M. Fallahi, M. Koch, and S. W. Koch, "Room temperature continuous wave milliwatt terahertz source," *Opt. Express*, vol. 18, no. 26, pp. 27112-27117, 2010.
- [45] D. J. M. Stothard, J.-M. Hopkins, D. Burns, and M. H. Dunn, "Stable, continuous-wave, intracavity, optical parametric oscillator pumped by a semiconductor disk laser (VECSEL)," *Opt. Express*, vol. 17, no. 13, pp. 10648-10658, 2009.
- [46] H. Lindberg, S. Illek, I. Pietzonka, M. Furitsch, A. Plöbl, S. Haupt, M. Kühnelt, R. Schulz, U. Steegmüller, T. Höfer, and U. Strauß, "Recent advances in VECSELs for laser projection applications," *Proc. SPIE*, 7919, 79190D, San Francisco, CA USA, 2011.
- [47] S. Ranta, M. Tavast, T. Leinonen, R. Epstein, and M. Guina, "Narrow linewidth 1118/559 nm VECSEL based on strain compensated GaInAs/GaAs quantum-wells for laser cooling of Mg-ions," *Opt. Mat. Express*, vol. 2, no. 8, pp. 1011-1019, 2012.
- [48] "Coherent Verdi G series," Coherent Inc., 4 10 2016. [Online]. Available: <http://www.coherent.com/products/?1851/Verdi-G-Series>.

- [49] "Optically pumped semiconductor laser," Coherent Inc., 4 10 2016. [Online]. <http://www.coherent.com/products/?771/Optically-Pumped-Semiconductor-Laser-OPSL-Technology>.
- [50] U. Keller, K. J. Weingarten, F. X. Kartner, D. Kopf, B. Braun, I. D. Jung, R. Fluck, C. Honninger, N. Matuschek, and J. Aus der Au, "Semiconductor saturable absorber mirrors (SESAM's) for femtosecond to nanosecond pulse generation in solid-state lasers," *IEEE J. Sel. Top. Quantum Electron.*, vol. 2, no. 3, pp. 435-453, 1996.
- [51] B. W. Tilma, M. Mangold, C. A. Zaugg, S. M. Link, D. Waldburger, A. Klenner, A. S. Mayer, E. Gini, M. Golling, and U. Keller, "Recent advances in ultrafast semiconductor disk lasers," *Light: Sci. Appl.*, vol. 4, pp. e310, 2015.
- [52] D. J. H. C. Maas, A.-R. Bellancourt, B. Rudin, M. Golling, H. J. Unold, T. Südmeyer, and U. Keller, "Vertical integration of ultrafast semiconductor lasers," *Appl. Phys. B*, vol. 88, no. 4, pp. 493-497, 2007.
- [53] R. R. Nair, P. Blake, A. N. Grigorenko, K. S. Novoselov, T. J. Booth, T. Stauber, N. M. R. Peres, and A. K. Geim, "Fine structure constant defines visual transparency of graphene," *Science*, vol. 320, pp. 1308, 2008.
- [54] Q. Bao, H. Zhang, Y. Wang, Z. Ni, Y. Yan, Z. X. Shen, K. P. Loh, and D. Y. Tang, "Atomic-Layer Graphene as a Saturable Absorber for Ultrafast Pulsed Lasers," *Adv. Funct. Mater.*, vol. 19, no. 19, pp. 3077-3083, 2009.
- [55] C. A. Zaugg, Z. Sun, V. J. Wittwer, D. Popa, S. Milana, T. S. Kulmala, R. S. Sundaram, M. Mangold, O. D. Sieber, M. Golling, Y. Lee, J. H. Ahn, A. C. Ferrari, and U. Keller, "Ultrafast and widely tuneable vertical-external-cavity surface-emitting laser, mode-locked by a graphene-integrated distributed Bragg reflector," *Opt. Express*, vol. 21, no. 25, pp. 31548-31559, 2013.
- [56] S. Husaini and R. G. Bedford, "Graphene saturable absorber for high power semiconductor disk laser mode-locking," *Appl. Phys. Lett.*, vol. 104, no. 16, pp. 161107, 2014.
- [57] Y. Wang, G. Huang, H. Mu, S. Lin, J. Chen, S. Xiao, Q. Bao, and J. He, "Ultrafast recovery time and broadband saturable absorption properties of black phosphorus suspension," *Appl. Phys. Lett.*, vol. 107, no. 9, pp. 091905, 2015.
- [58] L. Kornaszewski, G. Maker, G. P. A. Malcolm, M. Butkus, E. U. Rafailov, and C. J. Hamilton, "SESAM-free mode-locked semiconductor disk laser," *Laser Photonics Rev.*, vol. 6, no. 6, pp. L20-L23, 2012.
- [59] H.-C. Liang, Y.-C. Lee, J.-C. Tung, K.-W. Su, K.-F. Huang, and Y.-F. Chen, "Exploring the spatio-temporal dynamics of an optically pumped semiconductor laser with intracavity second harmonic generation," *Opt. Lett.*, vol. 37, no. 22, pp. 4609-4611, 2012.

- [60] A. R. Albrecht, D. V. Seletskiy, J. G. Cederberg, and M. Sheik-Bahae, "Self-mode-locked vertical external-cavity surface-emitting laser (VECSEL)," in *CLEO, CW1G.5*, San Jose, CA, USA, 2013.
- [61] M. Gaafar, P. Richter, H. Keskin, C. Möller, M. Wichmann, W. Stolz, A. Rahimi-Iman, and M. Koch, "Self-mode-locking semiconductor disk laser," *Opt. Express*, vol. 22, no. 23, pp. 28390-28399, 2014.
- [62] A. R. Albrecht, Y. Wang, M. Ghasemkhani, D. V. Seletskiy, J. G. Cederberg, and M. Sheik-Bahae, "Exploring ultrafast negative Kerr effect for mode-locking vertical external-cavity surface-emitting lasers," *Opt. Express*, vol. 21, no. 23, pp. 28801-28808, 2013.
- [63] E. A. Shaw, A. H. Quarterman, A. P. Turnbull, T. C. Sverre, C. R. Head, A. C. Tropper, and K. G. Wilcox, "Reflection z-scan measurements of the non-linear lens in VECSEL gain structures," *Proc. SPIE*, 9734, 97340L, San Francisco, CA, USA, 2016.

Chapter 2

DBR-free Semiconductor Disk Lasers:

Analysis

This chapter will discuss the advantages of DBR-free semiconductor disk lasers, and the opportunities inherent therein. Both thermal management and gain spectrum will be analyzed. For the latter, two approaches are adopted, including the position dependent integrated gain model and the transfer matrix method.

2.1 DBR-free geometries: Advantages and opportunities

As mentioned in section 1.1, typical VECSELs have a high reflectivity semiconductor DBR integrated behind the active region, as shown in Fig. 1.1. A DBR consists of multiple pairs of quarter-wave optical thick high (n_H) and low (n_L) refractive index layers. All the Fresnel reflection components from interfaces at the design wavelength constructively interfere. As a result, DBRs provide high reflectivity. Utilizing the transfer matrix method, at normal incidence and at the design wavelength, the reflectivity of integrated m DBR pairs is $R_{DBR} = \left[\frac{1 - (n_L/n_H)^{2m}}{1 + (n_L/n_H)^{2m}} \right]^2$ [1]. When the refractive index contrast (n_H/n_L) is large, less DBR pairs (m) are needed for the same reflectivity and broader HR bands can be achieved.

Compared with traditional VECSEL geometry, DBR-free geometries bring many changes in both SDL design and performance. First, DBR-free geometries greatly enrich SDLs' material system choices. For example, for the GaN system, it is challenging to epitaxially grow high reflectivity semiconductor DBRs (AlInN/GaN [2] and AlN/GaN [66] combinations), due to large lattice mismatch and distinct growth conditions. For InP and InGaP systems, which lack good semiconductor DBRs with low thermal resistance and

broad HR bandwidth due to small refractive index contrast, DBR-free geometries provide a solution.

Second, semiconductor DBRs have high thermal resistance [4] for extracavity heatsinking schemes. Because of the small refractive index contrast tens of semiconductor DBR pairs are typically needed. As a result, semiconductor DBRs are thick. For example, for the widely used GaAs/AlAs DBR, 25 pairs are needed for 99.9% reflectivity at 1 μm , of which the total thickness is 4.1 μm . For the $\text{In}_{0.18}\text{Ga}_{0.82}\text{As}_{0.4}\text{P}_{0.6}/\text{InP}$ DBR, only 95.5% reflectivity is obtained with 48 pairs at 1.55 μm , which is about 11.5 μm thick. Considering the relatively low thermal conductivity of semiconductor materials, thick semiconductor DBRs have high thermal resistance. Additionally, these interfaces, which scatter phonons, slow down the thermal diffusion process, and increase thermal resistance [5]. For some material systems, semiconductor ternary or quaternary alloys are used in DBRs due to limited material choices. Thermal conductivity coefficients of these compounds are lower than binary compounds, due to phonon scattering in alloys.

In these aforementioned material systems, semiconductor DBRs are thicker than active regions. DBR-free chips, therefore, have much shorter growth times and cost significantly less. As will be discussed in section 2.3.2, because DBR-free gain structures are typically far from the global cavity nodes, they are intrinsically more robust to growth errors.

Third, compared with semiconductor DBRs, dielectric DBR components have more choices and larger refractive index contrast, resulting in broader HR bandwidth. The HR band of total internal reflection is even broader. As a result, DBR-free geometries can support broader bandwidth than typical VECSELs. Also, the active mirror configuration may limit the laser gain bandwidth, as will be discussed in section 2.3.

Fourth, for many material systems, some semiconductor DBR components absorb at pump wavelengths, generating extra heat near active regions, which may impair the thermal management. A detailed thermal analysis will be presented in section 2.2.

Furthermore, the DBR-free approach brings in geometry flexibility. In cavities, lasers can either transmit through or be total internal reflected at active regions, rather than reflected by a semiconductor DBR. With the total internal reflection in particular, DBR-

free active regions allow for monolithic geometries, as will be discussed in section 4.2. In the transmission geometry, multi-pass pumping schemes are also viable.

2.2 Thermal analysis

Lasers usually take high energy, high entropy pump photons and convert them to low energy, low entropy photons, necessarily generating heat in this mode conversion process. As mentioned in section 1.2.2, microscopically, both the quantum defect and energy lost in the nonradiative recombination process will be converted to heat. Macroscopically, for SDLs the difference between the absorbed pump and laser power is the heat load, since the photoluminescence power is negligible. Semiconductor active regions are sensitive to temperature, due to the strong temperature dependence of carrier distribution. Overheating in active regions could decrease material gain, and even lead to optical damage. Thermal distribution in active regions also deteriorates the beam quality [6]. Efficient thermal management, therefore, is crucial to SDL's performance.

Thin-disk lasers with solid state gain media were demonstrated in 1994 [7]. With one surface of the gain disk attached to a heat sink, heat flow in the disk is nearly parallel to the laser propagation direction [8]. The one-dimensional heat flow allows for power scaling by increasing mode size, while the gain medium experiences little temperature change. This makes solid state thin-disk lasers suitable for high power operation. To date, commercial thin-disk lasers from TRUMPF, Inc. [9] possess average output power of 16 kW and thin-disk laser based weapon systems have been reported with output powers up to 50 kW [10].

SDLs were first demonstrated three years after the thin-disk laser [11] and, after two decades of development, have only achieved CW output powers of about 100 W [12]. With the thin-disk geometry, failure of the power scaling law for SDLs is due mainly to stronger pump absorption, which results in higher heat density. For SDLs with a barrier pumping scheme, the average absorbed pump power reaches about 5 MW/cm^3 , in contrast to a mere 0.08 MW/cm^3 for typical Yb:YAG thin-disk lasers. Additionally, semiconductor gain is more sensitive to temperature. In order to efficiently remove the heat, highly thermal

conductive extracavity heatspreaders are integrated with the chips. However, the high thermal resistance of semiconductor DBRs hinders the thermal conduction process, so intracavity heatspreaders are introduced for heat extraction, bypassing DBRs.

The thermal analysis can be performed by solving the heat equation

$$\rho c_p \frac{\partial T}{\partial t} - \nabla \cdot (\kappa \nabla T) = H \quad (2.1)$$

where c_p , ρ , and κ are specific heat capacity, material density, and thermal conductivity, T is the temperature, and H is the heat source. In the analysis, we only consider the approximate temperature raise while at steady state, $\partial T / \partial t = 0$. A constant temperature boundary condition is applied to the surfaces in contact with the cooling block. With complicated gain-cooling assembly, solving the thermal diffusion problem analytically has proved challenging and unnecessary. Instead, a numerical thermal analysis is performed with the commercial finite element software COMSOL Multiphysics 4.4 and the heat transfer module, with a few approximations to simplify the problem. First, the model is assumed with cylindrical symmetry: a circularly symmetric (Gaussian or flat-top) beam is incident at the center of the circular gain chip, simplifying a three-dimensional problem to a two-dimensional one. Therefore, the steady-state heat equation can be written as

$$\frac{1}{r} \frac{\partial}{\partial r} \left(\kappa r \frac{\partial T}{\partial r} \right) + \frac{\partial}{\partial z} \left(\kappa \frac{\partial T}{\partial z} \right) + H(r, z) = 0 \quad (2.2)$$

Second, for all involved materials, the thermal conductivity coefficients are assumed to be independent with temperature (for synthetic diamonds, the thermal conductivity is about 2300 W/(m K) at 300 K and 1700 W/(m K) at 400 K [13]). Third, the detailed heat generation processes are ignored in this section and the heat source distributions are assumed following the incident pump power distribution, with constant proportions. In contrast to [14], the assumed proportion in the active region is higher than the quantum defect (η_q in Eq. 1.10). This is because Auger recombination contributes to heat generation under high temperature and high carrier density conditions. As mentioned earlier, for a SDL with a slope efficiency of 60% with respect to the absorbed pump power, the remaining 40% of absorbed pump power will be the heat load.

Third, since thin layers take many fine meshes in the FEM simulation, structures are simplified to reduce the computation time. The DBR is approximated as one layer with equivalent parameters, and the active region as a two- or three-layer structure. An effective thermal conductivity coefficient is defined for each layer. The thermal conductivity inhomogeneity in multilayer structures is ignored. Lastly, a perfect bonding interface is assumed and the roughness dependent interface thermal resistances are ignored.

In this section, we will compare the thermal performance among four configurations with constant pump intensity: thin-device VECSELs with one extracavity heatspreader, VECSELs with both intracavity and extracavity heatspreaders, and transmission geometry DBR-free SDLs with one and two heatspreaders. For the DBR-free SDLs at 1 μm , the active region is approximated as two (top and bottom) 0.16 μm thick InGaP window layers and a 2.25 μm thick GaAs active region. For the active regions in VECSEL configurations, the bottom window layer is neglected since the AIAs layer in the DBR confines the carriers. In regards to the heat distribution, exponential decay is considered in both the gain region and the DBR layers with different absorption coefficients.

The active region radius is set as 3 times the pump spot radius in the evaluation process, so as to reduce the computation time. The diamonds are 1 mm thick, and 5 mm in diameter. The bonded assembly is mounted on a copper heat sink with a 2 mm diameter clearance hole. The cross-section view of the mount is presented in Fig. 5.9 in section 5.2. Indium foil with a thickness of 50 μm is applied between the diamond and copper mount in order to reduce the thermal resistance in a ring shape, whose inner radius measures 1 mm and whose outer radius measures 2.5 mm. For intracavity heatspreader mounts, constant temperature boundary condition is assumed on the bottom surface of the copper mount, in a ring shape. For extracavity heatspreader mounts of a ring shape, the condition is applied to the entire bottom surface. Thermal conduction processes between air and other surfaces are all neglected. A side view of the model is shown in Fig. 2.1 (a). In the simulations, all the geometry and material parameters are tabulated in Tables. 2.1 and 2.2.

With the cylindrical symmetry, a Gaussian distributed heat source can be written as

$$Q(r, z) = \frac{2P_i}{\pi w_0} e^{-\frac{2r^2}{w_0^2}} e^{-\alpha_0(z_0-z)} \quad (2.3)$$

where P_i is the incident pump power, α_0 is the absorption coefficient, w_0 is beam radius, and z_0 is the position of the top active region surface. In the active region, the heat source is

$$Q_g(r, z) = \frac{2\eta_g P_i}{\pi w_0} e^{-\frac{2r^2}{w_0^2}} e^{-\alpha_g(z_{0g}-z)} \quad (2.4)$$

and for the VECSEL configurations, the heat source in the semiconductor DBR is

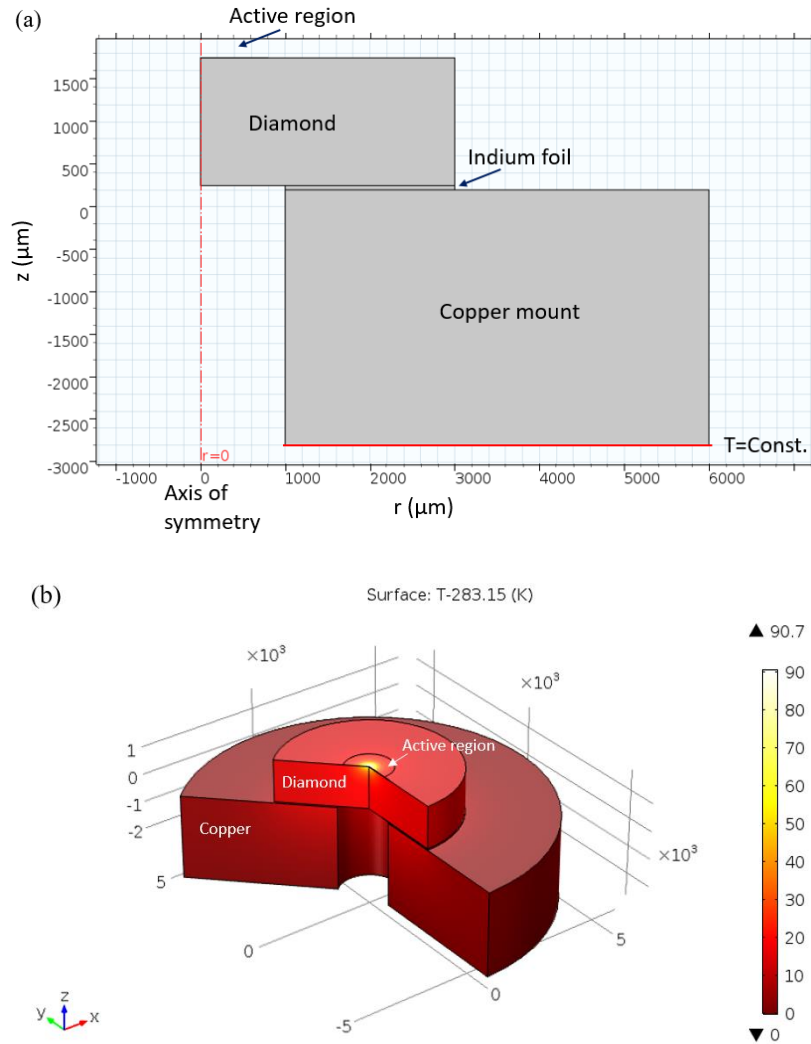


Figure 2.1 (a) Cross-sectional view of the simulation model for a DBR-free SDL with one heatspreader in COMSOL interface. The red line on the bottom of the copper mount signifies where the constant temperature condition applies. Since the z axis is a linear scale, the active region is very thin and therefore not visible. (b) Simulation results: temperature raise contour map.

$$Q_{\text{DBR}}(r, z) = \frac{2\eta_{\text{DBR}}P_i}{\pi w_0} e^{-\frac{2r^2}{w_0^2}} e^{-\alpha_g d_g} e^{-\alpha_{\text{DBR}}(z_{0\text{DBR}}-z)} \quad (2.5)$$

where η_g and η_{DBR} are the ratios of absorbed pump power converted to heat in the active region and DBR, α_{DBR} is the pump absorption coefficient in the DBR, and $z_{0\text{DBR}}$ is the position of the top DBR surface.

With the finite element method, the structure must be discretized first and the “finer” grade mesh on the software user interface chosen. The mesh for the VECSEL geometry is

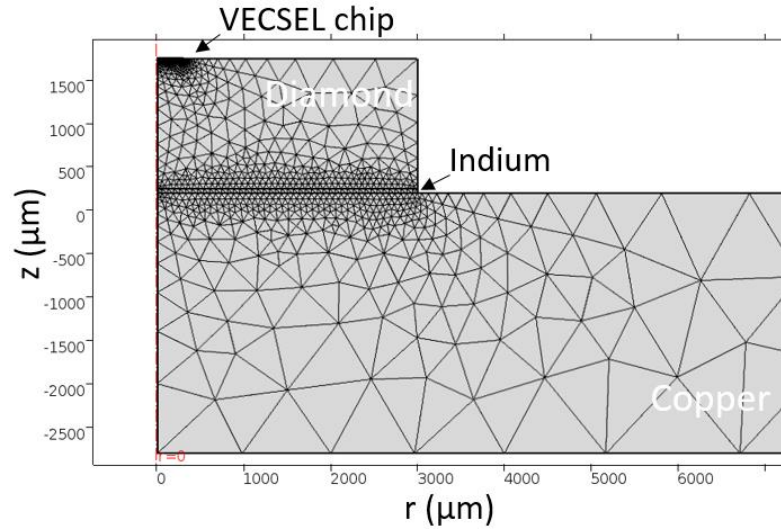


Figure 2.2 “Finer” mesh generated with COMSOL for the VECSEL simulation.

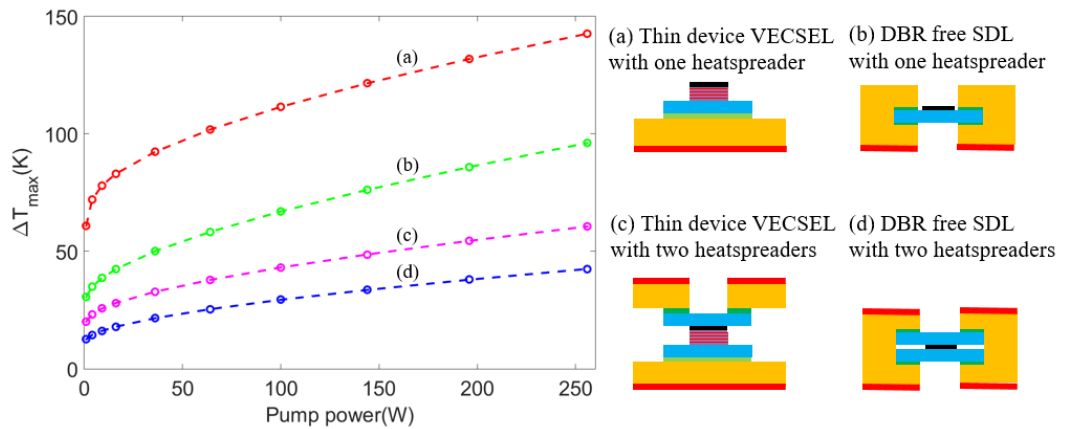


Figure 2.3 Maximum temperature rise for different geometries as a function of incident pump power with constant pump density (80 kW/cm^2). The absorption coefficient for the pump at the gain region is 1000 mm^{-1} and the pump at the DBR region is 457 mm^{-1} . For the simulation model diagrams, the red lines denote where the fixed temperature boundary conditions are applied.

shown in Fig. 2.2. Utilizing “extra finer” or “extremely finer” grade meshes, the maximum temperature varies by less than 1% , though the calculation take much longer.

Table 2.1 Summary of material parameters for 1 μm SDLs

Symbol	Quantity	Value
κ_{win}	Thermal conductivity of the window layer	10 W/(m K)
κ_{g}	Thermal conductivity of active region	24 W/(m K)
κ_{DBR}	Effective thermal conductivity of semiconductor DBR	61 W/(m K)
κ_{d}	Thermal conductivity of diamond	1800 W/(m K)
κ_{c}	Thermal conductivity of copper	400 W/(m K)
κ_{in}	Thermal conductivity of indium	84 W/(m K)
κ_{s}	Thermal conductivity of solder	162 W/(m K)
ρ_{win}	Mass density of the window layer	$4.482 \times 10^3 \text{ kg/m}^3$
ρ_{g}	Mass density of the active region	$5.320 \times 10^3 \text{ kg/m}^3$
ρ_{DBR}	Mass density of the DBR	$4.479 \times 10^3 \text{ kg/m}^3$
ρ_{d}	Mass density of diamond	$3.515 \times 10^3 \text{ kg/m}^3$
ρ_{c}	Mass density of copper	$8.700 \times 10^3 \text{ kg/m}^3$
ρ_{in}	Mass density of indium	$7.310 \times 10^3 \text{ kg/m}^3$
ρ_{s}	Mass density of solder	$7.310 \times 10^3 \text{ kg/m}^3$
C_{win}	Thermal capacity of the window layer	368.8 J/(kg K)
C_{g}	Thermal capacity of the active region	330 J/(kg K)
C_{DBR}	Thermal capacity of the DBR	394.7 J/(kg K)
C_{dia}	Thermal capacity of diamond	520 J/(kg K)
C_{c}	Thermal capacity of copper	385 J/(kg K)
C_{in}	Thermal capacity of indium	233 J/(kg K)
C_{s}	Thermal capacity of solder	233 J/(kg K)
α_{g}	Absorption coefficient of active region	$1 (\mu\text{m})^{-1}$
α_{DBR}	Absorption coefficient of DBR	$0.457 (\mu\text{m})^{-1}$
η_{g}	Ratio of absorbed power converting to heat in gain	0.4
η_{DBR}	Ratio of absorbed power converting to heat in DBR	1

Table 2.2 Summary of geometry parameters for 1 μm SDLs

d_{win}	Thickness of the window layer	0.214 μm
d_{act}	Thickness of active region	2.25 μm
d_{dia}	Thickness of diamond	250 μm
d_{ind}	Thickness of indium	50 μm
d_{sol}	Thickness of solder	2 μm
d_{DBR}	Thickness of semiconductor DBR	3.72 μm
I_{p}	Pump power density	80 kW/cm^2
r_{act}	Radius of active region	3 mm
r_{oco}	Outer radius of copper mount	6 mm
r_{ico}	Inner radius of copper mount	1 mm

With the same configuration and parameters, our model reproduces the results in [14]. By keeping the pump power intensity the same (80 kW/cm^2) and increasing pump power and mode size, the temperature rise curves for the four configurations are shown in Fig. 2.3. Because of the relatively thick diamond heatspreader (1 mm) and high pump absorption in DBRs, the thin-device VECSEL configuration presents higher temperature elevations than the one heatspreader DBR-free SDL configuration at the same pump conditions. By integrating another intracavity diamond heatspreader, the temperature elevations for both configurations drop and the two-heatspreader DBR-free SDL configuration still outperform the two-heatspreader thin-device VECSEL configuration. It is evident, therefore, that DBR-free geometries exhibit advantages in thermal management.

2.3 Integrated gain analysis

A laser, evident in its acronym “light amplification by stimulated emission of radiation”, is a product of the photon-electron coupling. Unlike gas or other solid state gain media, semiconductor active regions—the host for such interaction—can be engineered down to

single-atomic-layer precision in the material growth process. Therefore, the coupling strength could depend on the gain structure, particularly for SDLs.

Since the early days of surface-emitting lasers, the overlap between the optical standing wave and the longitudinal inhomogeneous active region has been studied extensively for the PGS in the VCSEL and VECSEL configurations. It was quantified by “the integrated gain factor” [15], or “longitudinal mode confinement factor” [16]. In these studies, the active region is attached to at least one cavity end mirror (semiconductor DBRs). This type of active mirror configuration is well understood as a spectral filter for the gain spectrum due to the subcavity effect, while the independent PGS has been fully neglected. In this section, we will discuss the spectral properties of such independent PGSs in both standing wave and ring cavities.

In a standing wave cavity, there are two cavity nodes at the end mirrors with fixed phases for all longitudinal modes. For two longitudinal mode orders within semiconductor material gain bandwidth near a cavity node (the distance between one of the cavity node to the gain z is small), the maximum phase difference $\Delta\varphi=(k_1-k_2)z=\pi z\Delta m/L$ (Δm is the maximum longitudinal mode order index difference, L is the cavity length) is less than π , which gives orderly positioned field antinodes, similar to the colorful fringes near the bright center fringe ($\Delta\varphi=0$) in the white light interferometry. In contrast, with far from cavity nodes, $\Delta\varphi$ is much larger than π , so antinodes (or nodes) for different longitudinal modes can overlap in space ($\varphi_2-\varphi_1=N\pi$ and $\varphi_1=M\pi+\pi/2$, here both N and M are positive integers), which brings in the field-gain overlap differences.

Fig. 2.4 (a) shows a PGS designed at normalized wavelength 1, with QWs positioned at the standing wave antinodes. There are increasing offsets between QWs and antinodes of the two longer wavelengths, and by eye the field of wavelength 1.03 overlaps better with the PGS than wavelength 1.05. In Fig. 2.4 (b), when the gain structure is far from both cavity nodes, at a certain position a field at wavelength 1.05 has better overlapping than at 1.03. Therefore, the spectral property of such PGS varies with both wavelength and gain position. Even though the overlap between periodic standing wave field and gain structure is like a moiré pattern, it is the integrated gain that determines which modes are favored. Similar gain-position-dependent laser linewidth phenomena [17] due to spatial-hole

burning have been reported in solid state lasers, which is also consistent with the simple picture. It is difficult to understand all the spectral properties from Fig. 2.4, and quantitative analysis is needed.

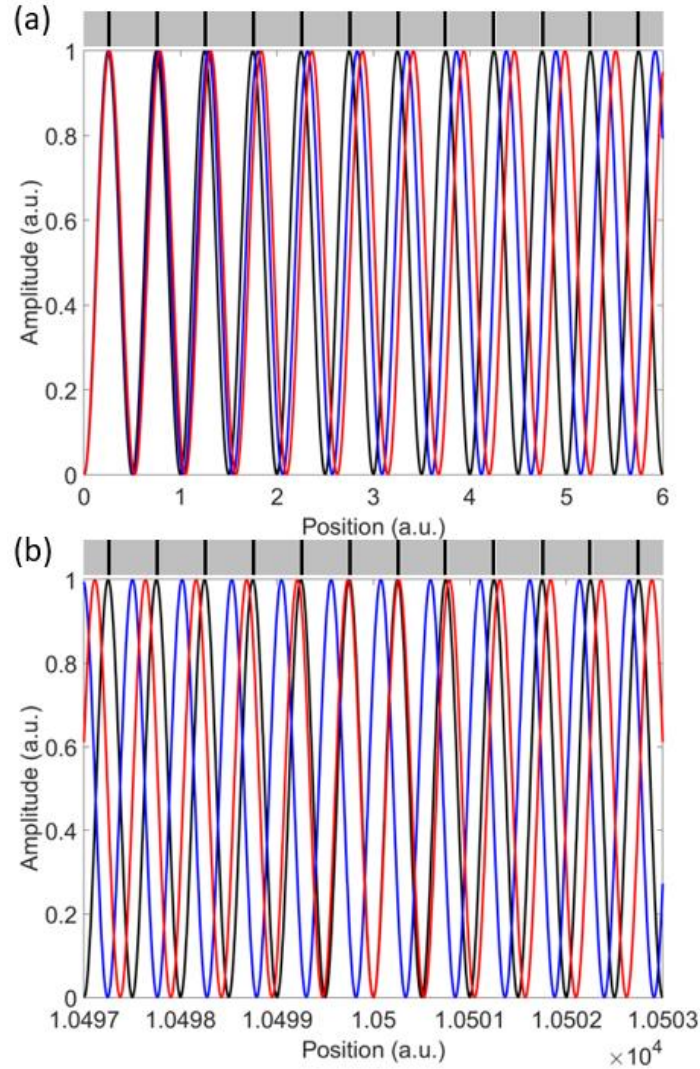


Figure 2.4 Optical standing wave field pattern with PGS. The black lines above the plots stand for QWs, located at the antinodes of the field at the design wavelength 1 (black curve); the gray squares stand for barriers. The blue curve is at wavelength 1.03, and the red curve is at 1.05. The field distribution is plotted when the gain structure is close to (a) or far from (b) a cavity end mirror.

2.3.1 Integrated gain factor

To simplify the analysis, we have all the distances in optical thickness and neglect multiple beam interference effects. The QW gain saturation is also not included in the simple

analysis. With a small incident signal at normalized intensity, the integrated gain (amplified signal) for the m^{th} order longitudinal mode is

$$G(\lambda, z) = \int_0^L g(\lambda, z - z') \sin^2 \left[\frac{\pi m(\lambda) z'}{L} \right] dz' \quad (2.6)$$

where z is the distance between a cavity node to the closest gain layer, L is the cavity length, and $g(\lambda, z)$ is longitudinal gain profile. Considering typical gain layers (QW or QD) are much thinner than the periodicity (half design wavelength), with one gain layer per period, the longitudinal gain profile is approximated as

$$g(\lambda, z) = \sum_{i=1}^N \delta \left[z - \frac{(i-1)\lambda_0}{2} \right] g_m(\lambda) \quad (2.7)$$

where N is the number of periodicity, $\delta(z)$ is the delta function, λ_0 is the design wavelength, and $g_m(\lambda)$ is the gain layer material gain. By bringing Eq. 2.7 back to the definition Eq. 2.6, with a simple derivation, the integrated gain can be expressed as

$$G(\lambda, z) = \left[\frac{N}{2} - \frac{\sin \left(\frac{N\pi\lambda_0}{\lambda} \right)}{2 \sin \left(\frac{\pi\lambda_0}{\lambda} \right)} \cos \left[\frac{\pi\lambda_0}{\lambda} \left(N - 1 + \frac{4z}{\lambda_0} \right) \right] \right] g_m(\lambda) \quad (2.8)$$

Here we define the first term in the big bracket as the integrated gain factor $G'(\lambda, z) = G(\lambda, z)/g_m(\lambda) = \frac{N}{2} - \frac{\sin \left(\frac{N\pi\lambda_0}{\lambda} \right)}{2 \sin \left(\frac{\pi\lambda_0}{\lambda} \right)} \cos \left[\frac{\pi\lambda_0}{\lambda} \left(N - 1 + \frac{4z}{\lambda_0} \right) \right]$, which is imposed by the periodic configuration of the gain structure. Within the usual semiconductor material gain bandwidth, $\lambda_0/\lambda \approx 1$, therefore G' can be approximated as

$$G'(\lambda, z) \approx \frac{N}{2} \left[1 - (-1)^N \text{sinc} \left(\frac{N\pi\lambda_0}{\lambda} \right) \cos \left[\frac{\pi\lambda_0}{\lambda} \left(N - 1 + \frac{4z}{\lambda_0} \right) \right] \right] \quad (2.9)$$

When $z=0.25\lambda_0$, it is like a typical VECSEL and the integrated gain factor is

$$G'(\lambda, z) = \frac{N}{2} \left[1 - (-1)^N \text{sinc} \left(\frac{2N\pi\lambda_0}{\lambda} \right) \right] \quad (2.10)$$

When $z \gg \lambda_0$ like the DBR-free SDL scenario except at certain points, which will be discussed later, the cosine term is a fast modulation term, and the envelope function for G' can be written as

$$G''(\lambda, z) \approx \frac{N}{2} \left[1 \pm \text{sinc} \left(\frac{N\pi\lambda_0}{\lambda} \right) \right] \quad (2.11)$$

Comparing Eqs. 2.10 with 2.11, the bandwidth of the envelope function for $z \gg \lambda_0$ is twice as much as $z=0.25\lambda_0$. In the typical VECSEL design, with the field penetration into the semiconductor DBR considered, z is larger than $0.25\lambda_0$ ($0.25\lambda_0 < z < 10\lambda_0$), which narrows the bandwidth further.

Now we can numerically evaluate the position dependent integrated gain factor. In Fig. 2.5, the integrated gain factors are plotted at three z values. Having the gain structure near a cavity node when $z=0.75\lambda_0$ is similar as a typical VECSEL in the straight cavity geometry. By having the gain structure further from the node, a wavelength dependent fine modulation appears for the integrated gain factor, which is from the cosine term in Eq. 2.9. Like the DBR-free SDL geometry, at a further distance $z=10$ mm, such modulation becomes even finer, beyond the resolution of the figure, which has the bandwidth broader than the VECSEL scenario. A detailed discussion on the mode structure will be presented in the next subsection.

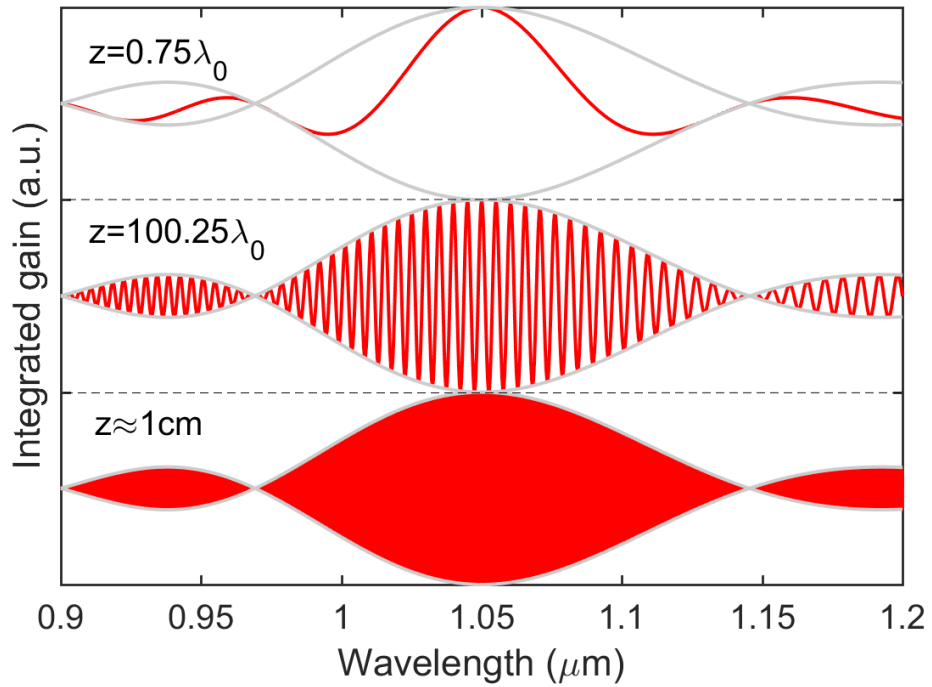


Figure 2.5 Integrated gain factors for different z values for a 12 QW PGS with one gain layer per period. $\lambda_0=1.05 \mu\text{m}$ is the design wavelength and cavity length L is 100 mm. The gray solid thin curves are the envelopes.

By having the PGS far from cavity nodes, broad bandwidth is attained. An intuitive question is: how about the gain bandwidth for a V-shaped cavity with the VECSEL chip in the cavity center? It is similar to the typical straight cavity configuration. For the V-shaped cavity, the cavity folding angle is usually small in air and even smaller in semiconductor materials. At normal incidence, the incident and reflected beams interfere, forming a standing wave pattern along the beam propagation direction with half wavelength periodicity in optical length. The same pattern is seen for the oblique incidence, though with a different periodicity. Due to the small tilting angle, the reflection phase is close to the normal incidence case. In other words, there is a cavity node at the DBR, same as the straight cavity scenario, and with no extra advantage for a V-shaped cavity in the integrated gain bandwidth.

The fast modulation brings in other advantages to transmission geometry DBR-free SDLs. As shown in Fig. 2.6 (a), changing z by $0.05\lambda_0$, the integrated gain factor for the VECSEL geometry changes significantly in both the peak wavelength and peak amplitude (dropping by 2%). In contrast, the DBR-free geometry has much smaller changes in Fig. 2.6 (b)—0.5% drop in amplitude for $z=100.25\lambda_0$, but smaller with larger z . Therefore, DBR-free gain chips have much larger tolerance to window layer thickness errors. It is the same for the periodicity error. If the real gain structure periodicity is larger than the design periodicity, shown in Fig. 2.13, both integrated gain factors will peak at the longer wavelength side by the same amount. At the design wavelength, the integrated gain factor of the DBR-free gain chip will experience lower gain drop. DBR-free gain chips are more robust.

From the envelope function of integrated gain factor in Eq. 2.9, PGSs with more QWs (no more than 1 QW per period) have narrower gain bandwidth, shown in Fig. 2.7. This is why thin gain structures are adopted for VECSEL mode locking [18]. It is also one of the reasons that certain QD based SDLs have broader tuning ranges than VECSELs with thicker QW gain structures in the same wavelength range [19]. A comparison of the integrated gain factors with different QW numbers is shown in Fig. 2.7. By having more than one QW per period, it can also broaden the integrated gain bandwidth, at the sacrifice of peak integrated gain factor. For an infinitely long bulk gain medium, the integrated gain

factor is $\frac{1}{2}$ and the integrated gain bandwidth will only be limited by the material gain bandwidth.

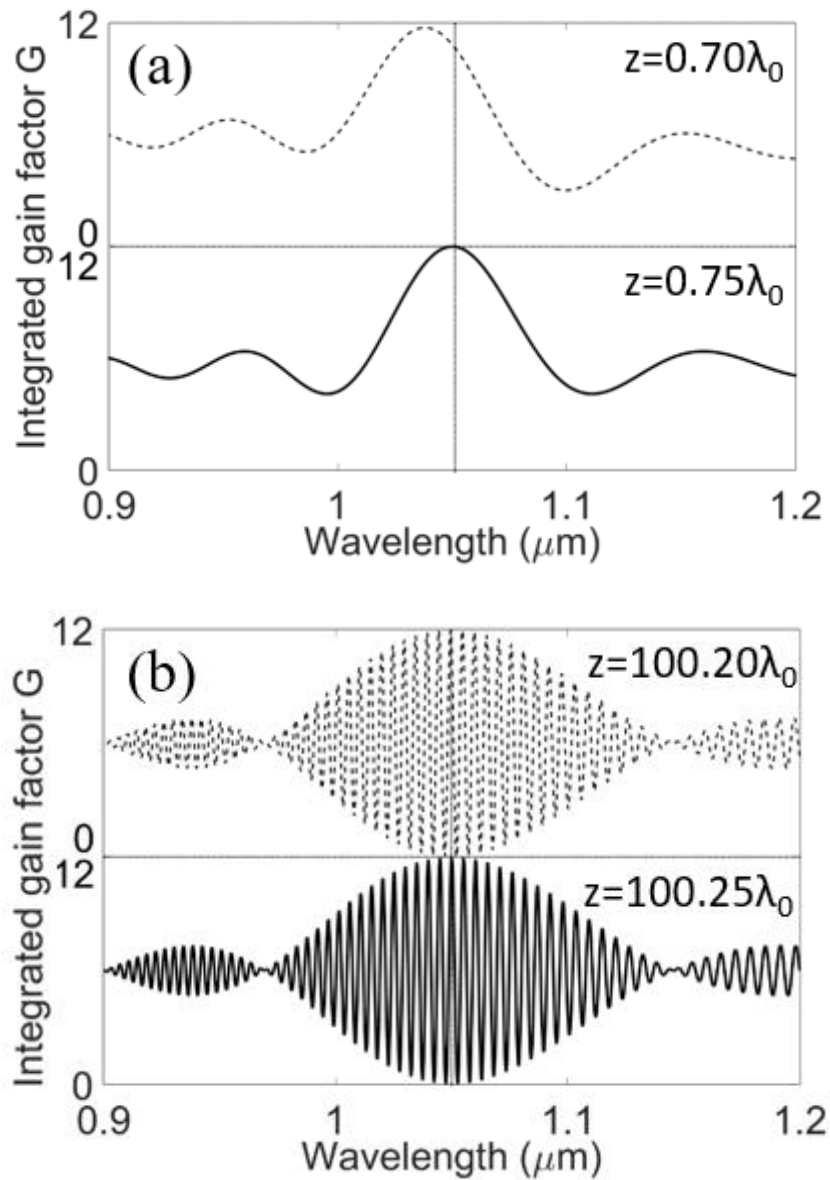


Figure 2.6 Stability of integrated gain factor with z for a typical VECSEL geometry (a) and DBR-free transmission geometry (b).

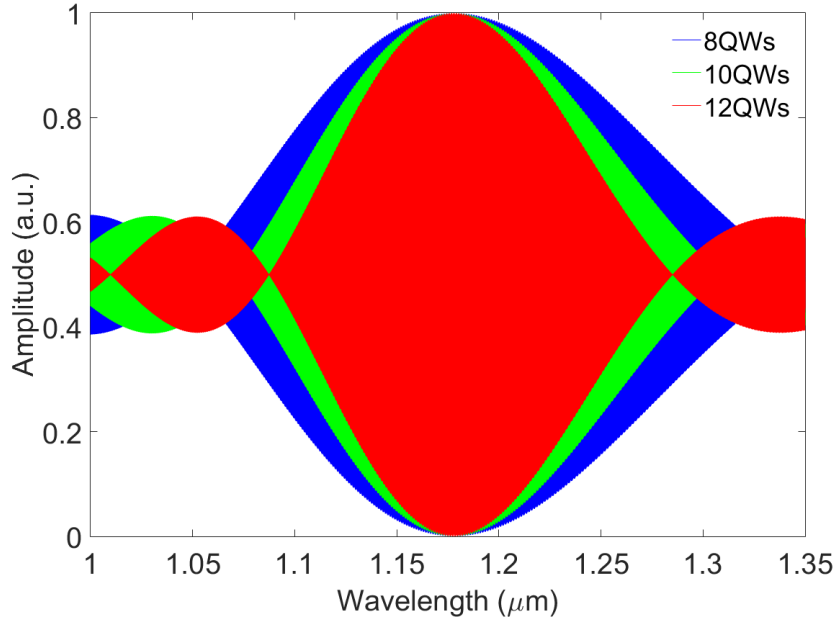


Figure 2.7 Integrated gain factors for transmission geometry DBR-free SDLs with different number of QWs.

2.3.2 Mode structure

In the figures of the last subsection, the integrated gain factor has a fast modulation term with a large z value, filling the region between the upper and lower limit of the envelope functions. This is true for most positions but there are exceptions. When z is equal to $r*L$ (rational number $r=q/p$, and both p and q are integers with $p>q>0$ and q/p is irreducible), the envelope function of the integrated gain factor can be modified by an extra cosine term in Eq. 2.8. Mathematically, this is because the position dependent phase term $\frac{4\pi z}{\lambda} = \frac{2\pi p m}{q} = 2\pi s + \frac{t}{q} 2\pi$ in Eq. 2.8 (m is the longitudinal mode order, s and t are integers) is in a finite set, rather than a random number. In other words, the phase terms of the sine and cosine functions are correlated. As a result, the cosine term cannot be ignored any longer in the envelope function. In the wavelength range for the sine phase term changing by 2π , there are $q-1$ wavelengths at which the cosine term is very close to 1 (or -1). As a result, such phase modulation brings in an amplitude modulation, with a depth of $1 - \cos\left(\frac{\pi}{q}\right)$, which narrows the bandwidth in some cases (as when $z/L=0.5$, the integrated gain

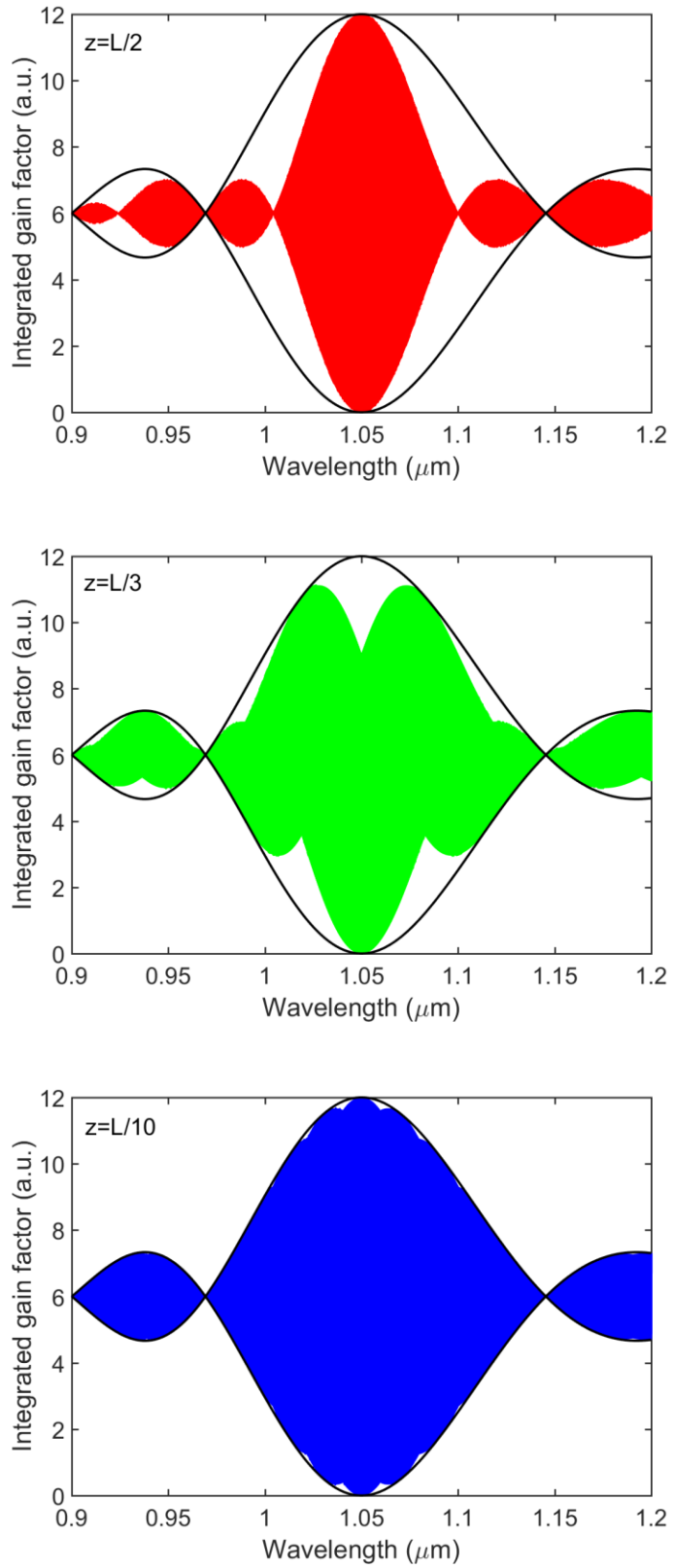


Figure 2.8 Integrated gain factors with $z=L/2$, $L/3$, and $L/10$. L is the cavity length.

bandwidth is half of the maximum bandwidth). As shown in Figs. 2.8 and 2.9, the modulation depth decreases significantly with the integer q . Because of the slow varying phase term, the longitudinal modes will exhibit slow phase shift in the fine modulation, which will be discussed soon.

The extra modulation is not stable with gain position z . As shown in Fig. 2.10, for a 100 mm long cavity, the strongest modulation at $z=L/4$ dies off in about 100 μm . It is easy, therefore, it is easy to avoid these points in experiment. Our strategy for avoiding these extra modulation (of more than 10%) is having z satisfy one of the two conditions for a 100 mm long cavity: (1) $500\lambda_0 < z < L/6$; or (2) when $L/6 < z < L/2$, avoid jL/K ($K=2, 3, \dots, 6$, $j=1, \dots, K-1$) points by at least $100\lambda_0$.

Asides from the envelope function, the fine modulation is also modified, which allows for interesting mode structures. Zoomed-in views for the integrated gain factors at near the design wavelength for a series of L/z values are presented in Fig. 2.11. If the laser threshold is sufficiently high, the lasing mode spacing is an integer times of cavity repetition rate. It is also worth noting that, far from the design wavelength, the zoom-in view will be different since the sine function term brings in an extra phase term.

Mode locked with such mode structure, the pulse repetition rate will be integer times of cavity repetition rate, which is harmonic mode locking (HML). This is exactly what happens in some solid state lasers [20]. In contrast to QWs, bulk gain has a unity factor and

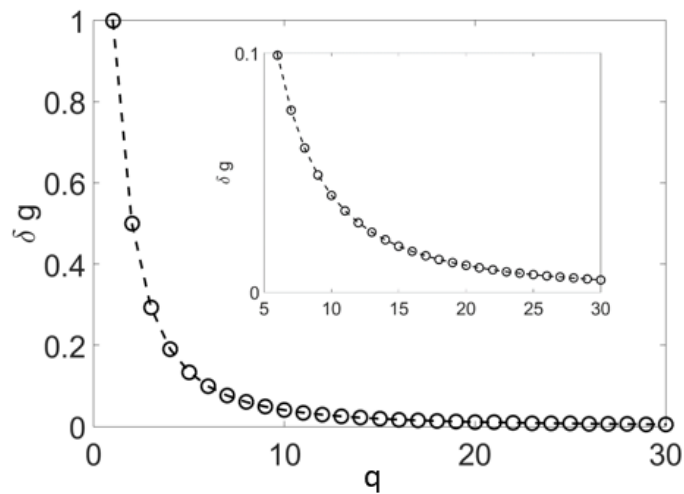


Figure 2.9 Modulation depth with q . The inset is a zoom-in view between $q=6$ to 30.

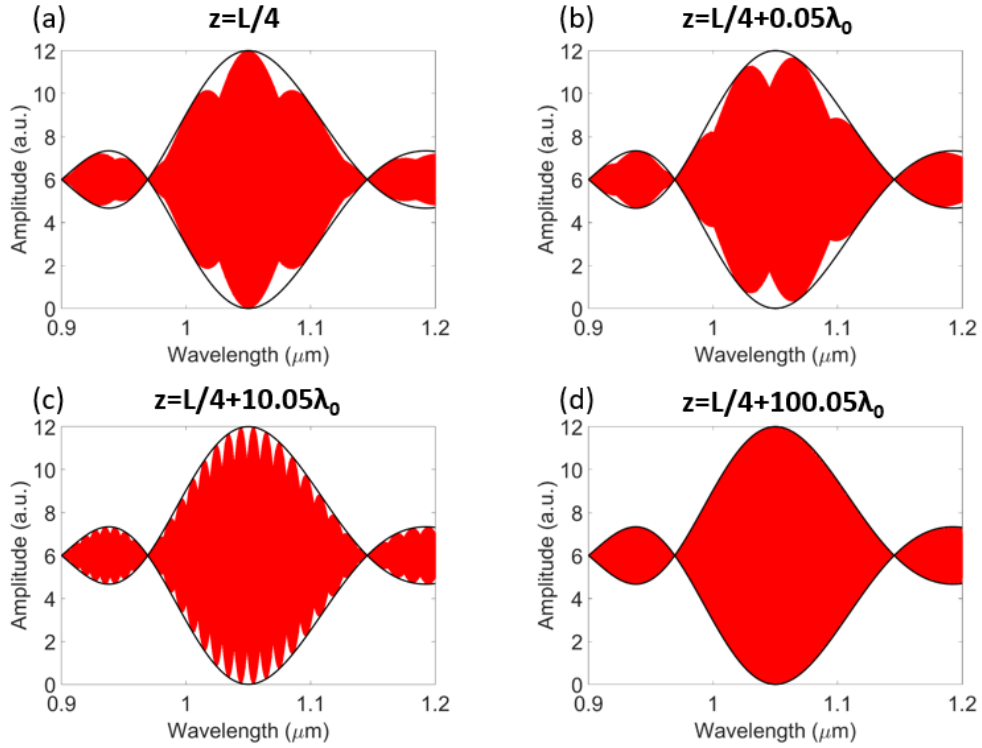


Figure 2.10 position dependent integrated gain factor. Cavity length $L=100$ mm and $\lambda_0=1.05$ μm . (a) $z=L/4$; (b) $z=L/4+0.05\lambda_0$; (c) $z=L/4+10.05\lambda_0$; (d) $z=L/4+100.05\lambda_0$.

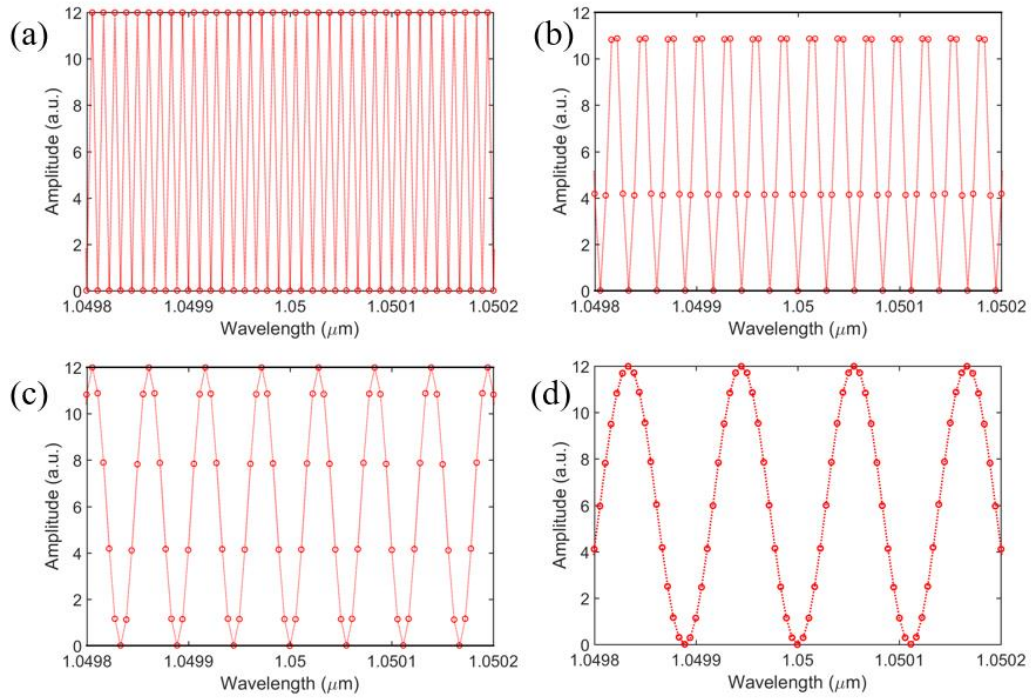


Figure 2.11 Calculated mode gain near the design wavelength $\lambda_0=1.05$ μm for different z values, $L/2$ (a), $L/5$ (b), $L/10$ (c), and $L/20$ (d). Circles stand for the longitudinal modes supported by cavity length $L=100$ mm.

a similar integrated gain analysis can be carried out in a standing-wave cavity.

Assume a bulk gain with thickness d , distance z away from a cavity node of the standing wave cavity and the cavity length L . Different from the periodic gain, the continuous bulk gain profile is

$$g(\lambda, z) = [H(z) - H(z + d)]g_m(\lambda) \quad (2.12)$$

here H is a Heaviside step function. With the definition in Eq. 2.6, the integrated gain is

$$G(\lambda, z) = \left[\frac{d}{2} - \frac{\lambda}{4\pi} \sin\left(\frac{2\pi d}{\lambda}\right) \cos\left(2\pi \frac{2z + d}{\lambda}\right) \right] g_m(\lambda) \quad (2.13)$$

As in Eq. 2.8, there is a gain position dependent cosine term and as a result, an interesting mode structure or harmonic mode locking could occur. This is exactly the case in reference [20]. In a straight laser cavity with $L=21.32$ mm cavity length, corresponding to 7 GHz in cavity repetition rate, an Nd:Sr₃Y₂(BO₃)₄ disordered bulk crystal is employed as the gain medium. When $L/z=10, 8,$ and $20/3$ (z is the distance between one of the end mirror and the crystal), harmonic mode locking with repetition rates of 70 GHz, 55 GHz, and 110 GHz are observed. According to our model, under these L/z conditions, the longitudinal mode spacing is 10, 8, and 20 times the original spacing. As a result, the predictions (70 GHz and 56 GHz) of our theory for the first two cases matches the experimental results. For the last case, our theory predicts 140 GHz, while the experiment shows 110 GHz. There may be other mechanisms involved.

So far, we have focusing on the standing wave cavity scenario. In a ring cavity, there may be no global cavity nodes. There is no phase restrictions on the two counter-propagating waves. As a result, the configuration with maximum gain is preferred. With an even number of QWs, all longitudinal modes will align their optical field nodes at the center of the active region; for an odd number ($2N+1$) of QWs, the longitudinal modes will align the antinodes at the N^{th} QW. This is essentially a typical VECSEL. Therefore, the aforementioned interesting mode structures will not occur in this scenario.

2.4 Reflectance analysis: transfer matrix method

In the integrated gain model, the refractive index discontinuities among the dielectric substrate and semiconductor layers are neglected, and only the gain modulation induced by the periodic configuration is considered. A full analysis of the gain spectrum should take all these factors into consideration: material dispersion, the integrated gain, and the multiple beam interference in the active region. This can be done with the transfer matrix method [21].

Following [21], we developed a MATLAB program based on the transfer matrix method for the calculation. As a check, a calculation is performed with a GaAs/AlAs DBR designed at 1.05 μm with 35 pairs of quarter-wavelength optical thick layers. The reflectivity spectrum is shown in Fig. 2.12, which matches well with the result by the commercial software RSoft DiffractMOD (based on Rigorous Coupled Wave Analysis, RCWA method [22] and enhanced with modal transmission line theory).

The code is then applied to the real configurations. In the VECSEL configuration, the wave propagates in air for 90 mm, through the active region, and 25.5 pairs GaAs/AlAs DBR at design wavelength 1.035 μm . The active region gain structure is shown in Fig. 3.4 (a). Constant refractive index $n=3.218$ is assumed for the InGaP layers. The GaAsP is approximated as GaAs, and its refractive index [23] is given by

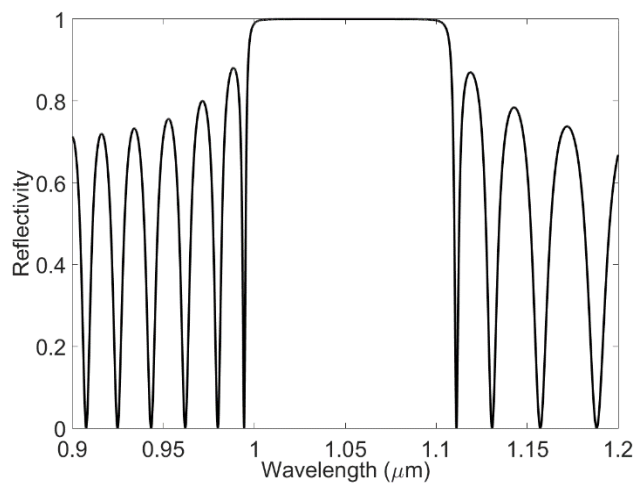


Figure 2.12 Reflectivity spectrum for a semiconductor DBR consisted of 35 pairs of GaAs/AlAs by transfer matrix method code.

$$n^2 = 5.372 + \frac{5.467\lambda^2}{\lambda^2 - (0.443 \mu\text{m})^2} + \frac{0.024\lambda^2}{\lambda^2 - (0.875 \mu\text{m})^2} + \frac{1.958\lambda^2}{\lambda^2 - (36.917 \mu\text{m})^2}$$

The refractive index of AlAs [23] is given by

$$n^2 = 2.079 + \frac{6.084\lambda^2}{\lambda^2 - (0.282 \mu\text{m})^2} + \frac{1.9\lambda^2}{\lambda^2 - (27.62 \mu\text{m})^2}$$

and InGaAs [23] is given by

$$n^2 = 8.95 + \frac{2.054\lambda^2}{\lambda^2 - (0.869 \mu\text{m})^2} + \frac{0.005i}{1 + [(\lambda - 1.035 \mu\text{m})/(0.06 \mu\text{m})]^2}$$

here a Lorentz-shaped material gain is included. For the DBR-free geometry, the beam propagates through the active region, 1 mm thick diamond with constant refractive index 2.39, 90 mm thick air, and the 25 pairs of SiO₂/HfO₂ dielectric DBR. The refractive index of SiO₂ [23] is given by

$$n^2 = 1 + \frac{0.696\lambda^2}{\lambda^2 - (0.068 \mu\text{m})^2} + \frac{0.408\lambda^2}{\lambda^2 - (0.116 \mu\text{m})^2} + \frac{0.897\lambda^2}{\lambda^2 - (9.896 \mu\text{m})^2}$$

and of HfO₂ [23]:

$$n^2 = 1 + \frac{1.956\lambda^2}{\lambda^2 - (0.155 \mu\text{m})^2} + \frac{1.345\lambda^2}{\lambda^2 - (0.063 \mu\text{m})^2} + \frac{10.41\lambda^2}{\lambda^2 - (27.12 \mu\text{m})^2}$$

The calculated reflection results are shown in Fig. 2.13. Generally, they are consistent with the integrated gain model predictions. First, the DBR-free transmission geometry offers much broader gain bandwidth than typical VECSEL geometry. Second, in contrast to the typical VECSEL results, the reflection of the DBR-free geometry has a fast modulation. The much broader base for the DBR-free geometry is due to the broad HR band of the dielectric mirror. Finally, the positions of the sub-peaks are also consistent with the predictions from our model. In the VECSEL geometry, the integrated gain reaches minimum at around 1.00 μm and 1.07 μm, and increases at even shorter and longer wavelengths than these two. Therefore, two extra sub-peaks appear at the HR band edges. For the DBR-free geometry, the two sub-peaks roughly match the sub-peaks of the integrated gain model in wavelength. It takes 25 minutes for each simulation in Fig. 2.13.

Finer wavelength steps can improve the image quality but it will require a much longer calculation time.

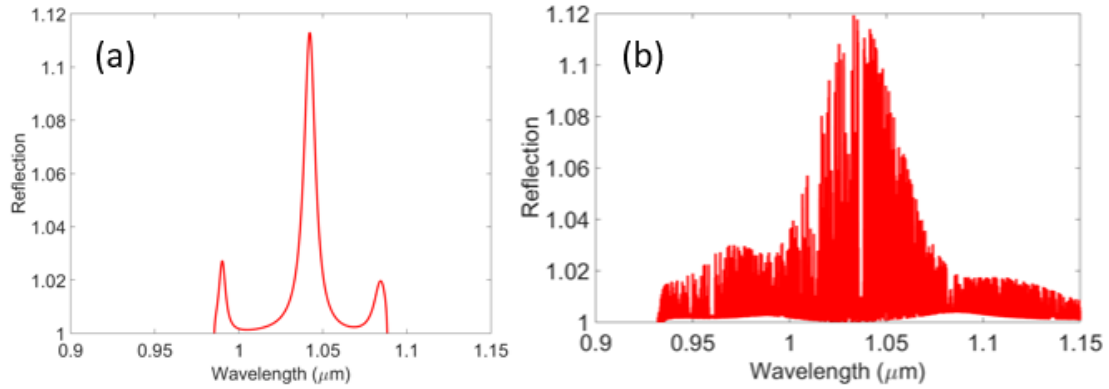


Figure 2.13 Reflection spectra calculated with transfer matrix method: (a) a VECSEL geometry and (b) DBR-free SDL geometry. The spectra width at $(R_{\max}+1)/2$ is 9 nm and 45 nm respectively.

2.5 Summary

DBR-free SDL geometries have advantages in material system choices, thermal management, and gain bandwidth. With intracavity diamond heatspreaders, according to the numerical thermal analysis, high power DBR-free SDLs could be achieved. Furthermore, a position dependent integrated gain model predicts broader integrated gain bandwidth and interesting mode structures for the DBR-free geometry, which agrees well with the results by the transfer matrix method. These two predictions will be further tested by experiments in chapter 5.

2.6 References

- [1] L. A. Coldren and S. W. Corzine, "Periodic structures and the transmission matrix," in *Diode Lasers and Photonic Integrated Circuits*, New York, Wiley, 1995, p. 477.
- [2] J.-F. Carlin, J. Dorsaz, E. Felton, R. Butte, N. Grandjean, and M. Illegems, "Crack-free fully epitaxial nitride microcavity using highly reflective AlInN/GaN Bragg mirrors," *Appl. Phys. Lett.*, vol. 86, no. 3, pp. 031107, 2005.
- [3] H. M. Ng, T. D. Moustakas, and S. N. G. Chu, "High reflectivity and broad bandwidth AlN/GaN distributed Bragg reflectors grown by molecular-beam epitaxy," *Appl. Phys. Lett.*, vol. 76, no. 20, pp. 2818-2820, 2000.
- [4] J. Piprek, T. Troger, B. Schroter, J. Kolodzey, and C. S. Ih, "Thermal conductivity reduction in GaAs-AlAs distributed Bragg reflectors," *IEEE Photon. Technol. Lett.*, vol. 10, no. 1, pp. 81-83, 1998.
- [5] W. S. Capinski, H. J. Maris, T. Ruf, M. Cardona, K. Ploog, and D. S. Katzer, "Thermal-conductivity measurements of GaAs/AlAs superlattices using a picosecond optical pump-and-probe technique," *Phys. Rev. B*, vol. 59, no. 12, pp. 8105-8113, 1999.
- [6] R. Paschotta, "Beam quality deterioration of lasers caused by intracavity beam distortions," *Opt. Express*, vol. 14, no. 13, pp. 6069-6074, 2006.
- [7] A. Giesen, H. Hugel, A. Voss, K. Wittig, U. Brauch, and H. Opower, "Scalable concept for diode-pumped high-power solid-state lasers," *Appl. Phys. B*, vol. 58, no. 5, pp. 365-372, 1994.
- [8] A. Giesen and J. Speiser, "Fifteen years of work on thin-disk lasers: results and scaling laws," *IEEE J. Sel. Top. Quantum Electron.*, vol. 13, no. 3, pp. 598-609, 2007.
- [9] "TruDisk TRUMPF Laser," TRUMPF, [Online]. Available: <http://www.trumpf-laser.com/en/products/solid-state-lasers/disk-lasers/trudisk.html>.
- [10] "Gen 3 High Energy Laser Completes Beam Quality Evaluation," <http://www.gasi.com/gen-3-high-energy-laser-completes-beam-quality-evaluation>, 2015.
- [11] M. Kuznetsov, F. Hakimi, R. Sprague, and A. Mooradian, "High-power (>0.5 W CW) diode-pumped vertical-external-cavity surface-emitting semiconductor lasers with circular TEM₀₀ beams," *IEEE Photon. Technol. Lett.*, vol. 9, no. 8, pp. 1063-1065, 1997.
- [12] B. Heinen, T.-L. Wang, M. Sparenberg, A. Weber, B. Kunert, J. Hader, S. W. Koch, J. V. Moloney, M. Koch, and W. Stolz, "106 W continuous-wave output power from vertical-external-cavity surface-emitting lasers," *Electron. Lett.*, vol. 48, no. 9, pp. 516-517, 2012.
- [13] S. Barman and G. P. Srivastava, "Temperature dependence of the thermal conductivity of different forms of diamond," *J. Appl. Phys.*, vol. 101, no. 12, pp. 123507, 2007.
- [14] A. J. Kemp, G. J. Valentine, J.-M. Hopkins, J. E. Hastie, S. A. Smith, S. Calvez, M. D. Dawson, and D. Burns, "Thermal management in vertical-external-cavity surface-

- emitting lasers: finite-element analysis of a heatspreader approach," *IEEE J. Quantum Electron.*, vol. 41, no. 2, pp. 148-145, 2005.
- [15] M. Y. A. Raja, S. R. J. Brueck, M. Osinski, C. F. Schaus, J. G. McInerney, T. M. Brennan, and B. E. Hammons, "Resonant periodic gain surface-emitting semiconductor lasers," *IEEE J. Quantum Electron.*, vol. 25, no. 6, pp. 1500-1512, 1989.
- [16] S. W. Corzine, R. S. Geels, J. W. Scott, R.-H. Yan, and L. A. Coldren, "Design of Fabry-Perot surface-emitting lasers with a periodic gain structure," *IEEE J. Quantum Electron.*, vol. 25, no. 6, pp. 1513-1524, 1989.
- [17] D. W. Hughes, J. R. M. Barr, and D. C. Hanna, "Mode locking of a diode-laser-pumped Nd:glass laser by frequency modulation," *Opt. Lett.*, vol. 16, no. 3, pp. 147-149, 1991.
- [18] D. Waldburger, S. M. Link, M. Mangold, C. G. E. Alfieri, E. Gini, M. Golling, B. W. Tilma, and U. Keller, "High-power 100fs semiconductor disk lasers," *Optica*, vol. 3, no. 8, pp. 844-852, 2016.
- [19] M. Butkus, J. Rautiainen, O. G. Okhotnikov, C. J. Hamilton, G. P. A. Malcolm, S. S. Mikhlin, I. L. Krestnikov, D. A. Livshits, and E. U. Rafailov, "Quantum dot based semiconductor disk lasers for 1-1.3 μm ," *IEEE J. Sel. Top. Quantum Electron.*, vol. 17, no. 6, pp. 1763-1771, 2011.
- [20] C. L. Sung, C. Y. Lee, H. H. Cho, Y. J. Huang, Y. F. Chen, Z. B. Pan, H. H. Yu, H. J. Zhang, and J. Y. Wang, "Theoretical and experimental studies for high-repetition-rate disordered crystal lasers with harmonic self-mode locking," *Opt. Express*, vol. 24, no. 4, pp. 3832-3838, 2016.
- [21] F. L. Pedrotti, L. S. Pedrotti, and L. M. Pedrotti, "Transfer matrix," in *Introduction to Optics*, Upper Saddle River, Pearson Prentice Hall, 2007, pp. 477-480.
- [22] M. G. Moharam and T. K. Gaylord, "Rigorous coupled-wave analysis of planar-grating diffraction," *J. Opt. Soc. Am.*, vol. 71, no. 7, pp. 811-818, 1981.
- [23] M. N. Polyanskiy, "Refractive index database," [Online]. Available: <http://refractiveindex.info/>.

Chapter 3.

DBR-free Semiconductor Disk Lasers:

Device Fabrication

In this chapter, the fabrication process of substrate transferred active regions will be presented. In section 3.1, a brief introduction to van der Waals bonding and its applications will be discussed. In sections 3.2 and 3.3, the substrate preparation, lift-off, and bonding process will be detailed. In section 3.4, thermal annealing and a few results will be discussed. With limited access to the characterization techniques, preliminary surface quality studies will be presented in section 3.5. Comparisons of photoluminescence and carrier lifetime, both before and after fabrication process, will be made in section 3.6.

3.1 Introduction

For a given target wavelength, there are limited semiconductor material system choices (combinations of substrates and alloys), due to the restrictions of lattice matching. Additionally, some applications place stringent requirements on substrates' thermal or optical properties, which cannot be satisfied by the growth substrates. On the other hand, dielectric, metallic, or even hybrid substrates offer more diverse properties, though these materials are not suitable as epitaxial growth substrates. A post-growth processing technique—lifting devices off from growth substrates, and bonding onto the destination substrates without compromising material quality—greatly enriches the semiconductor integration choices for many devices, including solar cells [1, 2, 3], LEDs [4, 5], and lasers [6, 7, 8]. Substrate transferred semiconductor films are of such high quality that even epitaxial regrowth has been demonstrated [9].

In our group, the lift-off and bonding technique has been applied to study laser cooling of semiconductors [10] for a long time. By transferring a double heterostructure sample onto a high optical quality hemispherical ZnS dome, an integrated device with a record of 99.5% external quantum efficiency has been demonstrated [11]. Recently, a commercial product enabled by this technique is the so-called crystalline mirror [12]. The monocrystalline semiconductor DBRs are lifted off and directly bonded onto destination substrates. Compared to the dielectric coatings, crystalline mirrors can achieve similar reflectivity, but exhibit much lower thermal noise [13]. It has been employed in applications such as optical metrology [13], cavity optomechanics [14], and cavity quantum electrodynamics [15]. Recently, the direct bonding technique has been further utilized to integrate SESAMs with heatspreaders for high power ultrafast lasers, and the substrate-transferred SESAMs have shown much less deformation at high power [16] than SESAMs integrated via solder or flip-chip bonding.

There is a proliferation of bonding techniques, which can be roughly categorized as either direct bonding or adhesive bonding. Adhesive bonding can be performed at room temperature without strict surface quality requirements. But it involves an intermediate layer, such as a polymer [17], which is usually optically lossy and thermally resistive. Therefore, adhesive bonding is not well suited for high power laser applications. Wafer bonding [18], a direct bonding technique, usually refers to bonding between mirror-polished single-crystalline wafers. By applying a slight pressure to the cleaned wafer pairs at room temperature, bonding can be achieved in seconds. The formed van der Waals bonds are weak and a heat treatment or fusion process is usually needed to improve the bonding strength. Therefore, it is also called wafer fusion bonding. This technique has been utilized in the fabrication of VCSELs [19] and VECSELs [20], allowing semiconductor DBRs and active regions to be grown separately.

Compared with semiconductor wafers, typical dielectric substrates have far inferior surface quality. The capillary bonding technique [21] has been adopted to bond VECSEL chips to dielectric [22] or semiconductor [23] heatspreaders. This method resembles the van der Waals bonding technique we use, but does not require the lift-off process. Retaining at least part of the growth substrates, chips only conform minimally to the

substrate during the capillary bonding process, making bonding to low surface quality substrates difficult.

Before discussing the fabrication process, we have to first understand the bonding forces. The van der Waals bonding is based on van der Waals force, which is an intermolecular collective force, induced by charge and electromagnetic field fluctuations [24] arising from both thermal agitation and quantum mechanical uncertainties. It constitutes the attraction and repulsion terms. The repulsion term only comes into effect at a very close distance, which is out of the range of our discussion. For the attraction term, there are three major contributions for neutral molecules [24]: Keesom interactions of permanent dipoles whose mutual angles tend to be in the attractive orientations, Debye interactions between the permanent dipole and induced dipole in another nonpolar molecule, and London dispersion interactions between instantaneous dipoles in nonpolar materials. With a pairwise summation approximation, de Boer [25] has shown that for two parallel planar blocks, when the separation is smaller than both their thicknesses and lateral physical dimensions, the free energy per area varies with the inverse square of the separation. Due to the separation dependence, surface cleanness and flatness are critical for both bonding strength and uniformity.

While microscopically weak [26, 27], the van der Waals force can be macroscopically strong: using van der Waals force, a Tokay gecko can hold itself on a smooth window glass (approximately 10 N with 1 cm² of pad area) [28], and a load of one ton has been held with the hand-sized man-made fabric GeckSkin (2950 N with 100 cm² of pad area) [29]. For our devices, strong bonding force means low thermal resistance, which has not been directly quantified in this dissertation. So far, with active cooling, our directly bonded semiconductor samples can withstand 100 W incident pump power or 40 W absorbed power over a 200 μm diameter pump spot.

We have bonded 2 μm thick semiconductor samples, such as double heterostructures (DHS), MQWs, and GaAs/AlAs DBRs, onto substrates of various materials, including fused silica, sapphire, ZnS, ZnSe, and diamond. Even though substrate quality matters, good bonding has also been achieved with regular laboratory microscope slides. Two large

area bonding results are shown in Figs. 3.1 (a) and (b). Currently, we see no obstacle to bond even larger size samples.

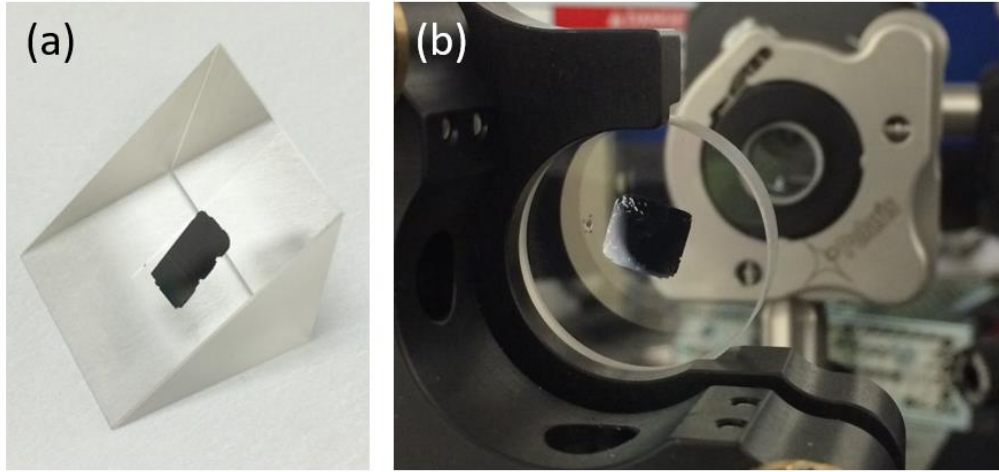


Figure 3.1 Large substrate transferred active regions: (a) 7.5 mm by 5.0 mm sample bonded onto a UV fused silica right angle prism (side lengths $A=B=20.0$ mm, $C=28.3$ mm, surface quality 40/20 scotch-dig, surface flatness $\lambda/10$, Thorlabs); (b) 8.0 mm by 7.5 mm sample bonded onto the back of a 1 inch diameter fused silica high reflector. Both samples lased and the device characterization will be discussed in sections 4.1 and 5.1.

3.2 Substrate surface cleaning and preparation

As mentioned, the surface condition of destination substrates is critical to the bonding results. A contaminated surface could create extra features, such as large interface bubbles or cracks, reduce the adhesion, and even de-bond the device. On the other hand, in addition to cleaning, surface pretreatment could activate surfaces and facilitate bonding. Therefore, the substrate surface cleaning and preparation process is crucial for bonding.

Thermal management is the key for high power SDLs. To facilitate heat extraction from active regions, substrates of high thermal conductivity and low optical loss, such as single-crystalline CVD diamonds, are used in the transmission geometry DBR-free SDLs. The specifications of the diamonds used in chapter 5 are summarized in Table 3.1.

Due to the limited access to high quality diamonds, substrate recycling is a common practice. Usually, bonded samples could be removed from diamond substrates with

adhesive scotch tape. But to avoid extra organic pollution, samples are etched with a strong oxidizing etchant, a mixture of hydrochloric acid and hydrogen peroxide solution. The etching process takes about 5 minutes. Then the substrate is cleaned with piranha solution (98% sulfuric acid and hydrogen peroxide ratio 3:1 by volume), which removes organic contaminants and hydroxylates the diamond surfaces.

The diamond is then dipped into the RCA-1 solution, a mixture of 2 parts of deionized (DI) water, 1 part of 30% aqueous hydrogen peroxide, and 1 part of 29% aqueous ammonium hydroxide, for a 10-minute ultrasonic bath. In such a high pH environment, the contaminants are solvated by ammonium hydroxide and oxidized by hydrogen peroxide. This cleaning process generates hydrophobic substrate surfaces. With diamond substrates, the hydrophobic surface condition yields consistently better bonding results than the hydrophilic one, although the reason is not fully understood. Studies have shown that a RCA-1 solution with certain mixing ratio could microroughen Si substrates [31], but its effect on diamond substrates is yet to be studied. For sapphire or fused silica substrates, the same cleaning procedure can be applied. Due to chemical reactions, ZnS or ZnSe substrates cannot be recycled in this manner.

Table 3.1 Diamond windows specifications

	Size	Absorption coefficient at 1 μm (cm^{-1})	Surface roughness (Ra, nm)	$n_e - n_o$
Regular diamond, Element Six, Inc.	4 mm in diameter, 0.50 mm thick	<0.1 (typically 0.05) 0.120 \pm 0.070 (by z-scan)	< 5 nm	<5 \times 10 ⁻⁴
Low absorption diamond, Element Six, Inc.	3 mm by 3 mm, 0.89 mm thick	<0.01 (typically 0.005) 0.011 \pm 0.003 (by Z-scan)	< 5 nm	<1 \times 10 ⁻⁵
Small diamond, Applied Diamond, Inc.	4 mm in diameter, 0.75 mm thick	0.056 \pm 0.008 (by z-scan)	< 3 nm	Not specified
Large diamond, Applied diamond, Inc.	6 mm by 4 mm, 0.53 to 0.57 mm thick	0.167 \pm 0.028 (by z-scan)	< 3 nm	Not specified

* The dual-beam thermal-lens z-scan measurements were carried out by Nathan Giannini, and the setup is described in [30].

Other than wet etching, gas plasma treatment, such as oxygen, hydrogen, or argon, could also clean and prepare surfaces [18]. Surface contaminants can be oxidized and vaporized with oxygen plasma. Plasma treated Si surfaces have shown enhanced chemical reactivity, partly due to the implantation of high energy ions [18]. After a 90-second oxygen plasma treatment, a hydrophobic diamond surface can be changed to hydrophilic condition. Fabricated by this approach, a DBR-free active region assembly, shown in Fig. 3.9 (a), provides 4 W output power (at 26 W incident pump power); its laser performance will be presented in section 5.2. Similar as it is to the wet etching method, it is not clear whether the plasma changes the diamond surface condition, which is important for diamond recycling.

3.3 Lift-off and bonding

The lift-off technique was first proposed and demonstrated by Konagai et al. [1] in 1978. Named peeled film technology, they observed high selectivity (the ratio of etching rates)

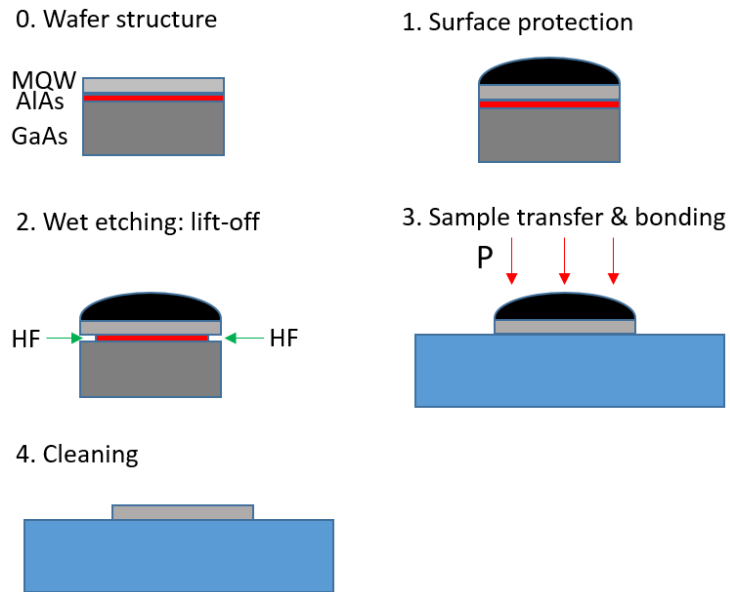


Figure 3.2 Lift-off and bonding procedure. Step 0, cleave the wafer to proper size; step 1, apply a thin black wax layer at 100°C; step 2, wet etch with 49% HF acid and rinse the sample after the etching; step 3, transfer the sample to the destination substrate and apply pressure; step 4, clean the black wax layer with toluene, and rinse the sample with acetone, methanol, and isopropanol.

with HF acid in undercutting AlGaAs layers from GaAs substrates, but their studies were hampered by the slow etching rate and the need for reactants circulation. In 1987, Yablonovitch et al. [32] measured the HF acid selectivity between AlAs and $\text{Al}_{0.4}\text{Ga}_{0.6}\text{As}$ as no less than 10^7 , and accelerated the etching process by depositing a thin tensioned wax layer onto the epitaxial surface. Our lift-off and bonding procedure, explained in Fig. 3.2, follows reference [33]. We try to standardize the processing but some of the parameters are not yet well controlled. Currently, with a recycled diamond substrate, 6 out of 8 bonded devices (approximately 3 mm by 2 mm in area) are bonded without obvious defects, while the remaining two have air bubbles.

3.3.1 Lift-off

One way to separate devices from their growth substrates is to laterally undercut the sacrificial layers. In the active region designs discussed in this dissertation, AlAs is reserved as the sacrificial layer (is also called release layer), which is about 100 nm thick, grown after the GaAs buffer layer and before the active region. Depending on the etchant used, it could also be an etch stop layer. There is evidence that alternative sacrificial layer InAlP generates less etching residue and improves substrate flatness for wafer reuse [34]. At present, it is not clear how much optical losses are due to reactant residue. If this is significant, replacing AlAs with InAlP as the sacrificial layer may be a promising technique.

The detailed active region designs used in this dissertation are presented in Figs. 3.3 and 3.4. For the active regions, there are usually two window layers with a wide bandgap material, usually InGaP for GaAs based material system, to confine carriers and avoid surface recombination. For the DHS sample, a 750 nm thick GaAs layer is sandwiched between two 750 nm thick InGaP layers, shown in Fig. 3.3 (a). For the MQW samples, QWs are in a PGS with a spacing of one half wavelength in optical distance, shown in Fig. 3.4 (a). Due to large indium composition (25%), InGaAs QW layers have a larger lattice constant than GaAs, thereby experiencing compressive strain. To ensure the crystalline quality, they are balanced by the tensile-strained GaAsP barriers. In Fig. 3.3 (b), the MQW

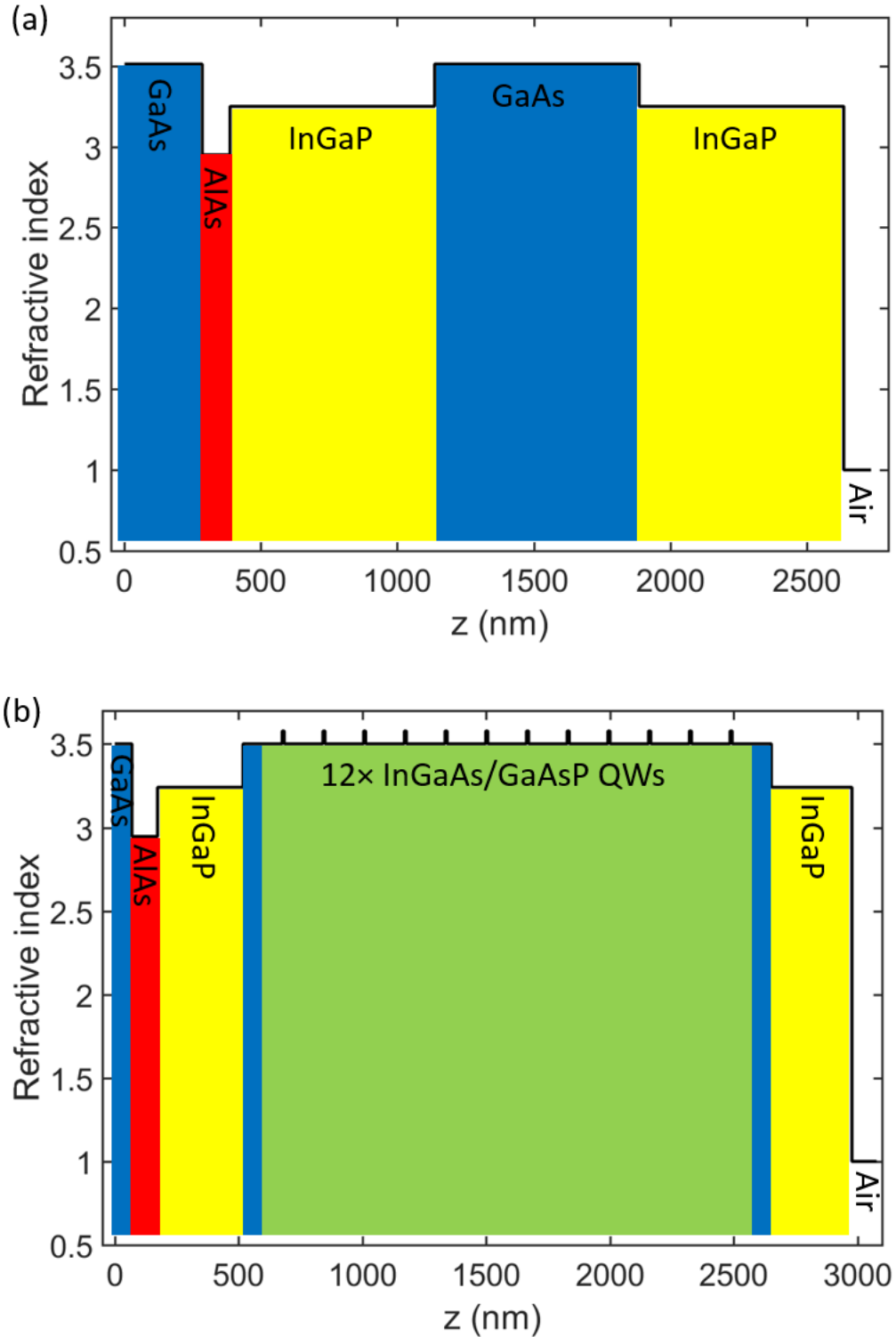


Figure 3.3 Active region designs: DHS (a) and MQW 1312-066 (b). (a) 750 nm $\text{In}_{0.49}\text{Ga}_{0.51}\text{P}/750\text{ nm GaAs}/750\text{ nm In}_{0.49}\text{Ga}_{0.51}\text{P}$; (b) InGaAs MQW at 1040 nm, sample 1312-066: 345 nm $\text{In}_{0.485}\text{Ga}_{0.515}\text{P}/80.4\text{ nm GaAs}/12\text{ QWs}/80.4\text{ nm GaAs}/325.4\text{ nm In}_{0.485}\text{Ga}_{0.515}\text{P}$, QW: 78.1 nm $\text{GaAs}_{0.97}\text{P}_{0.03}/8.3\text{ nm In}_{0.25}\text{Ga}_{0.75}\text{As}/78.1\text{ nm GaAs}_{0.97}\text{P}_{0.03}$.

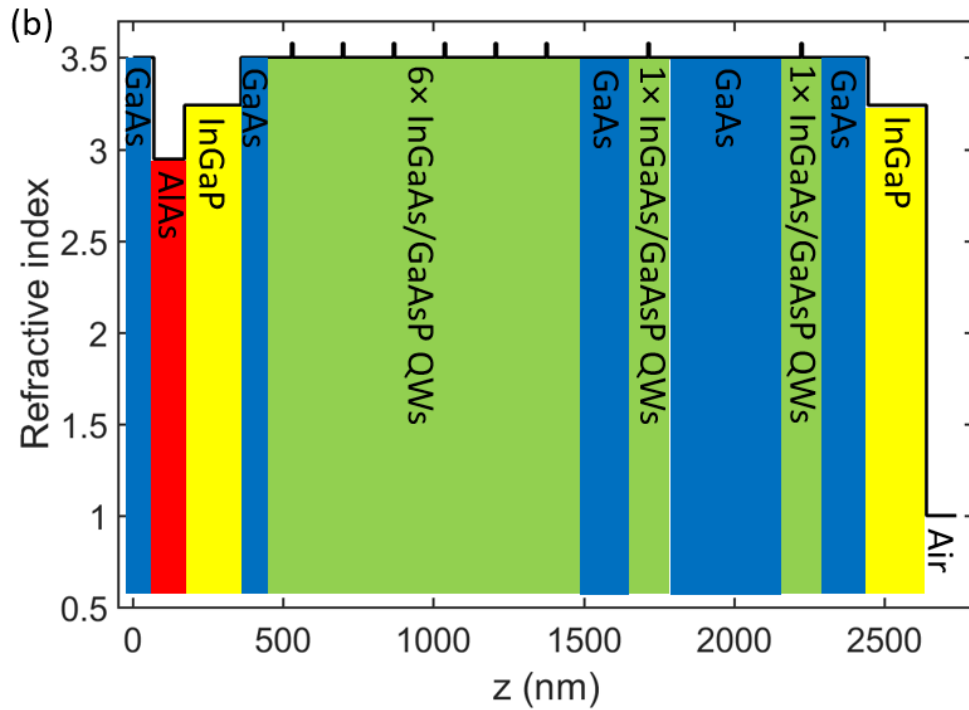
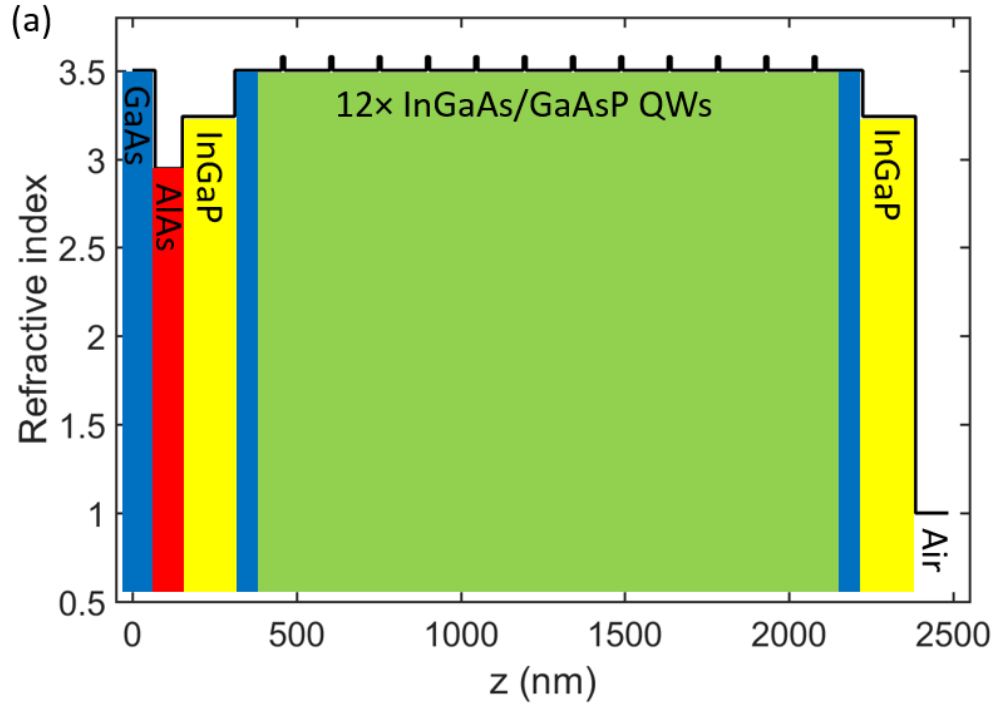


Figure 3.4 Active region designs. (a) InGaAs MQW at 1020 nm, sample 1315-059: 160 nm $\text{In}_{0.49}\text{Ga}_{0.51}\text{P}$ / 72.5 nm GaAs/12 QWs/72.5 nm GaAs/161 nm $\text{In}_{0.49}\text{Ga}_{0.51}\text{P}$, QW: 69 nm GaAs $_{0.97}\text{P}_{0.03}$ /9.4 nm $\text{In}_{0.25}\text{Ga}_{0.75}\text{As}$ / 69 nm GaAs $_{0.97}\text{P}_{0.03}$; (b) InGaAs MQW at 1160 nm, sample 1314-273: 188 nm $\text{In}_{0.49}\text{Ga}_{0.51}\text{P}$ /85.9 nm GaAs/6 QWs/170 nm GaAs/QW/340 nm GaAs/QW/136.7 nm GaAs/194 nm $\text{In}_{0.49}\text{Ga}_{0.51}\text{P}$, QW: 81.9 nm GaAs $_{0.97}\text{P}_{0.03}$ /5.6 nm $\text{In}_{0.36}\text{Ga}_{0.64}\text{As}$ /81.9 nm GaAs $_{0.97}\text{P}_{0.03}$.

structure was designed for the oblique incidence and the QW spacing is wider. In Fig. 3.4 (b), at the design wavelength 1160 nm, as a result of even higher indium composition (36%), a few QWs are skipped to avoid excessive strain accumulation. This forms a selective PGS and the QW locations have been optimized with respect to the absorbed pump power. At the same time, a thick structure ensures high pump absorption. All the samples were grown using MOCVD by Dr. Jeffrey Cederberg at Sandia National Laboratories.

Before etching, the epitaxial surface of the cleaved wafer chip is covered with a 0.3 mm thick black wax (Apiezon Wax W) film applied at 100°C, whose functions will be discussed soon. Then the wax-covered chip is mounted onto a U-shaped Teflon fixture from the substrate side, also with black wax. The whole mount is immersed into a 49% HF acid solution with the fixture upside down, shown in Fig. 3.5, so as to avoid the lift-off layer bonding to the substrate again due to gravity. Because of the high reacting selectivity [32], the sacrificial layer can be fully removed while the active region is almost intact. For a 3 mm by 3 mm sample, the etching takes approximately 2.5 hours, with a lateral etch rate of roughly 1 mm per hour, which is mainly limited by the small contact area between HF and AlAs layer. With larger samples, the etch rate is even slower. HF concentration is varied from 5% to 20%, but no significant change in the device performance is observed. It could be that the HF etching selectivity between InGaP and AlAs is not strongly concentration dependent. More diluted etchant leads to longer etching time.

Another way to accelerate the etch rate is by adopting a flexible, thin polymer film carrier. By adding extra weight on the film, the gap could be enlarged and an etching rate

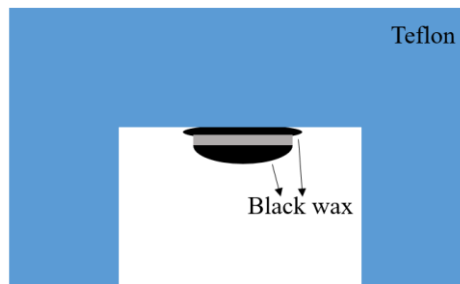


Figure 3.5 Teflon fixture with chip mounted.

of up to 30 mm per hour has been demonstrated [2]. Utilizing this technique, a study [35] shows a thinner sacrificial layer, down to 3 nm, and elevated solution temperature could facilitate the etching. This is a possible future direction, especially for large samples.

Only 2 μm thick, the free-standing active region film is very fragile and difficult to handle. Therefore, the black wax film serves as the mechanical support. In addition, the wax is also resistant to the etchant and protects the window layer from HF acid, which has a relatively slow etch rate but is detrimental to the device performance. Furthermore, such tensioned wax film could bow the lift-off area of the active region up [32] in the etching process, and accelerate the reaction rate by facilitating the diffusion of the reactant and reaction products.

After the sacrificial layer is fully etched, the waxed epitaxial film will come off by itself due to gravity. Sometimes, there could be extra wax near the substrate edge keeping the device attached, requiring a small amount of mechanical force to free it. Then the sample is rinsed with DI water multiple times until the pH of the rinsed water is near 7. Extra attention is needed to avoid introducing extra dirt or cracks to the semiconductor films.

In a post-bonding quality check, we noticed that corners of the top InGaP window layer were round, shown in Fig. 3.6. This could be due to the incomplete coverage of the black wax, which confirms a non-zero etch rate for InGaP in HF. For active regions in this dissertation, there is a second InGaP window layer for carrier confinement right on top of the sacrificial layer, which could also be roughened in the undercutting process. This may introduce extra optical losses and increase the thermal resistance of the fabricated devices.

Since the InGaP window layer is necessary and there is no easy substitute, this led us on a quest for other lift-off approaches. An easy alternative is to etch the complete substrate off, down to the etch stop layer (AIs), and then remove the AIs layer in a diluted HF acid. With this approach, the contact time between HF and the InGaP layer will be reduced from hours to seconds, better protecting the window. This method has been well studied [36] and widely used in the fabrication of traditional VECSEL chips, in which AIs or AlGaAs with a low gallium composition are usually the low index material in the DBR and the lateral undercutting method is no longer an option. The etchant is a mixture of hydrogen

peroxide and ammonium hydroxide at a 33:1 ratio, which is pumped at a constant flow to jet etch the GaAs substrate [10] from the substrate side. For a typical 3 mm by 3 mm sample with a 350 μm thick wafer, it takes about half an hour to etch off the substrate. After the removal of the substrate, there will be a shiny interface with uniform metallic reflection. Because the etchant also reacts with AlAs, the time window is not wide. Approaching the end of the etching process, careful observance is needed to stop the etching in time. Also, the sample mounting is slightly different here. After the black wax deposition, crystal bonding wax is applied to attach the sample to a glass slide, which is held by the fixture of the jet etcher. The crystal bonding wax can be cleaned with acetone after etching, and the released sample is dipped into a diluted 10% HF solution for 10 s to remove the AlAs layer. After careful rinsing with DI water, the sample is ready for bonding.

As mentioned in section 2.2, one of the advantages of DBR-free SDLs is more material system choices. With the van der Waals bonding technique, only a sacrificial layer or etch stop layer is needed; for many material systems, such sacrificial layer materials exist [37, 38, 39, 40].

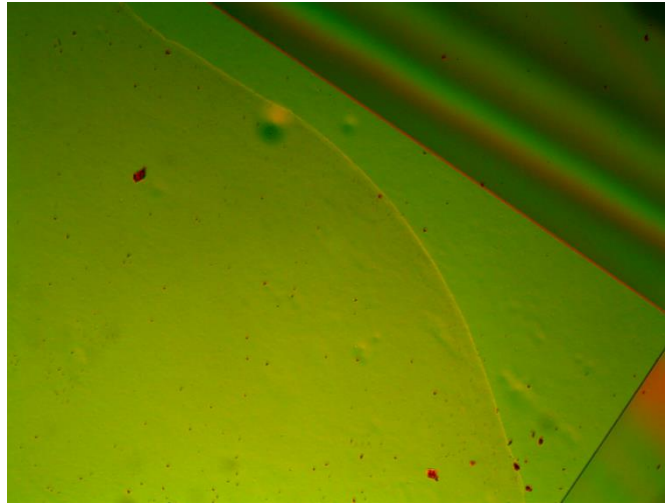


Figure 3.6 Normaski microscope image at a corner of a bonded sample. The sharp black and orange lines are the sample boundary. The top rounded layer is possibly the etched top InGaP window layer. This sample was dipped into the HF acid for 3 hours in the undercutting process. The field of view is about 200 μm by 150 μm .

3.3.2 Bonding

Bonding in air is convenient, but even in a cleanroom environment, the cleanness is difficult to control. Any dust on the bonding interface could result in a large unbonded area—an air bubble. To avoid this issue, our bonding process is performed under water. First, the newly etched sample is immersed in DI water with the etched surface facing up. Then the surface prepared destination substrate is transferred to the sample and the two are pressed together with tweezers, until the assembled part can be picked up from the water without disintegration. The assembly is covered with a cleanroom wipe and constant pressure is applied overnight. Squeezing out the water by applying higher pressure could facilitate the bonding process, but is not very repeatable and may introduce extra cracks.

For small samples, capillary forces may keep them afloat, which must be avoided since most of the particles are also on the water-air interface. Usually, samples could be sunk with a tweezer. If the etched surfaces are facing down, usually a small turbulence could fix that.

As shown in wafer bonding [41], a gas plasma cleaning before bonding can improve the bonding quality and increase the bonding strength. In plasma, the high energy ions and electrons could bombard the surfaces, penetrating and charging the substrate, which can

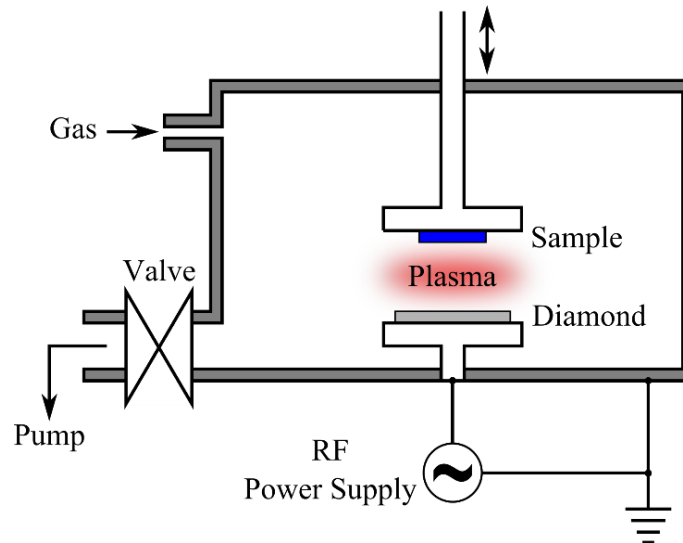


Figure 3.7 Schematic diagram of plasma assisted low temperature bonding apparatus [42].

enhance the bonding strength. As also mentioned, the van der Waals force is mainly caused by the attractions among permanent or transient dipoles. In a liquid environment, due to a shielding-like process with water molecules, the attraction between the substrate and sample are weaker as confirmed by the Hamaker constants [24]. In a vacuum, the attraction between two surfaces is strongest, which could facilitate the bonding. Fig. 3.7 presents a schematic for a proposed plasma assisted vacuum bonding apparatus, which may be a future method to improve bonding.

3.3.3 Cleaning

After constant pressure being applied overnight, the bonding energy is large enough for stable bonding and the black wax is removed with toluene. The solvent is changed thrice to reduce wax residues. Then the sample is rinsed with acetone, methanol, and isopropanol sequentially, and blown dry with N₂ gas. No water is used in the cleaning process, as it may debond the sample. At the end, the sample surface is inspected under an optical microscope and the cleaning process is repeated if necessary.

3.4 Post-processing: thermal treatment

After bonding, the bonding energy increases with storage time and gradually saturates [18]. Additionally, the saturation energy increases with temperature. Therefore, thermal treatment or annealing [43] is a common practice to boost the bonding strength. Both the annealing time and maximum temperature [43, 10] are critical to the annealing results. At low temperatures, bonding strength will not be improved much; at too high temperature, samples can be damaged. In a scotch tape test, Wang [10] showed that the bonding strength of GaAs DHS samples on ZnS substrates improved significantly after annealing at above 400°C.

In addition, the temperature ramping rate also affects the annealing results. For the MQW sample bonded onto a sapphire window in Fig. 3.8, the temperature was ramped

from room temperature to 400°C at 10°C/min and cooled down. The furnace was filled with a constant nitrogen gas flow at atmospheric pressure. Before annealing, there was no visible features on the sample, but many busted voids appeared afterwards. This may be due to the expansion or aggregation of the trapped gas at the bonding interface, despite that the sample having been bonded for more than 10 days before annealing. To avoid air bubbles, samples are degassed at low temperatures (50°C and 80°C) for hours before ramping the temperature up further.

The maximum annealing temperature is set at 340°C to avoid potential device degradations due to overheating. Following reference [39], the sample is annealed at a slow ramping rate, and the temperature curve is shown Fig. 3.9 (a). Figs. 3.9 (b) and (c) are the microscopic images of the sample before and after annealing. For a 2.5 mm by 2.5 mm sample, using a 10 times magnification objective, multiple images are needed for the full view. However, some images cannot be stitched together by software because of too few features, or too much change in color under the non-uniform illumination. So the pictures were aligned manually, which is far from ideal but gives us hints about the surface quality of the bonded or annealed sample.

As shown in the images, after annealing large voids shrink in size and the void density is reduced significantly. A few nearby voids aggregate to form structures, such as the ones

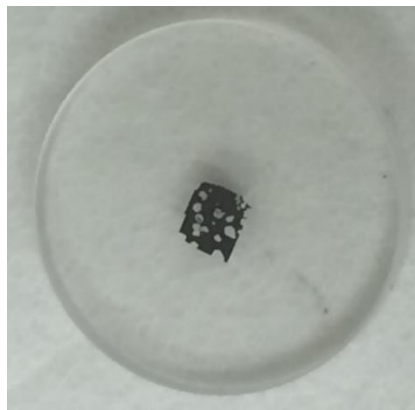


Figure 3.8 A 2.5 mm by 2.0 mm sample bonded on a 0.5 inch in diameter sapphire window, after annealing at a constant rate of 10°C/min up to 400°C. The whole process was in a nitrogen environment. Before annealing, no visible features were observed on the sample under a microscope with 20 times magnification objective. The white regions on the sample are caused by burst air bubbles.

on the left-bottom corner. Even at such a low temperature, the lattice relaxation, which is the subtle line feature, is observed. The laser performance before and after annealing is compared in Fig. 5.9. There is no significant improvement in both slope efficiency and roll-over pump power after annealing. At a certain gain spot, degradation may happen, which may relate to the lattice relaxation. Since the thermal expansion coefficients of GaAs and sapphire are very close, the thermal induced strain is ruled out as the cause of relaxation. If it is degassing, annealing in a vacuum might alleviate the relaxation problem. As to the absence of device performance improvement after annealing, perhaps 340°C is still below the bonding energy transition temperature for sapphire. More systemic studies of annealing conditions are needed.

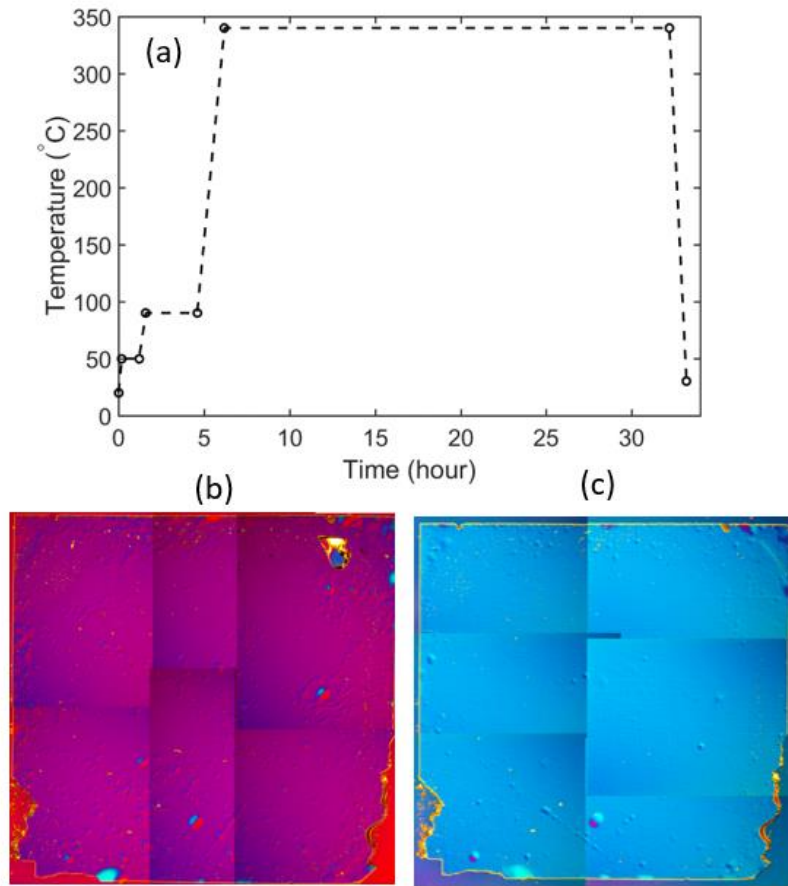


Figure 3.9 (a) The furnace temperature curve in the annealing process. Surface condition before (b) and after (c) annealing with Normaski microscope. The sample size is about 2.5 mm by 2.5 mm and the largest dome-like structure in the bottom middle is about 120 μm in diameter. The straight dark lines here are introduced in the image stacking process. The color differences between (b) and (c) are due to different polarizer angles.

3.5 Surface quality study

As has been discussed in [33], with a transmission electron microscope, an amorphous interfacial region is observed between the van der Waal bonded layer and the destination substrate. The amorphous layers tend to follow the substrates' surface undulations, and vary from 0 to 4 nm in thickness. Therefore, the substrates' surface condition could be the fundamental limit of surface roughness for the bonded layers. We will focus on the bonding defects in section 3.5.1 and surface roughness in section 3.5.2.

The most common bonding defects are interface voids (or bubbles), which could be caused by local surface features on substrates and etched samples, or particles, liquid, and air trapped in the bonding process. In practice, we also observed interface voids formed in the storage or annealing process. The voids are from one micrometer up to tens of micrometers in diameter, which are visible at a grazing angle. In contrast, a well-bonded surface should provide a uniform and featureless reflection.

With transparent substrates, the backside view of the bonding interface also provides a good check. More sophisticated techniques, such as scanning acoustic microscopy and X-ray diffraction topography, have been developed to detect defects in wafer bonding results [44]. For DBR-free geometries, characterization on the surface energy or bonding strength, optical scattering, and thermal resistance could help with the bonding optimization process, but we lack the proper equipment for that at this stage. Here we use a Normaski microscope, also called a differential interface contrast microscope to study the surface morphology, and an atomic force microscope (AFM) to quantitatively evaluate the surface conditions.

3.5.1 Surface morphology study with optical microscope

Optical microscope is applied to study the surface morphology of the substrate-transferred samples. Most artifacts are under the same background with subtle height changes, which are difficult to fully resolve in either transmission or reflection mode. With the interference of two beams at a small offset, the Normaski microscope mode significantly boosts the

image contrast for subtle features, especially along the shear direction in which the optical paths gradient is large. As shown in Fig. 3.10, a comparison is made among images taken at the three modes. The Normaski mode image provides the best contrast for all features, including cracks, interface bubbles, and dust.

In Fig. 3.11, we present two examples, which are bonded onto low absorption single-crystalline diamonds. Both samples provide a few watts output power and their laser conversion graphs will be presented in section 5.2. Especially for the sample in Fig. 3.11 (a), with so many interface voids, the sample not only survived intense optical pumping up to 26 W, but also provided a high slope efficiency. Considering its unoptimized gain structure



Figure 3.10 Optical microscope images of the bonded sample on a substrate from the top in reflection (a), transmission (b), and Normaski (c) modes. The field of view is about 0.7 mm by 0.5 mm. There are cracks (straight lines), interface bubbles, and black wax residues on the sample.

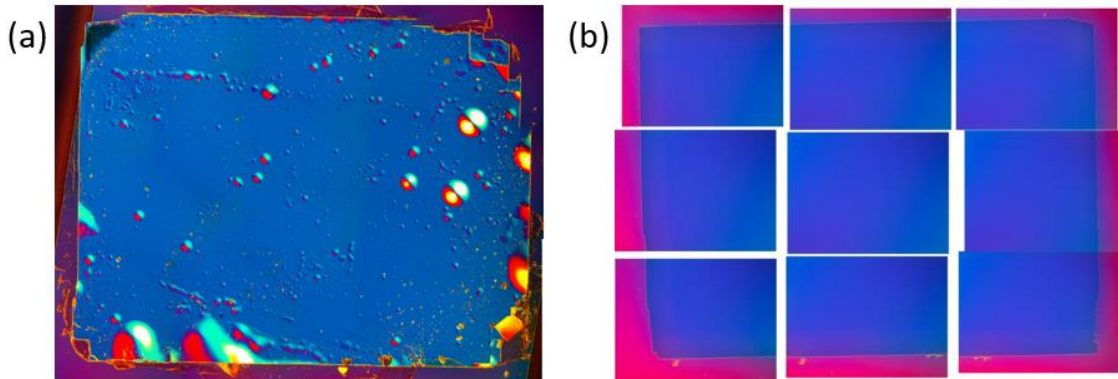


Figure 3.11 Bonding examples. (a) Normaski mode images for a 1312-066 sample bonded on regular diamond. The sample is 3.5 mm by 2.5 mm and lased with a maximum output power 4 W at 50 W incident pump power; (b) Normaski mode images for a 1314-059 sample bonded on a low absorption diamond, 3 mm by 2.5 mm, lased with a maximum output power 6 W at 50W incident pump power.

design, this is unexpected. Therefore, with only the surface morphology information, it is still difficult to precisely predict the device performance. Unfortunately, the sample was damaged later in the annealing process.

3.5.2 Surface topography study with AFM

In this section, AFM is applied to study the surface topography conditions of substrates and bonded devices. We focus on the characteristic length of acoustic phonons, which are on the nanometer scale for GaAs. Figs. 3.12 (a) and (b) show the surface conditions of a $2\ \mu\text{m}$ by $2\ \mu\text{m}$ region on the diamond substrate before bonding, and (c) and (d) show the conditions after bonding.

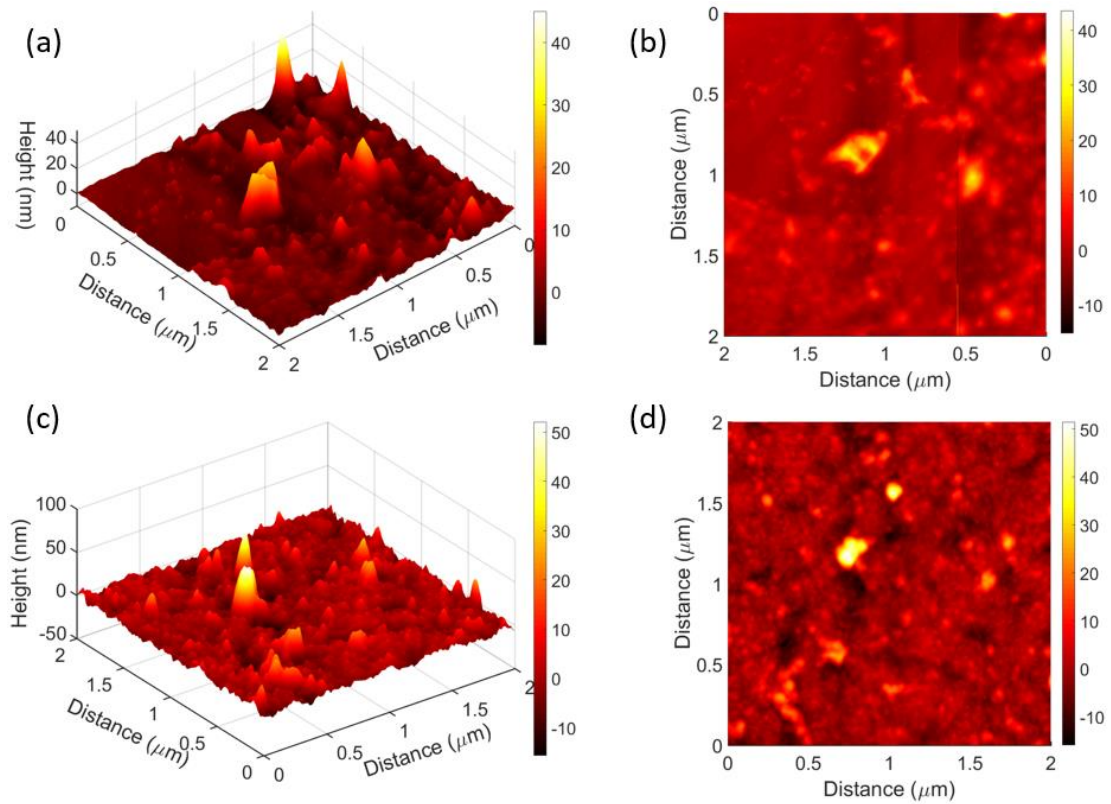


Figure 3.12 AFM scans on diamond surface and epitaxial surface of a van der Waals bonded MQW on a diamond. (a) and (c) are surface topography images of $2\ \mu\text{m}$ by $2\ \mu\text{m}$ regions on the diamond surface, one center of a bonded sample. (b) and (d) are the corresponding 3D images. The scanning areas are $2\ \mu\text{m}$ by $2\ \mu\text{m}$, with 512 steps along both directions. The Si tip radius is 8 nm, and AFM model number. All the scans were taken under the tapping mode.

We further analyze the surface roughness, the height variation distributions for which are shown in Fig. 3.13. For the diamond substrate, the FWHM of the height distribution is about 2.8 nm. On the bonded sample, the FWHM varies from 6.3 nm at the center to 7.2 nm near the edge. For the wafer before processing, a FWHM with less than 1 nm is obtained. So far, it is difficult to tell whether the roughness deterioration is introduced in the etching or bonding process.

We have attempted to scan a larger area, 200 μm by 200 μm , on both diamond substrates. For a new, regular diamond, scratches and pits tens of nanometers in depth are observed. Since diamond is much harder, silicon AFM tips are worn off quickly in the tapping mode and we do not have any good AFM images with a large scanning area.

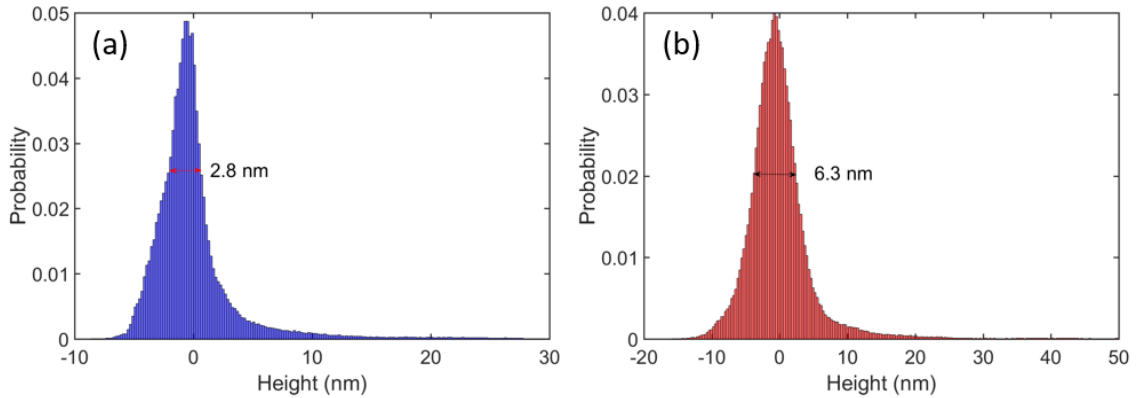


Figure 3.13 Surface roughness analysis: height variation (height minus average height) distribution of the AFM scans in Fig. 3.9. The FWHMs of the height distributions are 2.8 nm (diamond surface), 6.3 nm (center of the bonded sample). Probability is the normalized counts. The MQW sample is designed at 1040 nm.

3.6 Photoluminescence and carrier lifetime characterization

Fig. 3.14 shows the photoluminescence (PL) spectra of a MQW sample before and after the device fabrication. Under the same pump condition, the PL after bonding is consistently brighter at all five pump spots. This may be due to a combination of the thermal and Fabry-Perot effects. With a highly thermal conductive substrate—diamond—the bonded MQW experiences lower temperature rise. As a result, the temperature dependent nonradiative

losses are lower and PL is brighter. There is a blueshift of about 2 nm for the PL peak, which corresponds to about 7 K cooler, ignoring other factors. The strain condition may shift the PL but no strain is intentionally introduced. After bonding, the reflectivity on the semiconductor-substrate interface increases by 3%. Therefore, the PL from the multi-layer structure will experience stronger amplitude modulation and can be brighter but less than 20%.

One concern is that the nonradiative recombination rate via bulk or surface defects may increase after bonding. Therefore, the late-time PL lifetime of the sample is characterized before and after bonding at room temperature. The in-well pumping is performed with a pulsed laser diode at 910 nm, so as to avoid the influence of PL from barrier layers and the carrier transportation. By fitting the late-time PL counts when carrier density is relatively low, as shown in Fig. 3.15, the nonradiative recombination coefficient $A=1/\tau$ is derived. The variation between the fitted lifetime coefficients is within the fitting error, which verifies that the device quality is uncompromised after bonding. Our conclusion differs from [45], in which the lift-off process affects the interface recombination. This discrepancy may arise from the different bonding procedures. In reference [45], samples

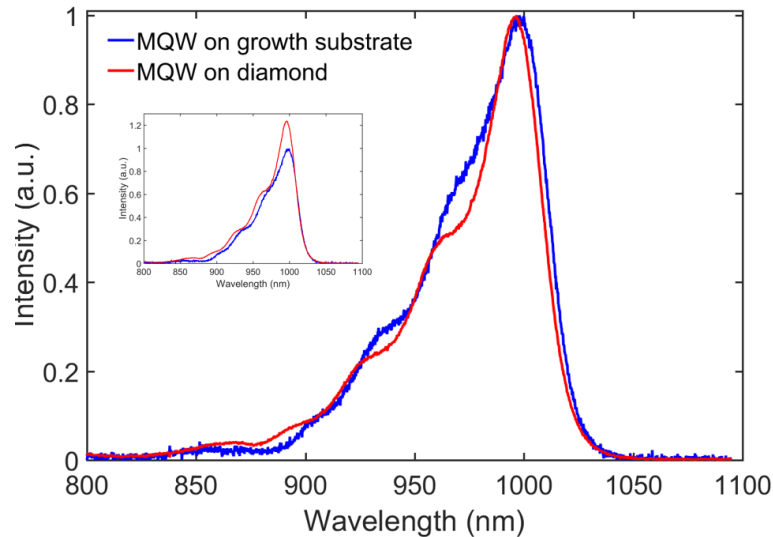


Figure 3.14 PL spectra of a MQW sample before (blue) and after bonding (red). Inset is the brightness comparison. Each spectrum is an average of five spectra collected from different pump spots. The sample is pumped with a CW Ti:sapphire laser at 790 nm, which is modulated with 2% duty cycle. Both the pump and PL collection setups were kept the same in measurements. The bonded MQW sample has a good surface quality and lased well.

are lifted off in free-standing conditions and any bending may cause crystalline defects. It is believed that the radiative recombination coefficient B is constant in the process, and a power-dependent PL measurement [46] could confirm this.

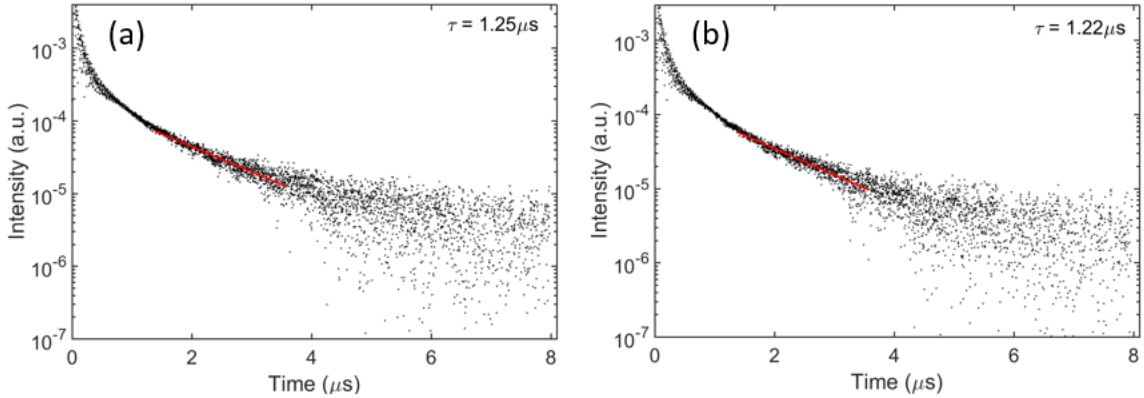


Figure 3.15 MQW lifetime measurements before (a) and after (b) bonding. A pulsed laser diode at 910 nm is used as pump source. The pulses are 10 ns long, at 6 kHz repetition rate with 1 mW in average power. The PL is collected with a telescope system and detected with a PMT. The vertical axis is the dark count removed signal. The MQW sample is bonded on a regular single-crystalline diamond, and lases well.

3.7 Summary

In summary, we have adapted the typical epitaxial lift-off and van der Waals bonding technique to fabricate DBR-free geometries. To improve bonding quality and yield, surface preparation and etching processes have been optimized, with the assistance of a Normaski microscope and an AFM, along with the device characterization, which will be discussed in chapter 5. Post-bonding thermal treatment has also been preliminarily studied and more systematic investigation is needed.

Even though we are focusing on the GaAs material system here, this technique can be potentially applied to almost all III-V [38], II-VI [40], and even IV-VI [47] material systems, as long as good sacrificial or etch stop layer materials exist which for many material systems, they do.

3.8 References

- [1] M. Konagai, M. Sugimoto, and K. Takahashi, "High efficiency GaAs thin film solar cells by peeled film technology," *J. Cryst. Growth*, vol. 45, pp. 277-280, 1978.
- [2] J. J. Schermer, G. J. Bauhuis, P. Mulder, E. J. Haverkamp, J. van Deelen, A. T. J. van Niftrik, and P. K. Larsen, "Photon confinement in high-efficiency, thin-film III-V solar cells obtained by epitaxial lift-off," *Thin Solid Films*, vol. 511-512, pp. 645-653, 2006.
- [3] F. Dimroth, M. Grave, P. Beutel, U. Fiedeler, C. Karcher, T. N. D. Tibbits, E. Oliva, G. Siefert, M. Schachtner, A. Wekkeli, A.W. Bett, R. Krause, M. Piccin, N. Blanc, C. Drazek, E. Guiot, B. Ghyselen, T. Salvetat, A. Tauzin, T. Signamarcheix, A. Dobrich, T. Hannappel, and K. Schwarzburg, "Wafer bonded four-junction GaInP/GaAs/GaInAsP/GaInAs concentrator solar cells with 44.7% efficiency," *Prog. Photovolt. Res. Appl.*, vol. 22, no. 3, pp. 277-282, 2014.
- [4] I. Pollentier, P. Demeester, A. Ackaert, L. Buydens, P. Van Daele, and R. Baets, "Epitaxial lift-off GaAs LEDs to Si for fabrication of opto-electronic integrated circuits," *Electron. Lett.*, vol. 26, no. 3, pp. 193-194, 1990.
- [5] J. M M Santos, B. E Jones, P. J. Schlosser, S. Watson, J. Herrnsdorf, B. Guilhabert, J. J D McKendry, J. De Jesus, T. A. Garcia, and M. C. Tamargo, "Hybrid GaN LED with capillary-bonded II-VI MQW color-converting membrane for visible light communications," *Semicond. Sci. Technol.*, vol. 30, no. 3, pp. 035012, 2015.
- [6] E. Yablonovitch, E. Kapon, T. J. Gmitter, C. P. Yun, and R. Bhat, "Double heterostructure GaAs/AlGaAs thin film diode lasers on glass substrates," *IEEE Photon. Technol. Lett.*, vol. 1, no. 2, pp. 41-42, 1989.
- [7] H. Yang, D. Zhao, S. Chuwongin, J.-H. Seo, W. Yang, Y. Shuai, J. Berggren, M. Hammar, Z. Ma, and W. Zhou, "Transfer-printed stacked nanomembrane lasers on silicon," *Nature Photon.*, vol. 6, pp. 615-620, 2012.
- [8] Z. Yang, A. R. Albrecht, J. G. Cederberg, and M. Sheik-Bahae, "DBR-free optically pumped semiconductor disk lasers," *Proc. SPIE*, 9349, 934905, San Francisco, CA, USA, 2015.
- [9] E. Yablonovitch, K. Kash, T. J. Gmitter, and L. T. Florez, "Regrowth of GaAs quantum wells on GaAs liftoff films 'van der Waals bonded' to silicon substrates," *Electron. Lett.*, vol. 25, no. 2, pp. 171-173, 1989.
- [10] C. Wang, "Precise characterization and investigation of laser cooling in III-V compound semiconductors," Ph.D dissertation, University of New Mexico, 2015.

- [11] D. A. Bender, J. G. Cederberg, C. Wang, and M. Sheik-Bahae, "Development of high quantum efficiency GaAs/GaInP double heterostructures for laser cooling," *Appl. Phys. Lett.*, vol. 102, no. 25, pp. 252102, 2013.
- [12] Crystalline Mirrors Solutions, [Online]. <http://www.crystallinemirrors.com/>.
- [13] G. D. Cole, W. Zhang, M. J. Martin, J. Ye, and M. Aspelmeyer, "Tenfold reduction of Brownian noise in high-reflectivity optical coatings," *Nature Photon.*, vol. 7, pp. 644-650, 2013.
- [14] G. D. Cole, "Cavity optomechanics with low-noise crystalline mirrors," *Proc. SPIE*, 8458, 845807, San Diego, CA, USA, 2012.
- [15] L. Greuter, D. Najer, A. V. Kuhlmann, S. R. Valentin, A. Ludwig, A. D. Wieck, S. Starsielec, and R. J. Warburton, "Epitaxial lift-off for solid-state cavity quantum electrodynamics," *J. Appl. Phys.*, vol. 118, pp. 075705, 2015.
- [16] A. Diebold, T. Zengerle, C. G. E. Alfieri, C. Schriber, F. Emaury, M. Mangold, M. Hoffmann, C. J. Saraceno, M. Golling, D. Follman, G. D. Cole, M. Aspelmeyer, T. Sudmeyer, and U. Keller, "Optimized SESAMs for kilowatt-level ultrafast lasers," *Opt. Express*, vol. 24, no. 10, pp. 10512-10526, 2016.
- [17] D. Chengher, Z. Hatzopoulos, S. Gallis, G. Deligeorgis, E. Aperathitis, M. Androulidaki, M. Alexe, V. Dragoi, E. D. Kyriakis-Bitaros, G. Halkias, and A. Georgakilas, "Fabrication of GaAs laser diodes on Si using low-temperature bonding of MBE-grown GaAs wafers with Si wafers," *J. Cryst. Growth*, vol. 251, no. 1-4, pp. 754-759, 2003.
- [18] Q.-Y. Tong and U. Gosele, *Semiconductor Wafer Bonding: Science and Technology*, Wiley, 1999.
- [19] A. Mircea, A. Caliman, V. Iakovlev, A. Mereuta, G. Suruceanu, C. A. Berseth, P. Royo, A. Syrbu, and E. Kapon, "Cavity mode-gain peak tradeoff for 1320 nm wafer-fused VCSELs with 3 mW SM power and 10 Gb/s modulation speed up to 70°C," *IEEE Photon. Technol. Lett.*, vol. 19, no. 2, pp. 121-123, 2007.
- [20] J. Lyytikainen, J. Rautianinen, A. Sirbu, V. Iakovlev, A. Laakso, S. Ranta, M. Tavast, E. Kapon, and O. G. Okhotnikov, "High-power 1.48 μm wafer-fused optically pumped semiconductor disk laser," *IEEE Photon. Technol. Lett.*, vol. 23, no. 13, pp. 917-919, 2011.
- [21] Z. L. Liao, "Semiconductor wafer bonding via liquid capillarity," *Appl. Phys. Lett.*, vol. 77, no. 5, pp. 651-653, 2000.
- [22] W. J. Alford, T. D. Raymond, and A. A. Allerman, "High power and good beam quality at 980 nm from a vertical external-cavity surface-emitting laser," *J. Opt. Soc. Am. B*, vol. 19, no. 4, pp. 663-666, 2002.

- [23] H. Lindberg, M. Strassner, J. Bengtsson, and A. Larsson, "High-power optically pumped 1550 nm VECSEL with a bonded silicon heat spreader," *IEEE Photon. Technol. Lett.*, vol. 16, no. 5, pp. 1233-1235, 2004.
- [24] V. A. Parsegian, *Van der Waals Forces: a Handbook for Biologists, Chemists, Engineers, and Physicists*, New York: Cambridge University Press, 2006.
- [25] J. H. d. Boer, "The influence of van der Waals' forces and primary bonds on binding energy, strength and orientation, with special reference to some artificial resins," *Trans. Farad. Soc.*, vol. 32, pp. 10-37, 1936.
- [26] A. P. Prosser and J. A. Kitchener, "Direct measurement of long-range van der Waals forces," *Nature*, vol. 178, pp. 1339-1340, 1956.
- [27] S. V. Aradhya, M. Frei, M. S. Hybertsen, and L. Venkataraman, "Van der Waals interactions at metal/organic interfaces at the single-molecule level," *Nature Mater.*, vol. 11, pp. 872-876, 2012.
- [28] K. Autumn, Y. A. Liang, S. Tonia Hsieh, W. Zesch, W. P. Chan, T. W. Kenny, R. Fearing, and R. J. Full, "Adhesive force of a single gecko foot-hair," *Nature*, vol. 405, pp. 681-684, 2000.
- [29] M. D. Bartlett, A. B. Croll, D. R. King, B. M. Paret, D. J. Irschick, and A. J. Crosby, "Looking beyond fibrillar features to scale Gecko-like adhesion," *Adv. Mat.*, vol. 24, no. 8, pp. 1078-1083, 2012.
- [30] N. Giannini, J. R. Silva, C. Wang, A. R. Albrecht, S. D. Melgaard, and M. Sheik-Bahae, "High sensitivity background absorption measurements in semiconductors," *Proc. SPIE*, 9380, 93800F, San Francisco, CA, USA, 2015.
- [31] M. Miyashita, T. Tusga, K. Makihara, and T. Ohmi, "Dependence of surface microroughness of CZ, FZ, and EPI wafers on wet chemical processing," *J. Electrochem. Soc.*, vol. 139, no. 8, pp. 2133-2142, 1992.
- [32] E. Yablonovitch, T. Gmitter, J. P. Harbison, and R. Bhat, "Extreme selectivity in the lift-off of epitaxial GaAs films," *Appl. Phys. Lett.*, vol. 51, no. 26, pp. 2222-2224, 1987.
- [33] E. Yablonovitch, D. M. Hwang, T. J. Gmitter, L. T. Florez, and J. P. Harbison, "Van der Waals bonding of GaAs epitaxial liftoff films onto arbitrary substrates," *Appl. Phys. Lett.*, vol. 56, no. 24, pp. 2419-2421, 1990.
- [34] C.-T. Cheng, K.-T. Shiu, N. Li, S.-J. Han, L. Shi, and D. K. Sadana, "Epitaxial lift-off process for gallium arsenide substrate reuse and flexible electronics," *Nature Comm.*, vol. 4, pp. 1577-1583, 2013.

- [35] J. J. Schermer, G. J. Bauhuis, P. Mulder, W. J. Meulemeesters, E. Haverkamp, M. M. A. J. Voncken, and P. K. Larsen, "High rate epitaxial lift-off of InGaP films from GaAs substrates," *Appl. Phys. Lett.*, vol. 76, no. 15, pp. 2131-3133, 2000.
- [36] J. J. LePore, "An improved technique for selective etching of GaAs and Ga_{1-x}Al_xAs," *J. Appl. Phys.*, vol. 51, no. 12, pp. 6441-6442, 1980.
- [37] A. R. Clawson, "Guide to references on III-V semiconductor chemical etching," *Mater. Sci. Eng. R, Rep.*, vol. 31, no. 1, pp. 1-438, 2001.
- [38] K. Hjort, "Sacrificial etching of III-V compounds for micromechanical devices," *J. Micromech. Microeng.*, vol. 6, pp. 370-375, 1996.
- [39] K. Matsumoto, R. Kobie, and K. Shimomura, "Thermal treatment for preventing void formation on directly-bonded InP/Si interface," *Jpn. J. Appl. Phys.*, vol. 53, pp. 116502, 2014.
- [40] C. Bradford, A. Curran, A. Balocchi, B. C. Cavenett, K. A. Prior, and R. J. Warburton, "Epitaxial lift-off of MBE grown II-VI heterostructures using a novel MgS release layer," *J. Cryst. Growth*, vol. 278, no. 1-4, pp. 325-328, 2005.
- [41] D. Pasquariello and K. Hjort, "Plasma-assisted InP-to-Si low temperature wafer bonding," *IEEE J. Sel. Top. Quantum Electron.*, vol. 8, no. 1, pp. 118-131, 2002.
- [42] A. R. Albrecht, "Private communication," 2015.
- [43] P. Demeester, I. Pollentier, P. De Dobbelaere, C. Brys, and P. Van Daele, "Epitaxial lift-off and its applications," *Semicond. Sci. Technol.*, vol. 8, pp. 1124-1135, 1993.
- [44] A. Plöbl and G. Kräuter, "Wafer direct bonding: tailoring adhesion between brittle materials," *Mater. Sci. Eng.*, vol. R25, pp. 1-88, 1998.
- [45] B. Imangholi, M. P. Hasselbeck, M. Sheik-Bahae, R. I. Epstein, and S. Kurtz, "Effects of epitaxial lift-off on interface recombination and laser cooling in GaInP/GaAs heterostructures," *Appl. Phys. Lett.*, vol. 86, no. 8, pp. 081104, 2005.
- [46] C. Wang, C.-Y. Li, M. P. Hasselbeck, B. Imangholi, and M. Sheik-Bahae, "Precision, all-optical measurement of external quantum efficiency in semiconductors," *J. Appl. Phys.*, vol. 109, no. 9, pp. 093108, 2011.
- [47] H. Z. Wu, X. M. Fang, R. Salas Jr., D. McAlister, and P. J. McCann, "Transfer of PbSe/PbEuSe epilayers grown by MBE on BaF₂-coated Si(111)," *Thin Solid Films*, vol. 352, no. 1-2, pp. 278-282, 1999.

Chapter 4

Total Internal Reflection Based DBR-free Semiconductor Disk Lasers

With the lift-off and van der Waals bonding technique detailed in the previous chapter, active regions can be integrated onto various substrates. This offers DBR-free SDLs with geometry flexibility: the TIR geometries with prisms, monolithic cavity geometries with quadrilateral or high refractive index triangular prisms, and transmission geometries with optical windows in standing wave and ring cavities. In this chapter, we will focus on designs and characterization of the TIR based DBR-free geometries.

4.1 TIR DBR-free SDLs

4.1.1 Proof-of-concept: lasers near 1 μm

The active region used in this section consists of 12 InGaAs QWs in a PGS and the detailed design is shown in Fig. 3.3 (b). With the aforementioned device fabrication process, the active region is bonded onto the hypotenuse side of a fused silica right-angle prism (Thorlabs PS608). The prism is 20 mm by 20 mm by 20 mm (side length by side length by height) and the bonded sample is 7.5 mm by 5.0 mm in area. An image of the active-region-prism assembly is presented in Fig. 3.1 (a). For laser geometries utilizing TIR, both the QW separation and cap layer thickness are critical to the effective gain, which will be discussed in section 5.6. The active region used here is not optimized for this configuration.

Two high reflectivity concave mirrors are used to form a V-shaped cavity [1], as shown in Fig. 4.1. The two mirrors have 50 mm and 100 mm radii of curvature (ROC), and are approximately 47 mm and 96 mm in optical length away from the active region. With the ABCD matrix method, the cavity mode is 140 μm in diameter at the active region.

The active region is pumped with a tunable, CW Ti:sapphire laser, of which the output is modulated by a mechanical chopper. By stacking two regular 50% duty cycle chopper blades together with a phase shift, open slits narrower than 1 mm can be achieved, resulting in a duty cycle of approximately 1%, as shown in Fig. 4.1. Since the Ti:sapphire beam size is larger than the slit width, the laser is focused with an AR coated lens of 25 mm focal length, and afterwards collimated with a second lens of 100 mm focal length. The laser beam after the telescope system is about 8 mm in diameter, which enables a tighter pump focus on the active region. With this technique, the modulated pulses are as short as 10 μs in FWHM and the average power is reduced by two orders of magnitude, while the peak power stays unchanged. This is critical to the lasing operation, since fused silica has low thermal conductivity and the prism is not actively cooled, while the threshold carrier density (about $2 \times 10^{18} \text{ cm}^{-3}$) is high. The Ti:sapphire laser can provide up to 2.5 W output power with approximately TEM₀₀ mode. Further increasing the pump power for the Ti:sapphire laser, the output beam quality deteriorates significantly due to the thermal effect in the crystal. In experiments, the pump wavelength is kept at 810 nm.

The V-shaped cavity geometry lases and to the best of our knowledge, this is the first SDL based on TIR. Fig. 4.2 presents the laser conversion graphs at two pump duty cycles. With 0.4% duty cycle, the output power scales with the pump power above the threshold. With 1.0% duty cycle, the laser output tends to roll-over at high average pump power,

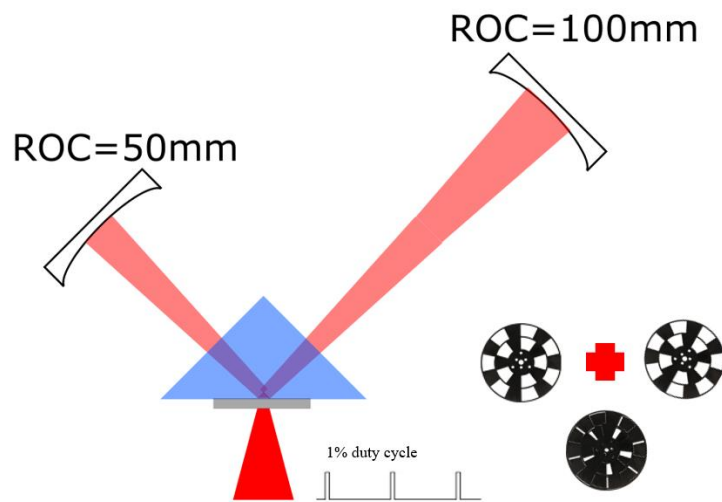


Figure 4.1 Schematic of the TIR based V-shaped cavity. All prism surfaces are uncoated. On the bottom right, the chopper blades stacking scheme is presented. The active region is from wafer 1312-066.

which may be due to the thermal effect in the active region. Firstly, the fused silica substrate has low thermal conductivity (about 1.3 W/(m K)), and the thermal conduction from the active region to the substrate is fairly limited. Additionally, the prism is clamped onto an aluminum platform without active cooling. For CW operation, a more efficient thermal management scheme is needed.

With 1.0% pump duty cycle, the laser operates at 1046 nm with 5 mW average pump power at threshold, as shown in Fig. 4.3, and the emission wavelength redshifts to 1060 nm with 15 mW average pump power. This is due to the gain spectrum shift with temperature. Considering the temperature induced gain shift rate at 0.3 nm/K, this corresponds to 47 K temperature raise in the active region. The laser output beam is close to TEM₀₀ mode.

Confirmed with a Glan-Thompson polarizer, the laser output is mainly TE polarized (with 100:1 output power ratio between TE and TM), which can be explained with the effective gain, as will be evaluated later in section 5.6. Although total internal reflected on the air-semiconductor interface, due to large refractive indices of semiconductor materials, the laser enters the active region at a small incident angle, about 17.6°. Therefore, the incident and totally reflected fields interfere, forming a standing wave pattern perpendicular to the semiconductor plane. With polarization dependent phase shifts from

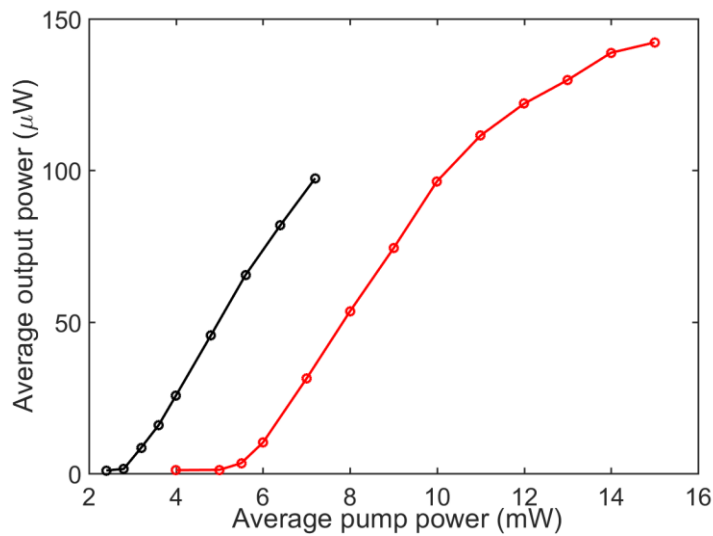


Figure 4.2 Power conversion graph with 0.4% (black) and 1.0% (red) duty cycle for the TIR based DBR-free SDL. For the 1% duty cycle curve, due to thermal roll-over, no output power measurements at peak pump power more than 1.5 W.

the TIR, the TE and TM polarized fields have their field extrema at different locations and, as a result, experience different effective gain. Additionally, the etalon effect in the semiconductor subcavity also varies with polarization. According to the calculation in section 5.6, with the PGS used here, TM polarization field experiences lower integrated gain and is not supported at low pump powers.

Lacking proper output couplers, the cavity coupling efficiency is optimized with a 1 mm thick fused silica optical window inserted into the cavity near Brewster's angle. Adjusting the window orientation changes the Fresnel reflection—the coupling efficiency. Since the laser is TE polarized, the rotation axis is parallel to the table plane, and perpendicular to the laser path. By optimizing the window tilting angle, about 0.5 mW average power is collected in total at 0.8% pump duty cycle, about 6.2% optical-to-optical efficiency. The laser performance is shown in Fig. 4.4.

Because both prism side surfaces are uncoated, and considering 3.4% Fresnel reflection losses (refractive index $n=1.45$ for fused silica at $\lambda=1.04 \mu\text{m}$) per interface and 4 times per roundtrip, the lasing of this geometry is a small surprise to us. Since the roundtrip gain is less than 13.6%, these reflections cannot be all losses, especially with such low threshold. For typical VECSELs at this wavelength range, the threshold pump intensity is on the order

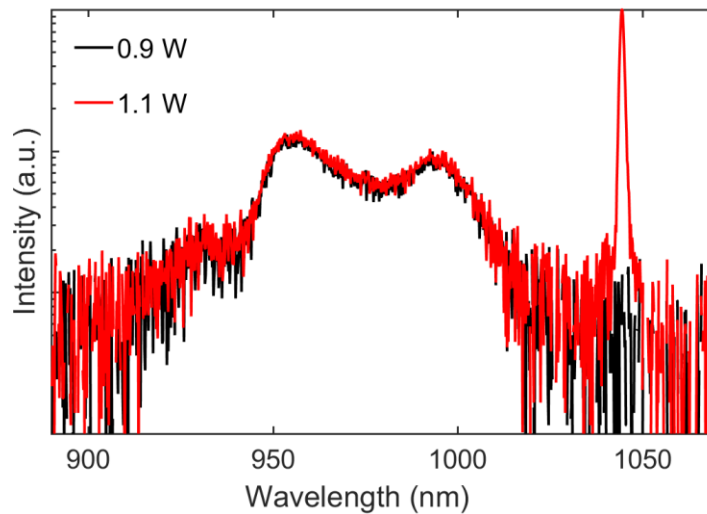


Figure 4.3 Spectra below and above threshold for a 1312-066 sample bonded onto a fused silica right-angle prism. The laser operates at around 1046 nm near threshold. The spectra are collected with a multimode fiber behind a high reflectivity mirror at 1030 nm.

of 1 kW/cm^2 , and the V-shape cavity is 3.9 kW/cm^2 . This implies the prism angles are very close to the specifications, and the whole active-region-prism assembly acts as an etalon, with reflections from interfaces coherently added back to the laser mode. These high quality prisms can be further used in monolithic cavities, or even assembled to high quality cubes, as will be discussed in the next section.

Fused silica substrates are good testbeds for novel geometries, since good surface and optical quality substrates are inexpensive and readily available. Limited by their poor thermal performance, these substrates are far from ideal for high power DBR-free SDLs. On the other hand, diamond substrates are superior in thermal conductivity, though they are high cost and of limited availability. Sapphire substrates, widely used in standard optical parts and with decent thermal performance (approximately 25 W/(m K) at $46 \text{ }^\circ\text{C}$, depending on the crystal axis), are good heatspreader candidates. Therefore, an active region is bonded onto a side surface of a sapphire equilateral prism (from Crystran Ltd. with uncontrolled optic axis), as shown in the inset of Fig. 4.6. The laser performance is shown in Fig. 4.5.

With a more thermal conductive prism, under the same pumping condition, the active region experiences lower temperature rise. With continuous pumping, it lases for less than

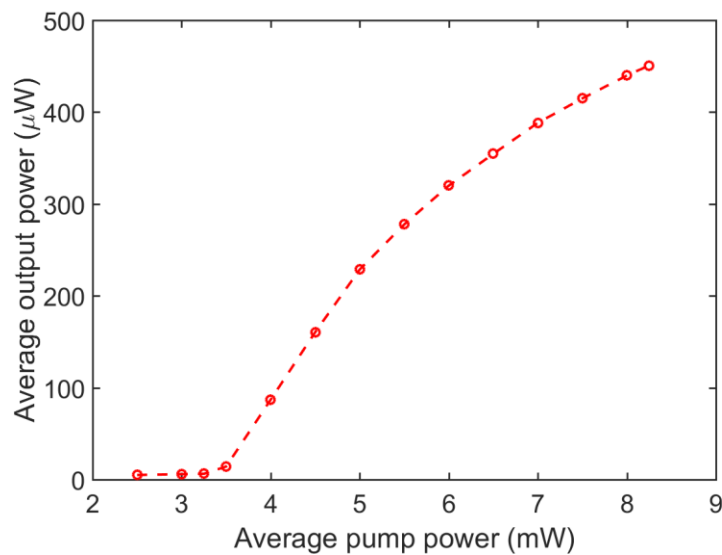


Figure 4.4 Laser conversion graph with a 1 mm thick fused silica window at near Brewster's angle to optimize the coupling efficiency.

1 s and stops. By blocking the pump laser in time, no permanent damage is induced and the process is repeatable, which is different from the fused silica case. This exhibits the potential for CW operation. In section 5.2, for a DBR-free SDL in transmission geometry, CW operation is achieved with gain chips bonded onto sapphire windows with active

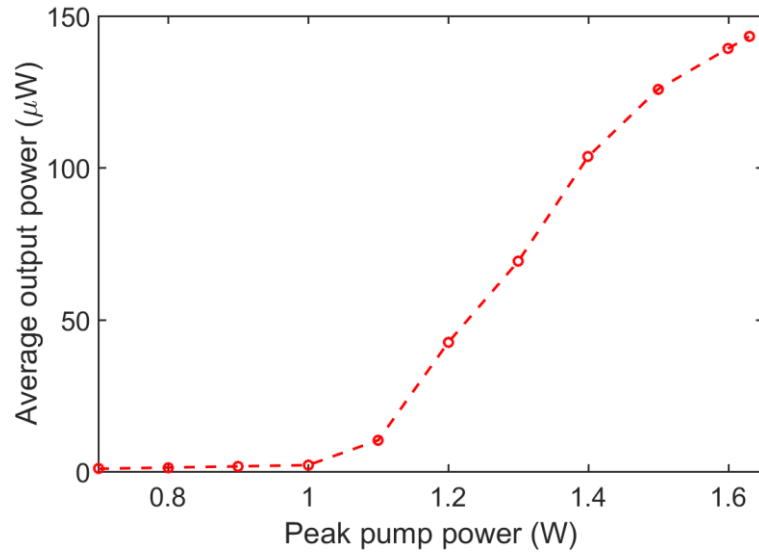


Figure 4.5 Power conversion graph for a 1312-066 sample bonded onto a sapphire equilateral prism. The prism is 1 cm long in side length and 1.5 cm in height. All side surfaces are uncoated. The pump is the same as mentioned earlier, at 0.6% duty cycle.

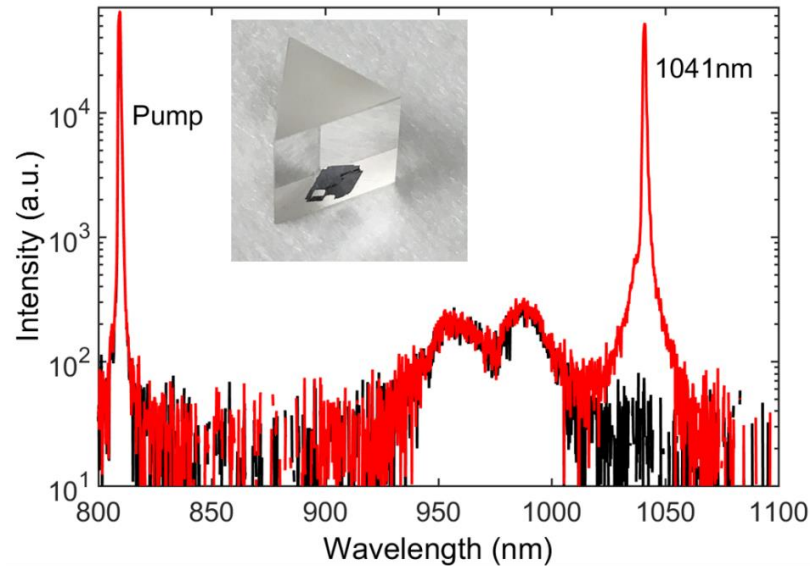


Figure 4.6 Spectra below and above threshold. The active region is bonded onto a sapphire equilateral prism, as shown in the inset. The black curve is the spectrum below threshold and the red one is above threshold. The spectra is collected behind a high reflector with Ocean Optics USB4000.

cooling. Near threshold, the laser operates at 1041 nm, as shown in Fig. 4.6.

Unlike the fused silica prism, the laser output with the sapphire prism is elliptically polarized. Moreover, three laser beams are coupled out, two from one mirror and one from the other. The polarization for these output beams are all different. Such abnormal polarization may be caused by the birefringence of the prism. Since the optic axis is unknown, it is difficult to analyze the polarization quantitatively.

4.1.2 Laser designs for longer wavelength

In the previous subsection, we demonstrated a TIR based DBR-free SDL, which could be further improved by reducing the intracavity losses and applying active cooling to the active region. For the former, either AR coating or Brewster's angle incidence on the air-prism interfaces could mitigate the potential Fresnel losses; for the latter, there are three options available: utilizing the prism as a heatspreader, employing other heatspreaders, or both. Brewster's angle geometry is attempted with both a fused silica right-angle and a sapphire equilateral prisms. Unfortunately, neither geometries lase, which may be due to the challenge of alignment.

Directly cooling the prism is only feasible with a high thermal conductivity material, such as SiC (for 4H-SiC, the thermal conductivity coefficient is 370 W/(m K) at room temperature) for red to NIR wavelengths, or Si (150 W/(m K) at room temperature) for MIR wavelengths. Single-crystalline diamond is optimal in both optical quality and thermal conductivity, but large-size diamond prisms are costly. Utilizing an extra heatspreader, such as a diamond window, is cost-effective. The active region could be sandwiched in between, or bonded onto the heatspreader which is attached to the prism seamlessly from the no-sample side, either with index matching liquid or via direct bonding. For the first proposed geometry, with a 300 μm thick diamond window, there is at least 140 μm offset between the two spots in one roundtrip, which may be difficult for good pump laser mode overlap.

For the prism-semiconductor-heatspreader geometry, the heatspreader is not necessarily in the cavity, by having the laser beam total internal reflected before the gain structure. By

inserting a low-index layer between the prism and the active region, TIR could be achieved at the prism-low-index-layer interface and the active region is coupled into the cavity via the evanescent wave, which propagates through the active region and total internal reflected back at the gain-heatspreader interface. A schematic of the laser geometry is shown in Fig. 4.7. By adjusting the low-index layer thickness, the evanescent wave penetration depth is varied. As a result, the coupling between the laser cavity and the semiconductor subcavity and the gain spectrum can be tailored. Fig. 4.8 presents the calculated reflection spectra with the SiO₂ layer of various thicknesses. The gain or imaginary refractive index of the QW layers may be higher than the experimental condition,

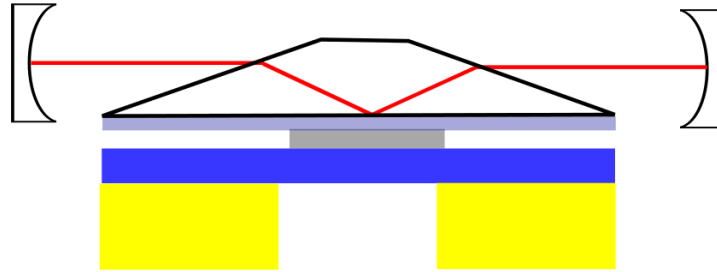


Figure 4.7 Schematic of an evanescent-wave-coupled DBR-free SDL at a MIR wavelength [2]. The light blue rectangular box below the prism is a thin layer with low refractive index, the dark blue is a heatspreader, and yellow boxes are heatsinks. TIR is achieved at the interface between low refractive index and prism. The laser is incident into the prism at Brewster's angle.

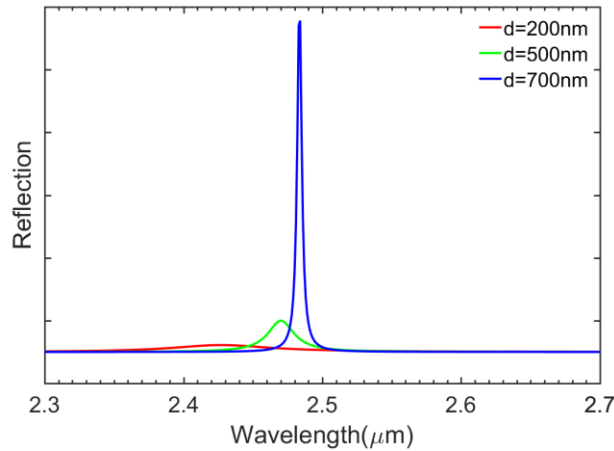


Figure 4.8 Low index layer thickness dependent reflection for an evanescent-wave-coupled DBR-free SDL. The simulation starts from the beam's entry to the active region to the exit. The prism is made of silicon ($n_{Si}=3.44$ at $2.5 \mu\text{m}$), and the low index layer is SiO₂ ($n_{SiO_2}=1.43$ at $2.5 \mu\text{m}$). The base angle of the prism is 16.2° and the laser beam $2.5 \mu\text{m}$ the prism at Brewster's angle $\theta_B=16.2^\circ$. The simulation is carried out with the DiffractMOD module of the commercial software RSoft, based on the RCWA method [3].

but only affects the reflection amplitude. This laser geometry could be useful for high power single-frequency lasers at MIR wavelengths.

4.2 Monolithic geometries

A monolithic laser is formed with all cavity elements rigidly integrated without air gap. Monolithic lasers are compact and alignment-free with long operation lifetimes. One of the biggest successes is the nonplanar ring oscillator [4] (NPRO), also called monolithic isolated single-mode end-pumped ring (MISER), which is an ultrastable, high power [5], high efficiency, and narrow linewidth [6] source with good beam quality. It has been widely used in applications including gravitational wave detection [7], high resolution spectroscopy [8], and remote sensing [9].

Compared with solid state lasers, semiconductor lasers are wavelength versatile. Typical edge-emitting semiconductor lasers are in monolithic packages, but with poor beam quality. A monolithic semiconductor ring laser usually refers to the deep-etched waveguide-based in-plane ring laser [10], which is on the order of 100 μm . For such small devices, the output powers are fairly limited. For surface-emitting semiconductor lasers, both VCSEL and microchip VECSEL [11] (μVECSEL) are also packaged monolithically. Compared with their edge-emitting counterparts, they provide better beam quality but lower output power. Additionally, both allow 2D array geometries [12, 13], which enables power scaling with multiple lasers in phase, and allows for far-field beam profile control.

With the geometric flexibility enabled by the active region lift-off and bonding technique, novel monolithic surface-emitting lasers are possible [1]. In this section, we focus on the geometries TIR made possible.

4.2.1 Monolithic standing-wave cavity geometry

Fig. 4.9 presents a monolithic standing-wave cavity geometry. The active region is bonded onto a side surface of a fused silica right-angle prism. By attaching a HR mirror to the hypotenuse side, a monolithic standing-wave cavity— half of a monolithic ring cavity—

is formed, which will be discussed in section 4.2.2. Therefore, this could give us a hint as to the monolithic ring cavity specifications.

The aforementioned Ti:sapphire laser in section 4.1.1 is applied to pump the active region, which is not actively cooled. To reduce the thermal load, the mechanical chopper scheme is adopted to reduce the pump duty cycle. Both the pump laser and active region are detailed in section 4.1.1. The horizontal incidence of the pump laser enables good overlap with the cavity mode.

Two factors determine the lasing operation: the prism specifications and the thermal lens effect in the active region. A good prism should have low surface roughness, good surface flatness and parallelism, and high angle accuracy. All these requirements have been indirectly confirmed with the lasing behavior of the V-shape cavity geometry in section 4.1.1.

For the plano-plano cavity, positive thermal lens effect in the active region is required to stabilize the cavity. With a super-Gaussian (flat-top) pump beam, the pump spot center experiences a larger temperature rise because of the thermal diffusion process. With positive thermo-optic coefficients for typical semiconductors, the effective refractive index is larger at the center than in the peripheral area. With such transverse refractive index distribution, the active region acts as a positive lens for the laser mode. Additionally, the temperature induced mechanical stress may bring in an extra transverse refractive index gradient. With the ABCD matrix method, the cavity mode size has been calculated at presumed thermal lens focal lengths for prisms of different sizes, shown in Fig. 4.10 (a),

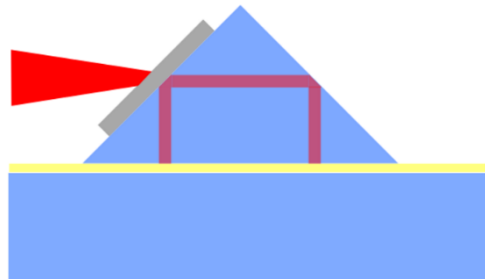


Figure 4.9 Schematic of a monolithic standing-wave cavity. A high reflectivity mirror (yellow layer is the HR coating and blue is the substrate) is under the prism in a good contact. Viewing through the prism leg faces, no obvious interference fringes are observed. The active region (grey) is from the wafer 1312-066.

assuming the pump spot is near the prism corner. The pump position weakly affects the mode size, shown in Fig. 4.10 (b). Considering the limited pump power (2.5 W maximum output power with decent beam quality) and the prism manufacturing tolerances, a small fused silica prism (5 mm side length, Thorlabs, PS609) is chosen.

At 0.8% pump duty cycle, by optimizing the pump spot size only, such monolithic geometry lases. Figs. 4.11 (a) and (b) present the spectra of the scattering from the air-

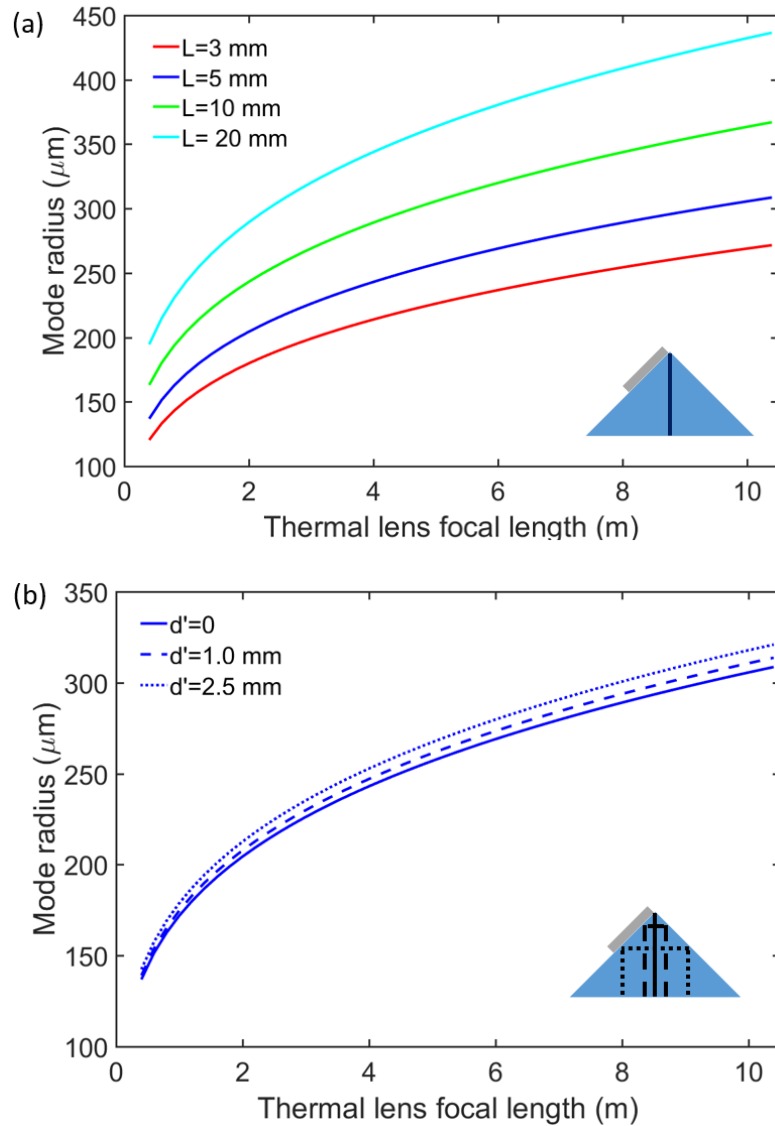


Figure 4.10 (a) Cavity mode radius at the active region with respect to the thermal lens focal length for different sizes prisms, assuming the pump spot is close to the prism corner. L is the side length. (b) Cavity mode radius for a 5 mm prism with an offset d' , the distance from the prism corner to the pump center along the active region layer direction.

prism interface and output through the HR mirror. Lateral lasing is ruled out by the observation of two up-converted laser spots on a NIR sensor card below the HR mirror, shown in Fig. 4.12 inset.

By further optimizing the pump focus and position, the average output power reaches about $6 \mu\text{W}$ at 2.1 W peak power, or 1.6 mW average power. The laser conversion graph is shown in Fig. 4.12. The laser output power is limited by the coupling efficiency of the HR mirror, which is about 0.02% , confirmed with a scanning Fabry-Perot interferometer.

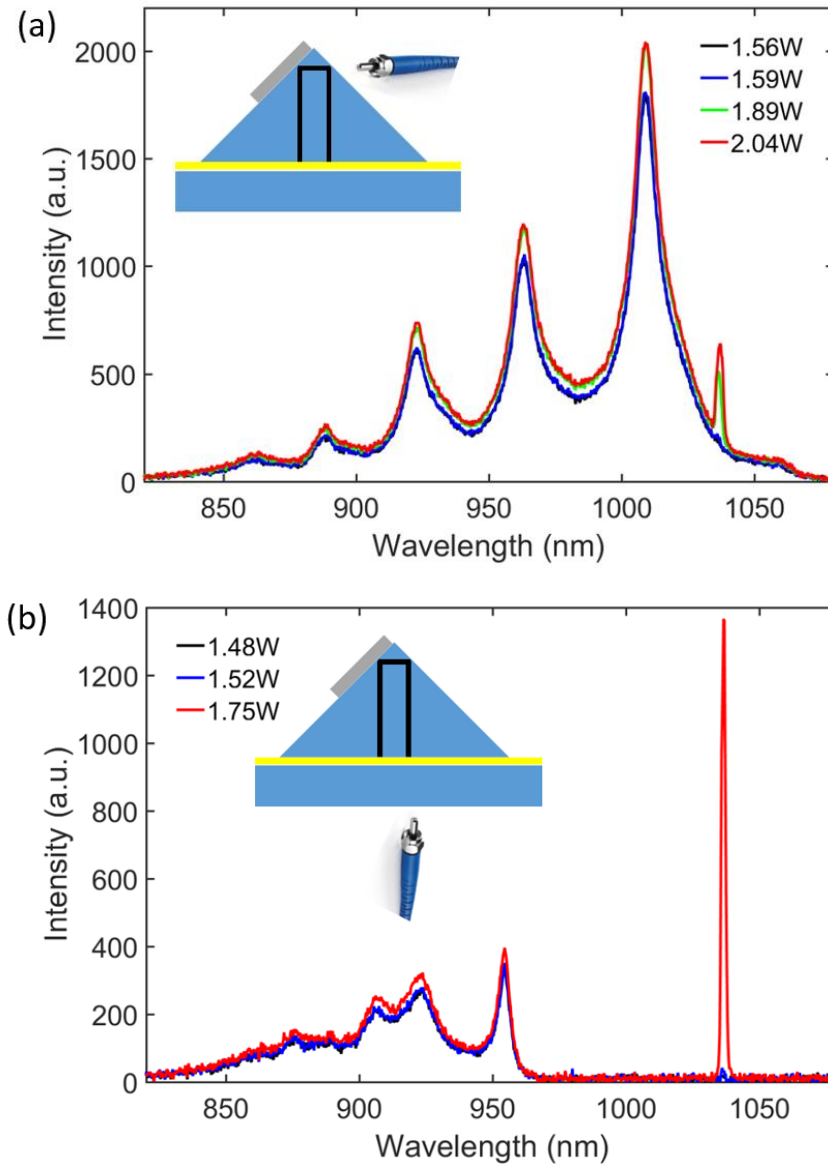


Figure 4.11 PL and laser spectra collected from the side of the prism (a) and bottom of the mirror (b). Laser operates at 1037 nm at low pump power. The legends are in peak pump power.

To optimize the coupling efficiency, two more mirrors or OCs have been used and the corresponding laser conversion graphs are shown in Figs. 4.13 (a) and (b). With a 1% transmission OC, i.e. 2% effective coupling efficiency, 0.2 mW average output power is collected. It is worth noting that after varying the roundtrip optical losses by 2%, the laser threshold stays almost constant.

Such small changes in threshold imply that it may be limited by factors other than the coupling efficiency, such as diffraction losses or thermal lens effect. Therefore, we study the laser dynamics, especially the timing between the pump and laser pulses, as shown in Fig. 4.14 (a). In the experiment, one detector collects the reflected pump laser from the air-semiconductor interface as the trigger, and another collects the laser outputs. Both are high-speed detectors (Thorlabs DET10A, silicon detectors) with 1 ns rise time. At a 600 Hz chopping rate with 1 mm slit width, the pump pulses are about 30 μ s in FWHM. Right after the arrival of the pump pulse, the signal rises by a small amount due to spontaneous emission, but the lasing only starts 26 μ s after the arrival of the pump pulse. Since the carrier lifetime is a few nanoseconds, such long delay is likely to be caused by the thermal effect, rather than gain. In the pre-lasing window between the arrival of pump pulse and the onset of lasing, the temperature of the pumped region keeps on rising, until thermal

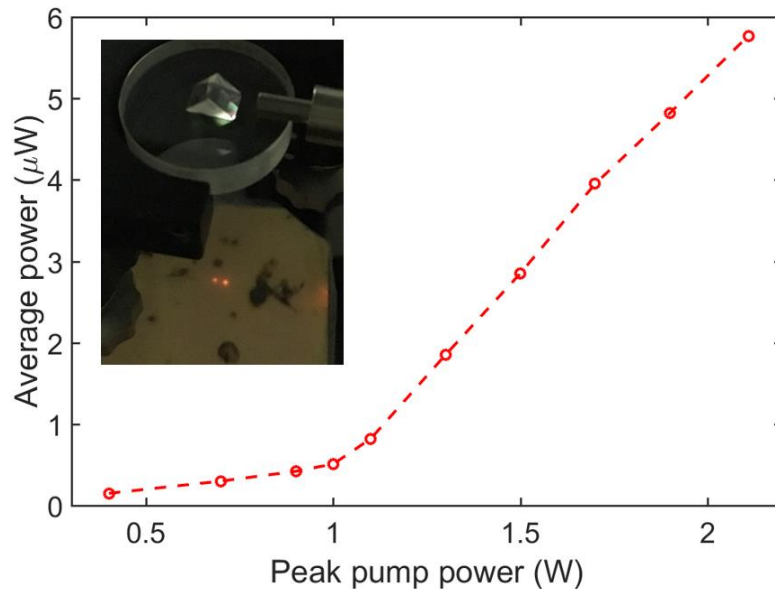


Figure 4.12 Laser conversion graph for the standing wave cavity geometry. The laser threshold is about 1.0 W in peak power and 0.7 mW in average power. The inset is a picture of the laser setup, and the two bright spots are the upconverted laser outputs on a NIR sensor card.

lens effect is strong enough to lower diffraction losses and stabilize the cavity. After the pump pulse, it stops lasing either because the gain is drained, or the thermal lens effect no longer supports the stable cavity.

To test the thermal lens effect build-up time hypothesis, we further vary the chopper frequency, changing pump pulse lengths while keeping the average thermal load constant. Shown in Fig. 4.14 (b), for all three pump pulse lengths, the pre-lasing windows are of almost the same length, and the minor variation may be due to the pump amplitude difference in the pump-on process. Further experiments on thermal load dependent pre-

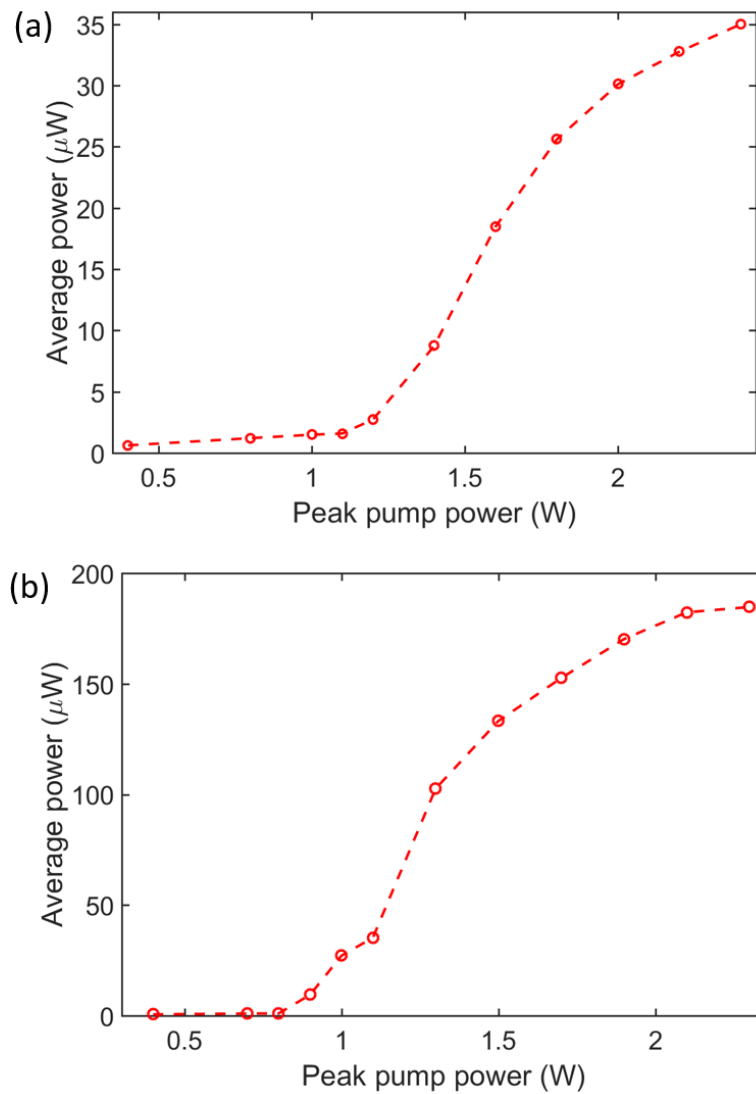


Figure 4.13 Laser conversion graph with a 99.8% HR (a) and 1% OC (b). The pump conditions are the same as the HR (99.98%) mirror scenario. The duty cycle is 0.8%.

lasing window width could further support the thermal lens effect claim.

Such a constant pre-lasing window width suggests that longer pump pulses may offer higher laser conversion efficiency. Varying the pump pulse length or the chopping rate, the average output power is measured and the results are shown in Fig. 4.15. The average output power tends to increase with pulse length until rolling over, which may be due to overheating in the active region.

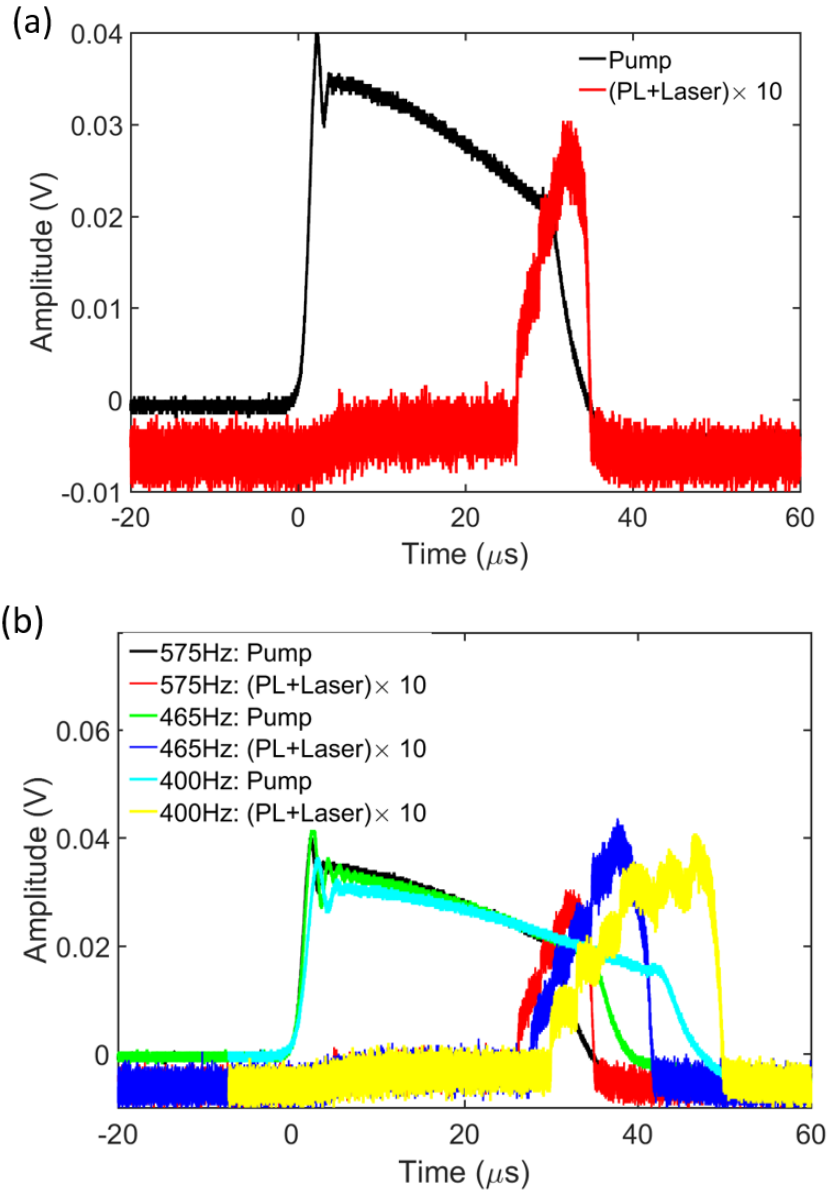


Figure 4.14 Laser pulse dynamics. (a) Laser dynamics at 575 Hz chopping rate, 2.0 W peak pump power and 0.8% pump duty cycle. (b) Laser dynamics comparison among three different chopping rates at 2.0 W peak pump power and 0.8% pump duty cycle.

As mentioned, viewing from the prism leg surface, half of the contact area is slightly bluish, the other is reddish, with no other visible interference fringes. By intentionally introducing dust on the mirror, more interference fringes are observed. Therefore, the gap between prism and mirror is narrower than 1 μm in the dust-free condition. Such thin air gap may bring about extra Fresnel reflection losses.

To understand the Fresnel reflections on surfaces, a 180 μm thick air gap is introduced by inserting two thin microscope slides as spacers between the prism and mirror, leaving a void on the optical path. The geometry lases and the scattering and transmission spectra are shown in Fig. 4.16. Near the threshold, the laser may operate with a single mode. At 0.5 W above the threshold, there are two peaks in the laser spectrum, at 1033 nm and 1036 nm. The wavelength separation matches the modulation periodicity for the 180 μm thick air etalon. Therefore, the Fresnel reflections are coherently added back to the cavity. As a result, this experiment confirms the angle accuracy of the right angle prism.

To further reduce the possible Fresnel reflection losses, the index matching liquid (for BK7, from Cargille, Inc.) is applied in between. With the same sample characterized in Fig. 4.12, the sample lases but with worse performance, shown in Fig. 4.17, which may be due to the non-uniform liquid layer, extra optical losses in the liquid, or that it is at a bad spot on the active region. More systematic investigations are needed. But the lasing behavior gives us the confidence to use the liquid to assemble other monolithic geometries,

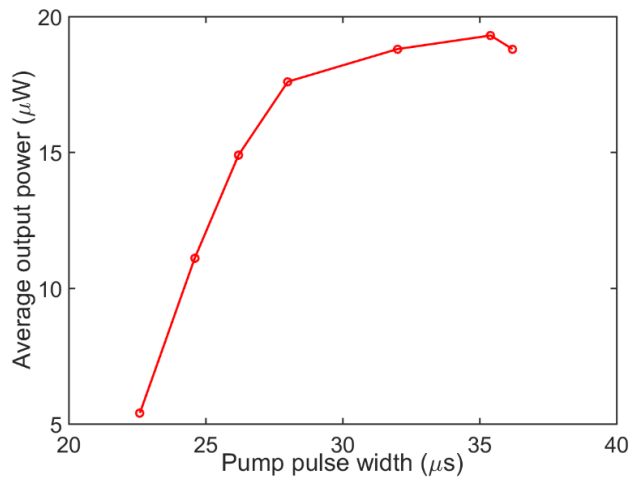


Figure 4.15 Pump pulse width dependent average output power at 2.0 W peak pump power and 0.8% pump duty cycle.

as will be discussed soon.

Besides vertical lasing, lateral lasing [14] has also been observed, which presents with sharp laser lines only in the scattering spectra. For a sample, the lateral lasing wavelengths span from 1041 nm to 1065 nm, shown in Fig. 4.18 (a). Checking under an optical microscope, a small cracked region is observed. With the same sample (a different sample from the one characterized in Figs. 4.12-4.15), at a spot far from the lateral lasing region, it lases vertically at 1060 nm, shown in Fig. 4.18 (b).

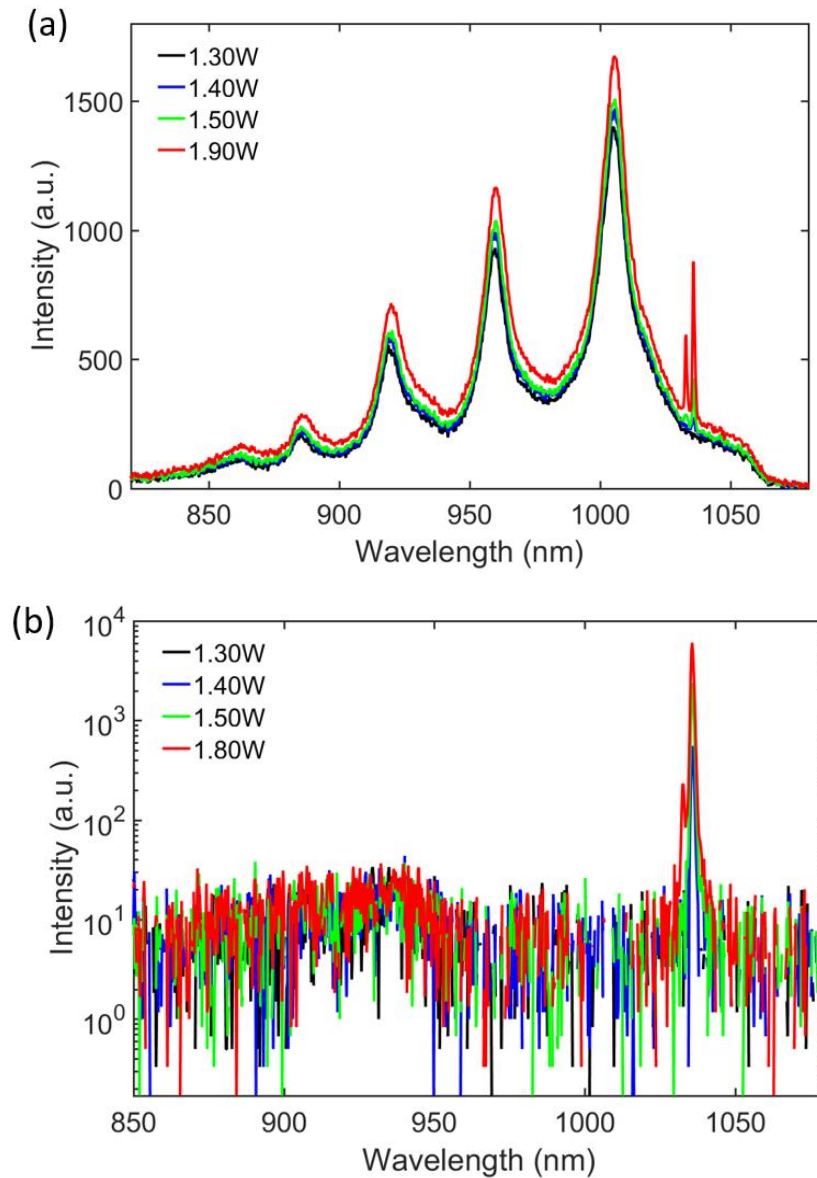


Figure 4.16 Scattering (a) and transmission spectra (b) of a DBR-free standing wave geometry with a 180 μm air gap at different pump power.

Even though it is only quasi-continuous operation to date, the monolithic standing wave cavity geometry could potentially operate continuously by using a high thermal conductivity prism or integrating a heatspreader, such as sapphire, SiC or even diamond, shown in Fig. 4.19. The active region could be sandwiched between the heatspreader and prism. A thick heatspreader brings in a significant offset between the two laser spots on the active region, which makes the regular pumping scheme less efficient. With a sapphire heatspreader, as will be discussed in the section 4.3, a DBR-free SDL is shown with more than 100 mW CW output power. The heatspreader may affect the focal length of the induced thermal lens and a detailed thermal analysis [15] is needed.

The monolithic standing wave geometry is compact and can be made mechanically robust, by having the HR coating on the prism hypotenuse surface. For certain optical elements, it keeps the intracavity access, which is good for frequency conversion and mode locking with saturable absorbers. Compared to monolithic solid-state lasers [16], semiconductor lasers are more frequency versatile using bandgap engineering techniques. Additionally, the coupling efficiency could be variable with via evanescent wave coupling.

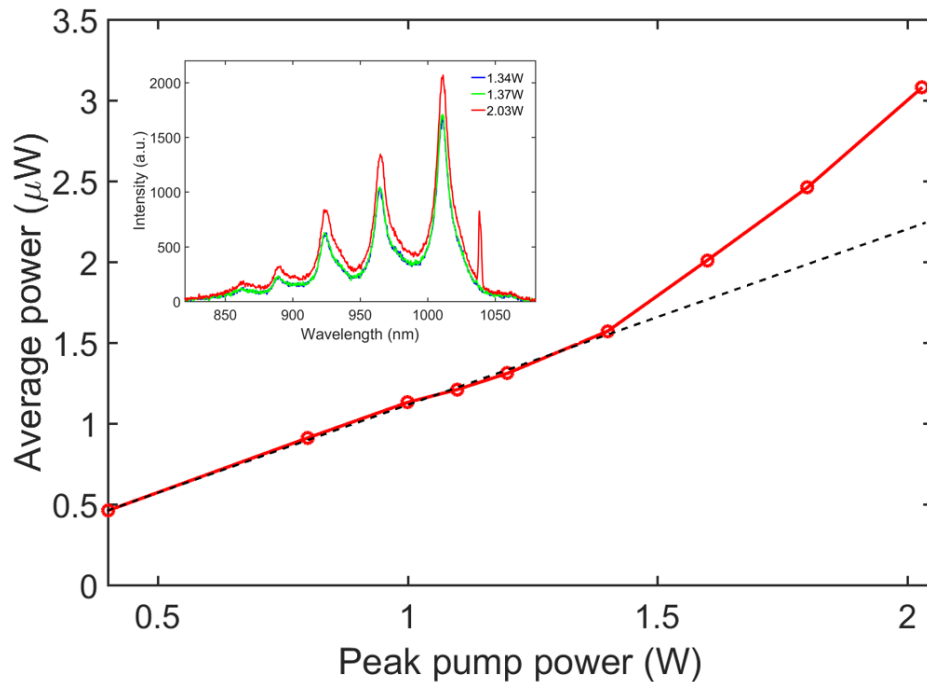


Figure 4.17 Laser conversion graph of a fused silica prism in standing wave cavity geometry with index matching liquid. The dash line is a guide of eye for the PL power. Inset is the PL and laser spectra from a side surface of the prism.

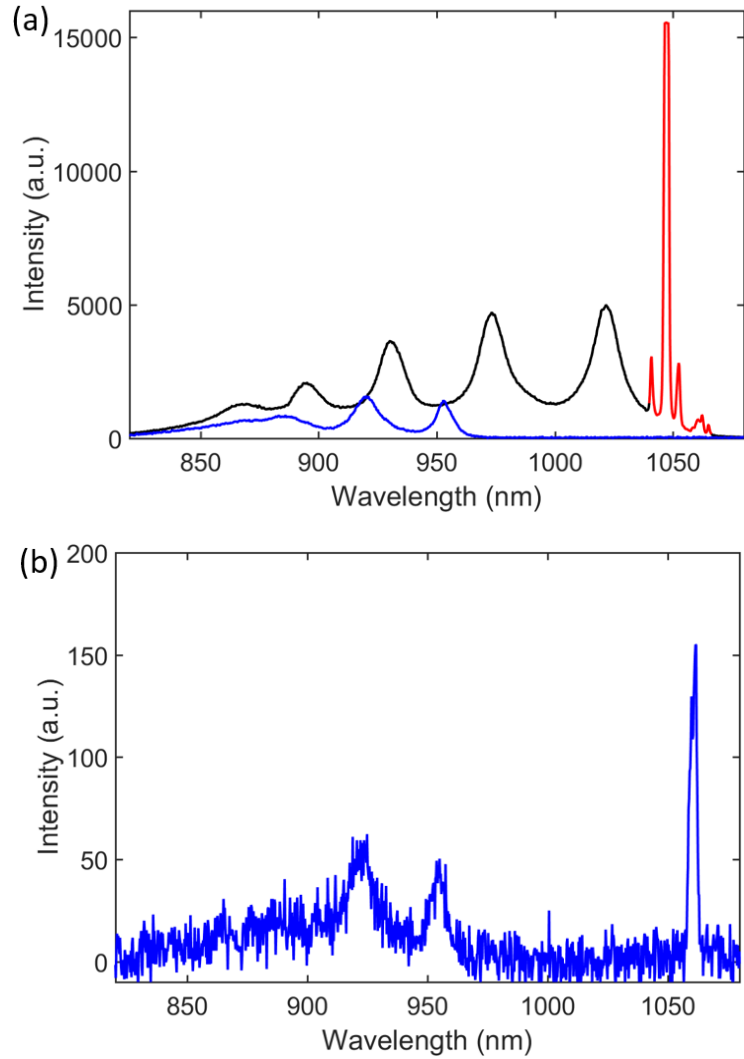


Figure 4.18 Spectra for lateral lasing (a) and vertical lasing (b) scenarios. (a) The black-red curve is the scattering spectrum from a side surface of the prism, and the peaks in the red part are caused by lateral lasing. The blue spectrum is the transmission spectrum behind the mirror. (b) The vertical lasing spectrum collected behind the HR mirror.

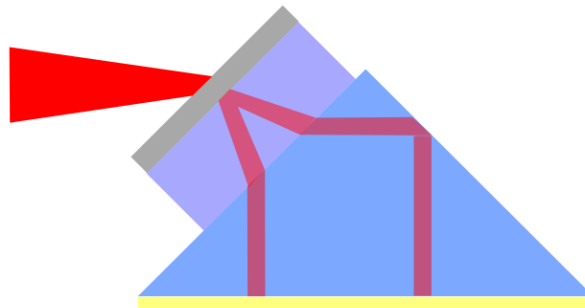


Figure 4.19 Schematics of a CW standing wave cavity laser geometry. The purple rectangular is a heatspreader for extracting heat from the active region. The yellow layer on the prism hypotenuse surface is a dielectric HR coating or a van der Waals bonded semiconductor DBR.

4.2.2 Monolithic ring cavity designs

Assisted by TIR, monolithic ring cavity geometries are feasible and two examples are presented in Fig. 4.20. For both in-plane cavities, good surface parallelism is required. Like the monolithic standing-wave cavity, pump induced thermal lens effect in the active region is needed to stabilize the cavity. For the quadrilateral prism geometry, extra geometrical conditions have to be satisfied, as will be discussed next.

With simple geometrical relations and the law of reflection, we can analyze these monolithic ring cavities. Assume a quadrilateral shape as the optical path; it is easy to draw the four sides of the prism, following the law of reflection, as shown in Fig. 4.21. Assume all incident angles a_i ($i=1, 2, 3,$ and 4) satisfy the TIR condition ($n \sin(a_i) > 1$). With the sum of interior angles in a quadrilateral being 360° ,

$$2a_1 + 2a_2 + 2a_3 + 2a_4 = 360^\circ$$

With the sum of angles in a triangle being 180° ,

$$\angle DAB + (90^\circ - a_4) + (90^\circ - a_1) = 180^\circ$$

Therefore, $\angle DAB = a_4 + a_1$. Same for the angle DCB, $\angle DCB = a_2 + a_3$. As a result, the two opposite angles are supplementary. This is a sufficient condition but may not be necessary for an ideal quadrilateral cavity.

Following the same procedure, assume the triangle DFE as the self-repeated optical path in the prism, shown in Fig. 4.22. With the law of reflection, $\angle AFE + \alpha_2 = 90^\circ$ and

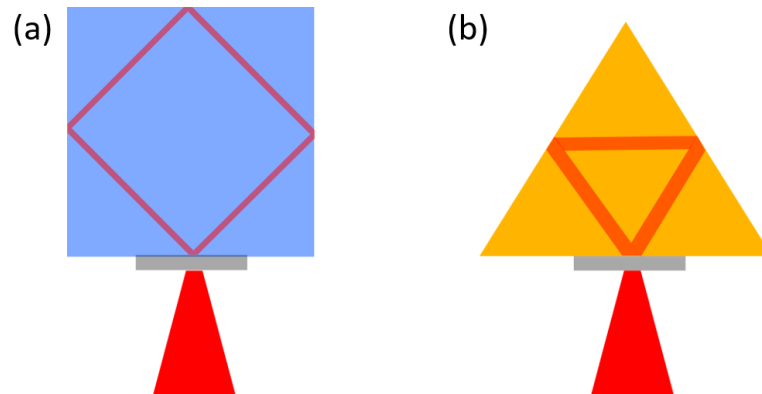


Figure 4.20 DBR-free SDLs in monolithic ring geometries, (a) quadrilateral prism with $n > 1.42$, (b) equilateral prism with refractive index $n > 2$ material, such as ZnSe, ZnS or diamond.

$\angle AEF + \alpha_3 = 90^\circ$. With the sum of angles in the triangle AEF is 180° , $\angle AFE + \angle AEF + \angle CAB = 180^\circ$. As a result, $\angle CAB = \alpha_2 + \alpha_3$. In the triangle DEF , $2\alpha_1 + 2\alpha_2 + 2\alpha_3 = 180^\circ$. Therefore, $\alpha_1 = 90^\circ - \angle CAB$. Similar relations hold for the other two angles. In other words, if a self-repeated path in a prism exists, then the shape of the path is known.

Is such a self-repeated path unique? In Fig. 4.23, we translate the path DE in parallel to D_1E_1 , and reflect the beam on all three interfaces. By eye, a self-repeated path $D_1E_1F_1D_2E_2F_2$ is found, shown in Fig. 4.24. This is fairly straightforward for an equilateral

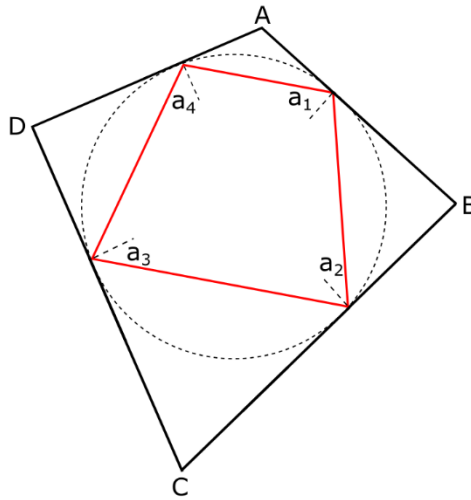


Figure 4.21 A self-repeated optical path in a generalized quadrilateral prism $ABCD$ by TIR only assuming the minimum angle is no smaller than the critical angle. The solid black lines are the prism surfaces, the dashed black lines are normal lines of corresponding surfaces, the red solid lines are optical paths. The dashed circular is for the guide of eye.

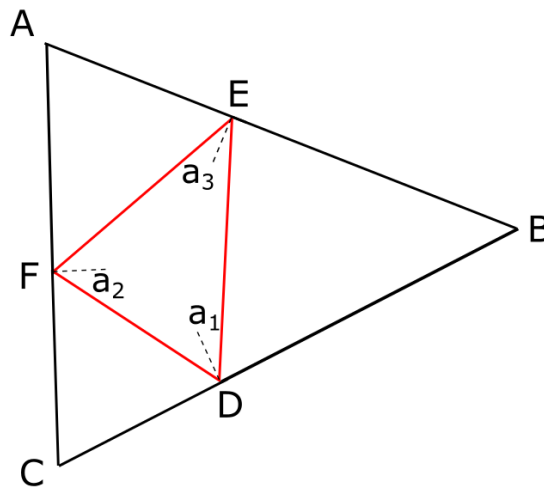


Figure 4.22 A self-repeated optical path $DEFD$ in a generalized triangular prism ABC by TIR only, assuming the minimum angle is no smaller than the critical angle.

prism, which is a special scenario. For an arbitrary prism, this has to be proved, which is equivalent to prove that $DD_3=DD_1$ and D_3 is the cross point on BC with $F_2D_3//BD$.

With $DE//D_1E_1$ and similar triangles BDE and BD_1E_1 , $BD/BE=DD_1/EE_1$. By the law of sines, in the triangle BDE, $BD/BE=\sin(\angle BED)/\sin(\angle BDE)$. By the law of reflection, $\alpha_1+\angle BDE=90^\circ$ and $\alpha_3+\angle BED=90^\circ$. Therefore, $BD/BE=DD_1/EE_1=\cos(\alpha_3)/\cos(\alpha_1)$.

Similarly, we can derive that $EE_1/FF_1=\cos(\alpha_2)/\cos(\alpha_3)$ and $FF_1/DD_2=\cos(\alpha_1)/\cos(\alpha_2)$. With the product of the three equations, $DD_1/DD_2=1$. Following the same procedure, it is easy to prove that $DD_2/DD_3=1$. Therefore, $DD_1=DD_2$ and there are infinite self-repeated optical paths in a triangle. With prism angles known, it is easy to plot self-repeated paths. In experiments, the positions of the bonded sample and pump spot matters. In Fig. 4.23, if the active region is bonded on the BC side and D_1 is the center of the pump spot, D_2 is either pumped or not covered with the active region, so as to avoid extra optical losses.

In addition to flat substrates, active regions can also be bonded onto curved surfaces, a sphere, for instance, as in Fig. 4.24 (a). Pumping the active region, PL is coupled into the sphere cavity and certain paths form stable cavities with TIR. At above threshold, modes are formed. With the ABCD matrix method, cavities with integer number of reflection are not always stable, as shown in Fig. 4.24 (b). Smaller spheres have less optical losses, including scattering and absorption losses, and higher Q factors, but the highly curved surfaces are more challenging for bonding. Smaller samples are easier for bonding, since

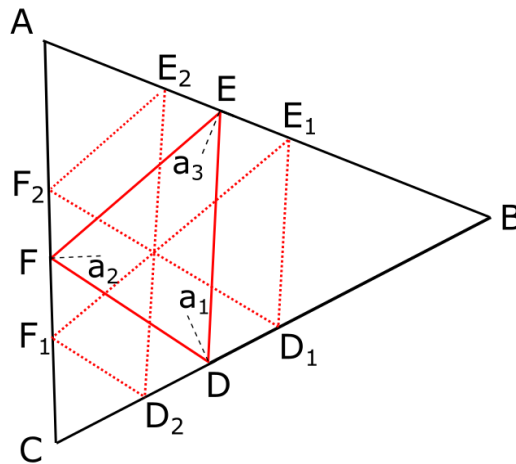


Figure 4.23 An alternative optical path $D_1E_1F_1D_2E_2F_2D_1$ in a triangular prism.

less deformation is needed, but lateral lasing may be involved. Transverse cavities come with higher gain but a lower Q factor, and quite on the reverse for the vertical cavity. Also the sample size may influence the cavity mode pattern, since the below transparency region may absorb the lasing wavelength and limit the bounce numbers in the cavity. Bonding has been attempted with 6 mm and 9 mm in diameter sapphire spheres (Edmund Optics, Inc.) but no stable bonding has been achieved yet.

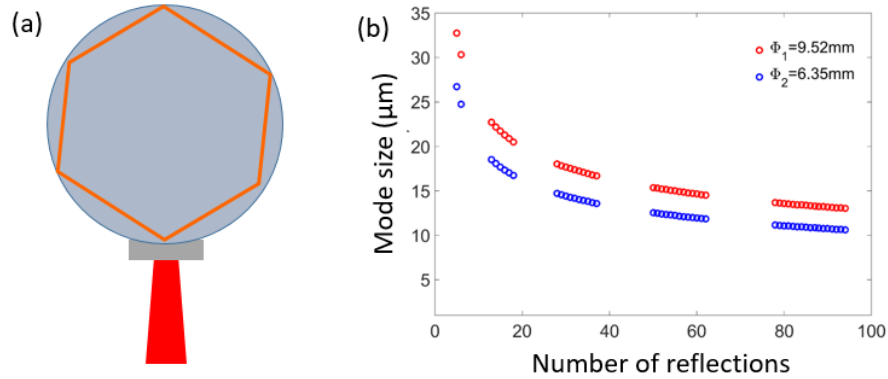


Figure 4.24 Schematic and reflection number analysis for a monolithic ring cavity. (a) Monolithic ring cavity based on a sphere. The path in the figure is only one possibility; (b) Cavity mode size calculation (in the laser path plane) based on ABCD matrix method with astigmatism considered. The mode sizes for unstable cavities are not shown. The spheres are made of sapphire with 9.52 mm (red) and 6.35 mm (blue) in diameter.

4.3 Summary

With the lift-off and van der Waals bonding technique, we have demonstrated the first quasi-continuously operated TIR based DBR-free geometry, by bonding active regions onto prisms, forming a V-shaped cavity, and proposing designs for continuous operation, including one based on evanescent-wave coupling for MIR wavelengths. By bonding an active region onto a side surface of a right-angle prism, a monolithic DBR-free standing wave geometry is demonstrated, assisted with a HR mirror. The effects of air etalon and index matching liquid are studied. Two monolithic DBR-free ring cavity designs are proposed and analyzed on the geometries requirements.

4.4 References

- [1] Z. Yang, A. R. Albrecht, J. G. Cederberg, and M. Sheik-Bahae, "Optically pumped DBR-free semiconductor disk lasers," *Opt. Express*, vol. 23, no. 26, pp. 33164-33169, 2015.
- [2] M. Sheik-Bahae, "Laser amplifier and method of making the same," US patent 7627017 B2, 2009.
- [3] M. G. Moharam and T. K. Gaylord, "Rigorous coupled-wave analysis of planar-grating diffraction," *J. Opt. Soc. Am.*, vol. 71, no. 7, pp. 811-818, 1981.
- [4] T. J. Kane and R. L. Byer, "Monolithic, unidirectional single-mode Nd:YAG ring laser," *Opt. Lett.*, vol. 10, no. 2, pp. 65-67, 1985.
- [5] E. A. P. Cheng and T. J. Kane, "High-power single-mode diode-pumped Nd:YAG laser using a monolithic nonplanar ring resonator," *Opt. Lett.*, vol. 16, no. 7, pp. 478-480, 1991.
- [6] B. Willke, S. Brozek, K. Danzmann, V. Quetschke, and S. Gossler, "Frequency stabilization of a monolithic Nd:YAG ring laser by controlling the power of the laser-diode pump source," *Opt. Lett.*, vol. 25, no. 14, pp. 1019-1021, 2000.
- [7] B. Willke, K. Danzmann, C. Fallnich, M. Frede, M. Heurs, P. King, D. Kracht, P. Kwee, R. Savage, F. Seifert, and R. Wilhelm, "Stablized high power laser for advanced gravitational wave detectors," *J. Phy. Conf. Ser.*, vol. 32, pp. 270-275, 2006.
- [8] J. Ye, L.-S. Ma, and J. L. Hall, "Sub-Doppler optical frequency reference at 1.064 μm by means of ultrasensitive cavity-enhanced frequency modulation spectroscopy of a C_2HD overtone transition," *Opt. Lett.*, vol. 21, no. 13, pp. 1000-1002, 1996.
- [9] F. Heine, H. Salheiser, G. Seel, T. Schwander, and B. Smutny, "Seed laser for space borne LIDAR applications," in *CLEO*, Long Beach, CA, USA, 2002.
- [10] T. Krauss, P. J. R. Laybourn, and J. Roberts, "CW operation of semiconductor ring lasers," *Electron. Lett.*, vol. 26, no. 25, pp. 2095-2097, 1990.
- [11] J. E. Hastie, J.-M. Hopkins, C. W. Jeon, S. Calvez, D. Burns, M. D. Dawson, R. Abram, E. Riis, A. I. Ferguson, W. J. Alford, T. D. Raymond, and A. A. Allerman, "Microchip vertical external cavity surface emitting lasers," *Electron. Lett.*, vol. 39, no. 18, pp. 1324-1325, 2003.
- [12] M. Orenstein, E. Kapon, N. G. Stoffel, J. P. Harbison, L. T. Florez, and J. Wullert, "Two-dimensional phase-locked arrays of vertical-cavity semiconductor lasers by mirror reflectivity modulation," *App. Phys. Lett.*, vol. 58, no. 8, pp. 804-806, 1991.

- [13] J. E. Hastie, L. G. Morton, S. Calvez, M. D. Dawson, T. Leinonen, M. Pessa, G. Gibson, and M. J. Padgett, "Red microchip VECSEL array," *Opt. Express*, vol. 13, no. 18, pp. 7209-7214, 2005.
- [14] Chengao Wang, Kevin Malloy, and Mansoor Sheik-Bahae, "Influence of coulomb screening," *Opt. Express*, vol. 23, no. 25, pp. 32548-32554, 2015.
- [15] J. J. Zayhowski, "Thermal guiding in microchip lasers," in *Advanced Solid-State Lasers*, Washington, D.C., 1990.
- [16] B. Zhou, T. J. Kane, G. J. Dixon, and R. L. Byer, "Efficient, frequency-stable laser-diode-pumped Nd:YAG laser," *Opt. Lett.*, vol. 10, no. 2, pp. 62-64, 1985.

Chapter 5

Transmission Geometry DBR-free

Semiconductor Disk Lasers

In this chapter, we will present the transmission geometry DBR-free SDL designs and characterization in the first five sections, revisit the integrated gain model in section 5.6, and discuss the abnormal pump power dependent photoluminescence peak blueshift phenomena in section 5.7.

5.1 DHS based transmission geometry DBR-free SDL

In addition to prisms, active regions can be bonded onto windows, forming transmission geometries. As shown in Fig. 5.1, a 6 mm by 6 mm GaAs DHS (the structure detailed with Fig. 3.3 (a) in section 3.3.1) is bonded on the back of a commercial flat HR mirror centered at 895 nm. The laser cavity is completed with a curved HR mirror with 25 mm ROC. Two lasers, a 18 W commercial Verdi laser at 532 nm and a tunable CW Ti:sapphire laser, are

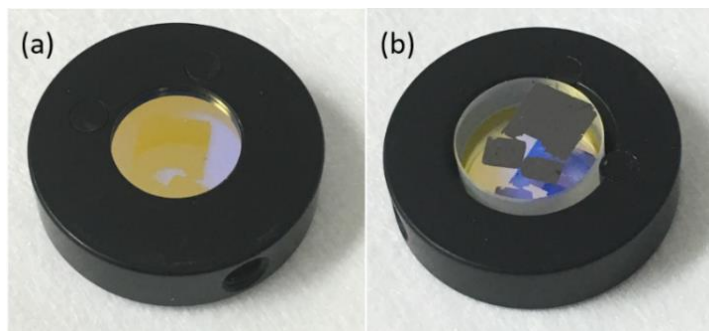


Figure 5.1 The first lased DBR-free active mirror. (a) HR coating side and (b) active region side. The active region is a DHS sample (structure is detailed in Fig. 3.3(a) in subsection 3.3.1), bonded on the back of the 6.3 mm thick, half inch in diameter flat mirror. The mirror is highly reflective between 850 nm and 950 nm. Dr. Chengao Wang performed the bonding.

used as pump sources separately and the collimated pump beams are focused on the active region with a 100 mm focal length lens. Two pumping schemes are shown in Fig. 5.2.

Initially, the active region was end-pumped with a Verdi laser through the HR mirror at normal incidence. The mirror has about 10% reflection at 532 nm. The schematic and setup are shown in Figs. 5.2 (a) and 5.3 (a). No active cooling is applied to the assembly. To reduce the thermal load, the pump laser is modulated with a modified mechanical chopper, as detailed in section 4.1.1. The modulated pump pulse is 25 μ s in FWHM, at 600 Hz repetition rate, shown in Fig. 5.3 (b). At 1.0% pump duty cycle, the active region can take up to 18 W peak pump power without optical damage.

The pump dependent PL spectra are presented in Fig. 5.4 (a). At high pump powers, there are extra features at longer wavelengths than 900 nm, which could be due to amplified spontaneous emission (ASE). Increasing the pump power further, the total PL power tends to roll over, as shown in Fig. 5.4 (b), due to overheating.

To reduce the quantum defect and the thermal load, we switch to a tunable CW Ti:sapphire laser as the pump laser. Same as the green laser, the laser duty cycle is reduced with a mechanical chopper. The pump laser at 805 nm is focused on the active region from the side at 45° angle of incidence, as shown in Fig. 5.2 (b). With careful alignment, such geometry lases with 1.8 W threshold, corresponding to 10 kW/cm² pump density (approximately 3×10^{18} cm⁻³), which is much higher than the regular QW based VECSEL with threshold pump density 1 kW/cm². This is expected since bulk materials are known

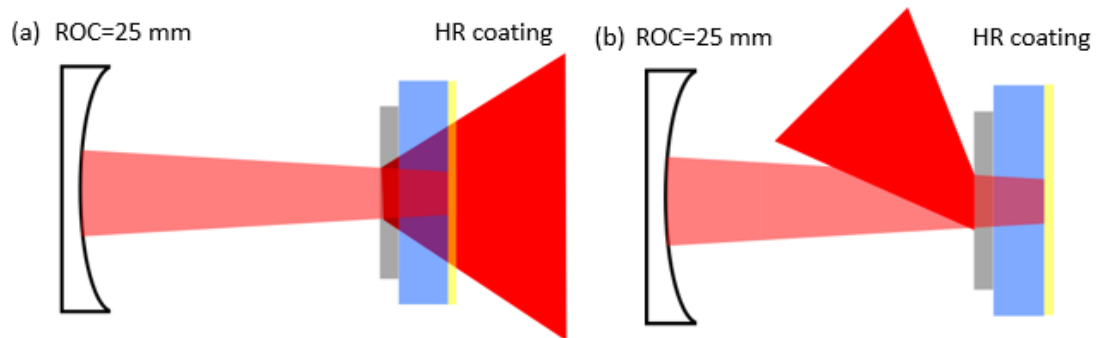


Figure 5.2 Schematics of DHS based DBR-free SDLs. (a) End-pumping and (b) front-pumping schemes. The active region is bonded onto the back of a HR mirror. The curved HR mirror with 25 mm ROC is about 15 mm away from the active region.

for higher threshold compared with QWs, because of higher density of states. Varying the cavity length and monitoring with a CCD camera, the laser changes from off to on and then off. Therefore, lateral lasing is ruled out and the laser spectrum is shown in Fig. 5.5. The laser operates between 890 nm and 910 nm, depending on pump positions. This may be due to the non-uniform bonding quality, which leads to different local temperatures and gain spectra. In the laser aligning process, some pump spots are easily damaged, and some lases. To check the laser pulse width, a high speed silicon detector with a longpass filter is employed behind the curved mirror. The time traces of ASE and laser pulses are shown in Fig. 5.6 (a). At below threshold, the broad and low amplitude ASE signal peaks are

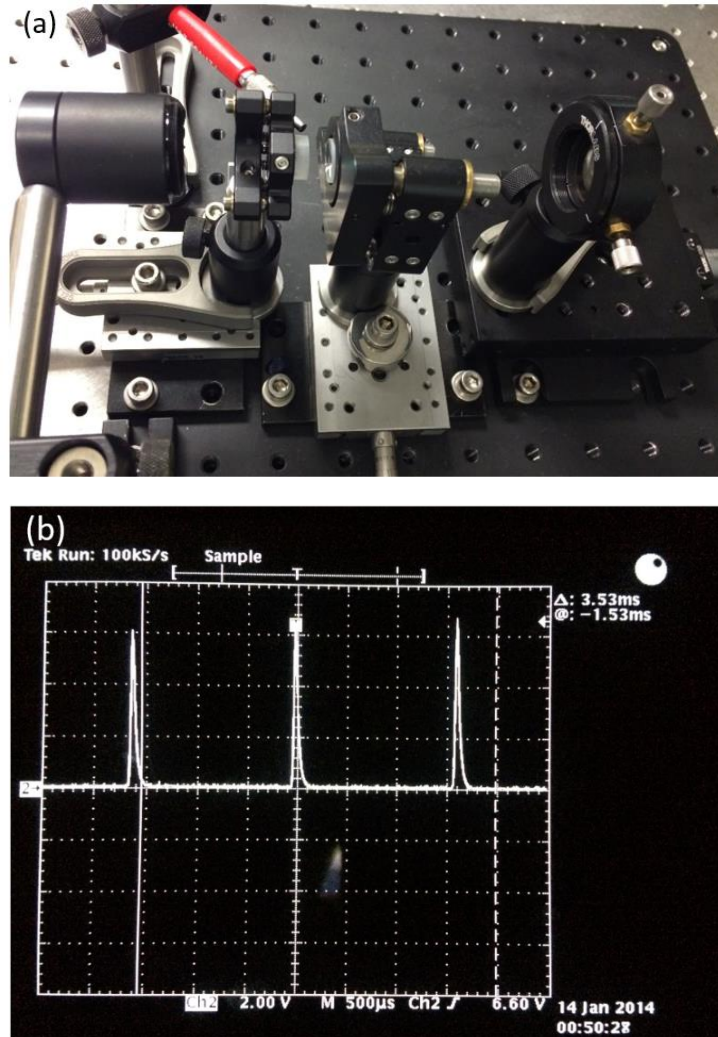


Figure 5.3 (a) End-pumping setup with a commercial Verdi laser at 532 nm. (b) At 1.0% duty cycle, the pump pulse signal on an oscilloscope. The pump pulses are about 25 μ s in FWHM, at 600 Hz repetition rate.

observed, which are sensitive to cavity alignment. This rules out the possibility of the pump residue. At right above the threshold, high amplitude, narrow laser spikes appear intermittently from the broad ASE signal peaks. With different trigger signals, the offset between the two pulses in Fig. 5.6 (a) does not mean their relative timing. Near threshold, the laser spikes locate at the peak of ASE signals. At 1% duty cycle, the laser conversion graph is shown in Fig. 5.6 (b). The beam profile is characterized with a CCD camera, shown in the inset of Fig. 5.6 (b). The laser output is mainly TE polarized, confirmed with a Glan-Thompson polarizer.

Semiconductor laser was reported [1] right after the first lasers. Due to high internal

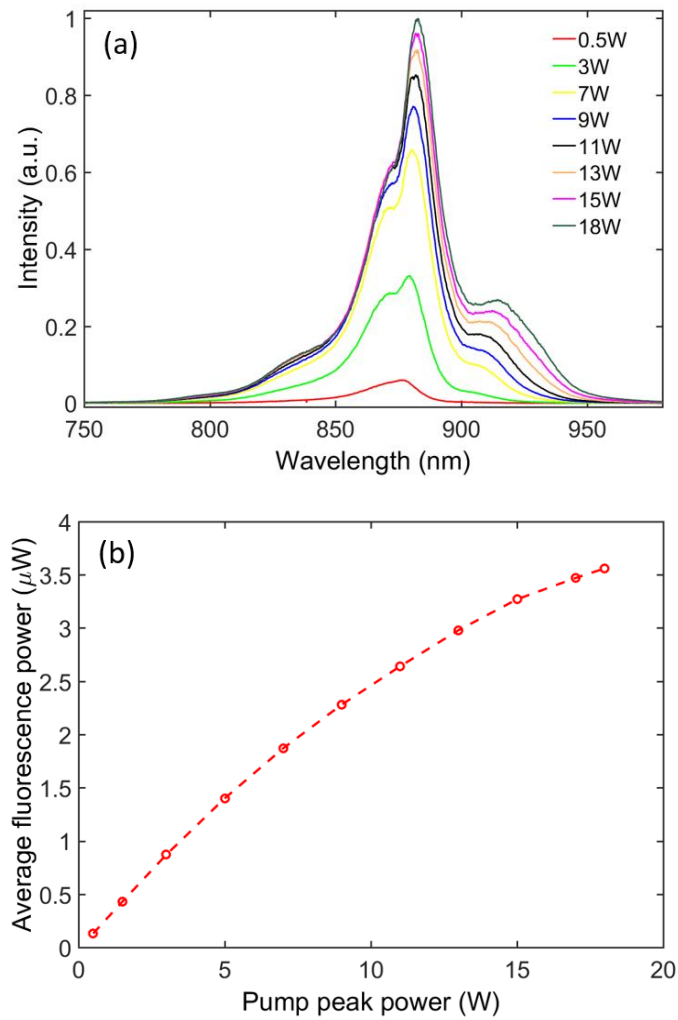


Figure 5.4 PL characterization with quasi-CW pumping at 532 nm. (a) PL spectra with peak pump power at 1.0% duty cycle. Estimated peak pump power density is 102 kW/cm^2 at 18 W incident pump power. (b) PL power collected after the curved mirror with an 850 nm longpass filter.

losses and poor thermal performance, the development of semiconductor lasers had been stagnated for a long time until the introduction of heterojunction [2]. Since then, with better carrier confinement and modified density of states, the laser threshold has been reduced significantly, especially for QW lasers. With QW gain structures, more than 10 kW output has been achieved with laser diode modules [3] and more than 100 W with a VECSEL [4]. Therefore, QW active regions are taken as the gain media for high power SDLs.

This may deserve more investigations. For high power lasers, multiple factors affect devices performance. Thermal property plays a role. As mentioned in chapter 2, the multi-layer structures hamper the thermal diffusion and increase thermal resistance. From the thermal perspective, bulk lasers might outperform QW lasers.

It is widely accepted that the semiconductor bulk materials have lower gain but this may not be the case, as shown in Fig. 5.7. The figures are plotted according to the three-parameter gain model fits in Table 4.4 in [5]. For QWs, the barrier pumping scheme is assumed and the material gain is calculated by assuming all carriers fall into the QW instantaneously. At above certain carrier density levels, both GaAs and InGaAs bulk materials have advantages in gain. There are disadvantages for bulk materials, such as large Auger coefficients and limited material choices. Bulk gain media might be good for high power SDLs at certain wavelengths.

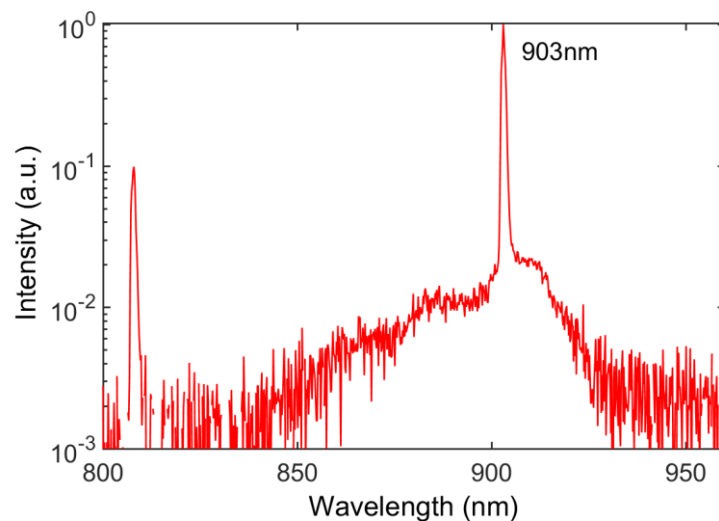


Figure 5.5 Laser spectrum of the DHS based DBR-free SDL.

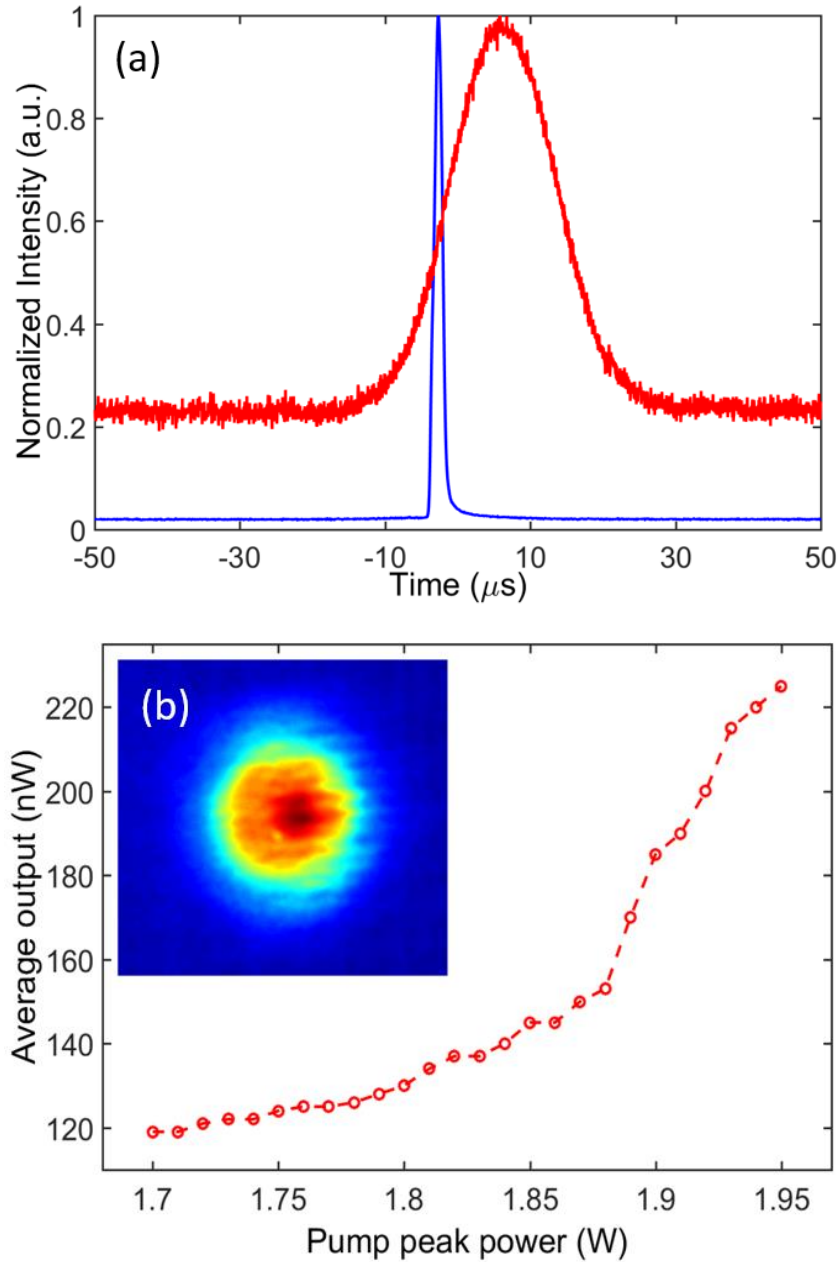


Figure 5.6 (a) ASE (red) and laser (blue) signals detected by a silicon detector. The laser signal amplitude is about 50 times of the ASE signal. The FWHM of the ASE signal is 17 μs , and the laser signal is 1.2 μs at near threshold. The FWHM of the pump pulse is about 25 μs . (b) Optical output from the curved mirror. The laser threshold is about 1.76 W. Inset is the beam profile characterized with a CCD camera. The fringes are caused by the rapidly rotating chopper blades.

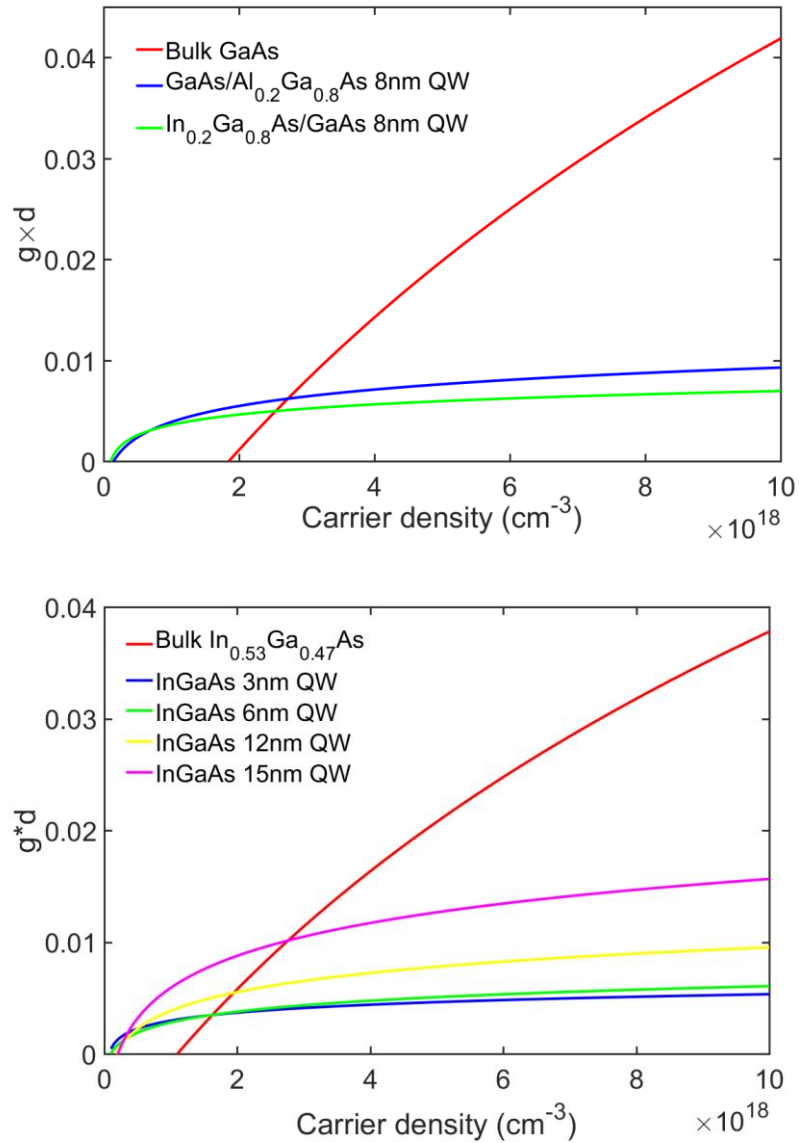


Figure 5.7 Average carrier density dependent integrated gain comparison between bulk materials and QW gain structures. (a) Bulk GaAs vs GaAs and InGaAs QWs; (b) bulk InGaAs vs InGaAs QWs.

5.2 QW based transmission geometry DBR-free SDLs at 1 μm

SDLs near 1 μm have various applications. With the intracavity access and broad tunability, they are good for intracavity enhanced absorption measurements, including ultrasensitive intracavity laser absorption spectroscopy (ICLAS) [6] and intracavity laser cooling of solids [7]. Additionally, intracavity frequency doubled SDLs cover broader spectrum than

solid state lasers, and have been used in applications such as ion trapping [8]. With difference frequency generation, widely tunable SDLs are good for tunable terahertz generation [9]. Semiconductor materials have broad gain and SDLs have been mode locked [10, 11] to generate ultrashort pulses.

Similar to the DHS sample, a MQW active region (from wafer 1312-066) is bonded on the back of a flat HR mirror, whose HR band centers at 1020 nm. The assembly is shown in Fig. 3.1 (b) in section 3.1. The same chopper modulated Ti:sapphire laser is used to pump the active region from the front without active cooling. The cavity is formed with a curved HR mirror (ROC=100 mm), 90 mm in cavity length. The laser alignment is easy and the laser conversion graph is presented in Fig. 5.8. The laser beam profile is characterized with a CCD camera, shown in Fig. 5.8 inset, close to a TEM₀₀ mode. Due to lack of cooling, increasing the duty cycle leads to optical damage in the active region.

For CW operation, more efficient thermal management techniques are adopted: employing better thermal conductive substrates and applying active cooling to the gain assembly. Active regions are bonded onto commercial sapphire windows (Meller Optics, MSLW050/020M, surface roughness RMS 0.2-0.3 nm). The assembly is clamped with a

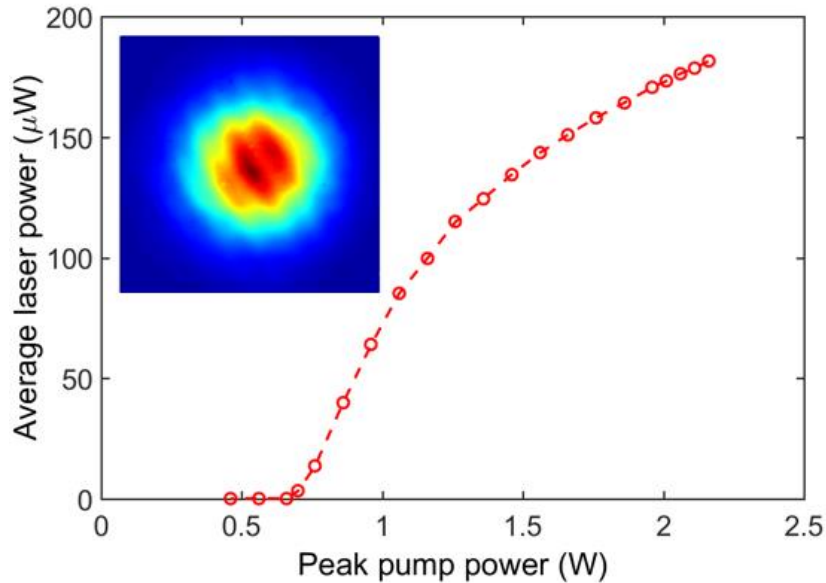


Figure 5.8 Laser performance for a MQW bonded on dielectric HR mirror. Laser conversion graph at 0.22% duty cycle, 600 Hz chopping rate. Inset is the beam profile characterized with a CCD camera. The modulation on the image is caused by the interference on the camera window.

custom-made copper mount, which is mounted onto a water-cooled copper base. Indium foil is applied between the assembly and copper mount to reduce thermal resistance. An image and a cross-section view of the mount are shown in Figs. 5.9 (a) and (b). At the center, a 2 mm diameter aperture is kept for both pump and laser access. Two HR curved mirrors, one 250 mm ROC and one 100 mm ROC, are utilized to form the cavity and the laser schematic is shown in Fig. 5.9 (c).

Pumped with the Ti:sapphire laser at 810 nm, CW operation is achieved and the laser performance is shown in Fig. 5.10. As mentioned in section 3.4, to study the annealing process, a comparison is made on laser performance before and after annealing. The temperature curve is shown in Fig. 3.9 (a) and the surface conditions of the active region before and after annealing are presented in Figs. 3.9 (b) and (c). After annealing, the density of large surface features (voids) reduce significantly but lattice relaxation happens, which is surprising since the linear thermal expansion coefficients of sapphire and GaAs are close. The sample degradation may explain the absence of improvement in both the slope efficiency and roll-over pump power after annealing.

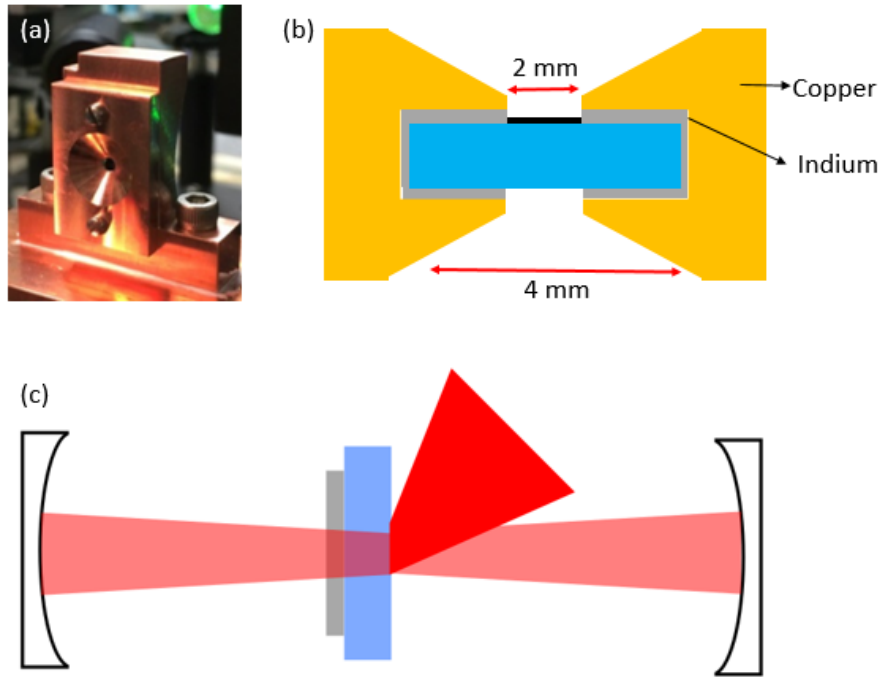


Figure 5.9 (a) Custom-made copper mount for clamping diamond or sapphire windows. (b) Cross-section view of the mount with specifications. (c) Schematic of transmission geometry DBR-free SDL. The grey rectangular is the active region, and the blue one is the substrate.

Switching to a 25 W fiber-coupled laser diode module as the pump laser, a MQW chip (1312-041) bonded on a sapphire window lases. The laser conversion graph is shown in Fig. 5.11 (a). Thermal roll-over is observed with 2 W incident pump power. At threshold, the laser operates at 1017 nm, shown in Fig. 5.11 (b).

For the gain assembly, both air-sapphire and semiconductor-air interfaces are uncoated. With 7.5% and 30% reflectivity on these two interfaces, good surface parallelism for the window is needed for the lasing operation. According to the specification, it is less than 2 arcseconds. To reduce potential Fresnel losses, the assembly is mounted on a rotary stage for orientation optimization. As shown in Fig. 5.12 (a), the output power is critically dependent on the angle, and the peak wavelength and laser spectra are also modulated, shown in Figs. 5.12 (b) and 5.13.

A 2.5 mm by 2.0 mm active region (1315-059, the structure is detailed with Fig. 3.4 (a) in section 3.1) is bonded onto a low absorption single-crystalline diamond (detailed with Table 3.1 in section 3.2) and clamped with a similar copper mount as Figs. 5.9 (a) and (b), which is water cooled to 13°C. The output of a 50 W fiber-coupled laser diode module is focused down to 200 μm in diameter to pump the active region. Both the cavity length and pump focusing condition are optimized to overlap pump and cavity mode.

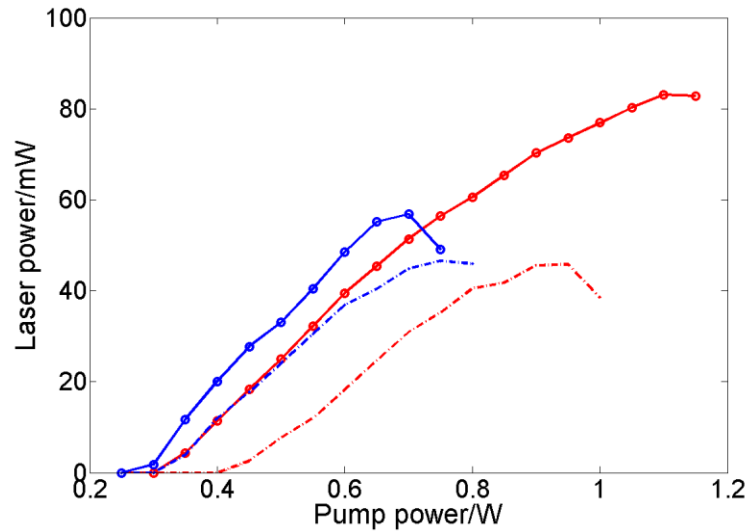


Figure 5.10 Laser conversion graph for a transmission geometry DBR-free SDL with the gain assembly before (solid line) and after annealing (dash line). A CW Ti:sapphire laser output is utilized to pump the active region. Different colors stand for different pump spots.

With a 2% OC (ROC=250 mm) and a HR mirror (ROC=100 mm), more than 6 W output power is collected with 50 W pump power, corresponding to 14.6% slope efficiency with respect to the incident pump power, as shown in Fig. 5.14. There are 20% of the incident pump power reflected at the air-diamond interface and 11% transmitting through the active region. The slope efficiency is 21% with respect to the absorbed pump power. Compared with more than 40% slope efficiency for VECSELs [4] in the same wavelength range, the efficiency of DBR-free SDLs is fairly low, which will be discussed later this subsection. No thermal roll-over is observed and the output power is limited by pump power.

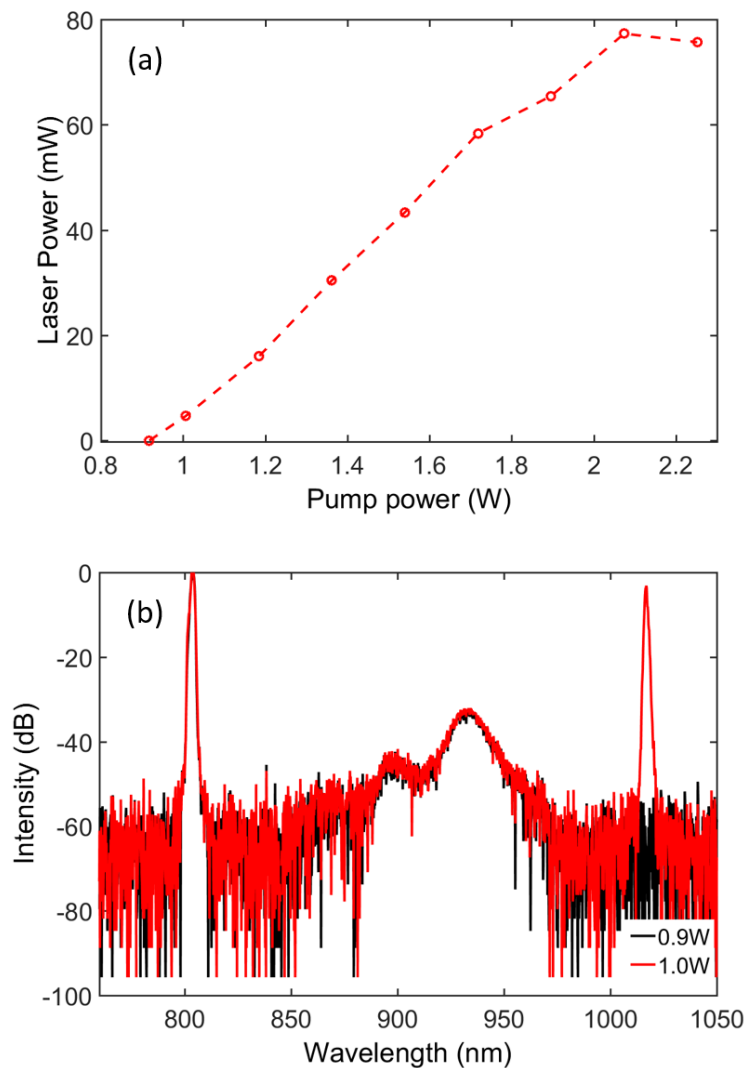


Figure 5.11 (a) Laser conversion graph and (b) Spectra below (black curve with 0.9 W incident pump power) and above threshold (red curve with 1.0 W pump power). The pump diode operates at 803 nm and laser at 1017 nm.

As shown in Fig. 5.15, the laser emission wavelength is 1040 nm at threshold, and redshifts to 1054 nm at 50 W incident pump power, which corresponds to a redshift rate of 0.35 nm/W. Assume the gain spectrum peak redshifts at 0.3 nm/K, the active region temperature raises by 47 K from threshold to 50 W pump power. From this estimation, the active region could survive 100 W incident pump power with the same pump spot size.

Inserting a 0.5 mm thick quartz birefringent filter (BRF) at Brewster's angle into the cavity, the laser wavelength can be tuned by rotating the BRF. With two HR mirrors, at 31 W incident pump power, the laser can be tuned from 994 nm to 1074 nm, over 80 nm in tuning range, which, to the best of our knowledge, is a record for SDLs near 1 μm . With

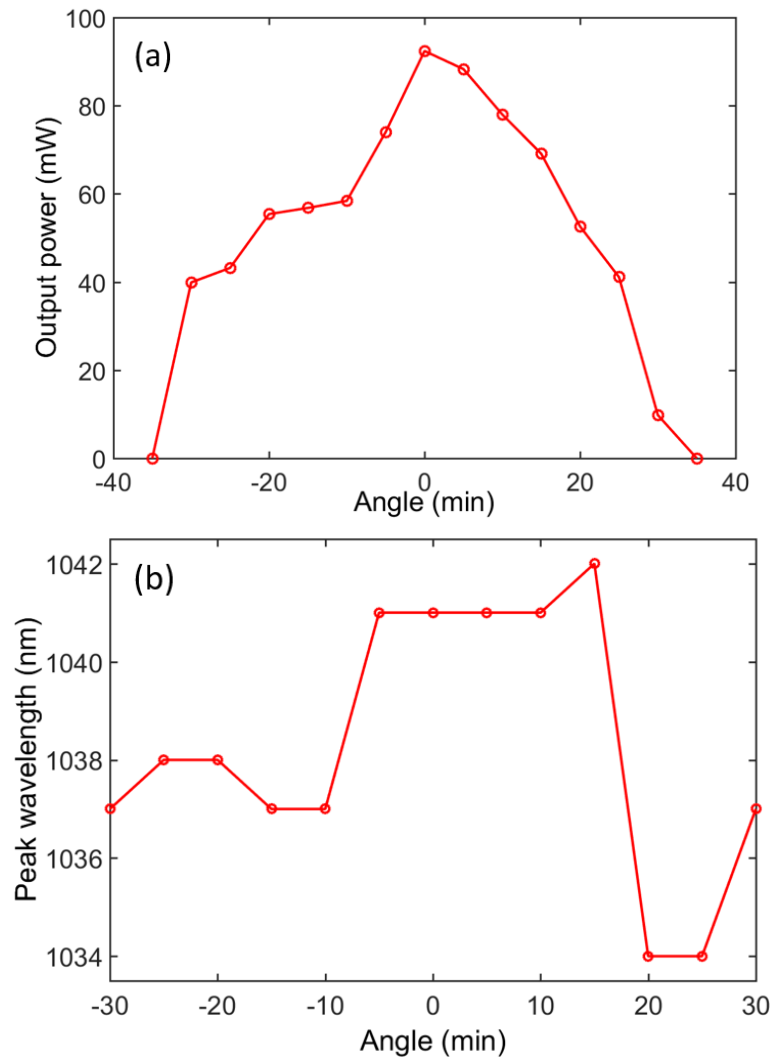


Figure 5.12 Angle dependent output power (a) and peak lasing wavelength (b) for an active region bonded onto a sapphire window. The pump power is kept constant.

HR mirrors, the output power is relatively low, 130 mW at 1050 nm. Both the laser tuning range and corresponding output powers are shown in Fig. 5.16. At higher pump powers, thermal roll-over is observed due to the low coupling efficiency.

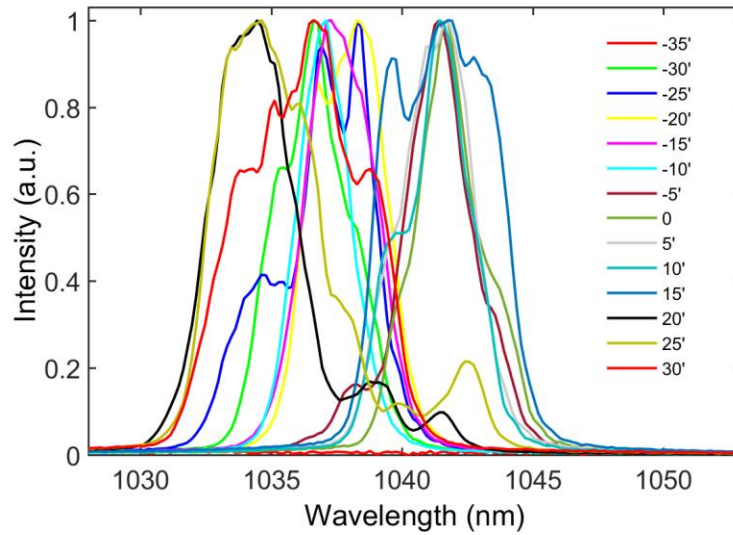


Figure 5.13 Angle dependent laser spectra for an active region bonded on sapphire.

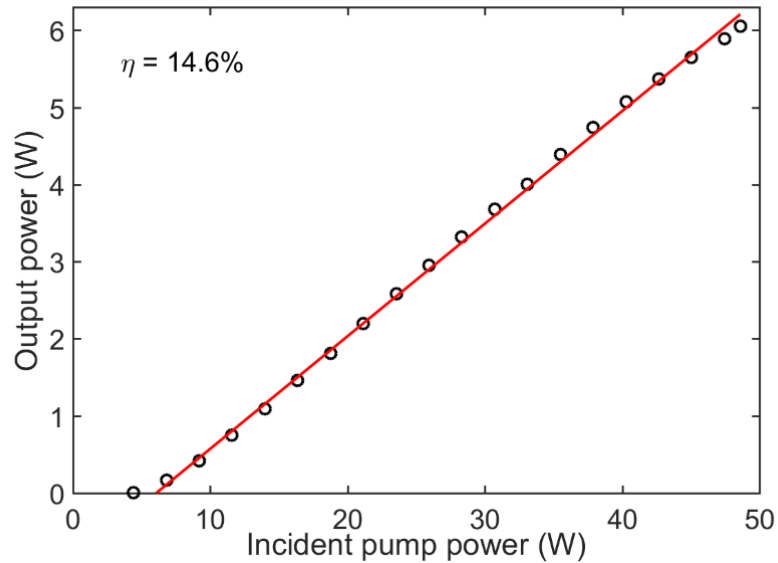


Figure 5.14 Laser conversion graph for an active region designed at 1040 nm bonded on a low absorption diamond. The concentric cavity is consisted of a ROC=250 mm HR mirror and a ROC=100 mm 2% transmission OC. The optical distance between OC and the active region is about 94 mm and 245 mm between HR and the active region. The coolant temperature is 13°C. With respect to the incident pump power, the laser slope efficiency is 14.6%.

Semiconductor materials have broad gain bandwidth. With InGaAs QWs, external-cavity diode lasers have been reported with up to 170 nm tunability [12]. In comparison, typical VECSELs with InGaAs MQW near 1 μm have fairly limited tunability, about 30 nm, as shown in Fig. 5.17. To expand the gain bandwidth, much effort has been focused on managing the subcavity gain modulation, as well as increasing the material gain bandwidth. For the former, AR coating on the air-semiconductor interface and antiresonant PGS [13] are used; for the latter, multiple gain chips with different spectral reflection, or

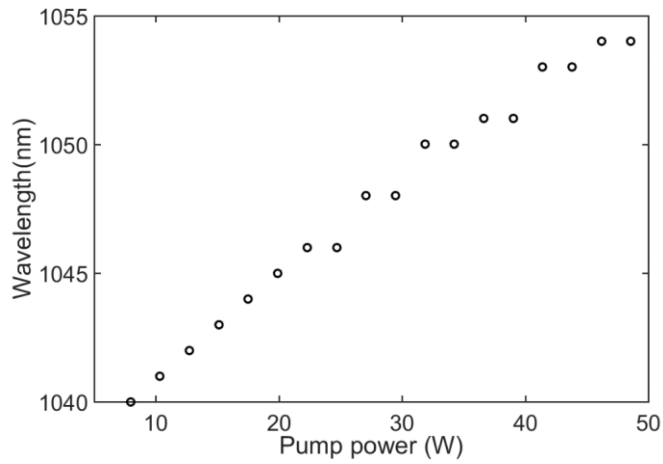


Figure 5.15 Pump power dependent operation wavelength for a free-running transmission geometry DBR-free SDL.

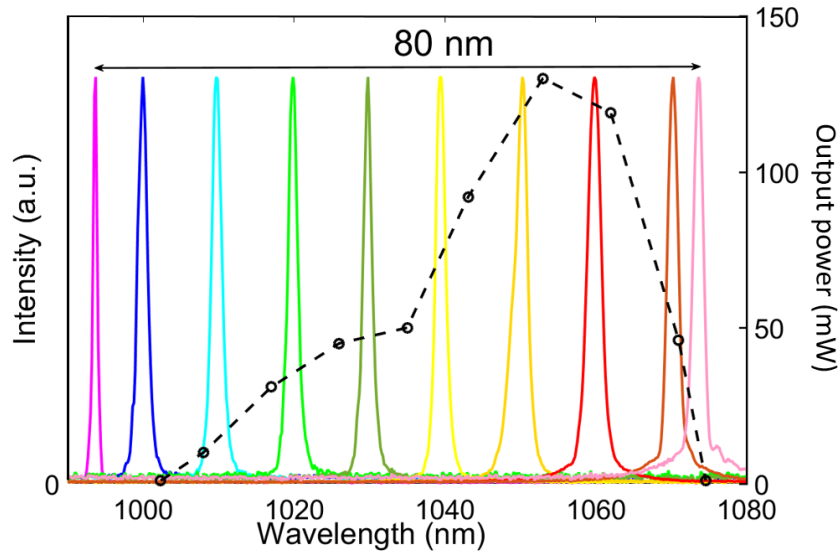


Figure 5.16 Wavelength tuning and corresponding output power for a transmission geometry DBR-free SDL with a BRF of 0.5 mm thickness. The incident pump power is 31 W.

even inhomogeneous QD [14] active regions are incorporated. A VECSEL, consisting of two serially interconnected and separately pumped active regions with 4 nm center emission wavelength offset, has been reported with 33 nm tuning range [15]; another QW VECSEL with specially designed antiresonant gain structure was demonstrated 43 nm tuning range [13]; a QD VECSEL achieved 60 nm tunability with a thinner ($7.5 \lambda/2$ optical thick) gain structure [14]. In another reference [6], a tuning range of 75 nm was achieved by translating the gain chip, taking advantage of the wafer nonuniformity. Additionally, thinner gain structures, as discussed in section 2.4.1, offer broader gain bandwidth. Even though some of these lasers are with watt-level output power, from our experience with 1160 nm DBR-free SDLs in the next subsection, the tunability advantage of DBR-free SDLs is still significant.

Multiple factors contribute to the broad tuning range. First, with the active region directly bonded onto diamond, the reflectivity at the semiconductor-diamond interface (about 3%) is negligible because of the small relative refractive index n_H/n_L (about 1.42, n_H and n_L are the refractive indices of the high and low refractive index layers). This leads to a low finesse semiconductor subcavity and subsequently a reduced modulation over the gain spectrum. Second, with larger relative refractive index between the high and low index layers, dielectric DBR mirrors offer wider high reflection band than semiconductor DBRs [16]. Most importantly, dropping the active mirror geometry and having the PGS far from the cavity global nodes, the DBR-free transmission geometry has a broader effective gain.

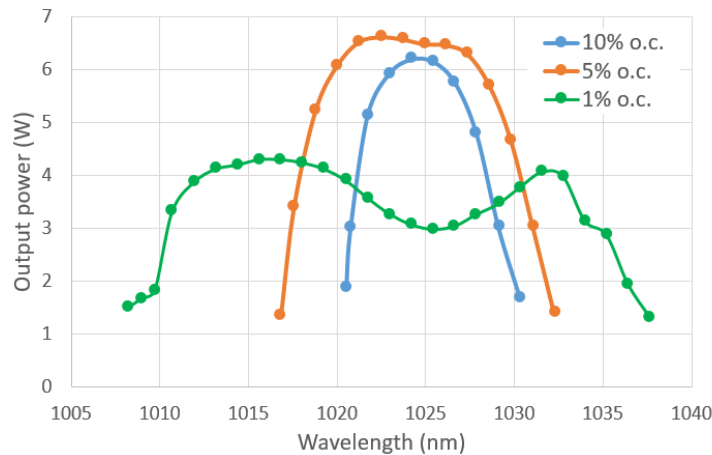


Figure 5.17 Tuning ranges for a typical VECSEL at 1020 nm with different output couplers, measured by Mohammadreza Ghasemkhani.

This has been analytically and numerically evaluated with the position dependent integrated gain model in section 2.4.1. A simple picture to understand this is: in VECSEL geometry, the PGS is close to a cavity global node, and only a narrow range of continuous longitudinal modes have a good overlapping with the periodic gain; in the DBR-free transmission geometry, the gain structure is far from cavity global nodes, and a broader range of modes can experience high effective gain. Exceptions apply for certain gain positions, which was discussed in section 2.4.2.

For semiconductor lasers, slope efficiency can be expressed as:

$$\eta = \eta_{\text{abs}}\eta_q\eta_i \frac{T_{\text{oc}}}{T_{\text{oc}} + \alpha_o} \quad (5.1)$$

where η_{abs} is the absorption efficiency for pump power, η_q is the quantum defect rate, η_i is the internal quantum efficiency, T_{oc} is the output coupling efficiency, and α_o is the total intracavity optical losses. Concerning the low slope efficiency, we have ruled out the possibility of pump parameters. With a well-characterized VECSEL chip, the laser slope efficiency is compared between a “good” pumping system and the system we use in the DBR-free geometry. With the 50 W diode and the pump focusing system used in the DBR-free experiments, the VECSEL provides 16.9% slope efficiency with a 2% transmission OC (not optimal coupling condition), which is comparable to the result with the “good” one. Similarly, at the same pump condition, a comparison is made on the thresholds between the VECSEL chip and a DBR-free gain assembly. For the VECSEL chip, with the two curved mirrors (ROC=100 mm), the threshold are 1.74 W and 2.59 W respectively. Switching to the DBR-free gain assembly with AR coated diamond, the threshold is 3.22 W with two mirrors. The two geometries are very close in threshold and it is difficult to draw a conclusion.

Another possibility, the gain-drain due to the lateral lasing [17, 18], has also been ruled out. With the custom-made copper mount, the top plate clamps the diamond on the copper mount, but also blocks the sides of active region. It has to be removed for checking the lateral lasing, but may lower the thermal extraction efficiency. Therefore, only 30 W pump power is applied. The vertical lasing is also suppressed by blocking one mirror. By scanning the four sides of the active region, no lasing is observed with an Ocean Optics

spectrometer. Therefore, for this gain chip, the threshold for lateral lasing (> 30 W) is much higher than vertical lasing (5 W). Furthermore, with the LI curve shown in Fig. 5.14, there is no obvious drop in slope efficiency. As a result, there is no sign of lateral lasing, or lateral lasing affecting the laser efficiency. In the device fabrication process, active regions are kept as big as possible to suppress lateral lasing. With CW pumping, the carrier density is not very high and lateral lasing happens near the gain spectrum peak, which could be absorbed by the area below transparency. Larger samples bring in more optical losses to the lateral cavities, and prevent lateral lasing.

The laser coupling efficiency also affects the slope efficiency, as mentioned earlier. Fig. 5.18 presents a summary of laser slope efficiency for an active region with five sets of OCs. For this chip, the optimum coupling efficiency is about 2%; typical high power VECSELs at around 1 μm is about 3% [4] or higher. It is also worth to note that this is not the same sample with 6 W output power, but the similar evaluation process has been carried out for every sample we characterized. With the fitting parameters, it appears the intracavity optical losses are low but the internal quantum efficiency is low, since the other two parameters—quantum defect rate and pump absorption efficiency—are known.

Another possibility for the low slope efficiency is the Fresnel reflection losses on the air-diamond or air-semiconductor interface. A low absorption diamond has been AR coated

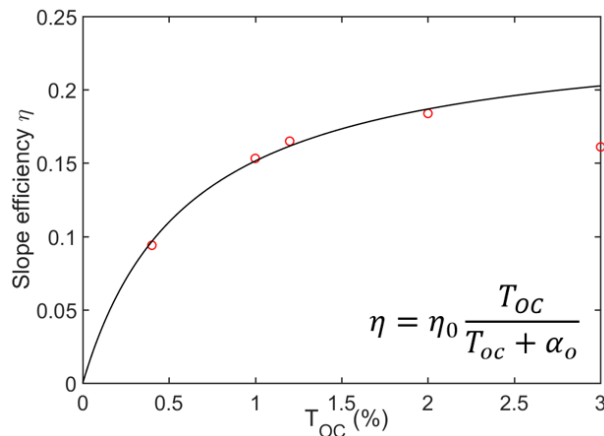


Figure 5.18 Laser output coupling efficiency optimization. The active region is a 1315-086 sample with two types of QWs and diamond is an uncoated, low absorption one. The black line is the fitting curve and the function is shown in inset. The fitting parameter $\eta_0=0.244$ and total intracavity losses $\alpha_0=0.6\%$.

($R < 0.5\%$ according to the specifications) on one side and used as a heatspreader in a transmission geometry DBR-free SDL. With an active region designed at 1160 nm discussed in the next subsection, about 2 W output power is collected with 14.4% slope efficiency. No significant improvement is observed over the 11% slope efficiency with the coated diamond. Brewster's angle geometry could also mitigate these losses but the integrated gain changes with angle. As a result, it is difficult to make a direct comparison. As to the potential scattering losses due to the diamond surface roughness, a comparison is made with sapphire substrates in the next subsection.

Another bonded sample worth to mention is from wafer 1312-066 (detailed with Fig. 3.3 (b) in section 3.3.1), which is not designed for the normal incidence geometry. As shown in Fig. 3.9 (a), there are many surface features on the bonding results. With this sample, however, about 3.5 W output power is collected with 26 W incident pump power, showing a slope efficiency of 16.5%. The laser conversion graph is shown in Fig. 5.19. Unfortunately, the sample is later damaged in the annealing process.

Lack of proper equipment, it is challenging to directly characterize the bonding uniformity. Under the same pump and cavity conditions, translating active regions horizontally, the spatial dependent laser output power could give us a hint. An uncoated diamond is used as the bonding substrate. Before the experiments, both the cavity

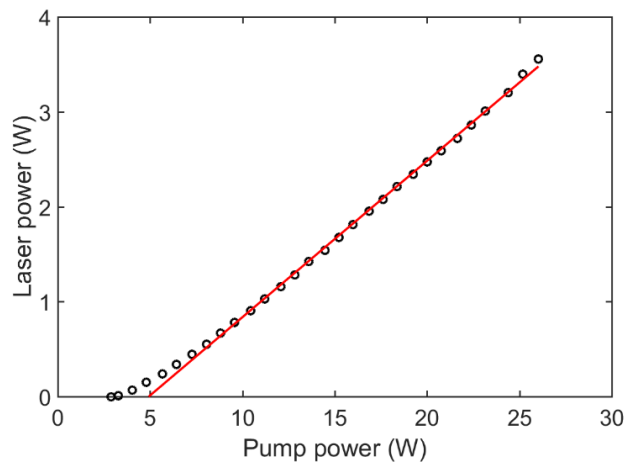


Figure 5.19 Laser conversion graph for the assembly shown in Fig. 3.9 (a), of which the diamond window is preprocessed in oxygen plasma at 100 W RF power for 90 s. The slope efficiency is 16.5% with respect to the incident pump power.

(including the sample orientation) and pump parameters are optimized at 16.4 W pump power for maximum output power with near TEM₀₀ mode. Then the pump condition is kept constant, and the active region is scanned transversely, with the position dependent normalized output power graphs are shown in Fig. 5.20. The scanning range is limited by the aperture size of the copper mount. Near threshold, the laser power fluctuates significantly with position; at higher pump power, there is less than 10% change in power over 1 mm length. Therefore, the bonding is relatively uniform over 1 mm horizontally.

For the active region bonded on an AR coated low absorption diamond (0.2% absorption per roundtrip), a second regular diamond is directly clamped onto the active region. Parallel interface fringes are observed, shown in Fig. 5.21 (a) inset. With the second diamond, the thresholds are much higher and slope efficiencies are lower than the single diamond case, shown in Figs. 5.21 (a) and (b). Therefore, the optical losses in the second diamond (1.2% roundtrip absorption) or at clamping interface are significant. Due to either the Fabry-Perrot or thermal effect, the emission wavelengths with two diamonds are much shorter.

In experiments, different from natural diamonds [19], no obvious birefringent effect is observed with these high quality synthetic single-crystalline diamonds. Recently, Professor Michael Jetter's group at University of Stuttgart realized a diamond-sandwiched gain

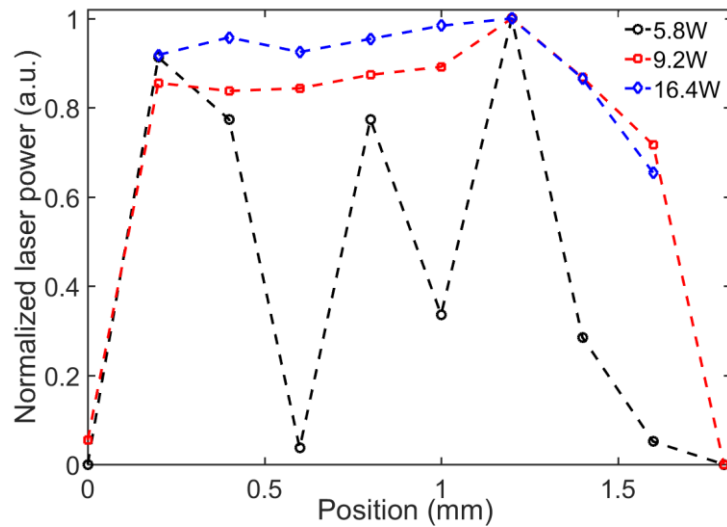


Figure 5.20 Active region uniformity check at different pump powers. With 5.8 W, 9.2 W, and 16.4 W pump power, the maximum output powers are 10 mW, 140 mW, and 810 mW, respectively.

membrane geometry [20] with GaInP QWs designed at 640 nm. With two AR coated diamonds, under the same condition, the slope efficiency of the diamond-sandwiched geometry is comparable to VECSELs' [21] at the same wavelength range.

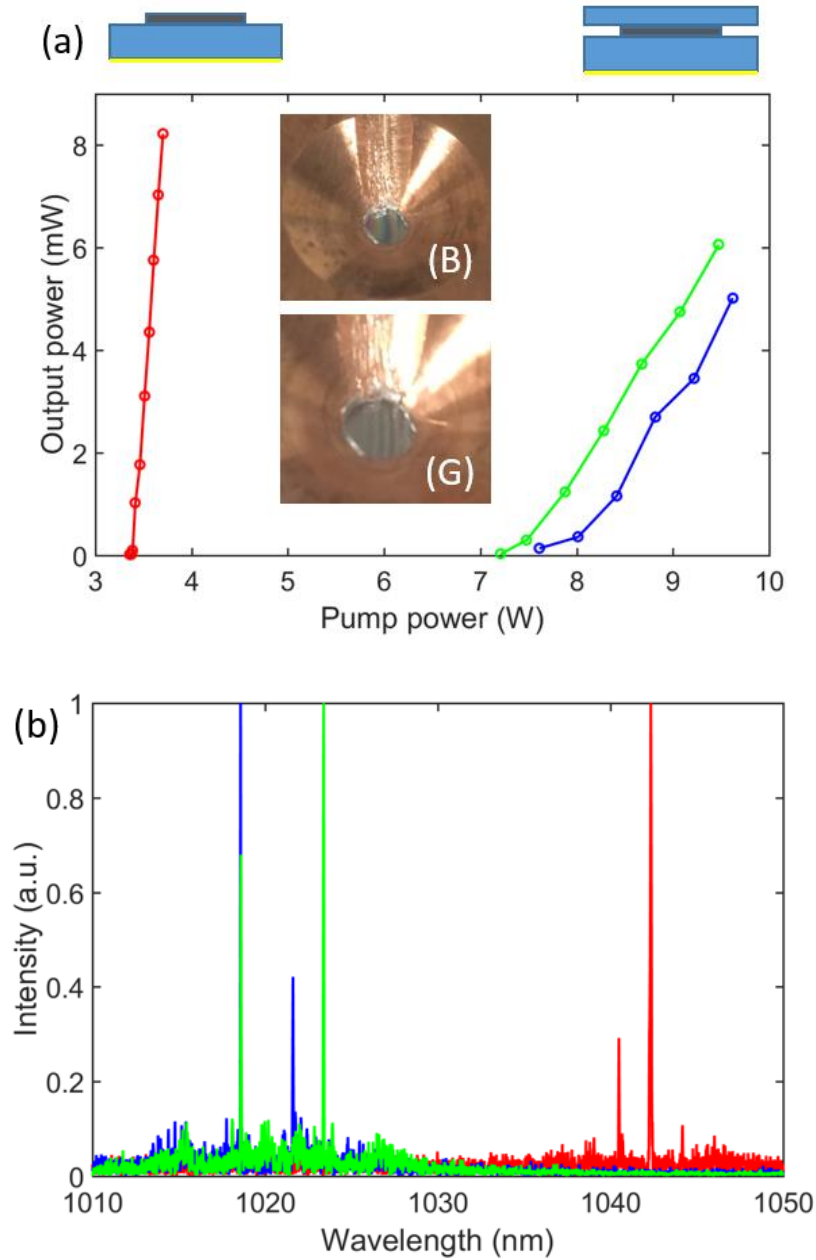


Figure 5.21 Laser performance comparison with one and two diamonds (the second diamond is directly clamped on). (a) Laser conversion graphs for a single-diamond (red), and two-diamond configuration (blue and green). The cross-section views of the gain assemblies are shown on top of the figure. For blue and green curves, the clamping forces are different and their interface patterns are shown in the inset (B) and (G). (b) Laser spectra for three different scenarios collected with a Thorlabs optical spectrum analyzer.

5.3 QW based transmission geometry DBR-free SDLs at 1.16 μm

High power SDLs at near 1160 nm has a myriad of applications. High power, narrow linewidth 589 nm lasers intracavity frequency doubled from a SDL at 1178 nm, can be used to excite the D_2 line of sodium atoms at the Earth's mesosphere layer [22], creating an artificial star. The laser guide star is used to calibrate adaptive optics systems for the atmosphere turbulences [23, 24]. Additionally, a multi-watt single-frequency SDL at 1140 nm could be adopted as the second excitation source for the $3P_{3/2}$ to $4S_{1/2}$ transition [25], creating another guide star at NIR. With the guide stars at different wavelengths, the dispersion dependent aberration can be further corrected. The current monochromatic laser guide star systems are mostly using frequency converted fiber lasers [24], which are bulky, complicate and expensive. SDL, as a compact, reliable, high power, and cost-effective laser source, is very attractive to this application.

For other solid-state lasers, there are limited high power sources in the yellow wavelength range [26], which is accessible to the intracavity frequency-doubled SDLs utilizing the bandgap engineering technique. Single-frequency 571 nm laser frequency doubled from 1142 nm [27], and 280 nm quadrupled from 1120 nm SDLs are employed in laser cooling of magnesium ions [28]. The frequency-doubled yellow spectral range SDLs can be used in bio-fluorescence imaging [29] and laser treatment in ophthalmology [30] and dermatology [31]. So far, in this wavelength range, typical VECSELs have achieved up to 50 W fundamental output power [32] and 20 W second harmonic output [33].

In SDLs, different materials have been utilized for reaching this wavelength range with GaAs substrates, including InGaAs QWs, GaInNAs QWs [34], and InGaAs quantum dots [14]. Here we choose the InGaAs QWs. For InGaAs QWs center emitting near 1160 nm, compared to QWs at 1020 nm, a higher indium composition (approaching 40%) is needed, which poses a problem to the material growth [35, 36]. To balance the strain introduced by the large lattice mismatch between the InGaAs layers and GaAs substrate, $\text{GaAs}_{0.96}\text{P}_{0.04}$ has been employed as the barrier layer. Additionally, a low growth temperature (520°C) condition for the QW region is required to observe luminescence, which implies high crystalline quality with little or no strain related defects, such as threading dislocations. However, for the barrier layers, low temperature growth condition may degrade the

interface quality. Epitaxial surface with roughness RMS (root mean square) exceeding 8 nm has been observed. In comparison, the roughness RMS for a typical GaAs layer is less than 1 nm. Therefore, a two-temperature growth approach has been adopted. Even though this method alleviates the lattice mismatch problem, it is still challenging to grow regular periodical gain structures with more than 9 QWs. For active regions (wafer 1314-273) discussed in this section, there are 8 QWs in a barrier of 11 half-wavelength optical thickness, and the detailed structure is presented in Fig. 3.4 (b).

An active region is lifted off and directly bonded onto a regular diamond window. The diamond-gain assembly is clamped with the aforementioned copper mount, which is water cooled to 10°C. The cavity adopts the typical transmission geometry, consisting of a concaved HR mirror with 100 mm ROC and a concaved OC with 250 mm ROC (approximately 1% transmission, but may vary with wavelength). Pumped with a 25 W fiber-coupled laser diode, laser operation is achieved and the laser conversion graph is shown in Fig. 5.22. About 2.5 W output power is collected with 25 W incident pump power, showing a slope efficiency of 11% with respect to the incident pump power. The beam profile, as shown in Fig. 5.23, is close to TEM₀₀ mode. At near threshold, the free-running laser operates at 1155 nm with multiple unstable longitudinal modes, shown in Fig. 5.24 (a). At higher pump powers, stable operation with multiple evenly spacing longitudinal modes is observed as shown in Fig. 5.24 (b), in which the spacing is about 0.53 nm. This matches the free spectral range of the diamond (or diamond-semiconductor) subcavity.

By inserting a 0.5 mm thick BRF at Brewster's angle into the cavity, the lasing wavelength can be tuned by rotating the BRF. With two HRs, at 10.5 W incident pump power, the laser can be tuned from 1118 nm to 1196 nm, corresponding to 78 nm tuning range, as shown in Fig. 5.25. Further increasing the pump power, thermal roll-over is observed with HRs. In comparison, in the same wavelength range, a frequency-doubled VECSEL [33] is reported about 26 nm tuning range in yellow (about 52 nm tuning range in the NIR); a QD based VECSEL [180] is demonstrated 69 nm tuning range with a thinner gain structure and broad material gain bandwidth (one QD has narrow gain but the QD size distribution provides broad effective material gain). With a 1% OC, the laser can be tuned about 62 nm with 6.5 W incident pump power [37]. For this OC, the transmission increases

significantly at long wavelengths, which explains the distorted laser power curve in Fig. 5.26.

A chip from the same wafer is lift-off and bonded onto an AR coated ($R < 0.5\%$ between 1000 nm and 1200 nm) low absorption diamond. With the same set of optics, 2 W output power is collected with 18 W incident pump power. The slope efficiency is 14.4%, shown in Fig. 5.27. Compared to the results in Fig. 5.22, there is no obvious improvement.

With the compromised optical quality, diamond surfaces could bring in scattering losses and lower the laser efficiency. Direct measurement of the scattering losses is difficult to

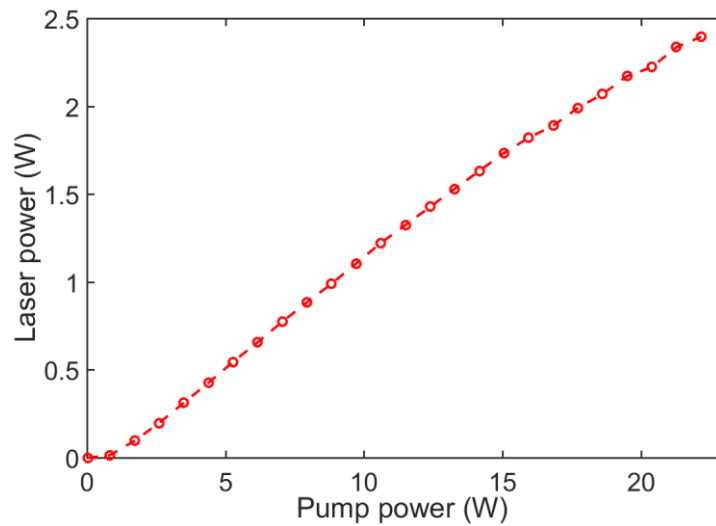


Figure 5.22 Laser conversion graph for an active region designed at 1160 nm bonded on a diamond. The slope efficiency with respect to absorbed pump power is 11%.

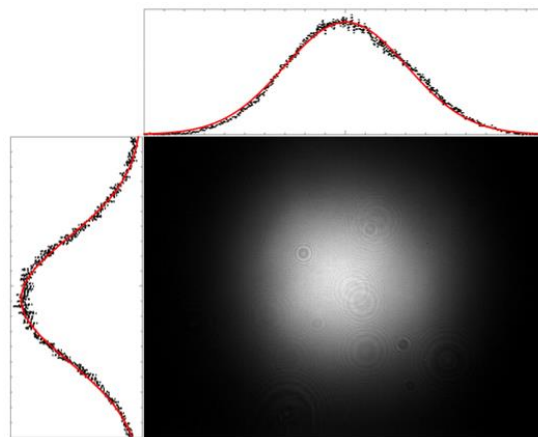


Figure 5.23 Laser beam profile characterized with a CCD camera. The top and left are the cross-section (black) and their Gaussian fittings (red).

perform. Therefore, the laser thresholds are compared for active regions bonded onto different substrates. With the same laser cavity, a sample bonded onto sapphire is with the threshold of 2.66 W, pumping from the semiconductor side, while a chip bonded onto diamond is 2.39 W pumping from the diamond side. Considering the transmitted pump power to the active region, the threshold is 1.86 W with sapphire substrate, and 1.91 W with diamond. The threshold powers are very close. Considering the potential bonding quality variation, it is difficult to rule this factor fully out.

For the first bonded sample bonded in October 2014, it has been pumped up to 25 W multiple times and no obvious device degradation (increase in threshold or decrease in slope efficiency) has been observed to date, August 2016. There are a few optical damage

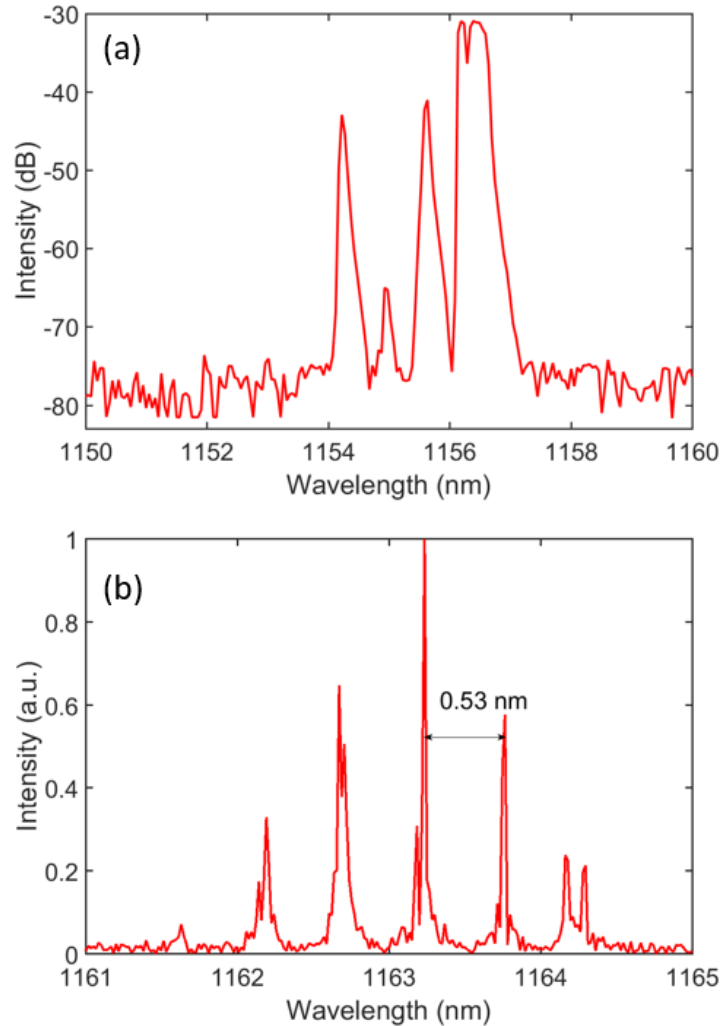


Figure 5.24 Free-running laser spectra. (a) The spectrum is collected at near threshold with an OSA with 0.2 nm resolution. (b) The spectrum is collected at a higher pump power with a Thorlabs OSA.

spots due to water condensation, when the humidity was high in the lab and the coolant temperature was too low.

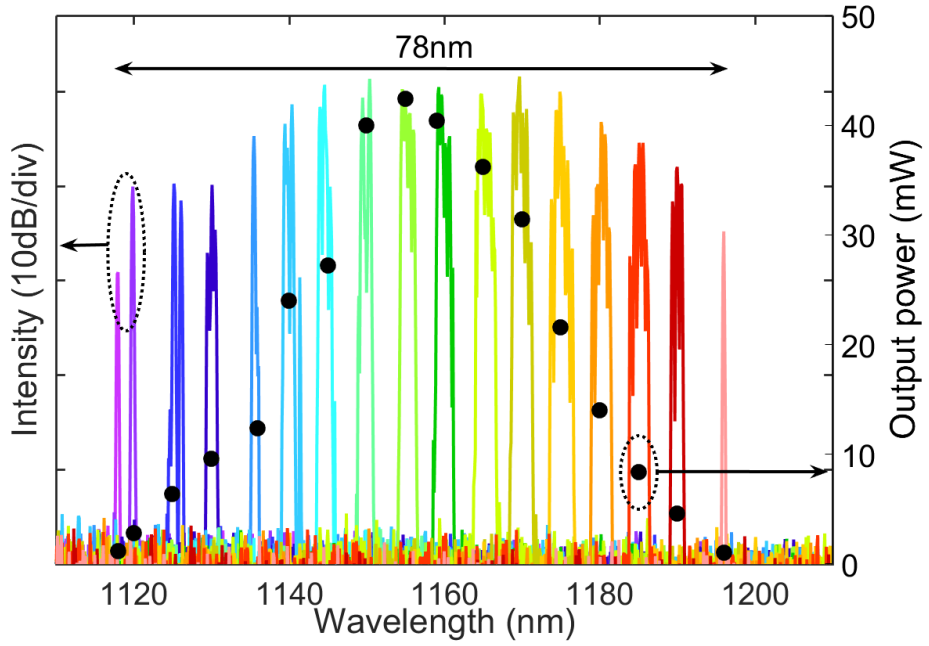


Figure 5.25 1160 nm DBR-free SDL tuning range and output power. The spectra are collected with an optical spectrum analyzer at 0.02 nm resolution.

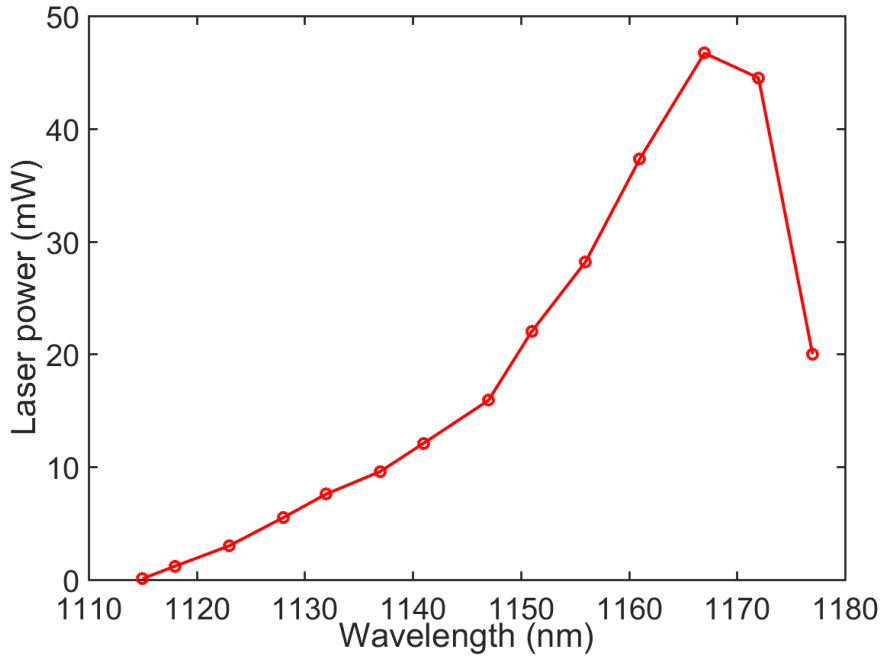


Figure 5.26 DBR-free SDL power with wavelength at 6.5 W incident pump power.

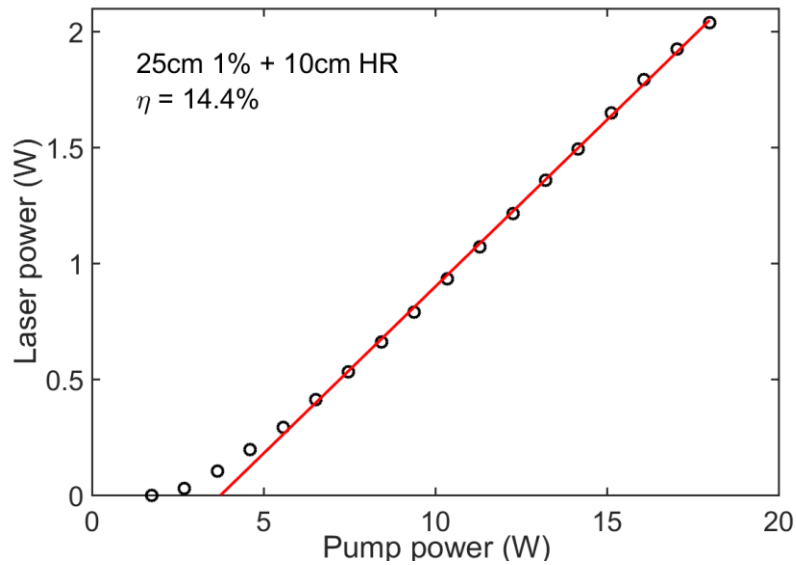


Figure 5.27 Laser conversion graph of an active region bonded on an AR coated diamond with a 1% transmission OC.

5.4 Brewster's angle geometry DBR-free SDLs

As mentioned in the last two subsections, the current transmission geometry DBR-free SDLs suffers from low slope efficiency. With the Z-scan technique, the laser absorption in diamond is confirmed fairly low, 0.2% per roundtrip for the low absorption diamonds and 1.2% for the regular diamonds. One of the possible culprit is the Fresnel reflection losses on the diamond-air interface, due to imperfect surface parallelism. AR coating at the laser wavelength can mitigate the losses, but is inconvenient since the diamonds have to be dipped into both strong acid and base solutions in the device fabrication process and the coatings could be damaged.

With Brewster's angle incidence on the air-diamond interface, no coating is needed. Compared with the normal incidence scenario, the periodicity for the gain structure has to be redesigned. To avoid this, in this subsection, we will use the GaAs DHS sample as the active region and the laser geometry is shown in Fig. 5.28 (a). With the Brewster's angle incidence on diamond, by calculation, the Fresnel reflection are approximately 2.3% at 900 nm on the air-semiconductor and semiconductor-diamond interfaces, even though the refractive index are very different on two sides. The 2 μm thick active region has good

parallelism, acting as an etalon with a small modulation. Zero Fresnel losses can be achieved. With the same reflectivity at air-semiconductor and semiconductor-diamond interfaces, the two geometries in Figs. 5.28 (a) and (b) have the same transmission modulation, as shown in Fig. 5.29. By coincidence, one diamond acts as a pair. With the material dispersion included, minor difference may exist.

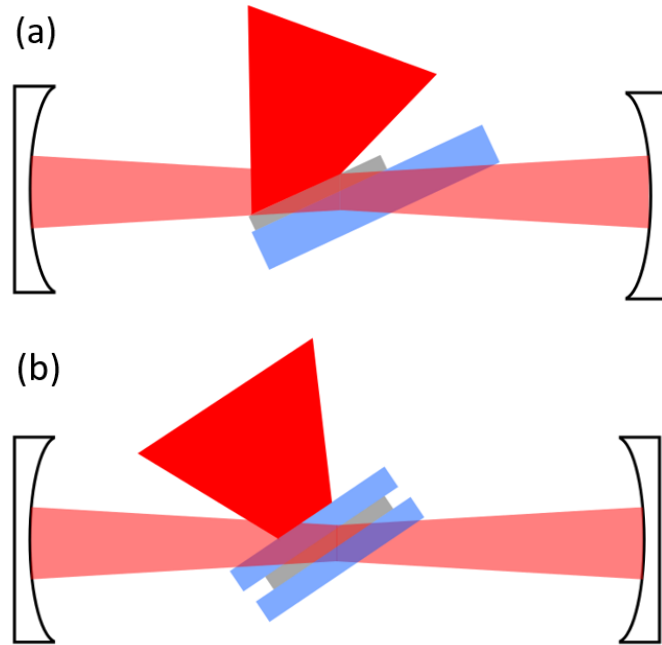


Figure 5.28 (a) Single-diamond DBR-free SDL in Brewster angle geometry. The diamond is at 67° with respect to the laser path. Fresnel reflection at both the air-semiconductor and semiconductor-diamond interfaces are 2.3%. (b) The double-diamond DBR-free SDL in Brewster angle geometry.

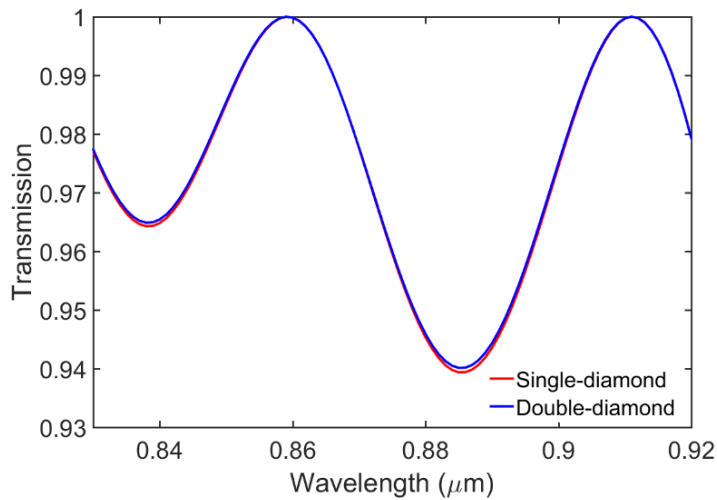


Figure 5.29 Transmission spectra of the two active region assemblies shown in Fig. 5.28. Calculated with RSoft DiffractMOD.

A fiber-coupled 100 W laser diode is used to pump the active region. The focused pump is at approximately 60° angle of incidence, so as to achieve good overlapping with the cavity mode. Since the laser is at oblique incidence to the diamond-gain assembly, a larger size diamond window (6 mm by 4 mm) is employed. A significant amount of ASE is observed, as shown in Fig. 5.30, however, no lasing operation is observed even up to the full pump power, 100 W. With the z-scan technique, it is found 2% absorption per roundtrip in this diamond window. Additionally, it is wedged. These might account for the high laser threshold. Further studies with sapphire substrates are ongoing.

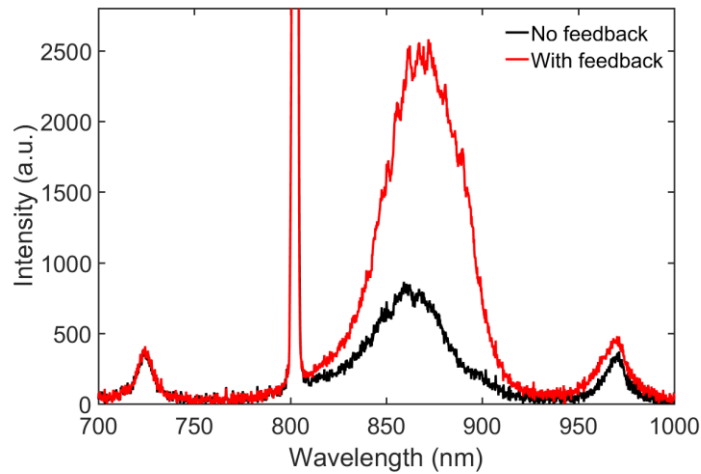


Figure 5.30 DHS sample PL spectra. The spectra are collected with an Ocean Optics USB4000 spectrometer. The “without feedback” and “with feedback” spectra are collected by blocking and unblocking the vertical cavity at 60 W incident pump power.

5.5 Ring cavity geometry

Ring lasers have unique properties. With the Sagnac effect, ring lasers have been used in laser gyroscopes [38]. For ring cavity VECSELS, there have been a few attempts with single-frequency [39] and mode locking [40] operations. In both references, the regular VECSEL chips were in double-V shaped cavities, locating at (or close to) cavity nodes.

Our motivation to study ring cavity geometry is to test the predictions of the position dependent integrated gain model, by comparing with standing wave cavity on both tuning range and longitudinal mode spacing. The laser schematic and experimental setup are shown in Fig. 5.31. Similar to the transmission geometry, the diamond-gain assembly is

clamped with a water-cooled copper mount. Both the cavity (including the alignment, curve mirrors separation, long arm length) and pump parameters are optimized for good overlap between cavity modes and pump focus. Based on the ABCD matrix method, a cavity mode size contour map is presented in Fig. 5.32.

The ring cavity lases and the laser conversion graph is shown in Fig. 5.33 with four HR mirrors. To measure the laser tuning range, a 0.5 mm thick quartz BRF is inserted into the cavity at Brewster's angle near the midpoint of the flat mirrors. As shown in Fig. 5.34, at

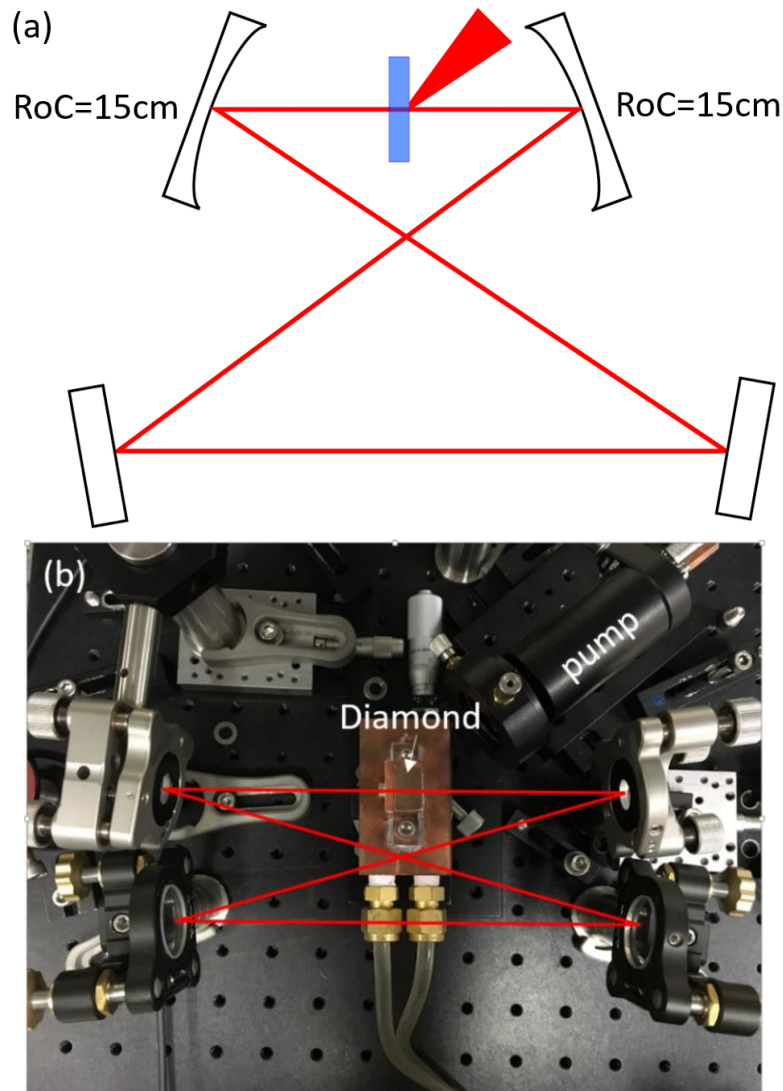


Figure 5.31 Bow-tie ring cavity schematic (a) and experimental setup (b) of the bow-tie ring laser geometry. The separation between two curved mirrors is 180 mm, and 213 mm between two flats. The optical paths are 200 mm and 203 mm between the curved mirrors and flat mirrors. The folding angles are 10° and 13° on the curved mirrors.

12 W pump power, the laser wavelength can be tuned from 1006 nm to 1062 nm, 56 nm in tuning range. Rotating the two flat mirrors to normal incidence, an X cavity is formed. On the gain position, special attention is given to avoid the cavity midpoint. With the same BRF at Brewster's angle near one flat mirror, the laser wavelength is tuned from 1010 nm

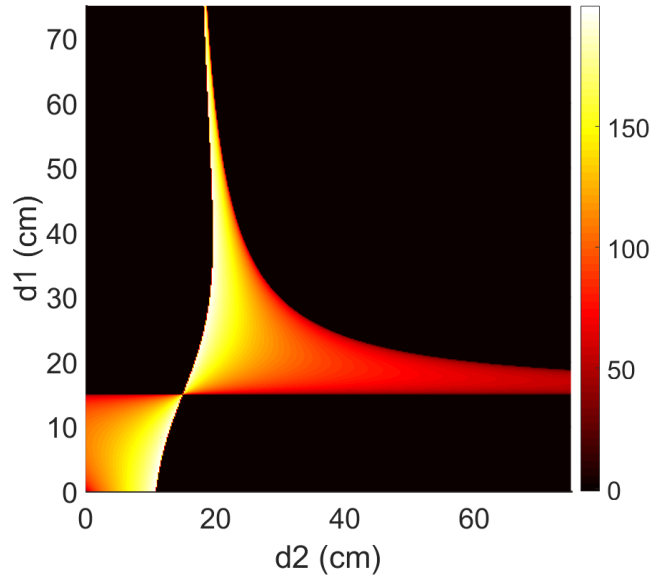


Figure 5.32 Cavity mode size in radius at the active region calculated with the ABCD matrix method. d_1 is the optical distance between two curved mirrors, and d_2 is the optical length from one curved mirror, reflected on two flats, and to the other curved mirror. The unit for the radius bar scale is μm , and larger than $200 \mu\text{m}$ beam radius situations are excluded in the contour map.

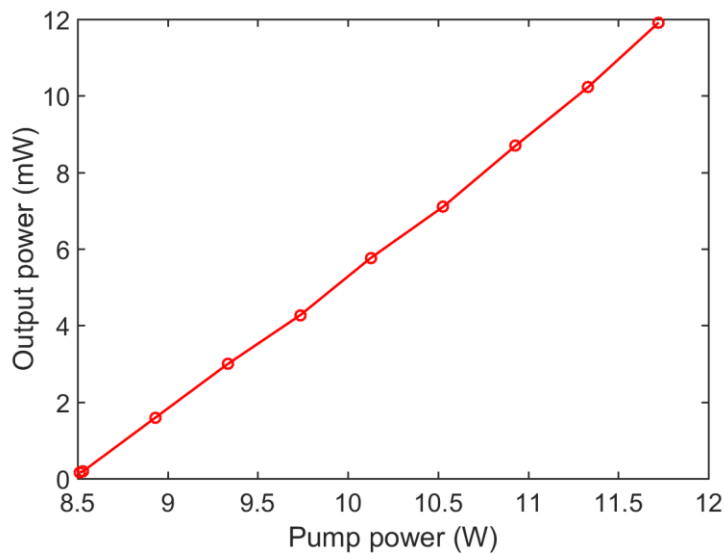


Figure 5.33 Laser conversion graph of the bow-tie ring cavity with a set of HR mirrors.

to 1063 nm, 53 nm in tuning range. The wavelength dependent output power graph is shown in Fig. 5.34. The two geometries have similar tuning ranges, but the ring geometry has much lower output power, which may be due to mirror losses. Assuming that the reflectivity of curved mirrors is R_c , and flat mirrors is R_f , and g is the threshold gain. For the ring cavity geometry, at the threshold,

$$R_c^2 R_f^2 \exp(N_w d_w g_r) = 1 \quad (5.2)$$

while for the standing wave cavity,

$$R_c^4 R_f^2 \exp(2N_w d_w g_s) = 1 \quad (5.3)$$

Here N_w and d_w are the number and thickness of QWs. Therefore, the standing wave cavity has lower threshold, 6.6 W in experiment, while the ring cavity is 8.5 W. Discussion on longitudinal mode spacing will be presented in section 5.6.

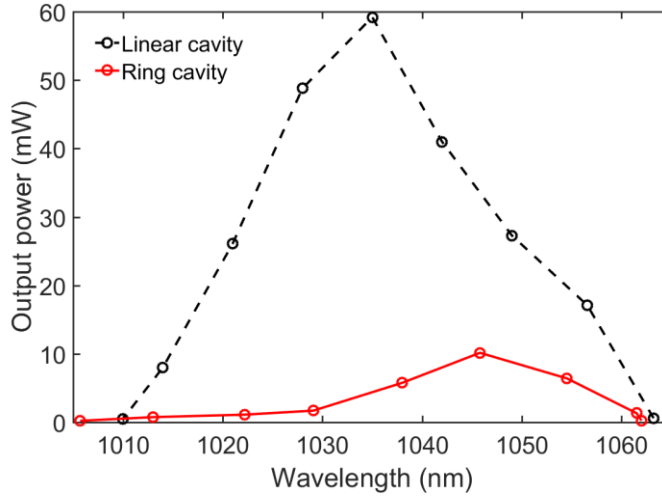


Figure 5.34 Tuning range comparison between the linear (X) cavity and ring cavities with a 1315-059 active region. Both geometries are realized with the same set of mirrors and in the stable operation regime. The incident pump power is 12 W.

5.6 Integrated gain model revisit: longitudinal mode spacing

In section 2.3, we have analytically evaluated the integrated gain of a PGS in a standing-wave cavity. Besides the verified broad effective gain bandwidth, the simple model also predicts interesting mode structures with a DBR-free geometry: with a large z value (gain

position $z \gg \lambda$, minimum distance between the active region and cavity nodes), not every longitudinal modes within the material gain bandwidth reach laser threshold. To test this prediction, we check the laser RF spectra.

The cavity is formed with two HR concave mirrors with 100 mm ROC separated by about 200 mm, as shown in Fig. 5.9 (c). To vary the gain position without changing the pump condition, two mirrors are translated parallel to the laser path instead while the active region stays unchanged. The laser output is collected with a high speed detector (EOT InGaAs photodiode with 15 GHz bandwidth) and the time trace is recorded with a high speed oscilloscope (Tektronix DPO70804 with 8 GHz bandwidth). The RF spectra, or the Fourier-transform of the time trace, at two z values are shown in Figs. 5.35 (a) and (b). When the active region is away from the cavity center by 5 mm, the RF spectrum contains peaks at the integer multiples of the cavity repetition rate f_{rep} , with the even multiples at higher amplitudes. Having the gain-diamond assembly closer to the center ($z \approx L/2$), the odd multiples are eliminated and only the even multiples are observed with the strongest signal at $2f_{rep}$, and the longitudinal mode spacing doubles.

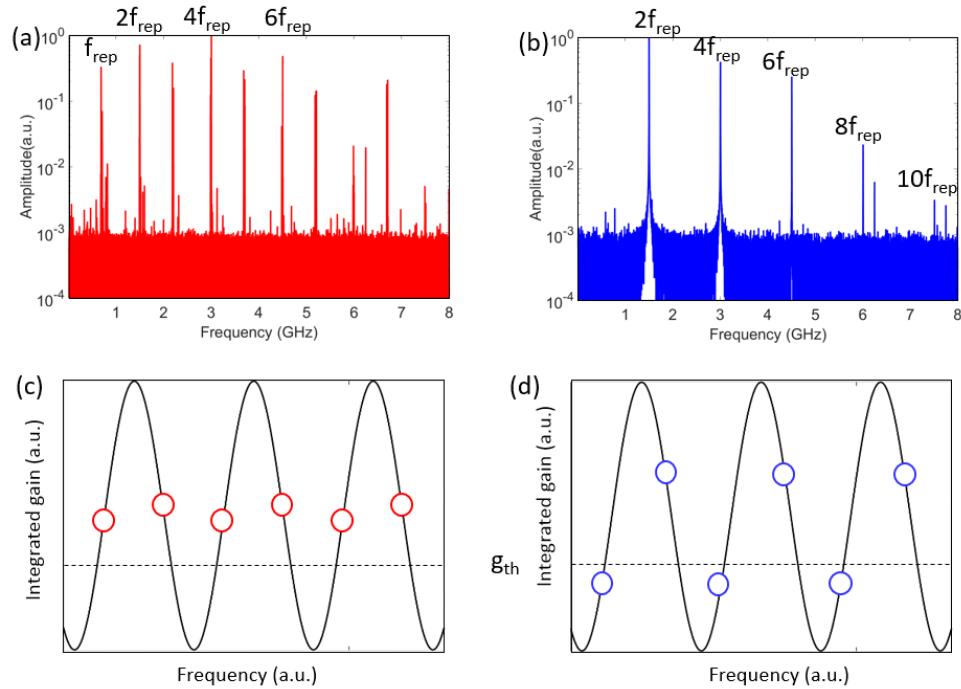


Figure 5.35 Laser RF spectra for $z/L=0.475$ (a) and $z/L=0.490$ (b) in a standing wave cavity with cavity length $L \approx 200$ mm. f_{rep} is the cavity repetition rate. (c) and (d) are the possible integrated gain for longitudinal modes (circles) in (a) and (b) scenarios, where g_{th} is the threshold integrated gain.

Such mode spacing doubling is consistent with the prediction from the integrated gain model in section 2.3.2. When the active region is near the cavity center, there are approximately two modes per fine modulation from the cosine term in Eq. 2.9 in section 2.3.1. Near the design wavelength (twice the periodicity in optical length for the gain structure), one of the longitudinal mode experiences higher gain and the neighboring mode has lower gain and is below threshold—the mode spacing doubles, shown in Fig. 5.35 (d). When z is away from $L/2$, both modes in each modulation experience medium amounts of gain and both could be above threshold, shown in Fig. 5.35 (c). The mode

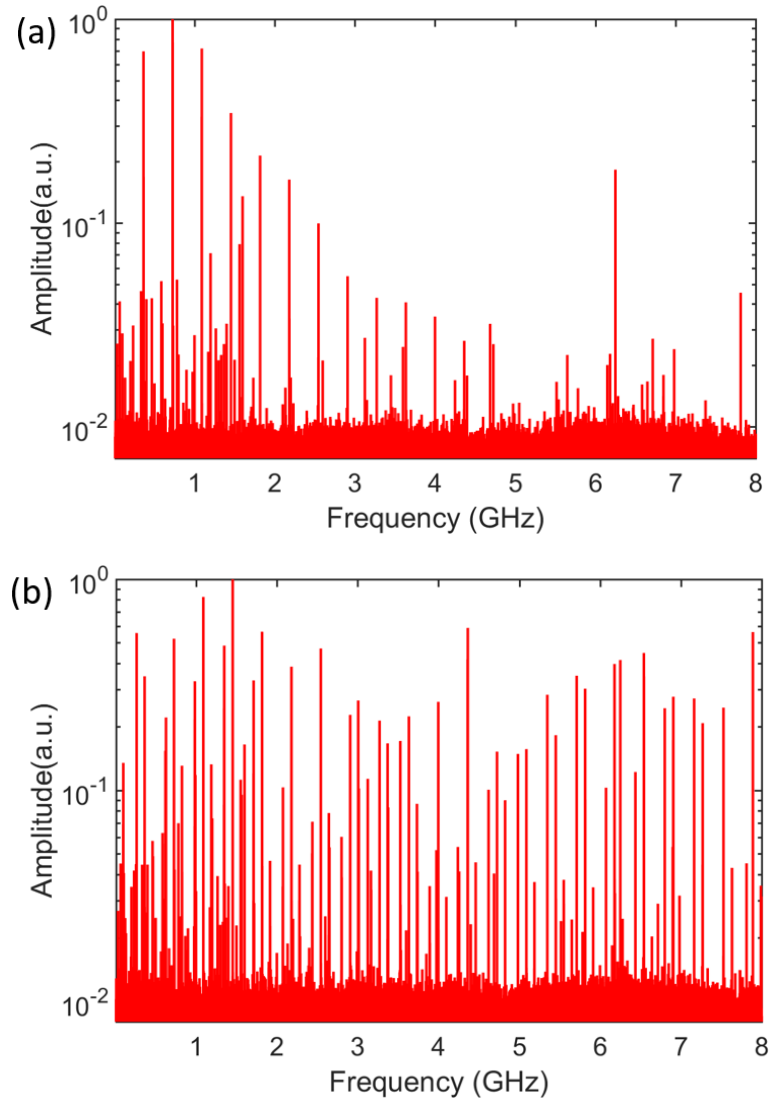


Figure 5.36 Laser RF spectra for the bow-tie ring cavity (a) and (b). From (a) to (b), the mirrors are translated by 5 mm. The longitudinal mode spacing is about 0.36 GHz and the peak at 6.25 GHz is an artifact. There is an extra frequency component 0.1 GHz in (b).

spacing is f_{rep} . The gain difference between the even and odd longitudinal modes implies that the even multiples in the RF spectrum are with higher amplitude.

As mentioned in section 2.3.2, such mode spacing change is caused by varying the gain position (far from cavity global nodes) in the standing wave cavity. In a bow-tie ring cavity shown in Fig. 5.20, by moving both curved mirrors by about 5 mm, the output power doubles and the corresponding RF spectra are presented in Figs. 5.36 (a) and (b). The mode spacing generally stays the same, except an extra 0.1 GHz frequency component in (b), which may be due to higher order transverse modes. The constant mode spacing is also consistent with the integrated gain model. In a ring cavity, there is no restriction on global cavity nodes for the two counter-propagating waves, and all the modes will be aligned for higher integrated gain. Therefore, with the constant cavity length, by moving the active region around, mode spacing does not change.

With the integrated gain model, the TE polarization preference in the TIR based V-shaped DBR-free cavity is mainly due to the phase difference in the TIR. A multilayer reflection calculation is performed with the commercial software RSoft DiffractMOD. Compared with the integrated gain model, this calculation considers the refractive index

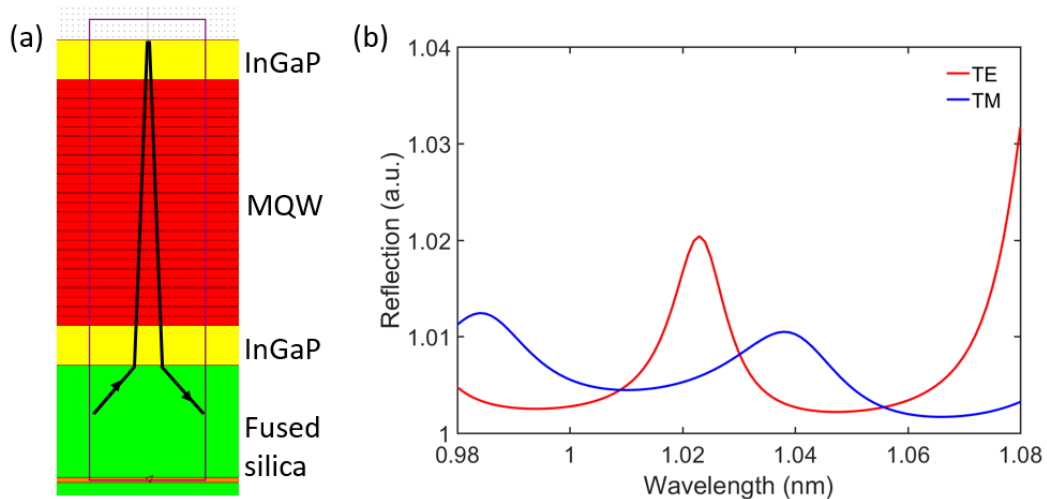


Figure 5.37 Reflection calculation with RSoft DiffractMOD. (a) Schematic of the simulation model. (b) Wavelength dependent reflection for the V-shape cavity for two polarizations. The active region is bonded on a fused silica right-angle prism with a constant gain (or imaginary refractive index $n_i = -0.003$) in the QW layers. The beam is incident from the fused silica prism to semiconductor and total reflected back to prism. No dispersion is considered for all the materials and the refractive indices are: fused silica 1.45, InGaP 3.245, GaAs 3.4833, InGaAs 3.4833-0.003i, air 1.

difference of the gain structure layers. The simulation model schematic is presented in Fig. 5.37 (a). The laser is incident from the fused silica layer (stands for the prism) to the active region at 45° angle of incidence. The active region structure is following the growth sheet. To simplify the simulation, a constant gain is assumed in the QW layers with the imaginary refractive index of $-0.003i$. The wavelength dependent reflection for both polarizations are plotted in Fig. 5.37 (b). With the QW spacing of $0.57 \mu\text{m}$ in optical distance and the tilted incidence, there is a major peak at $1.08 \mu\text{m}$ for TE polarization, and at about $1.10 \mu\text{m}$ for TM polarization. In experiment, these peaks will not lase, due to limited material gain bandwidth. Near the QW gain peak, TE mode experiences higher integrated gain and is preferred, as observed in the experiment. Since material dispersion is not considered here, the reflection dispersion in Fig. 5.37 (b) is as the result of multiple-beam interference.

5.7 PL peak blueshift analysis

In the laser aligning process, an abnormal phenomenon of PL peak blueshift with pump power is observed; on contrary, typical VECSEL usually exhibits redshift [41] for the PL peaks due to the bandgap narrowing in the active region at elevated temperatures, shown in Fig. 5.38. The pump power dependent PL spectra map for a DBR-free active region on diamond is shown in Figure 5.39. The PL spectra are collected in free-space with an Ocean Optics USB4000 spectrometer at an angle of 15° from the semiconductor side of the gain chip. The angle is chosen to circumvent a strong modulation on the PL peak by the diamond window's etalon effect. Fig. 5.40 (a) presents two PL spectra collecting from the diamond and semiconductor sides, which exhibit the modulation by subcavities. For the PL peaks observed from two sides, as shown in Fig. 5.40 (b), they blueshift by the same amount, but have a constant offset.

We attribute most of the PL blueshift to the band filling effect [42] in QWs. By ramping up the pump power, both the carrier density and the PL peak energy, which is roughly the energy difference between the quasi-Fermi levels, increases. For typical VECSELs, such effect has been cancelled out by the temperature induced PL redshift [41]. For DBR-free

geometries, without the integrated semiconductor DBRs, the semiconductor subcavity effect is weaker, thereby the temperature induced subcavity resonance redshift is much smaller. This blueshift phenomenon may also imply less temperature rise, and higher heat extraction efficiency for the gain assembly, but further investigations are needed to test this hypothesis.

To estimate the band filling effect induced PL shift, a calculation is performed. For simplicity, bulk GaAs materials parameters is used for the InGaAs QWs due to the lack of available data. The pump spot size is $d_0=200\ \mu\text{m}$ in diameter, the absorption coefficient for the buffer layers is $\alpha=1\times 10^4\ \text{cm}^{-1}$. Assuming all excited carriers fall into the QWs instantaneously and are with lifetime $\tau=1\ \text{ns}$, the carrier rate equation can be written as

$$\frac{dn}{dt} = \frac{\alpha P}{h\nu(\pi d_0^2/4)} - \frac{n}{\tau} \quad (5.4)$$

At the equilibrium state ($dn/dt=0$), the carrier density can be estimated. With the low carrier density, the bandgap renormalization effect is not considered. Considering constant active region temperature, quasi-Fermi levels can be calculated [43]. Therefore, the PL peak shift can be calculated, as shown in Fig. 5.41. The calculated blueshift at 300 K is close to the experimental results at low pump powers. At higher pump power, the active region temperature rises, and the blueshift amount decreases. Additionally, the carrier lifetime

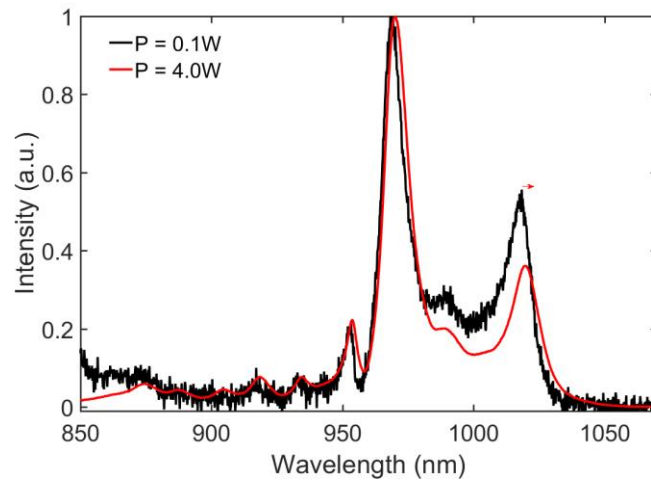


Figure 5.38 PL spectra for a VECSEL chip at two pump powers. Two main peaks at near 970 nm and 1018 nm redshifts by 2 nm and the peak near 954 nm redshifts by 1 nm. The chip is mounted on a water-impingement geometry cooled to 15°C. The spectra are collected at an angle of 30°.

also decreases since Auger recombination will become dominant. The combination of these effects may explain the flatness of blueshift curve at high pump powers.

In the literature [44], similar PL peak blueshift phenomenon was observed with pulsed pumping, where the thermal effect can be neglected. Further evidence, such as direct measurements of gain structure thermal resistance or active region temperature, are needed to support this hypothesis.

Additionally, the thermal expansion induced strain may also shift the PL peak [191, 192] to shorter wavelengths. After bonding, the active region is nearly stress-free. Due to the thermal expansion rates difference between the active region ($5.8 \times 10^{-6} \text{ K}^{-1}$ for GaAs at 20°C) and diamond substrate ($1 \times 10^{-6} \text{ K}^{-1}$), the active region will be compressed at elevated temperatures from the bonding condition. Similar phenomenon has been observed with $2 \mu\text{m}$ thick GaAs/AlGaAs MQW structures bonded on Si [47], which has a thermal expansion rate of $2.6 \times 10^{-6} \text{ K}^{-1}$. Assuming 100°C temperature rise after pumping, the mechanical strain will shift the PL peak by about 3 nm, which is much smaller than the 13 nm blueshift observed in experiments. Therefore, thermal induced strain may contribute to the blueshift but only plays a minor role. With a GaAs DHS sample bonded onto a diamond heatspreader, the similar PL blueshift phenomenon is also observed, as shown in the PL map Fig. 5.42.

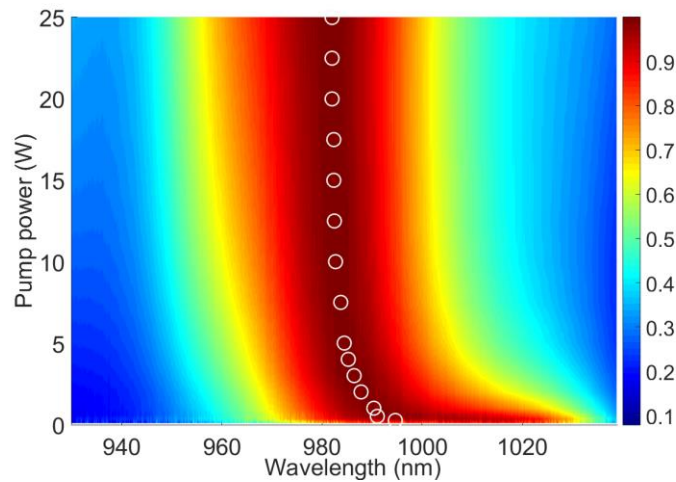


Figure 5.39 Normalized PL spectra map as a function of incident pump power for a 1315-059 MQW sample bonded on diamond. White circles represent the PL peak wavelength. The spectra are collected from the diamond side.

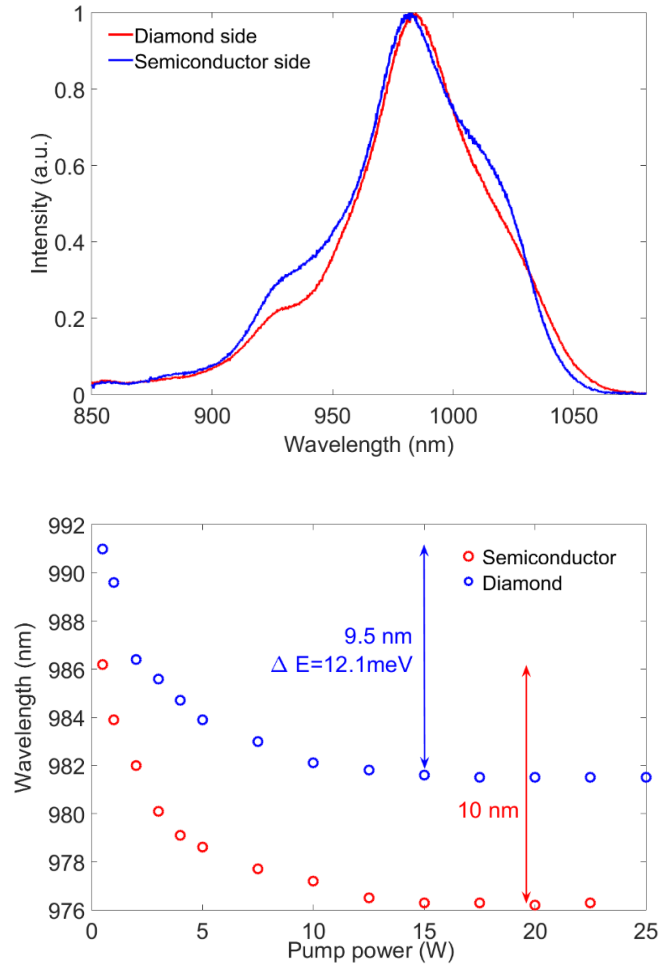


Figure 5.40 (a) PL spectra collecting from the semiconductor and diamond sides. (b) PL peak shift with incident pump power with PL collected from two sides of the diamond-gain assembly.

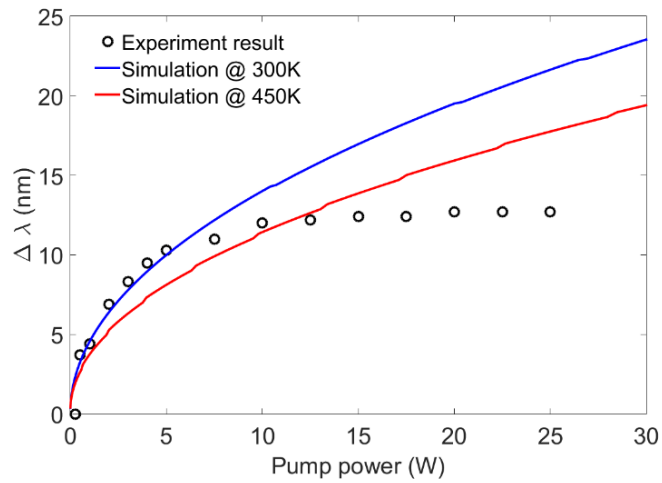


Figure 5.41 Peak PL wavelength versus incident CW pump power.

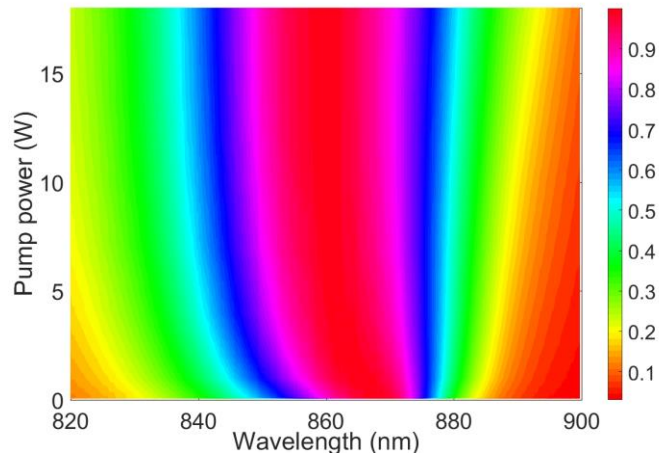


Figure 5.42 Normalized PL spectral map as a function of incident pump power for a DHS sample bonded on diamond.

5.8 Summary

With the lift-off and van der Waals bonding technique, we demonstrated a DHS based DBR-free transmission geometry as a proof-of-concept. Employing sapphire or diamond windows as heatspreaders, two high power CW DBR-free SDLs are reported at 1040 nm and 1160 nm. With an active region designed at 1040 nm, more than 6 W output power is collected without thermal rollover; about 2.5 W output power for a MQW designed at 1160 nm. Compared with typical VECSELs, the slope efficiency of DBR-free SDLs is relatively low and the culprits are under investigation. One of the possible losses is the Fresnel reflection on the air-diamond interface. AR coating has been applied to the air-diamond interface, but no obvious improvement in laser slope efficiency is observed so far. Study on Brewster's angle geometry is ongoing.

At the two wavelengths, much broader tunability is observed with the DBR-free transmission geometry, which is consistent with the prediction from the position dependent integrated gain model in section 2.3. The longitudinal mode spacing predicted by this model has been verified by experiments.

We end the chapter with the PL peak blueshift phenomena of both QW and DHS samples bonded on diamonds, which have been explained with the band filling effect. The

thermal induced strain may also contribute but fairly limited.

5.9 References

- [1] R. N. Hall, G. E. Fenner, J. D. Kingsley, T. J. Soltys, and R. O. Carlson, "Coherent light emission from GaAs junctions," *Phys. Rev. Lett.*, vol. 9, no. 9, pp. 366-369, 1962.
- [2] H. Kroemer, "A proposed class of hetero-junction injection lasers," *Proc. IEEE*, vol. 51, no. 12, pp. 1782-1783, 1963.
- [3] R. Roff, V. Negoita, H. An, T. Vethake, S. Heinemann, G. Treusch, and T. Gottwald, "Laser diodes: high-power laser diode modules pump disk lasers," *Laser Focus World*, 2013.
- [4] B. Heinen, T.-L. Wang, M. Sparenberg, A. Weber, B. Kunert, J. Hader, S. W. Koch, J. V. Moloney, M. Koch, and W. Stolz, "106 W continuous-wave output power from vertical-external-cavity surface-emitting lasers," *Electron. Lett.*, vol. 48, no. 9, pp. 516-517, 2012.
- [5] L. A. Coldren and S. W. Corzine, "Gain and current relations," in *Diode Lasers and Photonic Integrated Circuits*, New York, Wiley, 1995, pp. 167.
- [6] A. Garnache, A. A. Kachanov, F. Stoeckel, and R. Planel, "High-sensitivity intracavity laser absorption spectroscopy with vertical-external-cavity surface-emitting semiconductor lasers," *Opt. Lett.*, vol. 24, no. 12, pp. 826-828, 1999.
- [7] A. R. Albrecht, D. V. Seletskiy, J. G. Cederberg, A. Di Lieto, M. Tonelli, J. V. Moloney, G. Balakrishnan, and M. Sheik-Bahae, "Intracavity laser cooling using a VECSEL," *Proc. SPIE*, 8275, 827505, San Francisco, CA, USA, 2012.
- [8] A. Hein, S. Menzel, A. Ziegler, R. Rosch, and P. Unger, "Frequency doubled high-power semiconductor disk lasers for stereo projection and ion traps," *Proc. SPIE*, 8847, 88470J, San Diego, CA, USA, 2013.
- [9] M. Scheller, J. M. Yarborough, J. V. Moloney, M. Fallahi, M. Koch, and S. W. Koch, "Room temperature continuous wave milliwatt terahertz source," *Opt. Express*, vol. 18, no. 26, pp. 27112-27117, 2010.
- [10] M. E. Barnes, Z. Mihoubi, K. G. Wilcox, A. H. Quarterman, I. Farrer, D. A. Ritchie, A. Garnache, S. Hoogland, V. Apostolopoulos, and A. C. Tropper, "Gain bandwidth characterization of surface-emitting quantum well laser gain structures for femtosecond operation," *Opt. Express*, vol. 18, no. 20, pp. 21330-21341, 2010.
- [11] M. Mangold, V. J. Wittwer, O. D. Sieber, M. Hoffmann, I. L. Krestnikov, D. A. Livshits, M. Golling, T. Südmeier, and U. Keller, "VECSEL gain characterization," *Opt. Express*, vol. 20, no. 4, pp. 4136-4148, 2012.

- [12] L. E. Eng, D. G. Mehuys, M. Mittelstein, and A. Yariv, "Broadband tuning (170 nm) of InGaAs quantum well lasers," *Electron. Lett.*, vol. 26, no. 20, pp. 1675-1677, 1990.
- [13] C. Borgentun, J. Bengtsson, A. Larsson, F. Demaria, A. Hein, and P. Unger, "Optimization of a broadband gain element for a widely tunable high-power semiconductor disk laser," *IEEE Photon. Technol. Lett.*, vol. 22, no. 13, pp. 978-980, 2010.
- [14] M. Butkus, J. Rautiainen, O. G. Okhotnikov, C. J. Hamilton, G. P. A. Malcolm, S. S. Mikhlin, I. L. Krestnikov, D. A. Livshits, and E. U. Rafailov, "Quantum dot based semiconductor disk lasers for 1–1.3 μm ," *IEEE J. Sel. Top. Quantum Electron.*, vol. 17, no. 6, pp. 1763-1771, 2011.
- [15] L. Fan, M. Fallahi, A. R. Zakharian, J. Hader, J. V. Moloney, R. Bedford, J. T. Murray, W. Stolz, and S. W. Koch, "Extended tunability in a two-chip VECSEL," *IEEE Photon. Technol. Lett.*, vol. 19, no. 8, pp. 544-546, 2007.
- [16] L. A. Coldren and S. W. Corzine, "Appendice 7 Periodic structures and the transmission matrix," in *Diode Lasers and Photonic Integrated Circuits*, New York, Wiley, 1995, pp. 475-477.
- [17] C. Wang, K. Malloy, and M. Sheik-Bahae, "Influence of coulomb screening," *Opt. Express*, vol. 23, no. 25, pp. 32548-32554, 2015.
- [18] R. G. Bedford, M. Kolesik, J. L. A. Chilla, M. K. Reed, T. R. Nelson, and J. V. Moloney, "Power-limiting mechanisms in VECSELs," *Proc. SPIE*, 5814, 199-208, Bellingham, WA, USA, 2005.
- [19] F. van Loon, A. J. Kemp, A. J. Maclean, S. Calvez, J.-M. Hopkins, J. E. Hastie, M. D. Dawson and D. Burns, "Intracavity diamond heatspreaders in lasers," *Opt. Express*, vol. 14, no. 20, pp. 9250-9260, 2006.
- [20] H. Kahle, C. M. N. Mateo, U. Brauch, R. Bek, T. Schwarzback, M. Jetter, T. Graf, and P. Michler, "Gain chip design, power scaling and intra cavity frequency doubling with LBO of optically pumped red-emitting AlGaInP-VECSELs," *Proc. SPIE*, 9734, 97340T, San Francisco, CA, USA, 2016.
- [21] H. Kahle, "Private communication," Feb, 2016.
- [22] R. Foy and A. Labeyrie, "Feasibility of adaptive telescope with laser probe," *Astron. Astrophys.*, vol. 152, pp. L29-L31, 1985.
- [23] S. Hackett, A. R. Albrecht, Z. Yang, J. G. Cederberg, and M. Sheik-Bahae, "Vertical external cavity surface emitting lasers for sodium guidestar applications and improvement of current guidestar systems," *Proc. SPIE*, 9734, 97340Y, San Francisco, CA, USA, 2016.
- [24] C. d'Orgeville, and G. J. Fetzer, "From dye laser factory to portable semiconductor laser: four generations of sodium guide star lasers for adaptive optics in astronomy

- and space situational awareness," in *Advanced Maui Optical and Space Surveillance Technologies Conference*, Maui, HI, USA, 2015.
- [25] S. Hackett, A. R. Albrecht, Z. Yang, J. G. Cederberg, M. Sheik-Bahae, J. T. McGraw, R. L. Johnson, and J. W. Richey, "Development of vertical external cavity surface emitting lasers (VECSELs) for use as monochromatic and polychromatic sodium guidestars," in *SPIE Astronomical Telescopes and Instrumentation*, Edinburgh, UK, 2016.
- [26] Y. Feng, L. R. Taylor, and D. B. Calia, "25 W Raman-fiber-amplifier-based 589 nm laser for laser guide star," *Opt. Express*, vol. 17, no. 21, pp. 19021-19026, 2009.
- [27] S. C. Burd, T. Leinonen, J. P. Penttinen, D. T. C. Allcock, D. H. Slichter, R. Srinivas, A. C. Wilson, M. Guina, D. Leibfried, D. J. Wineland, "Single-frequency 571 nm VECSEL for photo-ionization of magnesium," *Proc. SPIE*, 9734, 973411, San Francisco, CA, USA, 2016.
- [28] S. Ranta, M. Tavast, T. Leinonen, R. Epstein, and M. Guina, "Narrow linewidth 1118/559 nm VECSEL based on strain compensated GaInAs/GaAs quantum-wells for laser cooling of Mg-ions," *Opt. Mat. Express*, vol. 2, no. 8, pp. 1011-1019, 2012.
- [29] E. Betzig, G. H. Patterson, R. Sougrat, O. Wolf Lindwasser, S. Olenych, J. S. Bonifacino, M. W. Davidson, J. Lippincott-Schwartz, and H. F. Hess, "Imaging intracellular fluorescent proteins at nanometer resolution," *Science*, vol. 313, no. 5793, pp. 1641-1645, 2006.
- [30] C. F. Blodi, S. R. Russell, J. S. Pulido, and J. C. Folk, "Direct and feeder vessel photocoagulation of retinal angiomas with dye yellow laser," *Ophthalmology*, vol. 97, no. 6, pp. 791-797, 1990.
- [31] E. L. Tanzi, J. R. Lupton, and T. S. Alster, "Lasers in dermatology: four decades of progress," *J. Am. Acad. Dermatol.*, vol. 49, no. 1, pp. 1-34, 2003.
- [32] E. Kantola, T. Leinonen, S. Ranta, M. Tavast, J.-P. Penttinen, and M. Guina, "1180 nm VECSEL with 50 W output power," *Proc. SPIE*, 9349, 93490U, San Francisco, CA USA, 2015.
- [33] E. Kantola, T. Leinonen, S. Ranta, M. Tavast, and M. Guina, "High-efficiency 20 W yellow VECSEL," *Opt. Express*, vol. 22, no. 6, pp. 6372-6380, 2014.
- [34] S. Sato and S. Satoh, "Room-temperature continuous-wave operation of 1.24 μm GaInNAs lasers grown by metal-organic chemical vapor deposition," *IEEE J. Sel. Top. Quantum Electron.*, vol. 5, no. 3, pp. 707-710, 1999.
- [35] J. G. Cederberg, D. L. Alliman, G. M. Peake, A. R. Albrecht, S. Hackett, Z. Yang, and M. Sheik-Bahae, "Development of strain-compensated InGaAs/GaAsP QW for optically pumped vertical external cavity surface emitting lasers at 1180 nm," in *20th*

American Conference on Crystal Growth and Epitaxy (ACCGE-20), Big Sky, MT, USA, 2015.

- [36] N. Tansu, and L. J. Mawst, "High-performance strain-compensated InGaAs-GaAsP-GaAs ($\lambda=1.17 \mu\text{m}$) quantum-well diode lasers," *IEEE Photon. Technol. Lett.*, vol. 13, no. 3, pp. 179-181, 2001.
- [37] Z. Yang, A. R. Albrecht, J. G. Cederberg, and M. Sheik-Bahae, "DBR-free optically pumped semiconductor disk lasers," *Proc. SPIE*, 9349, 934905, San Francisco, CA, USA, 2015.
- [38] G. E. Stedman, "Ring-laser tests of fundamental physics and geophysics," *Rep. Prog. Phys.*, vol. 60, pp. 615-688, 1997.
- [39] A. Mignot, G. Feugnet, S. Schwartz, I. Sagnes, A. Garnache, C. Fabre, and J.-P. Pocholle, "Single-frequency external-cavity semiconductor ring-laser gyroscope," *Opt. Lett.*, vol. 34, no. 1, pp. 97-99, 2009.
- [40] T. J. Ochalski, A. de Burca, G. Huyet, J. Lyytikainen, M. Guina, M. Pessa, A. Jasik, J. Muszalski, and M. Bugajski, "Passively modelocked bi-directional vertical external ring cavity surface emitting laser," in *CLEO/QELS*, San Jose, CA, USA, 2008.
- [41] A. Wójcik-Jedlińska, J. Muszalski, and M. Bugajski, "Photoluminescence studies of optical properties of VECSEL active region under high excitation conditions," *J. Phys: Conf. Ser.*, vol. 146, p. 012031, 2009.
- [42] M. Sheik-Bahae, "Effect of background absorption on EQE measurements using fraction heating," Private communication, 2008.
- [43] P. K. Baau, *Theory of Optical Processes in Semiconductors: Bulk and Microstructures*, New York: Oxford University Press, 1997.
- [44] M. Y. A. Raja, S. R. J. Brueck, M. Osinski, C. F. Schaus, J. G. McInerney, T. M. Brennan, and B. E. Hammons, "Resonant periodic gain surface-emitting semiconductor lasers," *IEEE J. Quantum Electron.*, vol. 25, no. 6, pp. 1500-1512, 1989.
- [45] N. Channrasekaran, T. Soga, and T. Jimbo, "GaAs film on Si substrate transplanted from GaAs/Ge structure by direct bonding," *Appl. Phys. Lett.*, vol. 82, no. 22, pp. 3892-3894, 2003.
- [46] C. M. N. Mateo, J. J. Ibanez, J. G. Fernando, J. C. Garcia, K. Omambac, R. B. Jaculbia, M. Defensor, and A. A. Salvador, "Transitions of epitaxially lifted-off bulk GaAs and GaAs/AlGaAs quantum well under thermal-induced compressive and tensile strain," *J. Appl. Phys.*, vol. 104, no. 10, pp. 103537, 2008.
- [47] D. Cengher, Z. Hatzopoulos, S. Gallis, G. Deligeorgis, E. Aperathitis, M. Androulidaki, M. Alexe, V. Dragoi, E.D. Kyriakis-Bitzaros, G. Halkias, and A. Georgakilas, "Fabrication of GaAs laser diodes on Si using low-temperature bonding

of MBE-grown GaAs wafers with Si wafers," *J. Crys. Growth*, vol. 251, no. 1-4, pp. 754-759, 2003.

Chapter 6

Summary and Outlook

6.1 Summary

SDLs are highly attractive laser sources with good beam quality, intracavity access, wavelength flexibility, and high output power. In a typical SDL, a semiconductor DBR is integrated behind the active region, which restricts the laser design and performance in many aspects, including material system choices, thermal management, and gain bandwidth. By discarding semiconductor DBRs, based on either transmission or TIR, DBR-free SDL geometries are free from these restrictions, opening up new possibilities.

We are the first group to successfully apply the lift-off and van der Waals bonding technique to DBR-free SDL fabrication. With this approach, we have demonstrated DBR-free SDLs in TIR geometries, monolithic standing-wave geometries, and transmission geometries in both standing-wave and ring cavities. We have also proposed the evanescent-wave coupled geometry for high power operation at MIR wavelengths, the monolithic ring cavity geometry, Brewster's angle geometry, and the double-heatspreader geometry for power scaling. In particular, with the transmission geometry, more than 2 W output power is accomplished at 1160 nm, and 6 W collected at 1040 nm, and both were limited by the available pump power. Furthermore, significantly broader tuning ranges have been observed at both wavelengths in the transmission geometry. A simple position dependent integrated gain model has been developed and successfully explained the origin of broad gain bandwidth. Predictions on longitudinal mode spacing have been confirmed with experimental results. Additionally, our numerical thermal analysis shows the thermal management advantages for the double-diamond DBR-free geometry.

In the future, a few directions can be pursued. First, as mentioned in chapter 3, the device fabrication process can be further optimized, especially the wet etching process and

annealing conditions. The former may improve the device quality, and the latter may facilitate improved thermal management. Second, further investigation is needed to explain and improve the low slope efficiency for transmission geometry DBR-free SDLs. Third, despite the double-diamond geometry outperforming the typical VECSEL geometry in thermal management, perfect power scaling is still out of reach. Multi-chip, multi-heatspreader, or even slab geometries as will be discussed in section 6.2, which could be potential options for higher power SDLs. By reducing the quantum defect, in-well-pumped DBR-free geometries may be candidates for high power SDLs, utilizing multi-pass pumping scheme. Fourth, with broad gain and geometric flexibility, DBR-free SDLs could be mode locked with SESAMs, TDMs, or Kerr-lens effect. Last but not least, high reflectivity SWG could be an alternative for semiconductor DBRs. Other functionalities of SWG, such as enhanced pump absorption and reflection wave front control, may improve the SDLs' performance further, as will be discussed in section 6.4.

6.2 Other approaches for power scaling

As discussed in previous chapters, due to the high thermal resistance of semiconductor DBRs [1], the output power of VECSELs cannot scale with the cavity mode area infinitely; the transmission geometry DBR-free SDLs, even with two heatspreaders, also rely on three-dimensional heat flow, not allowing perfect power scaling either. Additionally, large pump spots create more optical losses, such as scattering and lateral ASE losses. Therefore, there is a limited output power for a single gain chip. Other power scaling approaches are needed for kilowatt-level SDLs.

As mentioned in chapter 2, with the barrier pumping scheme, a significant amount of heat is generated in the active regions mainly due to the large quantum defect, which can be greatly reduced via in-well pumping [2] at longer wavelengths. However, in contrast to the barrier-pumping scheme, the pump laser is only absorbed in QW layers. To make efficient use of the pump power, either more QWs are needed or a multi-pass scheme for the pump laser. Multi-pass schemes are widely used in solid state disk lasers, and are viable for DBR-free transmission geometries.

To efficiently extract heat from the active regions, inspired by the double-diamond geometry, multiple heatspreaders can be employed. With consistent bonding quality, an assembly as shown in Fig. 6.1 could be fabricated. Due to its thickness, the assembly has to be end-pumped. Limited by the thicknesses of the heatspreaders and the Rayleigh range of the pump laser, an estimated 10 heatspreaders could be used with InGaAs/GaAs QWs at 1 μm . For typical barrier-pumped active regions, there could be 1 to 2 QWs per heatspreaders. For in-well-pumped active regions, more QWs could be integrated to avoid multi-pass pumping.

Another possibility is to daisy-chain multiple active regions in a cavity. Such multi-gain-element cavity was proposed by M. Kuznetsov et al. [3] in 1999, as shown in Fig. 6.2.

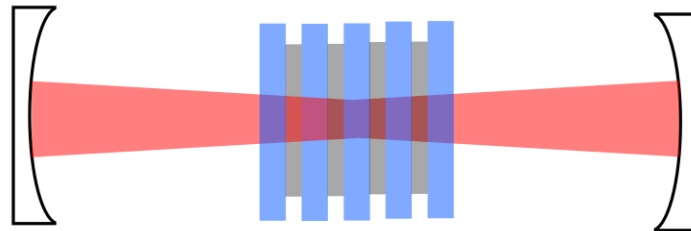


Figure 6.1 Schematic for a multi-heatspreader transmission geometry DBR-free SDL.

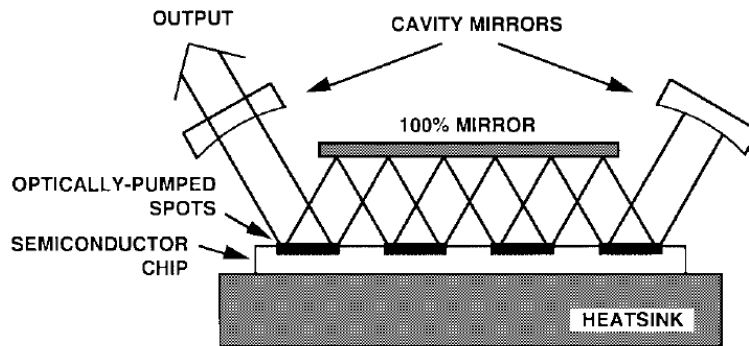


Figure 6.2 Multiple-gain-element multibounce cavity for power scaling for typical VECSEL [3].

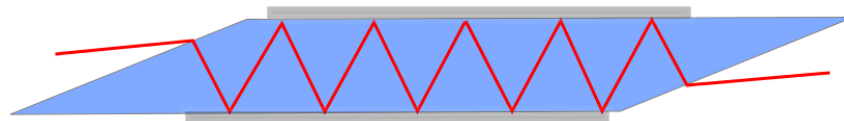


Figure 6.3 Slab geometry SDL. The laser is incident at Brewster's angle on the air-slab interfaces. The laser is total-internal-reflected at the semiconductor-air interface.

Similarly, two-chip VECSELS in the W-shaped cavity configuration have been demonstrated with multi-watt output power near 1 μm in 2006 [4, 5]. By reducing the thermal load in individual gain chips, the thermal rollover problem has been alleviated. Even a three-chip cavity is reported with more than 50 W output power at 532 nm [6] via intracavity second harmonic generation. Rather than multiple VECSEL chips, a large size active region can be bonded onto a slab heatspreader, and a multi-bounce configuration can be formed via TIR at the semiconductor-air interface, as shown in Fig. 6.3. To suppress lateral lasing, ion implantation or edge-mirror elimination could be adopted to introduce losses for lateral cavities. Compared with the cavity design in Fig. 6.2, the slab cavity design is much easier to in both fabrication and alignment.

6.3 Mode-locking

With broad gain bandwidth, SDLs have been mode-locked for ultrashort pulse generation. In particular, with the exceptionally broad gain bandwidth and interesting mode structures detailed in section 2.3, DBR-free SDLs may be superior for mode-locking. Firstly, we will search for a reliable mode-locking scheme with the typical VECSEL geometry and apply it to DBR-free geometries. The SESAM mode-locking scheme has been employed in a Z-shaped cavity, which is schematically shown in Fig. 6.4. With the ABCD matrix method, the cavity mode size at the active region is calculated to be about 100 μm in radius, and 40 μm in radius at the SESAM. With our current SESAMs, long-term stable pulsing behavior has been observed, shown in Fig. 6.5 (a) with a high speed InGaAs detector (with

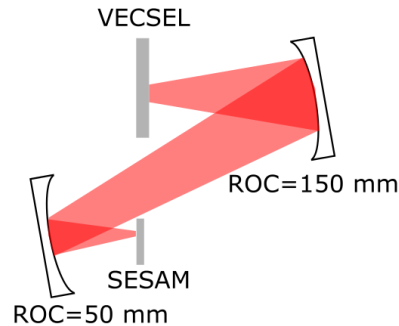


Figure 6.4 Z-cavity geometry. The distance between the VECSEL chip and the first curved mirror is about 100 mm, 140 mm between the two curved mirrors, and 30 mm between the second curved mirror and SESAM.

more than 15 GHz bandwidth). In Fig. 6.5 (b), the RF spectrum, Fourier transformed from the time trace, has a nonconstant envelope, which implies unstable mode-locking. Fig. 6.5 (c) is the linear autocorrelation result. As shown in the nonlinear autocorrelation result with a KTP crystal in Fig. 6.5 (d), there is a broad pedestal in addition to the main peak of 1.6 ps in FWHM. According to reference [7], this signature implies that certain modes are phase locked forming clusters, while the phases between clusters are not fully locked.

Since the discovery of graphene, TDMs have attracted a lot of attention as broadband saturable absorbers for mode-locking fiber lasers [8] and other solid state lasers [9]. Currently, studies on TDM-mode-locked VECSELs are concentrated on graphene [10, 11] and, to the best of our knowledge, there have been no reports of VECSELs mode locked with other TDMs. Few-layer WS_2 flakes were deposited on a GaAs/AlAs DBR by Dr. Bryan Kaehr at Sandia National Laboratories. With the Z-shaped cavity configuration, a pulsing operation is achieved with a VECSEL chip at 1030 nm. As shown in Figs. 6.6 (a) and (b), the pulse train is unstable in both short and long term, and the RF spectrum in

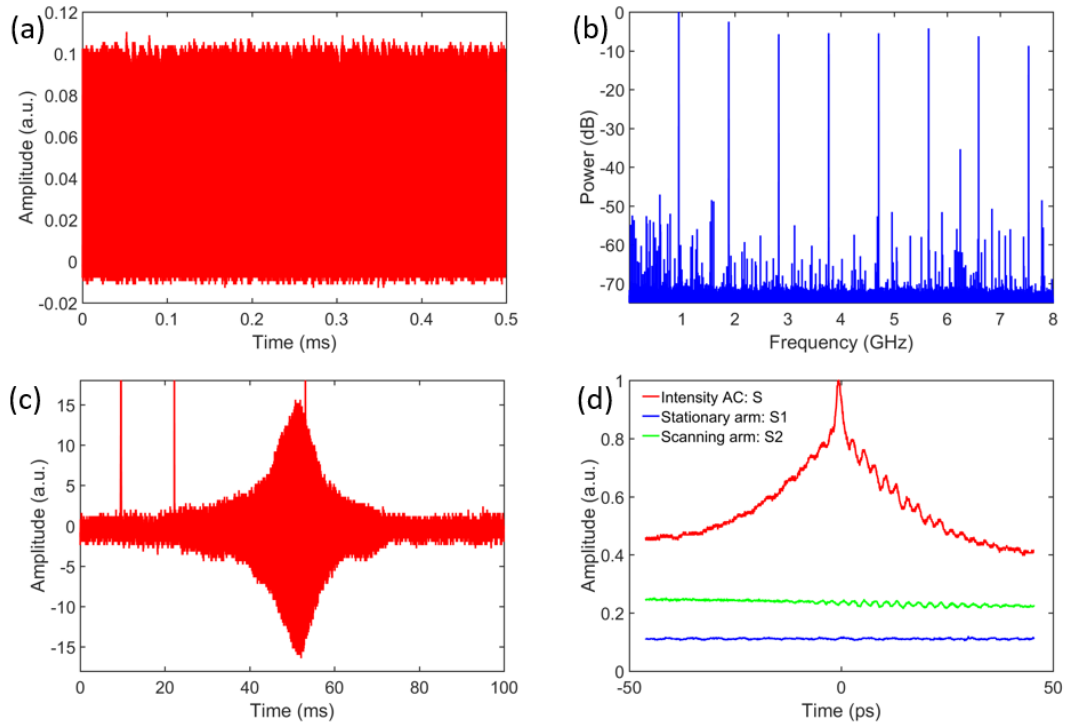


Figure 6.5 Preliminary SESAM modelocking results (a) Time trace; (b) RF spectrum; (c) Linear autocorrelation trace; (d) Nonlinear autocorrelation trace with a KTP crystal.

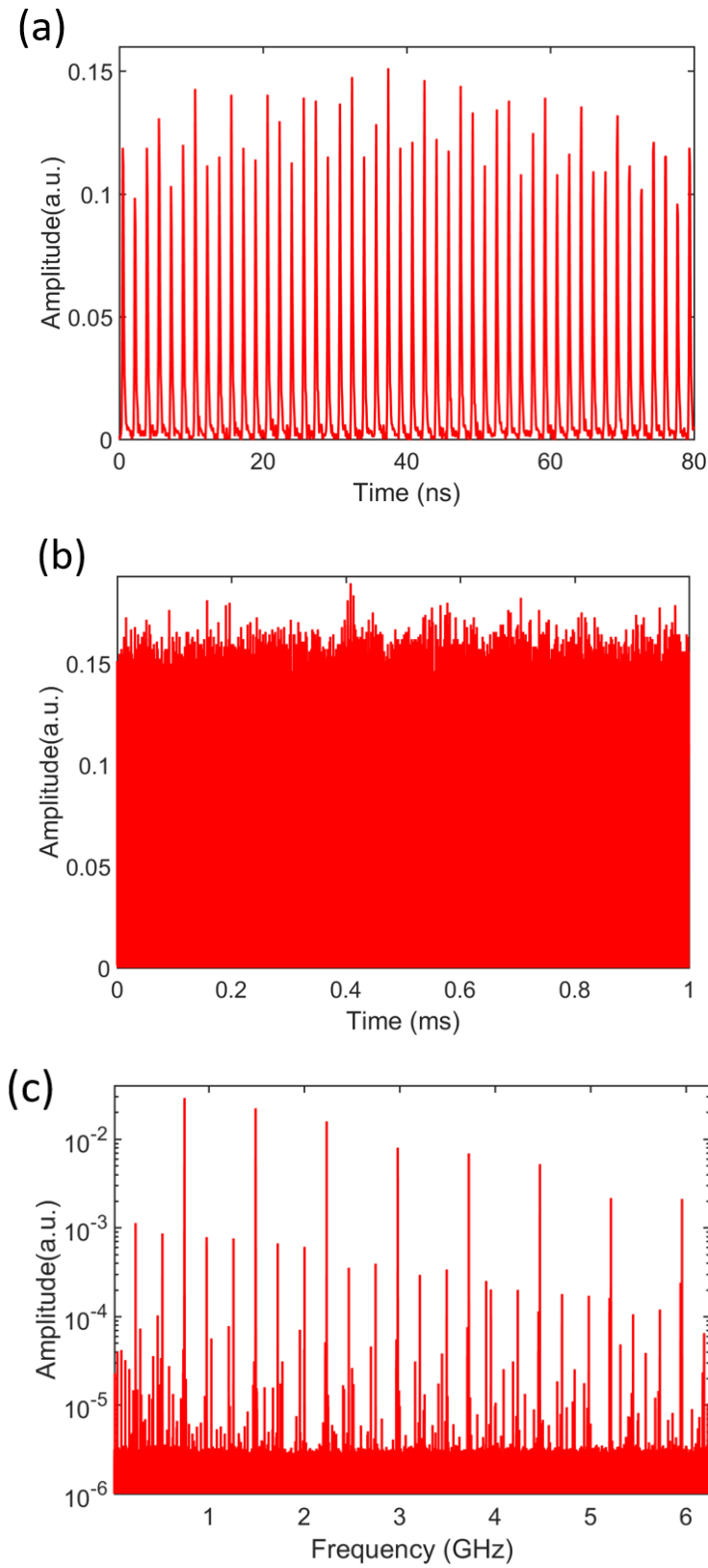


Figure 6.6 Pulsing results with WS_2 flakes coated onto GaAs/AlAs DBR mirror (a) Short-term behavior; (b) Long-term behavior; (c) RF spectrum of the long-term time trace.

Fig. 6.6 (c) confirms this. This may be due to the thick WS_2 film or potential oxidation. Further optimization of WS_2 thickness and cavity dispersion management are needed. Recently, similar few-layer black phosphorus has been shown to exhibit recovery times as short as 24 fs [12], much shorter than those of graphene (0.15-1.27 ps), which makes it appealing for future research.

As mentioned in chapter 1, Kerr lensing in the active region can mode lock SDLs and could potentially achieve higher peak power. With DBR-free geometries, the broader gain bandwidth could facilitate the ultrashort pulse generation. Particularly with the Brewster's angle geometry, by eliminating the semiconductor subcavity effect, it is easier for intracavity dispersion management (minimizing the group-delay dispersion).

6.4 High reflectivity subwavelength grating

Since semiconductor DBRs suffer from high thermal resistance, there are endeavors to replace semiconductor DBRs with other high reflectivity mirrors, such as compound mirrors, including metal-semiconductor [13, 14] and even semiconductor-dielectric-metal [15] mirrors. So far, the maximum output power for compound mirror based VECSELs is on the order of a few watts. Another alternative to semiconductor DBRs is the so called SWG, which has been fabricated and demonstrated with more than 99% reflectivity at 1064 nm [16, 17].

6.4.1 Introduction to subwavelength grating

Whereas grating reflection anomalies, including minima, maxima, or strong modulations in reflection spectra, were first investigated more than a century ago [18], SWGs attracted attention again after the advancement in e-beam patterning and photolithography. In 1998, SWGs were fabricated on InP and GaAs substrates and reported with more than 85% reflectivity at 1550 nm [19]. In 2007, Chang-Hasnain's group at UC Berkeley replaced a partial semiconductor DBR in a VCSEL with a single layer Si grating structure (also called a high contrast grating), and achieved lasing [20]. Bunkowski et al. proposed thin SWG

structures as low thermal noise alternatives to conventional mirror coatings for gravitational wave detectors [21] and Schnabel’s group reported more than 99% reflectivity at 1064 nm with SWGs [16, 17]. In addition to high reflectivity, other optical functionalities have also been developed for SWGs. In 2010, Hewlett-Packard Laboratories manipulated the reflection wave front by varying the grating parameters spatially, showing 20 mm focal length with about 90% reflectivity with non-periodic gratings [22]. Furthermore, in [23], with a graphene monolayer inserted under a SWG, more than 17 times absorption enhancement has been demonstrated, by utilizing the strong field confinement under grating structures.

The gratings’ anomalous reflection behavior can be categorized by two types [24]: one is the Wood-Rayleigh anomaly, which is related to the onset or disappearance of certain spectral orders; the other is a resonance type, where the grating diffractions are phase-matched to the transverse modes of the grating. Here we are concentrating on the second type, which is also called guide mode resonance.

RCWA method has been widely used in SWG design [25] and we utilize the commercial software RSoft DiffractMOD based on the RCWA method for numerical calculations, including the reflectivity and field distribution calculations. RCWA method represents the periodic permittivity function with Fourier harmonics and electromagnetic fields as a sum of coupled waves, allowing to solve the full vectorial Maxwell’s equations in the Fourier domain. It is good for designing subwavelength grating structures [25], and other grating-

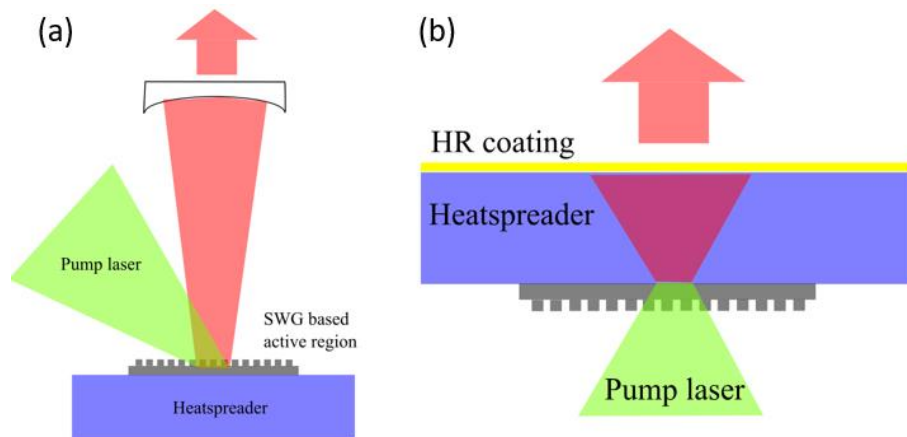


Figure 6.7 Schematics for SWG based SDL (a) and microchip SDL (b).

assisted devices. As a sanity check, following the SWG structure and parameters, our simulation results agree well with Fig. 2 in reference [26].

6.4.2 Guided mode resonance

There are many models explaining the near-unity reflection obtained with SWGs. Here we adopt the ray picture model [27] and focus on a simple scenario as shown in Fig. 6.8 (a). The light is incident from air to the subwavelength grating structure at normal incidence. As a result, diffraction occurs and the 0th order diffraction is transmitted through the grating layer. With the grating periodicity less than the wavelength, higher diffraction orders are not supported in air but may be inside the GaAs structure. By carefully engineering the grating parameters, the diffraction will be total internal reflected at the GaAs/diamond interface and guided by the slab waveguide structure. The guided mode can only be coupled out via diffraction at the grating structure, parallel to the 0th order diffraction. With certain waveguide parameters, the two diffractions destructively interfere and high reflectivity is obtained.

An analytical discussion of similar weakly modulated grating structures is presented in [25]. However, with the large modulation amplitude in dielectric constant, numerical methods are needed for the grating design. Before the numerical calculation, based on these mechanisms, the parameter space can be narrowed down. For the first order diffraction (diffraction order index $m=1$),

$$n_2 \sin \theta_2 - n_1 \sin \theta_{inc} = m \frac{\lambda_0}{p} \quad (6.1)$$

Here n_1 and n_2 are the refractive indices of air and GaAs, θ_{inc} and θ_2 are the angles of incidence and diffraction, λ_0 is the wavelength, and p is the grating periodicity. For the guided mode, it is supported in the GaAs waveguide and total internal reflected at the GaAs/diamond interface, as a result,

$$n_2 \geq n_2 \sin \theta_2 \geq \max(n_1, n_3) \quad (6.2)$$

Here n_3 is the refractive index of the substrate, diamond. At normal incidence, for the GaAs SWG on diamond, the conditions are

$$3.5 \geq \frac{\lambda_0}{p} \geq 2.4 \quad (6.3)$$

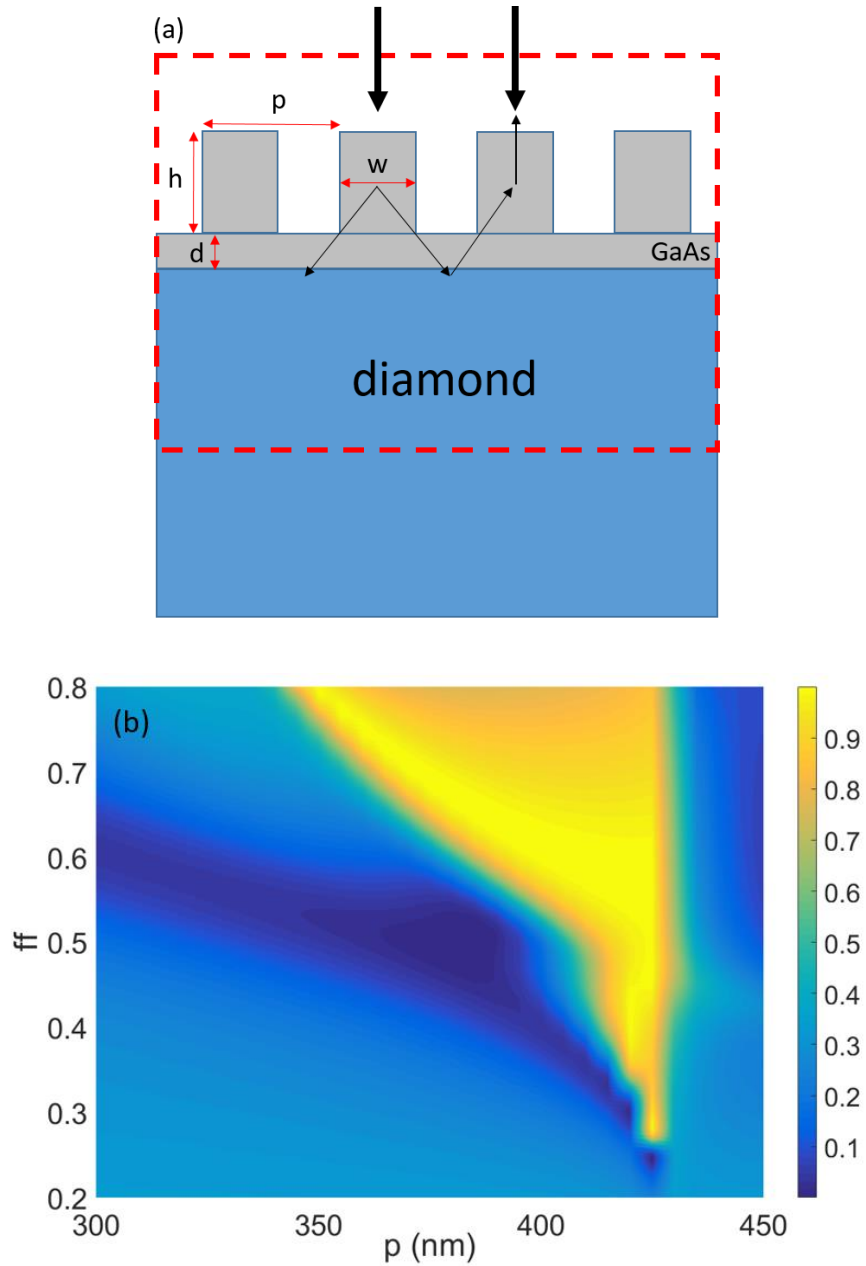


Figure 6.8 (a) GaAs GMR based SWG schematic; (b) Reflectivity map of a GaAs SWG on a diamond substrate, p is the grating periodicity, $ff=w/p$ is filling factor (w is the grating width). Grating depth $h=300$ nm, GaAs layer thickness $d=100$ nm, $\lambda_0=1035$ nm, TM polarization and beam incident from air to the grating structure.

At the design wavelength $\lambda_0 = 1035$ nm, the grating periodicity is between 296 nm and 431 nm. In theory, the propagation coefficient in the waveguide could be calculated. With the destructive interference conditions,

$$\phi_d + \phi_L + \phi_{\text{TIR}} = (2N + 1)\pi \quad (6.4)$$

where ϕ_d is the total phase shift in the two diffraction process, ϕ_L is the phase shift difference due to propagation between the fundamental diffraction and the rediffraction, ϕ_{TIR} is the phase shift due to TIR, and N is an integer. As a result, the optimum waveguide thickness can be estimated. With large refractive index modulation, only numerical calculation is feasible and we will perform numerical analysis from here on. With the wavelength periodicity range estimated above, by repetitive optimizing parameters, including waveguide thickness and grating depth, near unity reflection is observed, as shown in the contour map in Fig. 6.8 (b): 100 nm thick GaAs slab waveguide and 300 nm grating depth, at 1035 nm with TM polarization.

The slab waveguide thickness dependent reflectivity spectra, is shown in Fig. 6.9. More than 99% reflectivity can be achieved over a broad parameter space, which means the design is potentially feasible in fabrication.

In the simulation, the field distribution is also analyzed, as shown in Fig. 6.10 (a), and strong field confinement up to 6 times enhancement is observed. Two 10 nm thick QWs

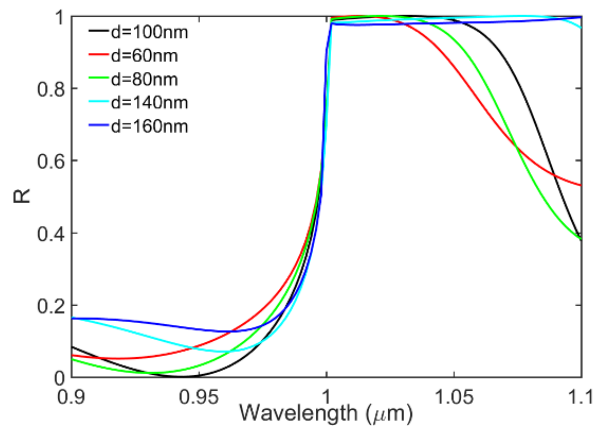


Figure 6.9 Slab waveguide thickness dependent reflectivity spectra. d is the distance from the grating peak to valley. The other parameters are the same as mentioned in Fig. 6.8 (b).

are inserted into the GaAs slab waveguide, as shown in Fig. 6.10 (b). Neglecting the refractive index difference and assuming a constant gain of $g=3500 \text{ cm}^{-1}$ (for InGaAs QW with the carrier density of $4 \times 10^{12} \text{ cm}^{-3}$), about 5% gain could be achieved in one round trip (assuming no other losses), as shown in Fig. 6.10 (c). This is promising for a SDL but the current slab waveguide is too thin to accommodate two QWs in practice. With a 1300 nm thick waveguide and the other parameters the same, the structure still exhibits 99.95% reflectivity. The magnetic field distribution is shown in Fig. 6.11 and multiple periodic gain could be placed at these field antinodes.

In addition to the enhanced gain at the lasing wavelength, enhanced pump absorption could potentially be achieved at the same time. With the GaAs design, at 1035 nm, in-well

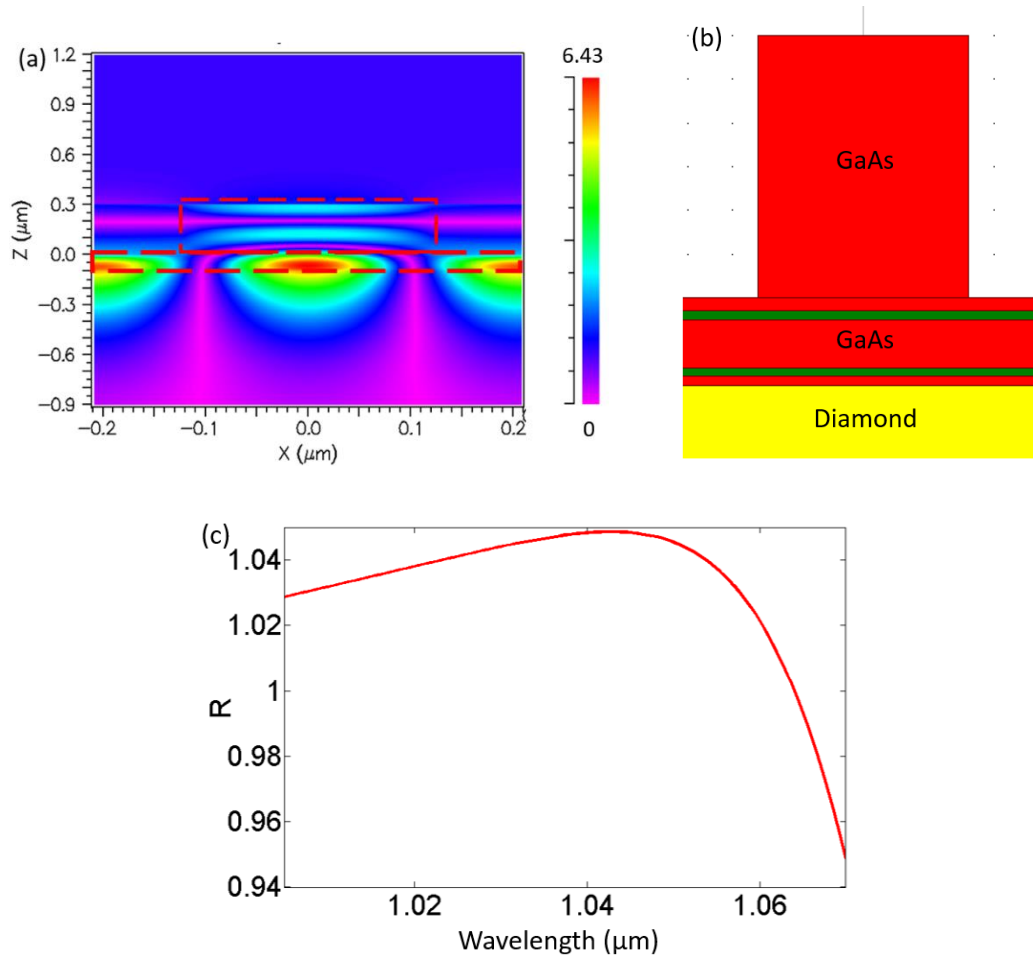


Figure 6.10 (a) Magnetic field (H_y) distribution in the SWG grating structure; (b) Schematic of the SWG with two 10 nm thick QWs with 60 nm separation; (c) Reflection spectrum of the active grating structure with assumed gain $g= 3500 \text{ cm}^{-1}$ in the QW.

pumping scheme is required to avoid surface recombination losses. As a result, the pumping wavelength is close to the laser wavelength and similar field confinement is possible, which enables relatively thin gain structures. In addition, by varying the pump wavelength and angle of incidence, an absorption resonance for the pump is attainable.

Furthermore, by spatially varying the grating parameters, the reflection profile and even the transverse mode can be controlled, which could be useful in micro-optical resonators [28], like the microchip SDL shown in Fig. 6.7 (b).

For a long time, we lacked access to high resolution electron-beam pattern writing, and the parameters proposed above are challenging for conventional interferometric lithography. Recently (08/12/2016), our user proposal on subwavelength grating based SDLs has been accepted by the Center for Integrated Nanotechnologies (CINT). In the next 12 months, we will have access to an electron beam lithography system (NPGS EBL), which has the capability to fabricate 1 mm by 1 mm size grating samples. Firstly, we will fabricate a sample based on GaAs only, to characterize the reflectivity and compare the measurements with simulation results, and optimize the simulation and etching parameters. Then we will fabricate the QW-embedded SWGs, or the gain embedded meta-mirror (GEMM), with enhanced absorption for the pump laser.

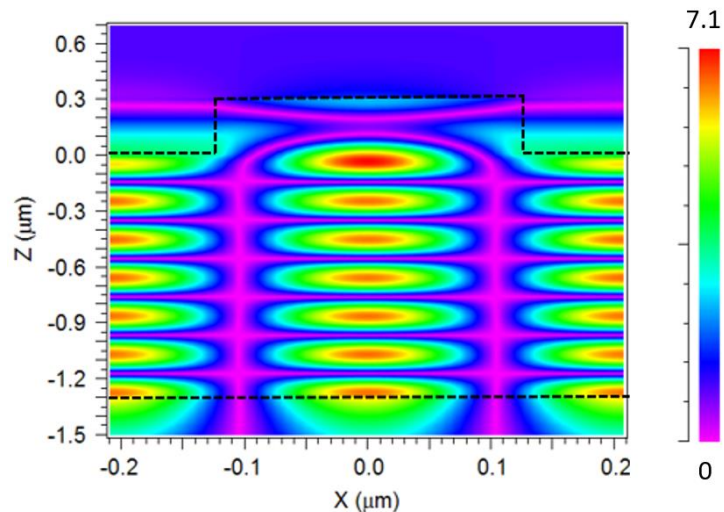


Figure 6.11 Magnetic field distribution for a SWG structure. The dash black line stands for the boundary of SWG. All the parameters are the same as Fig. but the slab waveguide thickness is 1300 nm rather than 100 nm. The calculated reflectivity at 1.035 μm is 99.95%.

6.5 References

- [1] A. J. Maclean, R. B. Birch, P. W. Roth, A. J. Kemp, and D. Burns, "Limits on efficiency and power scaling in semiconductor disk lasers with diamond heatspreaders," *J. Opt. Soc. Am. B*, vol. 26, no. 12, pp. 2228-2236, 2009.
- [2] S.-S. Beyertt, M. Zorn, T. Kubler, H. Wenzel, M. Weyers, A. Giesen, G. Trankler, and U. Brauch, "Optical in-well pumping of a semiconductor disk laser with high optical efficiency," *IEEE J. Quantum Electron.*, vol. 41, no. 12, pp. 1439-1449, 2005.
- [3] M. Kuznetsov, F. Hakimi, R. Sprague, and A. Mooradian, "Design and characteristic of high-power (>0.5 W CW) diode-pumped vertical-external-cavity surface-emitting semiconductor lasers with circular TEM₀₀ beams," *IEEE J. Sel. Top. Quantum Electron.*, vol. 5, no. 3, pp. 561-573, 1999.
- [4] L. Fan, M. Fallahi, J. Hader, A. R. Zakharian, J. V. Moloney, J. T. Murray, R. Bedford, W. Stolz, and S. W. Koch, "Multichip vertical-external-cavity surface-emitting lasers: a coherent power scaling scheme," *Opt. Lett.*, vol. 31, no. 24, pp. 3612-3614, 2006.
- [5] E. J. Saarinen, A. Harkonen, S. Suomalainen, and O. G. Okhotnikov, "Power scalable semiconductor disk laser using multiple gain cavity," *Opt. Express*, vol. 14, no. 26, pp. 12868-12871, 2006.
- [6] L. E. Hunziker, Q.-Z. Shu, D. Bauer, C. Ihli, G. J. Mahnke, M. Rebut, J. R. Chilla, A. L. Caprara, H. Zhou, E. S. Weiss, and M. K. Reed, "Power-scaling of optically pumped semiconductor lasers," *Proc. SPIE*, 6451, 64510A, San Jose, CA, USA, 2007.
- [7] H. A. Haus, "Theory of mode locking with a slow saturable absorber," *IEEE J. Quantum Electron.*, vol. 11, no. 9, pp. 736-746, 1975.
- [8] Z. Sun, T. Hasan, F. Torrisi, D. Popa, G. Privitera, F. Wang, F. Bonaccorso, D. M. Basko, and A. C. Ferrari, "Graphene mode-locked ultrafast laser," *ACS Nano*, vol. 4, no. 2, pp. 803-810, 2010.
- [9] J.-L. Xu, X.-L. Li, Y.-Z. Wu, X.-P. Hao, J.-L. He, and K.-J. Yang, "Graphene saturable absorber mirror for ultra-fast-pulse solid-state laser," *Opt. Lett.*, vol. 36, no. 10, pp. 1948-1950, 2011.
- [10] S. Husaini and R. G. Bedford, "Graphene saturable absorber for high power semiconductor disk laser laser mode-locking," *Appl. Phys. Lett.*, vol. 104, no. 16, pp. 161107, 2014.
- [11] C. A. Zaugg, Z. Sun, V. J. Wittwer, D. Popa, S. Milana, T. S. Kulmala, R. S. Sundaram, M. Mangold, O. D. Sieber, M. Golling, Y. Lee, J. H. Ahn, A. C. Ferrari, and U. Keller, "Ultrafast and widely tunable vertical-external-cavity surface-emitting

- laser, mode-locked by a graphene-integrated distributed Bragg reflector," *Opt. Express*, vol. 21, no. 25, pp. 31548-31559, 2013.
- [12] Y. Wang, G. Huang, H. Mu, S. Lin, J. Chen, S. Xiao, Q. Bao, and J. He, "Ultrafast recovery time and broadband saturable absorption properties of black phosphorus suspension," *Appl. Phys. Lett.*, vol. 107, no. 9, pp. 091905, 2015.
- [13] K. Gbele, A. Laurain, J. Hader, W. Stolz, and J. V. Moloney, "Design and fabrication of hybrid metal semiconductor mirror for high-power VECSEL," *IEEE Photon. Technol. Lett.*, vol. 28, no. 7, pp. 732-735, 2016.
- [14] M. Devautour, A. Michon, G. Beaudoin, I. Sagnes, L. Cerutti, and A. Garnache, "Thermal management for high-power single-frequency tunable diode-pumped VECSEL emitting in the near- and mid-IR," *IEEE J. Sel. Top. Quantum Electron.*, vol. 19, no. 4, pp. 1701108, 2013.
- [15] A. Rantamaki, E. J. Saarinen, J. Lyytikainen, K. Lahtonen, M. Valden, and O. G. Okhotnikov, "High power semiconductor disk laser with a semiconductor-dielectric-metal compound mirror," *Appl. Phys. Lett.*, vol. 104, no. 10, pp. 101110, 2014.
- [16] F. Bruckner, D. Friedrich, T. Clausnitzer, O. Burmeister, M. Britzger, E.-B. Kley, K. Danzmann, A. Tünnermann, and R. Schnabel, "Demonstration of a cavity coupler based on a resonant wavelength grating," *Opt. Express*, vol. 17, no. 1, pp. 163-169, 2009.
- [17] D. Friedrich, B. W. Barr, F. Brückner, S. Hild, J. Nelson, J. Macarthur, M. V. Plissi, M. P. Edgar, S. H. Huttner, B. Sorazu, S. Kroker, M. Britzger, E.-B. Kley, K. Danzmann, A. Tünnermann, , K. A. Strain, and R. Schnabel, "Waveguide grating mirror in a fully suspended 10 meter Fabry-Perot cavity," *Opt. Express*, vol. 19, no. 16, pp. 14955-14963, 2011.
- [18] R. W. Wood, "On a remarkable case of uneven distribution of light in diffraction grating problem," *Phil. Mag.*, vol. 4, pp. 60-65, 1902.
- [19] S. Goeman, S. Boons, B. Dhoedt, K. Vandeputte, K. Caekebeke, P. van Daele, and R. Baets, "First demonstration of highly reflective and highly polarization selective diffraction gratings (GIRO-grainings) for long-wavelength VCSELs," *IEEE Photon. Technol. Lett.*, vol. 9, no. 1205-1207, pp. 10, 1998.
- [20] M. C. Y. Huang, Y. Zhou, and C. J. Chang-Hasnain, "A surface-emitting laser incorporating a high-index-contrast subwavelength grating," *Nature Photon.*, vol. 1, no. 2, pp. 119-122, 2007.
- [21] A. Bunkowski, O. Burmeister, D. Friedrich, K. Danzmann, and R. Schnabel, "High reflectivity grating waveguide coatings for 1064 nm," *Class. Quantum Grav.*, vol. 23, pp. 7297-7303, 2006.

- [22] D. Fattal, J. Li, Z. Peng, M. Fiorentino, and R. G. Beausoleil, "Flat dielectric grating reflectors with focusing abilities," *Nature Photon.*, vol. 4, pp. 466-470, 2010.
- [23] M. Grande, M. A. Vincenti, T. Stomeo, G. V. Bianco, D. de Ceglia, N. Aközbek, V. Petruzzelli, G. Bruno, M. De Vittorio, M. Scalora, and A. D'Orazio, "Graphene-based absorber exploiting guided mode resonances in one-dimensional gratings," *Opt. Express*, vol. 22, no. 25, pp. 31511-31519, 2014.
- [24] A. Hessel and A. A. Oliner, "A new theory of Wood's anomalies on optical gratings," *Appl. Opt.*, vol. 4, no. 10, pp. 1275-1297, 1965.
- [25] S. S. Wang, R. Magnusson, J. S. Bagby, and M. G. Moharam, "Guided-mode resonances in planar dielectric-layer diffraction gratings," *J. Opt. Soc. Am. A*, vol. 7, no. 8, pp. 1470-1474, 1990.
- [26] R. Magnusson, "Wideband reflectors with zero-contrast gratings," *Opt. Lett.*, vol. 39, no. 15, pp. 4337-4340, 2014.
- [27] D. Rosenblatt, A. Sharon, and A. A. Friesem, "Resonant grating waveguide structure," *IEEE J. Quantum Electron.*, vol. 33, no. 11, pp. 2038-2059, 1997.
- [28] M. Kuznetsov, M. Stern, and J. Coppeta, "Single transverse mode optical resonators," *Opt. Express*, vol. 13, no. 1, pp. 171-181, 2005.